Department of Advanced Materials Engineering
Faculty of Physics, Astronomy and Applied Computer Science
Jagiellonian University

# *Structure and properties of macromolecular surfaces and patterns for biotechnological applications*

**Katarzyna Gajos**

A thesis submitted for the degree of Ph.D. in biophysics

advisor: prof. dr. hab Andrzej Budkowski
auxiliary advisor: dr hab. Jakub Rysz

KRAKÓW April 2017

Wydział Fizyki, Astronomii i Informatyki Stosowanej
Uniwersytet Jagielloński

# Oświadczenie

Ja niżej podpisana *Katarzyna Gajos* (nr indeksu: 1039650) doktorantka Wydziału Fizyki, Astronomii i Informatyki Stosowanej Uniwersytetu Jagiellońskiego oświadczam, że przedłożona przeze mnie rozprawa doktorska pt. „*Structure and properties of macromolecular surfaces and patterns for biotechnological applications*" jest oryginalna i przedstawia wyniki badań wykonanych przeze mnie osobiście, pod kierunkiem *prof. dr hab. Andrzeja Budkowskiego*. Pracę napisałam samodzielnie.

Oświadczam, że moja rozprawa doktorska została opracowana zgodnie z Ustawą o prawie autorskim i prawach pokrewnych z dnia 4 lutego 1994 r. (Dziennik Ustaw 1994 nr 24 poz. 83 wraz z późniejszymi zmianami).

Jestem świadoma, że niezgodność niniejszego oświadczenia z prawdą ujawniona w dowolnym czasie, niezależnie od skutków prawnych wynikających z ww. ustawy, może spowodować unieważnienie stopnia nabytego na podstawie tej rozprawy.

Kraków, dnia ...1.09.2017....

.....Katarzyna Gajos.....
*podpis doktorantki/doktoranta*

# *Streszczenie*

Celem niniejszej pracy jest rozwój metod charakteryzacji struktury i właściwości powierzchni i wzorów makromolekularnych w celu optymalizacji działania ich zastosowań biotechnologicznych. Rozważane są dwie klasy wzorów i powierzchni: sfunkcjonalizowanych za pomocą szczepionych łańcuchów polimerowych oraz pokrytych nanowarstwami biologicznego rozpoznawania międzymolekularnego. Pierwszy rodzaj powierzchni znajduje zastosowanie w rozwoju podłoży biofunkcjonalnych, natomiast drugi jest stosowany w biosensorach oraz urządzeniach analitycznych typu „lab-on-a-chip". Do charakteryzacji powierzchni zastosowano spektrometrię masową jonów wtórnych z analizatorem czasu przelotu (ang. TOF-SIMS), obejmującą mody spektroskopowy i obrazowania oraz wielowymiarową analizę danych (w szczególności analizę głównych składników ang. PCA), a także inne techniki analizy powierzchni takie jak pomiar kąta zwilżania wodą, mikroskopię sił atomowych (ang. AFM), mikroskopię fluorescencyjna, spektroskopię fotoelektronów (ang. XPS) oraz elipsometrię.

Kontekst naukowy pracy oraz przegląd literatury został przedstawiony w rozdziale 1, natomiast zastosowane techniki eksperymentalne zostały opisane w rozdziale 2. Rozdział 3 stanowi omówienie zbioru 5 artykułów naukowych (Artykuły I do V).

**Artykuł I** oraz **Artykuł II** opisują proces wytworzenia i charakteryzację podłoży sfunkcjonalizowanych za pomocą wrażliwych na bodźce polimerów szczepionych jednorodnie do powierzchni oraz wzorów polimerów szczepionych (obdarzonych ładunkiem elektrycznym) wytworzonych z wykorzystaniem techniki litografii elektronowej. Podłoża takie mogę znaleźć zastosowanie w tworzeniu innowacyjnych powierzchni o kontrolowanym przez człowieka oddziaływaniu z białkami.

W **Artykule I** prezentowane jest nowe podejście do tworzenia pokryć polimeru POEGMA246 (poli(metakrylanu eteru etylenowego glikolu oligoetylenowego)) poprzez polimeryzację z powierzchni oligomerów nadtlenkowych szczepionych do zmodyfikowanej uprzednio powierzchni szkła. Kompleksowa charakteryzacja uzyskanych pokryć za pomocą różnych technik powierzchniowych (w tym analiza temperaturowej zależności zwilżalności i topografii rozszerzona o pomiary w warunkach różnego pH) ujawniła ich niespodziewane właściwości, takie jak wrażliwość na dwa różne bodźce (temperaturę i pH) oraz silną zależność adsorpcji białek od pH. W celu optymalizacji warunków wytwarzania pokryć, temperaturowa zależność ich zwilżalności została zbadana dla różnych czasów polimeryzacji.

**Artykuł II** opisuje udane wysokorozdzielcze wytwarzanie, z wykorzystaniem litografii elektronowej, wzorów szczepionych polimerów, które nie było dotychczas szczegółowo badane. Submikrometryczne struktury biokompatybilnego polimeru PDMAEMA (poli(metakrylanu dimetyloaminoetylu)) zostały szczepione z filmów polimeru fluorowego a następnie zmodyfikowane do formy polikationu i wykorzystane do elektrostatycznego wiązania barwników organicznych oraz

białek. Połączenie technik mikroskopowych i spektroskopowych, w tym analizy TOF-SIMS rozszerzonej do wysokorozdzielczego chemicznego obrazowania wzorów polimerowych na podłożu polimerowym oraz molekularnej charakteryzacji ich późniejszej modyfikacji, potwierdziło efektywną funkcjonalizację powierzchni. Dodatkowo, wyniki procesu litograficznego szczepienia polimerów zostały porównane dla różnych warunków naświetlania wiązką elektronów w celu wyboru tych dających najlepsze rezultaty pod kątem zastosowań biotechnologicznych.

Wyniki charakteryzacji wielokrokowych protokołów biofunkcjonalizacji i testu immunologicznego, które wprowadzają kolejno różne molekuły do nanowarstw rozpoznawania międzymolekularnego osadzanych na powierzchni przetwornika krzemowego, przedstawione są w **Artykułach III**, **IV** i **V**. Charakteryzacja powierzchni biosensora, rozbudowana do wielokrokowej analizy używającej wielu technik, została zademonstrowana dla urządzenia typu „lab-on-a-chip" wykrywającego szkodliwe substancje w żywności, które zostało wyprodukowane w ramach projektu 7FP Wspólnoty Europejskiej o nazwie FOODSNIFFER. W szczególności, zmiany chemii powierzchni wyznaczone zostały za pomocą metody TOF-SIMS rozróżniającej poszczególne molekuły organiczne stosowane w protokołach biofunkcjonalizacji i testu immunologicznego. Subtelne zmiany w biomolekularnym składzie nanowarstw, zachodzące dla poszczególnych kroków protokołu, zostały wykryte i sklasyfikowane za pomocą wielowymiarowej analizy danych TOF-SIMS. Dodatkowo, dane na temat nanostruktury powierzchni i jej pokrycia molekułami - dostarczone dzięki zastosowaniu różnych technik badawczych - ujawniły złożone zjawiska powierzchniowe, które mogą wpływać na aktywność biomolekularną a nawet utrudniać wykrycie analitu (np. desorpcja białka detekcyjnego). Jest to szczególnie cenne w odniesieniu do optymalizacji działania biosensorów.

Przedmiotem badań **Artykułu III** jest protokół biofunkcjonalizacji stosowany w celu detekcji (alergenu) białka krowiej κ-kazeiny w mleku kozim. W artykule tym narzędzia analizy powierzchniowej spektrometrii TOF-SIMS (tj. obrazowanie i analiza molekularna) zostały rozwinięte do kontroli „in-situ" mikro-strukturyzowanych obszarów biosensorycznych na scalonym układzie „lab-on-a-chip". Dodatkowo, zbadana została jednorodność wzorów białka detekcyjnego, otrzymanych za pomocą automatycznego robota nakrapiającego i dopasowanych do obszarów biosensorycznych układu „lab-on-a-chip". Analiza ta pozwoliła na wybór optymalnych warunków immobilizacji białka detekcyjnego prowadząc do znacznej poprawy powtarzalności odpowiedzi biosensora i czułości detekcji.

W **Artykule IV** wyznaczony został, na powierzchni krzemu imitującej przetwornik biosensoryczny, skład molekularny oraz ułożenie i orientacja białek użytych w kolejnych krokach protokołu do wykrywania (mykotoksyny) ochratoksyny A. W tym przypadku zastosowany został test immunologiczny typu pośredniego, w którym sygnał wykrycia analitu zostaje wzmocniony przez powierzchniową reakcję pomiędzy przeciwciałem pierwszo- i drugorzędowym. W pracy tej wprowadzona została nowa metoda oszacowania masy powierzchniowej poszczególnych białek, która łączy informację o całkowitej powierzchniowej gęstości białek, dostarczaną przez elipsometrię, i o

składzie molekularnym, uzyskiwaną z analizy TOF-SIMS. Pozwala to na określenie stosunku molowego specyficznie wiążących się biomolekuł. Ponadto, badania nad orientacją przeciwciał immobilizowanych na powierzchni zostały po raz pierwszy rozszerzone do analizy orientacji zarówno przeciwciała pierwszo- jak i drugorzędowego. Wielowymiarowa analiza danych TOF-SIMS pozwoliła określić i porównać orientację przeciwciał zaadsorbowanych za pomocą powierzchniowych wiązań specyficznych i unieruchomionych bezpośrednio na podłożu.

Zaprezentowana analiza protokołów biofunkcjonalizacji powierzchni biosensorów została rozszerzona w **Artykule V** o porównanie dwóch sposobów nanoszenia roztworu białka detekcyjnego: za pomocą automatycznego robota nakrapiającego (przez nakładające się krople nanolitrowe) i ręcznie za pomocą pipety (jednej mikrolitrowej kropli). Zbadano również wpływu początkowej gęstości powierzchniowej białka detekcyjnego na przebieg następnych kroków protokołu funkcjonalizacji i detekcji analitu. Badany protokół mający służący do detekcji (pestycydu) tiabendazolu był analizowany zarówno na płaskich powierzchniach krzemowych jak i na mikro-strukturyzowanych powierzchniach biosensorów na układzie scalonym. Analiza nanostruktury utworzonych warstw białek, ich gęstości powierzchniowej oraz zawartości białka detekcyjnego ujawniła zaskakującą desorpcję białka detekcyjnego, zależną od jego początkowej gęstości powierzchniowej, zachodzącą podczas procedury blokowania i wpływającą na efektywność wiązania analitu przez uzyskane nanowarstwy rozpoznawania międzymolekularnego.

Podsumowanie i końcowe wnioski rozprawy doktorskiej zaprezentowane zostały w rozdziale 4.

## *Thesis overview*

This Thesis aims to develop the methods that characterize the structure and properties of *macromolecular surfaces and patterns* in order to enable optimized performance of their biotechnological applications. Two classes of surfaces (and their patterns), *functionalized with grafted polymers* as well as covered with molecular *biorecognition nanolayers*, are considered. The former are used to develop biofunctional substrates whereas the latter serve for biosensor and lab-on-a-chip applications. Methods applied to surface characterization involve Time of Flight Secondary Ion Mass Spectrometry (TOF-SIMS) - with spectroscopic and imaging modes and multivariate data analysis (Principal Component Analysis or PCA), and other surface science techniques such as water contact angle measurements, Atomic Force Microscopy (AFM), fluorescence microscopy, X-ray Photoelectron Spectroscopy (XPS) and Ellipsometry.

The scientific background and literature review is presented in Chapter 1, while the experimental techniques used are described in Chapter 2. Chapter 3 describes 5 articles (Paper I to Paper V).

Fabrication and characterization of solid substrates functionalized by a *stimuli-responsive polymer grafted over all their surface* and *patterned with a lithographically grafted charged polymer* is described in **Paper I** and **Paper II**, respectively, with the aim to create innovative interactive interfaces between solid substrates and proteins.

In **Paper I** a novel approach to fabrication of poly(oligo(ethylene glycol)ethyl ether methacrylate) (POEGMA246) coatings via polymerization from oligoperoxide grafted to pre-modified glass substrate is presented. The complex examination of coatings with multiple surface science techniques (with temperature-dependent analysis extended to various pH) reveals unexpected material properties such as dual thermal and pH sensitivity and strong protein adsorption response to pH. Thermally-dependent wettability is analyzed for the coatings with different polymerization times to determine optimal fabrication conditions.

**Paper II** demonstrates a successful application of e-beam lithography to high-resolution polymer grafting, a problem which has not been studied in detail before. Submicrometer structures of biocompatible poly(dimethylaminoethyl methacrylate) (PDMAEMA) are grafted from fluoropolymer film, postpolymerization-modified to polycationic form and applied to bind charged organic dyes and functional proteins. Combined microscopic and spectroscopic techniques, with TOF-SIMS analysis extended to high-resolution chemical imaging of polymer-on-polymer patterns and molecular characterization of post-polymerization modification, reveal effective formation of functionalized surfaces. Additionally, lithographic grafting with varied e-beam exposure conditions (energy, dose) is compared to determine the conditions advantageous for bioapplications.

Multi-step biofunctionalization and assay protocols, that introduce in sequence different molecules to *biorecognition nanolayers on silicon transducers*, are examined in **Papers III, IV** and **V**. Biosensor surface characterization, developed into multi-step and multi-technique analysis, is demonstrated for

the lab-on-a-chip device detecting harmful substances in food fabricated in the framework of the European FP7 project FOODSNIFFER. Namely, changes in surface chemistry are determined with TOF-SIMS resolving different organic molecules applied in the protocols. Such subtle changes in biomolecular composition varied between different protocol steps are also detected and classified by multivariate analysis. Additionally, complex surface phenomena, that might modify biomolecular activity and even hamper analyte detection (e.g. probe desorption), are revealed by data on layers' nanostructure and molecular surface coverage provided by the multi-technique analysis. This is particularly valuable with respect to biosensor performance optimization.

The protocol applied for detection of (allergen) bovine κ-casein in goat milk is examined in **Paper III**. Here, the extension of surface analytical TOF-SIMS tools (imaging and molecular characterization) enables in-situ chemical inspection of micro-structured on-chip sensors. In addition, examination of uniformity of *probe patterns*, obtained with robotic spotter to match the sensing areas, provides optimal immobilization conditions resulting in a considerable improvement of both biosensor response repeatability and detection sensitivity.

In **Paper IV** the arrangement, composition and orientation of proteins employed in the protocol aimed to detect (mycotoxin) ochratoxin A is specified step-by-step for silicon surface imitating biosensor transducer. Indirect immunoassay used involves surface reaction with primary antibody and a secondary antibody as a means to increase the specific signal. A novel method to evaluate individual mass loadings of all applied proteins is introduced that combines total protein surface density, provided by ellipsometry, with compositional analysis from TOF-SIMS. Based on this, binding molecular ratio can be evaluated. Additionally, for the first time the research defining orientation of immobilized antibodies is extended to cover molecular orientation of both the primary and secondary antibody. A multivariate TOF-SIMS analysis provides some hints about the orientation of the immunoadsorbed antibodies as compared to the orientation the same antibodies acquire when directly immobilized onto the surfaces by spotting.

Evaluation of biofunctionalization protocols is extended in **Paper V** to comparison of the probe solution deposition by contact pin-printing and hand macro-spotting as well as to examination of the impact of the initial probe surface density on protein layers created in subsequent steps. Namely, a protocol for the immuno-detection of the (fungicide) thiabendazole is examined on planar silicon surfaces and on micro-structured on-chip sensors. Analyzes of the nanostructure, surface density and probe composition of biorecognition layers reveals the surprising probe desorption, dependent on its initial surface density, taking place during the blocking procedure and affecting consequently also the immunoreaction efficiency.

The summary and final conclusions of this Thesis are presented in Chapter 4.

# *List of papers and author contribution*

This Thesis consists of five papers (each associated with supplementary data) published in peer-reviewed scientific journals from the Master Journal List. All these papers listed below are addressing the issue of examination of structure and properties of the macromolecular surfaces for biotechnological applications. Please note that surname of Thesis author 'Fornal' has changed to 'Gajos' due to marriage.

- **Paper I:** *Temperature and pH dual-responsive POEGMA-based coatings for protein adsorption*, Y. Stetsyshyn, K. Fornal, J. Raczkowska, J. Zemla, A. Kostruba, H. Ohar, M. Ohar, V. Donchak, K. Harhay, K. Awsiuk, J. Rysz, A. Bernasik, A. Budkowski. Journal of Colloid and Interface Science 2013, *411*, 247–256. http://dx.doi.org/10.1016/j.jcis.2013.08.007

- **Paper II:** *Electron-beam lithographic grafting of functional polymer structures from fluoropolymer substrates*, K. Gajos, V. A. Guzenko, M. Dubner, J. Haberko, A. Budkowski, C. Padeste. Langmuir 2016, 32, 10641-10650. http://dx.doi.org/10.1021/acs.langmuir.6b02808

- **Paper III:** *Imaging and chemical surface analysis of biomolecular functionalization of monolithically integrated on silicon Mach-Zehnder interferometric immunosensors*, K. Gajos, M. Angelopoulou, P. Petrou, K. Awsiuk, S. Kakabakos, W. Haasnoot, A. Bernasik, J. Rysz, M. M. Marzec, K. Misiakos, I. Raptis, A. Budkowski. Applied Surface Science 2016, 385, 529-542. http://dx.doi.org/10.1016/j.apsusc.2016.05.131

- **Paper IV:** *Indirect immunoassay on functionalized silicon surface: Molecular arrangement, composition and orientation examined step-by-step with multi-technique and multivariate analysis*, K. Gajos, A. Budkowski, V. Pagkali, P. Petrou, M. Biernat, K. Awsiuk, J. Rysz, A. Bernasik, K. Misiakos, I. Raptis, S. Kakabakos. Colloids and Surfaces B: Biointerfaces 2017, 150, 437-444. http://dx.doi.org/10.1016/j.colsurfb.2016.11.009

- **Paper V:** *Contact pin-printing of albumin-fungicide conjugate for silicon nitride-based sensors biofunctionalization: Multi-technique surface analysis for optimum immunoassay performance*, K. Gajos, A. Budkowski, Z. Tsialla, P. Petrou, K. Awsiuk, P. Dąbczyński, A. Bernasik, J. Rysz, K. Misiakos, I. Raptis, S. Kakabakos. Applied Surface Science 2017, 410, 79-86. http://dx.doi.org/10.1016/j.apsusc.2017.03.100

Accordingly to the enclosed authors contributions forms, the personal contribution of Thesis author to the individual articles can be specified as follows:

- **Paper I:** Thesis author made substantial original contributions to the article (reflected by the second position on the author list) involving following activities: planning of the methodology of coatings characterization and protein adsorption experiment, performance of protein adsorption experiment, data collection (water contact angle measurements, AFM and fluorescence microscopy), data analysis and interpretation, presentation of results (design of 5 figures), participation in the preparation of the manuscript.

- **Paper II:** Thesis author was a lead author of the article. The author's personal contribution involved development of methodology for samples characterization and protein adsorption experiments, design of the research and selection of methods, samples preparation (polymer grafting, post-polymerization modification, adsorption of protein), data collection (AFM, TOF-SIMS and fluorescence microscopy), data analysis and interpretation, presentation of results, literature research and preparation of the manuscript.

- **Paper III:** Thesis author was a lead author of the article and served as corresponding author. The author has contributed to the following elements of this article: development of concept of direct characterization of integrated on chip biosensors with TOF-SIMS and biomolecular composition evaluation, design of studies on biosensor surface characterization and selection of experimental methods, data collection (AFM and TOF-SIMS), multivariate PCA analysis of TOF-SIMS data, data analysis and interpretation, presentation of results, literature research, participation in the preparation of the manuscript.

- **Paper IV:** Thesis author was a lead author of the article and served as corresponding author. The author personal contribution involved development of concept of mass loadings of different molecules determination and antibody orientation determination, design of studies on biofunctionalized silicon surface characterization and planning of the methodology, data collection (AFM, ellipsometry and TOF-SIMS), multivariate PCA analysis of TOF-SIMS data, data analysis and interpretation, presentation of results, literature research, participation in the preparation of the manuscript.

- **Paper V:** Thesis author was a lead author of the article and served as corresponding author. The author personal contribution involved development of concept of contact pin-printing and hand macro-spotting solution deposition approaches comparison, design of studies on biofunctionalized silicon surface characterization and selection of experimental methods, data collection (AFM, ellipsometry and TOF-SIMS), data analysis and interpretation, presentation of results, literature research and preparation of the manuscript.

**Related papers not included in this Thesis:**

Please note that surname of Thesis author 'Fornal' has changed to 'Gajos' due to marriage.

- *Temperature and pH dual-responsive coatings of oligoperoxide-graft-poly(N-isopropylacrylamide): Wettability, morphology, and protein adsorption*, Y. Stetsyshyn, J. Zemla, T. Zolobko, K. Fornal, A. Budkowski, A. Kostruba, V. Donchak, K. Harhay, K. Awsiuk, J. Rysz, A. Bernasik, S. Voronov, , Journal of Colloid and Interface Science 2012, 387, 95-105. http://dx.doi.org/10.1016/j.jcis.2012.08.007

- *Temperature-responsive peptide-mimetic coating based on poly (N -methacryloyl- l -leucine): Properties , protein adsorption and cell growth*, J. Raczkowska, M. Ohar, Y. Stetsyshyn, J. Zemła, K. Awsiuk, J. Rysz, K. Fornal, A. Bernasik, H. Ohar, Colloids and Surfaces B: Biointerfaces 2014, 118, 270–279. http://dx.doi.org/10.1016/j.colsurfb.2014.03.049

- *Imaging and spectroscopic comparison of multi-step methods to form DNA arrays based on the biotin-streptavidin system*, K. Gajos, P. Petrou, A. Budkowski, K. Awsiuk, A. Bernasik, K. Misiakos, J. Rysz, I. Raptis, S. Kakabakos, Analyst 2015, 140, 1127-1139. http://dx.doi.org/10.1039/c4an00929k

(also advertised as a *back cover* of Volume 140, Issue 4, p.1360 http://dx.doi.org/10.1039/C5AN90015H)

- *Improved DNA microarray detection sensitivity through immobilization of preformed in solution streptavidin/biotinylated oligonucleotide conjugates*, E. Mavrogiannopoulou, P.S. Petrou, G. Koukouvinos, D. Yannoukakos, A. Siafaka-Kapadai, K. Fornal, K. Awsiuk, A. Budkowski, S.E. Kakabakos, Colloids abd Surfaces B: Biointerfaces 2015, 128, 464-472. http://dx.doi.org/10.1016/j.colsurfb.2015.02.045

- *Immobilization and detection of platelet-derived extracellular vesicles on functionalized silicon substrate: cytometric and spectrometric approach*, K. Gajos, A. Kamińska, K. Awsiuk, A. Bajor, K. Gruszczyński, A. Pawlak, A. Żądło, A. Kowalik, A. Budkowski, E. Stępień, Analitical and Bioanalitycal Chemistry 2017, 409, 1109-1119. http://dx.doi.org/10.1007/s00216-016-0036-5

# *Contents*

**STRESZCZENIE** ..... **1**

**THESIS OVERVIEW** ..... **5**

**LIST OF PAPERS AND AUTHOR CONTRIBUTION** ..... **7**

**1. INTRODUCTION** ..... **13**

1.1. POLYMER GRAFTING ..... 13
1.2. CHARACTERIZATION OF SURFACES FUNCTIONALIZED BY POLYMER GRAFTING ..... 15
1.3. SURFACE FUNCTIONALIZATION FOR BIORECOGNITION ..... 16
1.4. CHARACTERIZATION OF BIORECOGNITION LAYERS ..... 18

**2. SURFACE CHARACTERIZATION TECHNIQUES** ..... **20**

2.1. ATOMIC FORCE MICROSCOPY ..... 20
2.2. FLUORESCENCE MICROSCOPY ..... 21
2.3. SPECTROSCOPIC ELLIPSOMETRY ..... 22
2.4. X-RAY PHOTOELECTRON SPECTROSCOPY ..... 23
2.5. TIME-OF-FLIGHT SECONDARY ION MASS SPECTROMETRY ..... 24

**3. RESULTS** ..... **27**

3.1. PAPER I: TEMPERATURE AND PH DUAL-RESPONSIVE POEGMA-BASED COATINGS FOR PROTEIN ADSORPTION ..... 27
3.2. PAPER II: ELECTRON-BEAM LITHOGRAPHIC GRAFTING OF FUNCTIONAL POLYMER STRUCTURES FROM FLUOROPOLYMER SUBSTRATES ..... 29
3.3. PAPER III: IMAGING AND CHEMICAL SURFACE ANALYSIS OF BIOMOLECULAR FUNCTIONALIZATION OF MONOLITHICALLY INTEGRATED ON SILICON MACH-ZEHNDER INTERFEROMETRIC IMMUNOSENSORS ..... 31
3.4. PAPER IV: INDIRECT IMMUNOASSAY ON FUNCTIONALIZED SILICON SURFACE: MOLECULAR ARRANGEMENT, COMPOSITION AND ORIENTATION EXAMINED STEP-BY-STEP WITH MULTI-TECHNIQUE AND MULTIVARIATE ANALYSIS ..... 33
3.5. PAPER V: CONTACT PIN-PRINTING OF ALBUMIN-FUNGICIDE CONJUGATE FOR SILICON NITRIDE-BASED SENSORS BIOFUNCTIONALIZATION: MULTI-TECHNIQUE SURFACE ANALYSIS FOR OPTIMUM IMMUNOASSAY PERFORMANCE ..... 35

**4. CONCLUSIONS** ..... **37**

**REFERENCES** ..... **39**

**LIST OF ABBREVIATIONS** ..... **45**

**ACKNOWLEDGEMENTS** ..... **47**

# 1. Introduction

Surface functionalization is a crucial issue for a large number of applications of solid substrates. In particular, desired surface properties are often required for their biotechnological applications involving interactive interfaces, anti-fouling surfaces, cell culture substrates, scaffolds for tissue engineering, assays or biosensors. Functionalization of the materials' surface allows for tailoring interface properties while preserving the materials' bulk characteristics. Surface properties desired in biotechnology such as biocompatibility, anti-fouling, patterning, controlled interactions with proteins and cells or biorecognition can be achieved by modification of surface physical properties, introduction of functional chemical groups and immobilization of capturing molecules. In line with this demand, a great variety of surface functionalization methods were established depending on the type of applied solid material and required surface properties.

## *1.1. Polymer grafting*

Polymer grafting is a versatile method of adapting physico-chemical properties of a variety of materials, e.g. metals, glasses, polymers or biomaterials, by formation of polymer chains on their surface. The main advantage of this surface functionalization method is an attachment of polymer chains through chemical bonds providing a long stability of formed layers as compared to different polymeric coatings. Stability of grafted polymer layers enables their post-polymerization modification that opens the possibility of introducing a large variety of functional groups. Polymer grafting can be accomplished either by "grafting to" or "grafting from" approach. In the "grafting to" approach, pre-synthesized polymer chains are chemically bonded to the surface via functional anchor groups resulting, however, in limited surface density and thickness. In contrast, the "grafting from" method involves the in-situ growing of polymer chains from initiators bounded to the surface that allows to obtain a very high surface density [1]. The growth of polymer chains in the free radical polymerization process can be initiated by reactive species generated or introduced on the surface. Additionally the control over chains density, polydispersity and composition can be achieved by controlled radical polymerizations methods [2]. In case of polymeric substrates, initiators of the polymerization reaction (e.g. free radicals, peroxides, hydroperoxides) can be created directly on surface upon plasma treatment or irradiation with photons or particle beam what is termed radiation-induced grafting [3] (Fig. 1). Depending on type of radiation and irradiation conditions, grafting of polymer chains can be limited to the surface or extended into bulk of the polymer support [3,4].

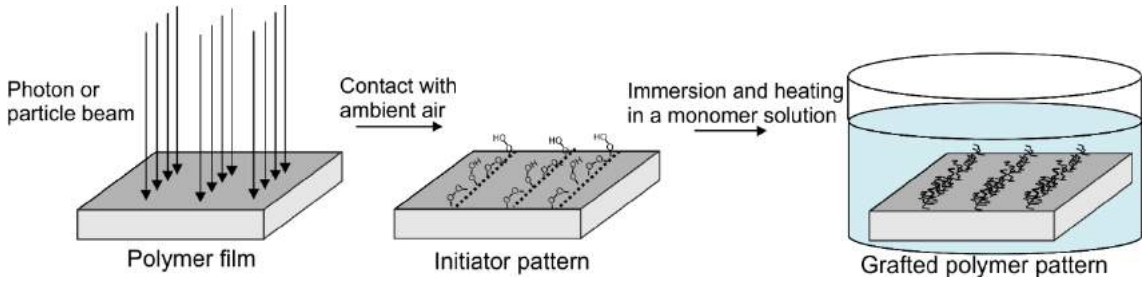


***Figure 1:*** *Scheme of the radiation-induced grafting process. First, a polymer film is exposed to photon or particle beam to create radical species on the surface, which are stabilized as hydroperoxides or peroxides. After immersion into monomer solution and heating these initiate the graft polymerization.*

Polymer grafting enables a modification of solid substrates' surface with a great variety of functional polymers. For applications in biotechnology polymers with desirable or controlled interactions with biomolecules such as biocompatible, anti-fouling, charged or stimuli-responsive polymers are particularly interesting. The stimuli-responsive polymers significantly and reversibly change their physico-chemical properties upon external stimuli such as temperature, pH, light or magnetic field. In particular, grafting of responsive polymers which have a capacity to change their affinity towards proteins and cells is attractive for applications such as bioseparation, drug delivery or tissue engineering [5]. For temperature and pH-responsive polymers, a slight change of environmental conditions results most often in transition from hydrophilic to hydrophobic state accompanied by conformational transition and macroscopic phase separation. In case of polymer chains covalently grafted to surface this phase transition is demonstrated by change of surface wettability and chains' conformation from hydrophilic loose coils (brushes regime) to hydrophobic collapsed chains (mushroom regime) (Fig. 2). For thermos-responsive polymers in water the transition is caused by intramolecular interactions which at certain temperature start to dominate over intermolecular interactions, by hydrogen bonds, between polymer chains and water. In turn, for pH-responsive polymers the transition mechanism is associated with protonation/deprotonation of polymer's side groups (generally carboxyl or amine groups) which influences formation of intramolecular hydrogen bonds [5]. Nowadays, considerable effort has been directed towards development of polymer coatings sensitive to more than one stimuli. Multi stimuli-responsive properties of grafted polymer chains are most often achieved by copolymerization of two or more responsive monomers or attachment of additional side chain to the responsive polymer backbone [6]. Recently, the dual temperature and pH sensitivity of thermo-responsive polymer coatings fabricated by grafting from the surface of oligoperoxide layer was demonstrated [7]. *Multi-responsiveness has implied the need for the development of surface analysis at various temperatures and pH conditions.*

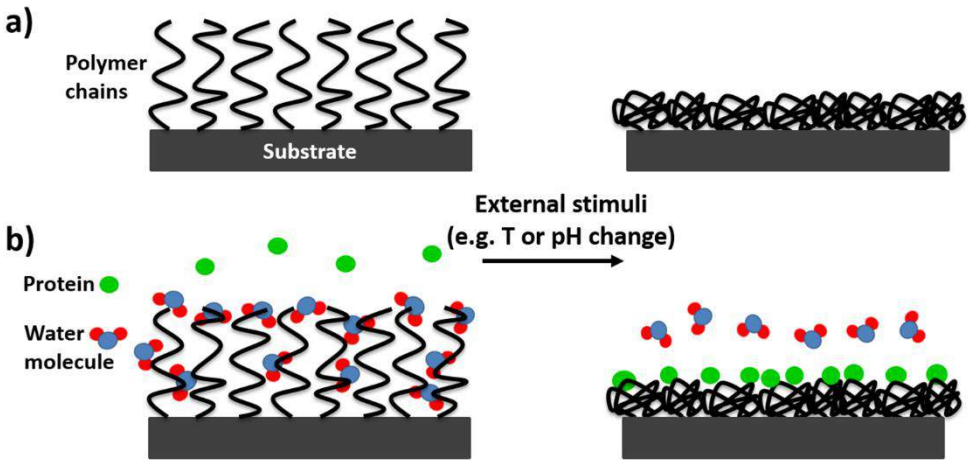


***Figure 2:*** *(a) A conformational transition of stimuli-responsive polymer chains grafted to surface from loose coils to collapsed chains upon external stimuli, (b) often associated with a change of surface wettability and affinity towards proteins.*

A number of possible application of solid substrates functionalized by polymer grafting significantly increases when spatial control over the grafted area is available. Formation of patterns with desired physical and chemical surface properties is especially useful in biotechnology for patterning of proteins and cells, which serves for bioassay, biosensing and tissue engineering applications. The patterned polymer grafting can be accomplished by creation of initiator patterns or subsequent patterning of homogenous grafted polymer layer. For this purpose various methods of spatially-resolved deposition (e.g. micro-contact printing, scanning probe lithography, dip-pen lithography) and modification (e.g. photolithography, electron-beam lithography, EUV-interference lithography) are applied [8]. Depending on the applied technique, patterns on different length scale and with different resolution (up to tens of nanometers [9]) can be achieved. Particularly in case of radiation-induced polymer grafting the irradiation techniques can be easily combined with structuring technologies that enable a direct generation of initiator patterns [4]. Radiation-induced patterned grafting with extreme UV [4,10], X-ray [11] and ions [12] has been established so far. However, only preliminary experiments have been reported on application of electrons for generations of grafted polymer patterns by means of radiation-induced grafting [4,10].

### *1.2. Characterization of surfaces functionalized by polymer grafting*

For the purpose of development of methods of surface functionalization by polymer grafting, the comprehensive characterization of resulted substrates is extremely important. In particular,

examination of surface functionality, e.g. for stimuli-responsive coatings, and spatial resolution of modification by patterned polymer grafting is highly required but also challenging.

The response of stimuli-responsive coatings to external stimuli is most often reflected in changes of the coatings' wettability, thickness or morphology that can be determined by water contact angle measurements [7,13–15], ellipsometry [16,17] and AFM [7,18], respectively. In turn, the coatings' response of protein adsorption is usually studied by fluorescence microscopy [7] (also combined with semi-quantitative integral geometry approach [7,19]), ellipsometry [20,21], radiolabeling [22] or TOF-SIMS [7,15,23] accompanied by Principal Component Analysis [7,23]. However, the necessity of the control and progressive change of environmental conditions (e.g. temperature and pH) often require an adjustment of experimental setups and protocols.

Although there are many techniques providing chemical and structural analysis of uniform grafted polymer layers, only few of them have a sufficient lateral resolution for examination of micro- and nanopatterned surfaces. Microscopy techniques, such as AFM and scanning electron microscopy, are commonly applied to characterization of grafted polymer structures [24]. The most widely used AFM microscopy can provide information about height and lateral resolution of polymer patterns as well as their mechanical properties [8,9,24]. However, the possibilities of the chemical analysis are limited, so it is usually performed on respective uniform substrates. Therefore, *information about a spatial resolution of chemical surface modification by grafting of polymer patterns is hardly provided*. TOF-SIMS is a powerful technique enabling surface chemical characterization and imaging with sub-100 nm lateral resolution, which is additionally suitable for analysis of organic materials [25,26]. Nevertheless, so far TOF-SIMS has been rarely applied to examination of surfaces patterned by polymer grafting and such analysis was limited to grafted structures with dimensions of tens of micrometers and silicon supports [27–29].

### *1.3. Surface functionalization for biorecognition*

Surface functionalization of solids substrates for biorecognition applications, such as assays, biosensors and lab-on-a-chip devices, requires the biomolecules' immobilization. Recognition biomolecules such as proteins or oligonucleotides are immobilized on solid supports or biosensor transducers to selectively bind a detected molecule, i.e. an analyte. The presence of an analyte on the surface is detected owning to its labeling or, in case of label-free biosensors, to a change of transducer's physical properties. In particular, for optical interferometric biosensors based on the Mach-Zehnder interferometer, the binding of analyte on transducer, located on one arm of a waveguide, causes a modulation of its refractive index, which is measured at the output as a phase shift [30].

The quality of the biorecognition layer is a crucial issue for sensitivity and reliability of the bioanalytical sensing performance. Therefore, many different strategies to biomolecules' immobilization on solid surface have been developed involving physical adsorption, covalent binding and affinity-based interactions [31]. Before the immobilization a proper surface modification depending on a kind of the substrate and applied strategy is required. For silicon-based materials the modification with silanes, which covalently bond to the surface and form self-assembled monolayers, is a versatile method to tailor surface properties [32]. In particular, modification of the transducer surface with aminosilanes to promote physical adsorption of biomolecules is frequently applied, since it is a simple but effective approach [33–36]. However, biomolecules' immobilization by physical adsorption introduces a possibility of molecules' desorption during subsequent steps of functionalization such as blocking of free surface sites with a non-functional protein or specific binding reactions.

One of the most powerful bioanalytical methods is an immunoassay based on an ability of antibodies to recognize and bind specifically to an antigen. Apart from conventional Enzyme-Linked ImmunoSorbent Assay test [37], the immunoassay can be performed on transducer surface for development of immunosensors [38]. Several formats of the immunoassay are currently in use involving a direct immunoassay, indirect immunoassay, sandwich immunoassay and competitive immunoassay [37]. In an indirect immunoassay two types of antibodies, namely the primary antibody specific for antigen and the secondary antibody with ability to bind to the primary one, are applied. The main advantage of the application of this assay format, with respect to immunosensors, is a sensitivity increase due to the fact that more than one secondary antibody can be bound per primary antibody. In turn, in a competitive immunoassay format antigens in the sample compete with antigens immobilized on surface for binding to antibody. Therefore, the presence of an antigen in the sample is measured as a reduction of the signal originating from binding of antibodies on the surface. The immobilization of antibodies on the surface, required for some immunoassay formats, is especially challenging since different antibody orientations, affecting their antigen binding efficiency, are possible [38,39]. The most commonly applied immunoglobulin G (IgG) antibody consists of two light and two heavy chains divided into constant and variable regions and forming a characteristic Y-shape. Antigen binding sites are located on both molecule "arms" named Fab domains, whereas Fc domain consists only of constant regions. Therefore, four different orientations of IgG antibody on the surface, i.e. head-on, end-on, side-on and flat-on (Fig. 3) can be distinguished resulting in different access to binding sites.

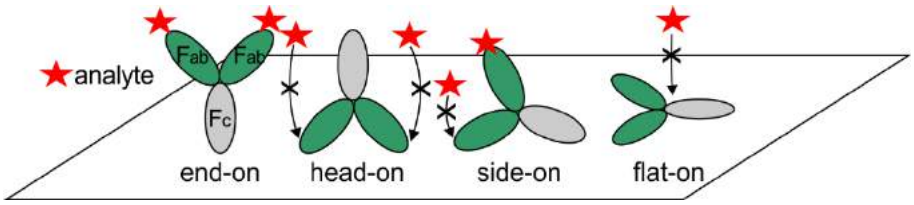


***Figure 3.*** *Possible orientations of IgG antibody immobilized on the surface resulting in different access of the analyte to antibody binding sites located on Fab domains* [39].

Moreover, miniaturization and design of biosensors often require the precise spatially-resolved immobilization of recognition biomolecules. In line with this demand, microfluidic approaches [40] as well as surface patterning methods, involving photolithography [41] and printing [42], are employed. Printing techniques, involving a deposition of nanoliter solution droplets by a robotic spotter, developed for DNA and protein microarrays can be applied to spatially-controlled solution deposition for formation of biomolecular patterns. This simple approach has been already applied to biofunctionalization of individual transducers of interferometric biosensors [33,40].

### *1.4. Characterization of biorecognition layers*

A comprehensive examination of the quality of the biorecognition layer, i.e. probe surface density, coverage uniformity, analyte binding capacity and resistance of non-specific binding, is extremely important to ensure the effective and reliable biosensors' performance. Functionalization of biosensor transducers' surface usually requires multi-step protocols involving the substrate modification, probe immobilization, blocking of free-surface sites and at least one specific binding reaction. To optimize the functionalization protocol and to investigate accompanied surface phenomena, surfaces should be examined after each subsequent step. Such a step-by-step surface characterization was already performed for model immunoassay [36,43] and DNA recognition layers [44,45] realized on planar silicon substrates. In many biosensor implementations the specific transducer geometry or surface microstructuring has to be employed, which hinders an examination of real transducer surface. Therefore, the *characterization of biorecognition layers and its evolution in subsequent protocol steps is commonly performed on planar substrates imitating the real transducer* [36,43–45].

The characterization of molecular layers formed on biosensing surfaces is limited mainly to the determination of the layers uniformity and the total amount of immobilized biomolecules. Additionally, the efficiency of the detection is examined based on the sensors response or by an application of labeled analytes. Microscopic techniques, especially Atomic Force Microscopy [36,43,46], are widely applied to visualization of biomolecular layers as well as evaluation of its uniformity and density. In turn, several spectroscopic techniques, e.g. X-ray Photoelectron

Spectroscopy [36,47], Spectroscopic Ellipsometry [48], Surface Plasmon Resonance Spectrometry [49], as well as Quartz Crystal Balance [46] enable a quantitative determination of the amount of immobilized biomolecules. *These methods*, however, *do not provide information about the composition of the biorecognition layer*, which is required due to a number of molecules employed in surface functionalization protocol. In particular, the biomolecules' immobilization by physical adsorption leaves the possibility of the molecules desorption during subsequent protocol steps. Therefore the verification of the amount of particular molecules is especially important. Time-of-Flight Secondary Mass Spectrometry is a technique which allows for discrimination between different molecules immobilized on surface, e.g. different proteins [50], based on differences in their chemical structure. However, while TOF-SIMS provides an insight into the composition of multi-molecular layers it does not allow for quantification of the amount of particular proteins on the surface. To describe a molecular composition of layers involving different proteins a multivariate analysis of TOF-SIMS data e.g. Principal Component Analysis, which allows for detection of subtle differences in surface chemistry and their classification, is especially useful. Recently, PCA analysis of TOF-SIMS spectra was used to reveal the composition of protein layers formed by adsorption from multi-component protein solutions [51–53]. This approach, however, *has not been applied so far to examine the changes* in composition of biorecognition layers formed *upon subsequent steps of the biosensor functionalization protocol*.

Another issue important in the examination of a molecular layer formed on a biosensing surface is the determination of the orientation of immobilized biorecognition molecules, especially antibodies, which influences their analyte binding efficiency [39]. Recently, the antibody orientation is most commonly inferred from their surface amount [54–57], which is an indirect approach prone to high uncertainty related to ambiguities of antibody orientations for some ranges of the surface density. Moreover, AFM is used to deduce antibody orientation from measured molecules dimensions or form surface topography [55,58]. Alternatively, TOF-SIMS combined with multivariate analysis has been already successfully employed to a direct determination of orientations of IgG antibodies immobilized on substrates [59–61]. Such analysis is based on differences in amino acid composition of Fab and Fc antibody's domains. However, the *examination of orientation of antibodies immobilized into multi-molecular layers, resulting from immunoassays and often involving both primary and secondary antibodies, has not been developed so far*.

*As can be inferred from this Introduction the potential of advanced surface science techniques has not been fully exploited for the characterization of macromolecular surfaces and patterns intended for biotechnological applications.*

# 2. Surface characterization techniques

## 2.1. Atomic Force Microscopy

Atomic Force Microscopy is a scanning probe technique enabling a high-resolution surface examination of a variety of materials ranging from metals to polymers and biomolecules. The AFM technique is based on the detection of the interaction between a very sharp tip mounted on a cantilever and a surface. This interaction is dominated by attractive Van der Waals forces and Coulombic repulsion forces, for a short tip-surface distance, which together constitute the Lennard-Jones potential. AFM can operate in different modes, depending on the type of the tip-surface interaction, involving contact, non-contact and tapping mode. For the contact mode, in which the tip constantly touches the surface (tip-surface distance is about 0.1 nm), atomic short-distance repulsive forces are probed. In contrast, in non-contact and tapping modes the tip with the cantilever oscillates at a distance of a few to tens nanometers above the sample surface, so consequently mainly attractive Van der Waals forces are probed. In the tapping mode, differently from the non-contact mode, the tip comes in an intermittent contact with the sample surface allowing to probe also repulsive forces. Non-contact and tapping modes are especially useful for characterization of biomaterials as well as layers of biomolecules and polymers due to less damage of soft surfaces. The basis of the probing of tip-surface interactions is a detection of the cantilever deflection, which is most often accomplished by means of the optical system involving a laser beam and a position-sensitive quadrant photodetector (Fig. 4). A deflection of the cantilever, whose back side is illuminated by a laser beam, is detected through dislocation of the laser beam, reflected from cantilever, from the center of the photodetector. The constant value of the cantilever deflection (for contact mode) or the amplitude/frequency of its oscillation (for non-contact and tapping modes) is ensured by changing the tip-surface distance by electronic feedback system controlling the piezoelectric scanner moving the sample or the tip. The topographic image of surface is created based on the data from feedback system collected point-by-point on sample surface moving by the piezoelectric scanner.

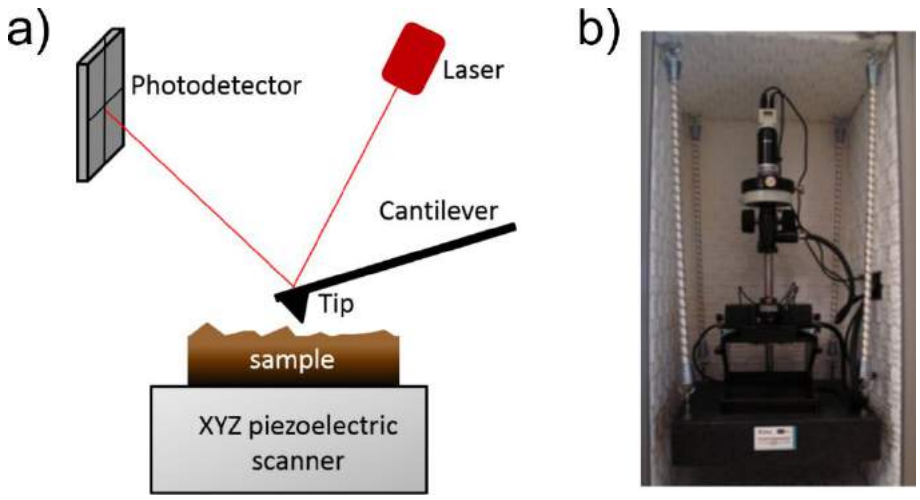


***Figure 4:*** *(a) A schematic setup of Atomic Force Microscopy. (b) The Agilent 5500 microscope applied in the described research.*

***AFM image analysis***

In addition to allowing for a visualization and measurement of dimensions of individual surface structures, AFM also provides insight into nanostructure of uniform layers of biomolecules or polymer chains immobilized on solid substrates. Such layers can be described as a random set of surface features and their nanostructure can be quantitatively characterized by several parameters calculated with AFM data [36,43–45,62]. The lateral nanostructure is described by feature size which can by calculated as doubled width-at-half-maximum of radial averaged autocorrelation function applied to AFM topographic image [63]. For imaging of molecules with dimensions comparable with the tip radius the bordering of the real molecule size on the image by AFM tip has to be taken into account [64,65]. In turn, the vertical nanostructure is characterized by parameters of the height distribution of the AFM image pixels such as the average height (the distribution's mean), the surface roughness (the distribution's spread) and the surfaces skewness (the distribution's asymmetry).

## *2.2. Fluorescence Microscopy*

Fluorescence microscopy is a form of optical microscopy which allows to observe the fluorescence light emitted from a sample. This technique became the essential and one of the most widely applied tools in biological and medical research, mainly due to a development of variety of fluorophores enabling specific labeling of molecules. The basis of this method is an irradiation of a specimen with a specific wavelength (selected by filters) adsorbed by fluorophores and a collection of the emitted fluorescence light (separated from a reflected excitation light by emission filters) with lower energy. Fluorescence microscopy can be applied to visualize the spatial distribution of the fluorophores (and labeled molecules), but also to compare the amount of the

fluorophores (and labeled molecules e.g. adsorbed proteins) on the surface. For the latter purpose the semi-quantitative approach based on integral geometry can be applied [19].

### *2.3. Spectroscopic Ellipsometry*

Spectroscopic ellipsometry is a an optical technique enabling examination of optical properties and determination of the thickness of thin layers on solid substrates [48,66]. Since ellipsometry is a simple high-precision and nondestructive method of thin films' analysis, allowing also for real-time experiments, it perfectly suits the requirements of biointerfaces examination. The principles of this technique are based on a measurement of the change of the (initially linear) light polarization upon reflection from a sample surface (Fig. 5). In particular, two values $\psi$ and $\Delta$, representing, respectively, the amplitude ratio and the phase difference between parallel $R_p$ and perpendicular $R_s$ components of the reflected light beam, are measured as a function of the wavelength. $\psi$ and $\Delta$ values are related to the intensity ratio of $R_s$ and $R_p$ components:

$$\frac{R_p}{R_s} = tan\psi \cdot e^{i\Delta} \qquad (1)$$

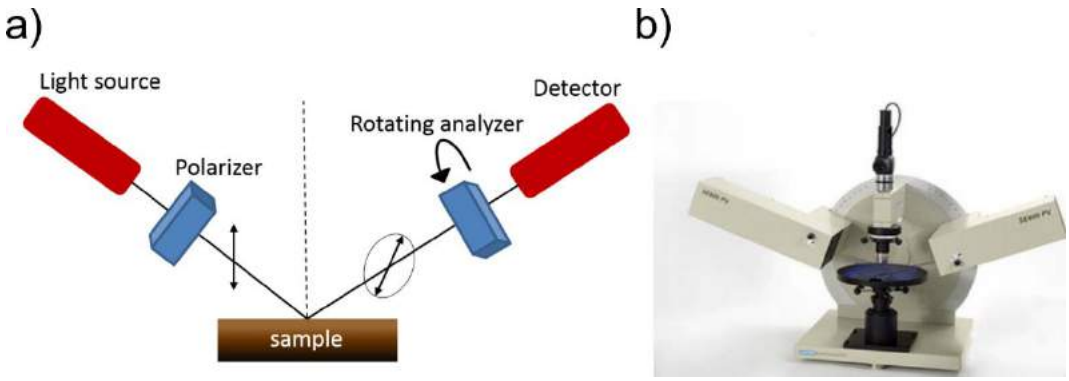


***Figure 5:*** *a) A schematic diagram of a spectroscopic ellipsometer. (b) The Sentech SE800 (Sentech Instruments GmbH) instrument applied in the described research* [67].

The measured change in light polarization is extremely sensitive to optical constants, thickness and microstructure that enables to examine these properties for thin layers deposited on a substrate. Both single layers and multiple layers (e.g. substrate/$Si_3N_4$/silane/protein) with thickness in range of few angstroms to several micrometers can be examined by means of the ellipsometry technique. However, since ellipsometry is an indirect characterization method, the data analysis requires an optical model defined by optical constants and layers' thickness.

### *2.4. X-ray Photoelectron Spectroscopy*

X-ray Photoelectron Spectroscopy is a surface sensitive technique, which enables elemental composition analysis and chemical state analysis of materials' surface and thin layers. This method is commonly used for characterization of a variety of material types involving polymers and biomaterials and is especially useful for examination of the chemical surface modification. The XPS technique involves a measurement of the energetic spectrum of electrons emitted from the sample upon irradiation with monochromatic soft (below 8 keV) X-ray radiation in a photoelectric effect. As an X-rays source a Roentgen lamp with magnesium or aluminum anode is typically used. After ejection from the sample placed in a high-vacuum chamber, the energy distribution of photoelectrons is measured by an energy analyzer and detectors (Fig. 6). The kinetic energy $E_{kinetic}$ of emitted photoelectrons is related to their binding energy $E_{binding}$ in an atom:

$$E_{kinetic} = h\nu - E_{binding} - \phi \qquad (2)$$

where $h\nu$ is the energy of X-ray photons being used and $\phi$ is the work function dependent on the spectrometer. Through this relation not only a detection of different elements in the sample but also their different chemical states is possible. For this purpose the energy scale is referenced to the neutral carbon C1s peak. Moreover, since the intensity of each characteristic photoelectron peak is directly related to the elemental composition (or relative amount of atoms in a respective chemical state of given element) within the XPS sampling volume, a quantitative chemical analysis is possible. XPS is a surface sensitive technique with a sampling depth $d$ determined by the attenuation length $\lambda$ of photoelectrons escaping from the material and undergoing both elastic and inelastic scattering [68]:

$$d = 3\lambda cos\theta \qquad (3)$$

where Θ is the take-off angle with respect to the surface normal. Due to its surface sensitivity, the XPS technique can be applied to estimation of thin ($<d$) layers' thickness if signals characteristic for the layer and the substrate can be identified [47,62].

In an Angle-Resolved XPS technique (ARXPS) measurements are performed at different take-off angles which modifies the sampling depth and allows to collect data from different depths in the sample. It is useful for determination of the chemical composition as a function of depth and for a more accurate estimation of the thickness of thin layers.

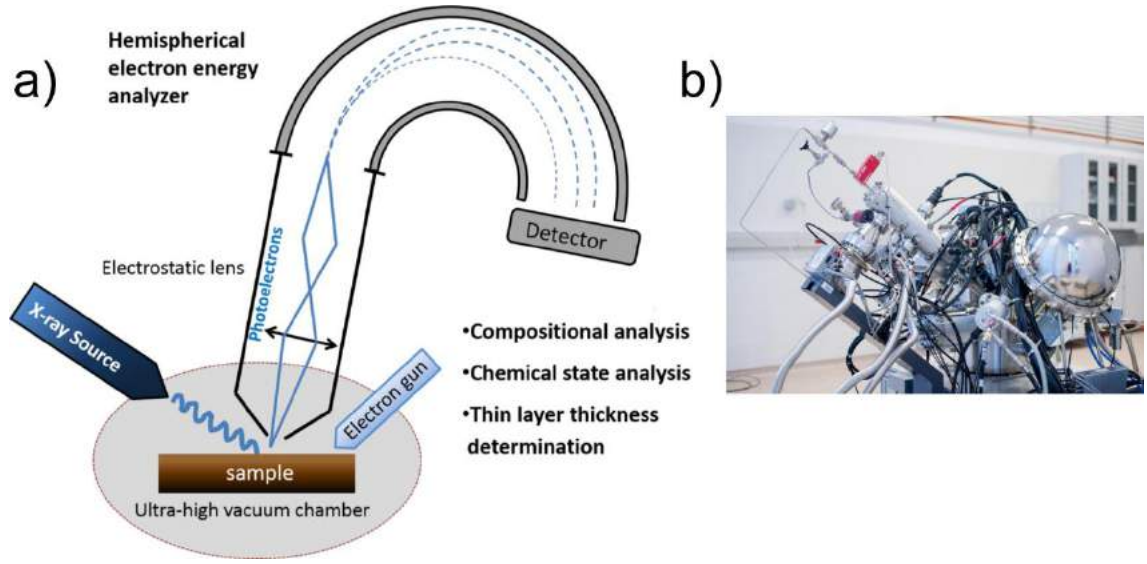


***Figure 6:*** *a) A general scheme of an XPS spectrometer. (b) The Versa Probe II (PHI) spectrometer applied in the described research.*

### *2.5. Time-of-Flight Secondary Ion Mass Spectrometry*

Time-of-Flight Secondary Ion Mass Spectrometry is a spectroscopic surface science technique enabling highly-sensitive (~1 ppm) chemical surface analysis. Due to its great sensitivity and specificity combined with a high mass, lateral and depth resolution, TOF-SIMS became one of the most powerful methods for characterization of organic materials involving also biomaterials and layers of immobilized biomolecules. TOF-SIMS technique is based on identification, from measured mass to charge ratio (m/z), of secondary ions emitted from surface upon bombarding by energetic primary ions. Metal ions ($Bi^+$, $Cs^+$, $Ga^+$) or clatters ($C_{60}^+$) with energy of several keV are commonly used as primary ions. Short pulses of the highly-focused beam of primary ions impinge on the solid surface and induce the collision cascade resulting in a sample sputtering with a small fraction emitted ionized particles, i.e. secondary ions. Secondary ions are fragments of molecules or (less frequently) whole molecules, forming a sample or adsorbed on its surface. Emitted ions are then accelerated and separated by the different arrival time to detector induced by various mass to charge ratio (m/z). Time-of-flight mass analyzer is characterized by mass resolution $\Delta m/m$ reaching 10 000. The collected data consist of a set of mass spectra taken at individual pixels determined by a focused beam scanning over a sample surface. TOF-SIMS can be accomplished in two operating regimes, namely static SIMS and dynamic SIMS [25,69]. In the static SIMS mode the primary ion dose density is kept below a specified limit ($<10^{12}$ ions/cm$^2$) ensuring that secondary ions originate exclusively from non-damaged areas of the investigated sample. Thereby, static SIMS is a highly surface sensitive technique collecting information only from the outermost 1-2 nm layer of the surface. In turn, dynamic SIMS allows for a chemical analysis as a function of

depth inside the sample, i.e. an in-depth profiling. Such analysis is possible due to a high flux density of primary ions resulting in sputtering and substantial erosion of the sample surface. Besides the spectroscopic mode characterized by a very high mass resolution, the image mode with high lateral resolution (reaching values below 100 nm) but limited mass resolution can be combined with static and dynamic TOF-SIMS regimes enabling 2D and 3D imaging.

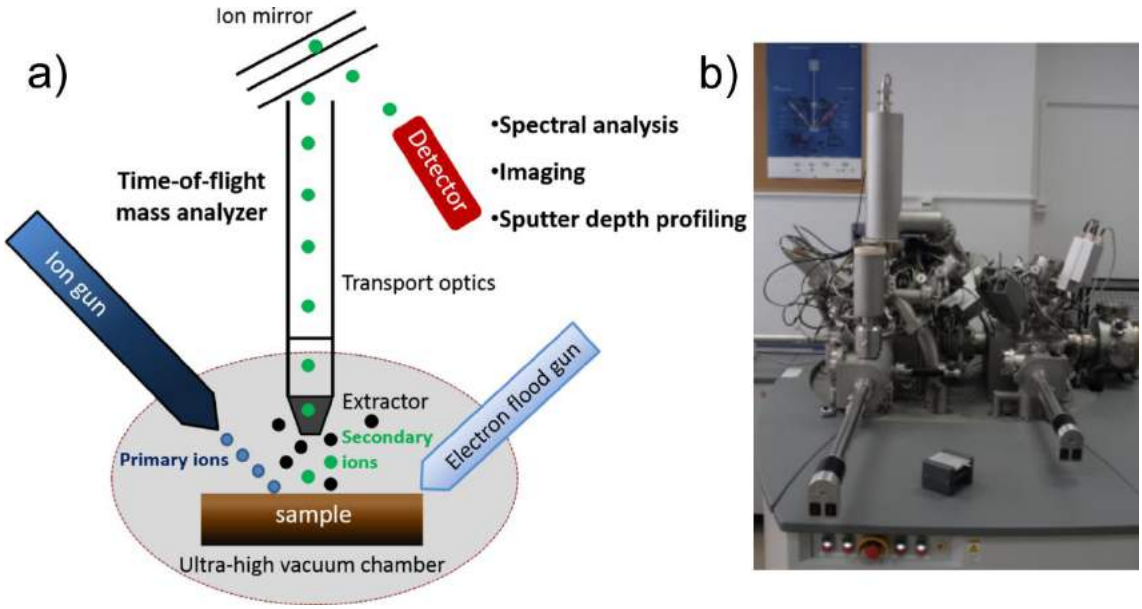


***Figure 7:*** *(a) A general scheme of a TOF-SIMS instrument. (b) The TOF.SIMS 5 (Ion-TOF GmbH) instrument applied in the described research.*

***TOF-SIMS data analysis***

The analysis of the TOF-SIMS spectrum can be performed based on individual characteristic signals, what can be called a single peak analysis, or by statistical analysis of the whole spectrum or a set of chosen peaks. Although signals characteristic for particular molecules are often classified based on measurements of reference substances, a single peak analysis could be hindered by surface contamination, matrix effect or complex structure of the analyzed layer consisting of different molecules with similar composition. Besides a single peak analysis, a multivariate analysis, with the most widely used Principal Component Analysis (PCA), is a powerful tool to support interpretation of the large data set generated by TOF-SIMS. A multivariate analysis is especially useful for processing the data from complex multi-component surfaces such as biomaterials or biomolecular layers [50,70]. The multivariate analysis is helpful in the detection of differences in a set of acquired TOF-SIMS spectra and identification of their major sources.

PCA looks at overall variance within a data set defined as a matrix with the rows corresponding to samples and columns containing variables. For TOF-SIMS data, samples are the acquired spectra, whereas variables are the intensities of individual peaks included in analysis. PCA converts an original set of correlated variables into a matrix of new uncorrelated variables called Principal Components by an orthogonal transformation which maximizes the variance of subsequent PCs. As a result, matrices of *scores*, which show the relationship between samples in a new basis given by PCs, and *loadings*, which show the relationship between old variables and individual PCs, are produced. Individual PCs capture more information than any of the original variables since each of them is a linear combination of all original variables. Therefore, PCA allows for a significant reduction of the dimensionality of the multidimensional data set while retaining a large amount of the original information [50,70]. The *scores* can be treated as the samples' compositions, expressed in terms of PCs, and the *loadings* as chemical spectra defining each PC.

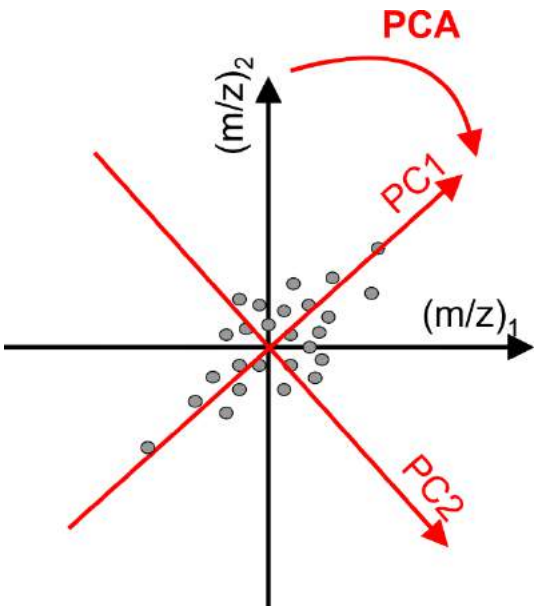


***Figure 8:*** *Geometrically PCA can be interpreted as an rotation which aligns new axes (Principal Components) with the directions of the maximal variance within a data set.*

# 3. Results

## 3.1. Paper I: Temperature and pH dual-responsive POEGMA-based coatings for protein adsorption

Highlights

- Poly(oligo(ethylene glycol) methacrylate) was polymerized from glass surface.
- Thermal but also pH-response is observed.
- Thermal sensitivity, observed in wettability, diminishes with decreasing pH.
- Such transition induces changes in protein adsorption.

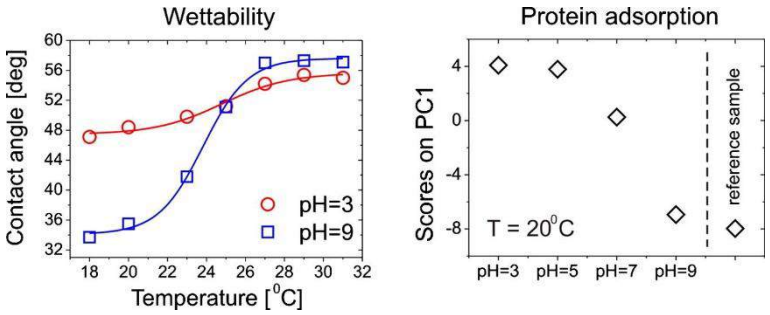


A novel approach to fabricate polymer coatings, thermo-responsive in physiological range, involving polymerization from oligoperoxide grafted to surfaces pre-modified with (3-aminopropyl)triethoxysilane APTES has been demonstrated recently for poly(N-izopropylacrylamide). This predominant 'intelligent' polymer, changing under external stimuli both physico-chemical properties and affinity towards proteins and cells, turned out to be moderately cytotoxic and therefore challenged by poly(ethylene glycol)-based polymers. This motivated **Paper I** where the fabrication approach has been extended to thermo-responsive coatings of antifouling poly(oligo(ethylene glycol)ethyl ether methacrylate) (POEGMA246). Different polymerization times were applied to optimize the fabrication for the most pronounced responsivity to external stimuli.

Surface coverage with grafted POEGMA was examined with ellipsometry to reveal monotonous increase with polymerization time. Overall composition of oligoperoxide-*graft*-POEGMA246 coatings was confirmed by TOF-SIMS. Temperature dependence of coatings wettability was determined by contact angle of sessile water droplets. Whereas the grafted oligoperoxide and the PEOGMA coatings with surface mass density lower than 20 mg/m$^2$ are hydrophobic and show almost no thermal response, longer polymerization times result in the coatings changing their hydrophobicity into hydrophilic behavior below 24–26 $^o$C. Thermo-sensitivity is explained by the competitive POEGMA-POEGMA and POEGMA-water interactions. However, when surface coverage of graft-oligoperoxide with POEGMA is low (< 20

mg/m$^2$) the complexes between POEGMA ether groups and oligoperoxide carboxyl groups are abundant enough to block the thermal response.

In addition, the thermal response of wettability and surface morphology (determined with AFM, see Supplementary Data) was examined at different pH conditions for the coatings polymerized for different times. Although the pure POEGMA brushes are not pH-sensitive, strong dual thermal- and pH-response was observed for the oligoperoxide-*graft*-POEGMA coatings with surface mass density of 30 mg/m$^2$ (30 h polymerization). Thermal response of wettability is prominent at pH = 9 and 7 but diminished at pH = 5 and 3, when carboxyl groups of oligoperoxide dominate over their carboxylate counterparts and form complexes with POEGMA ether oxygens.

The coatings, polymerized for the time of 30 h - optimal for strong dual response, were examined also for controlled protein adsorption. Adsorption of lentil lectin, a model protein, was examined at different pH for two temperatures (20 and 32 $^o$C) using fluorescence microscopy and PCA of TOF-SIMS data. A negligible adsorption was observed at both temperatures at pH = 9 in accordance with anti-fouling properties reported for the POEGMA polymer. However, a significant adsorption was unexpectedly determined to develop with decreasing pH. Weak thermal but strong pH dependence of the low-fouling properties of the fabricated POEGMA coatings has been concluded, suggesting their possible application as interfaces with controlled protein adsorption.

### *3.2. Paper II: Electron-beam lithographic grafting of functional polymer structures from fluoropolymer substrates*

Highlights

- 2.5 and 100 keV electron beams form radical patterns on fluoropolymer films.
- Patterns initiate graft polymerization of poly(dimethylaminoethyl methacrylate).
- Grafted polymer-on-polymer structures are analyzed with AFM and TOF-SIMS.
- Surface and subsurface grafting dominates for low and high e-beam energy, respectively.
- Post-polymerization modification is enabled by quaternization and electrostatic binding.

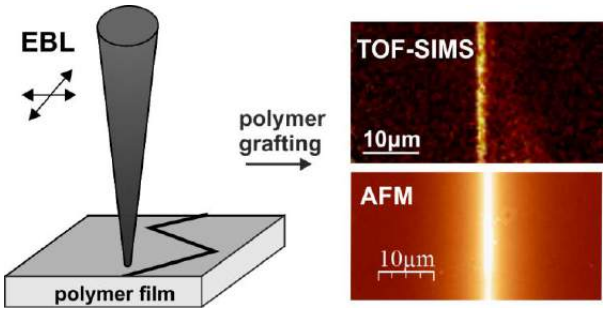


This paper reports on an application of electron-beam lithography to radiation-induced grafting of polymer structures, which has not been studied in detail to date. In the proposed approach, an electron-beam lithography was used for a direct generation of radical patterns at the surface of fluoropolymer film. Created radical species are stabilized as hydroperoxides or peroxides upon contact with air and initiate the subsequent graft polymerization. Subsequently, grafted polymer structures can be modified to obtain patterns with desired functionality. In this method arbitrary patterns can be achieved in a simple and fast way, since it does not require any mask or an interferometric set-up. Moreover, an attainable submicrometer resolution and a millimeter range of the modified area match perfectly the requirements for applications in biotechnology.

In particular, submicrometer structures of the biocompatible PDMAEMA polymer were grafted from ETFE fluoropolymer films. To explore the possibilities and limits of the method as well as to optimize the process, different conditions of the exposure with electrons were employed. Two different electron acceleration voltages 2.5 and 100 kV, various exposure doses as well as different widths of written lines and interline distances were compared.

The proposed method results in functionalization of fluoropolymer film with well-defined grafted polymer line structures with intrinsic resolution limit in the range of 300 nm as revealed via an analysis with AFM. In turn, the effective chemical surface modification with PDMAEMA was confirmed with spectroscopic analysis with TOF-SIMS and XPS. Additionally, TOF-SIMS was successfully applied to molecular imaging of such micrometer grafted polymer-on-polymer structures, which was hardy reported before.

A comparison of line profiles of structures grafted after substrate exposure with different e-beam energies determined with AFM showed a broad tailing and almost rectangular shape for 100 keV and 2.5 keV electrons, respectively. This difference was thoroughly investigated by combination of the AFM morphology characterization with examination of the extent of the surface chemical modification via TOF-SIMS imiging as well as by comparison of the surface density of grafted chains via TOF-SIMS and XPS. Such a complex analysis revealed preferential surface grafting for low e-beam energy and considerable grafting in the subsurface region, resulting in surface bulging, for higher energy. This result is also suggested by the difference in the electrons' penetration depth for different acceleration voltages predicted with a Monte Carlo simulation.

Moreover, the possibility of the post-polymerization modification of grafted polymer structures was demonstrated by quaternization of the grafted PDMAEMA. The effective PDMAEMA transformation to the polycationic QPDMAEMA form, with the surface yield of quaternization of about 80%, was confirmed with surface science spectroscopic techniques such as TOF-SIMS and XPS. Whereas positively charged quaternary ammonium species are commonly observed with XPS, an examination of the quaternization reaction with TOF-SIMS has not been reported to date.

The ETFE films functionalized with grafted polycationic polymer structures were employed for immobilization of charged molecules (negatively charged fluorescein sodium salt) and model proteins (bovine serum albumin and streptavidin). Performed studies showed that such substrates enable specially-resolved immobilization of charged molecules and proteins by electrostatic interactions and reduce nonspecific adsorption. This indicates their possible applications as biofunctional substrates for charge selective molecules' immobilization.

### *3.3. Paper III: Imaging and chemical surface analysis of biomolecular functionalization of monolithically integrated on silicon Mach-Zehnder interferometric immunosensors*

Highlights

- Optimization of probe immobilization with robotic spotter printing overlapping spots.
- In-situ inspection of microstructured surfaces of biosensors integrated on silicon.
- Imaging and chemical analysis of immobilization, surface blocking and immunoreaction.
- Insight with molecular discrimination into step-by-step sensor surface modifications.
- Optimized biofunctionalization improves sensor sensitivity and response repeatability.

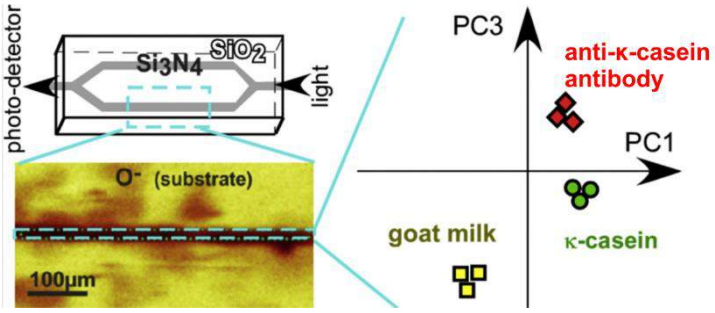


Miniaturized silicon-based optical biosensors are suited for label-free detection of analytes, enabling inherently high sensitivity at reduced costs. To take advantage of these features, biosensor surface should be homogeneously covered with different molecules that are subsequently introduced by biofunctionalization and assay protocols. Biosensor signal can monitor stages of these protocols but it reflects only a cumulative surface concentration of all different molecules. In addition, such monitoring cannot be applied to mass fabrication of biosensors integrated on a chip, where the contact pin-printing technique – initially developed for the fabrication of DNA arrays (e.g. [45]) – is applied to spatially-resolved biofunctionalization of individual on-chip biosensors.

To provide an insight into multi-step protocols with chemical discrimination of different molecules, surface science techniques have been introduced. Step-by-step examination of planar surfaces imitating sensor transducer has been reported by the combined microscopic and spectroscopic studies [36,43–45]. In **Paper III**, such an approach has been extended into chemical in-situ inspection of microstructured on-chip sensors, and demonstrated for monolithically integrated on silicon chip Mach-Zehnder interferometric immunosensors. Microscopic and spectroscopic characterization, providing a chemical discrimination of all molecules employed in the protocol to detect the bovine κ-casein allergen in goat milk, was performed for the sensing regions with specific geometry (20 µm wide, 600 µm long, 2.5 µm deep windows). Biosensor surfaces were examined with TOF-SIMS after: hydrophilization with oxygen

plasma, modification with amino-silane (APTES), immobilization of κ-casein by solution deposition with a microarray spotter, blocking with diluted goat milk, and finally immunoreaction with monoclonal antibodies against κ-casein.

To optimize the process of probe immobilization on the selected sensing areas of 36 $mm^2$ silicon chips, this paper analyzes also the planar surfaces with ca. 2.5 $mm^2$ κ-casein domains - created by contact pin-printing arrays of overlapping spots, with a robotic spotter applying different solution concentrations (ranging from 5 to 200 μg/mL) and different incubation times used (2 h and 24 h). TOF-SIMS chemical maps and molecular characterization of biofunctionalized surfaces showed their evolution from individual spots to uniform coverage with increasing solution concentration. Based on these results, the κ-casein solution concentration of at least 100 μg/mL and 2 h incubation time were chosen as optimal conditions for chip functionalization.

All individual molecular components used in the multi-step functionalization and assay procedure were well discriminated by different TOF-SIMS signals characteristic for silicon substrate, amino-silane, κ-casein, milk glycerides and antibodies. After each step on-chip biosensors were directly inspected with imaging and molecular TOF-SIMS characterization. It was shown that their surfaces were uniformly modified with amino-silane, with homogeneous κ-casein layer formed after immobilization. This layer is covered with milk components after blocking with diluted goat milk. Finally, an effective antibody binding onto the surface immobilized κ-casein is accompanied by nearly complete milk removal and partial casein desorption. Supplementary AFM and XPS data pointed to self-associated rather than monomer κ-casein molecules present on the surface and surface coverage with immobilized κ-casein not far from saturation limit.

Additionally, to enhance detection of subtle differences in the biomolecular composition of the biosensors integrated on chip - varied between subsequent functionalization and immunoassay steps - the multivariate method of PCA was applied to TOF-SIMS data. Principal components clearly distinguished between protein amino acids and milk glycerides, as well as between amino acids characteristic for κ-casein and antibodies. The plot of principal components' scores enabled direct visualization and classification of the step-by-step modifications of biosensor surfaces.

Finally, real-time κ-casein detection was tested with Mach-Zehnder sensors integrated on chip, which are functionalized following examined immunoassay protocol. It was shown that the application of determined optimal probe immobilization conditions considerably improved both the repeatability of the sensors responses and detection sensitivity (with 5x increase of the latter, see Supplementary Data).

### *3.4. Paper IV: Indirect immunoassay on functionalized silicon surface: Molecular arrangement, composition and orientation examined step-by-step with multi-technique and multivariate analysis*

Highlights

- Biofunctionalization and indirect immunoassay protocol analyzed for $Si_3N_4$ surface.
- Analyte-protein conjugate and blocking protein desorb during primary immunoreaction.
- Grouped secondary antibodies cover protein monolayer that contains primary antibody.
- Indirect immunoassay orients differently primary and secondary antibody.
- Orientation of directly immobilized antibodies depends on their surface density.

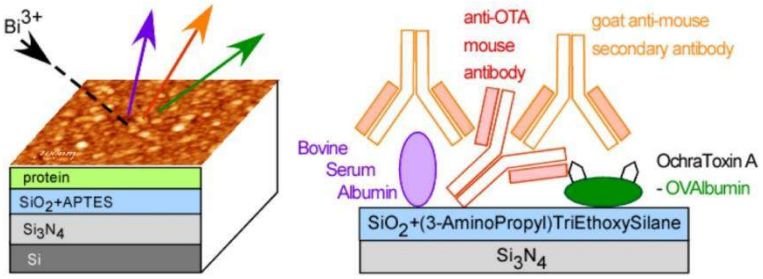


This paper presents a step-by-step multi-technique surface characterization of $Si_3N_4$ substrate imitating biosensor transducer after functionalization and performance of an indirect immunoassay for detection of the mycotoxin OchraToxin A (OTA). Multiple surface analysis techniques including AFM, TOF-SIMS and ellipsometry were combined to determine the arrangement, composition and orientation of biomolecules in protein layer for the improvement of multi-step procedures employed in biosensors.

In the presented work $Si_3N_4$ surfaces were prepared and functionalized in a similar way as the waveguides of integrated on silicon chips Mach-Zehnder interferometric sensors detecting OTA in beer by a competitive indirect immunoassay. $Si_3N_4$ surfaces were examined after the following steps: chemical modification with amino-silane (APTES), immobilization of the probe by spotting of the OTA-ovalbumin (OTA-OVA) conjugate solution over millimeter-sized areas using a robotic spotter (see **Paper III**), blocking of non-specific binding with bovine serum albumin (BSA), specific binding of primary mouse monoclonal antibody against OTA (anti-OTA Mab) and finally binding of secondary goat anti-mouse IgG antibody (anti-mIgG). Additionally, samples spotted with primary and secondary antibodies were used as references.

Molecular arrangement, resulting from subsequent protocol steps, was analyzed with AFM, which enables visualization of protein overlayers and provides measures of their vertical and lateral nanostructure. AFM revealed that the primary antibody is incorporated during the first immunoreaction into a multi-component monolayer - formed earlier during probe immobilization

and blocking steps. Then, this monolayer is covered with grouped secondary antibodies that form an additional protein layer and point to efficient affinity binding between primary and secondary antibodies.

The composition of OVA and cumulative albumin (OVA and BSA) in the protein overlayer after subsequent protocol steps was provided by characteristic TOF-SIMS signals. TOF-SIMS revealed that blocking step introduces BSA molecules on the surface but maintains the existing probe (OTA-OVA) coverage. However, the first immunoreaction is accompanied by partial desorption of both probe (OTA-OVA) and blocking (BSA) protein molecules. Then, the second immunoreaction hardly affects the composition. Compositional TOF-SIMS analysis was combined with total surface amount of all proteins (evaluated with ellipsometry) in order to evaluate individual mass loadings of each protein biomolecules in the course of the multi-step protocol. This novel approach enabled both the evaluation of molar binding ratio of secondary to primary antibody, close to 2.5, as well as pre-selection of molecular orientations of all proteins.

Finally, for the first time the research defining orientation of immobilized antibodies was extended to cover molecular orientation of both primary and secondary antibody. Multivariate PCA was applied to TOF-SIMS data. The first principal component clearly distinguished between amino acids characteristic for albumins and antibodies, pointing to immunoadsorbed and directly adsorbed antibodies, respectively. In turn, basing on the ion fragments of amino acids characteristic for Fc fragment of antibody molecules, the second principal component specified orientations of both primary and secondary immunoadsorbed antibodies as well as orientations of the same antibodies directly immobilized by spotting. It was found that the dominant orientation of immunoadsorbed antibody changes with increasing molar binding ratio (from side-on for primary antibody, to head-on for secondary antibody). In turn, the dominant orientation of directly immobilized antibody depends on the surface density (changes from flat-on to end-on with increasing coverage).

### *3.5. Paper V: Contact pin-printing of albumin-fungicide conjugate for silicon nitride-based sensors biofunctionalization: Multi-technique surface analysis for optimum immunoassay performance*

Highlights

- Contact pin-printing of overlapping probe spots and spotting by hand are compared.
- Contact pin-printing favors probe immobilization with two-fold higher surface density.
- Incomplete monolayer develops to bilayer as printing solution concentration increases.
- Blocking molecules complete probe monolayer but reduce probe bilayer.
- Surface immunoreaction increases with probe concentration in printing solution.

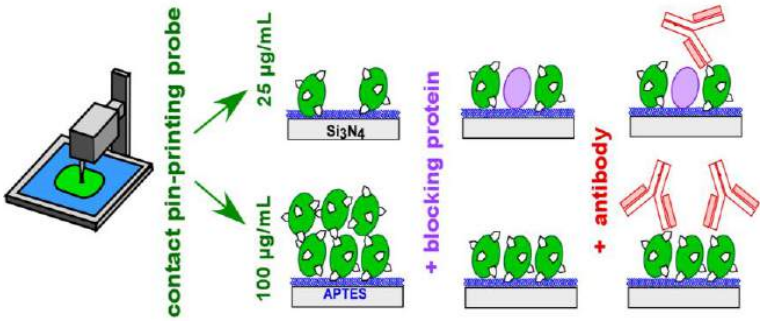


The complex step-by-step surface characterization of the sensors' transducer with the course of the biofunctionalization and assay protocol, presented in previous papers, has been extended to examine the impact of the initial probe surface density. In particular, the nanostructure, surface coverage and probe composition of biorecognition layers resulting from subsequent protocol steps (blocking free surface sites and specific binding reaction) were evaluated for different probe surface densities obtained in the first functionalization step. Moreover, contact pin-printing method applied already to spatially-resolved biofunctionalization of sensors' transducers has been consistently compared to solution deposition by pipette, i.e. hand macro-spotting.

The reagents and protocol of immunoassay for detection of fungicide thiabendazole (TBZ) were employed in this study. Both solution deposition approaches, contact pin-printing of multiple overlapping spots and hand macro-spotting, were applied to immobilization of BSA-TBZ conjugate (probe) from solutions with three different concentrations of 25, 50 and 100 µg/mL. Additionally, planar $Si_3N_4$ surfaces as well as transducers of Mach-Zehnder interferometric sensors were examined after immobilization of BSA-TBZ conjugate, applying contact pin-printing approach of the solutions with these concentrations, as well as after subsequent protocol steps involving blocking of free surface sites with BSA and immunoreaction with a monoclonal anti-TBZ antibody.

To compare two solution deposition approaches used for probe immobilization, the protein surface density and layers' nanostructure were determined by spectroscopic ellipsometry and

AFM, respectively. The obtained probe surface coverage increases with solution concentration, as expected, for both applied approaches. However, it was found that application of contact pin-printing method results in much higher immobilization efficiency, providing even twice probe surface density. Moreover, the evolution of BSA-TBZ layers from an incomplete monolayer into a bilayer with increasing solution concentration was revealed for the contact pin-printing method and applied range of solution concentrations.

Surfaces with the probe contact-printed with different coverages were examined after blocking with BSA: Changes in the protein surface coverage (determined from ellipsometry and XPS) and the vertical extent of the formed layer (AFM) appear to depend on the initial probe surface density. It was inferred that, for low BSA-TBZ coverage (pin-printed with a 25 μg/mL solution), free surface sites are filled with BSA to form a complete monolayer, consisting of both BSA-TBZ and BSA. In turn, for surfaces with high BSA-TBZ density (pin-printed with a 100 μg/mL solution), the loosely bound molecules of the second layer of probe bilayers desorb during blocking, to leave a monolayer of BSA-TBZ molecules. This conclusion was confirmed by TOF-SIMS, resolving the BSA-TBZ conjugate from the BSA molecule, and revealing the changes upon blocking of the probe relative amount in the protein layer.

Finally, the efficiency of the specific immunoreaction, which is a final step of the assay protocol, is compared for surfaces functionalized by contact pin-printing of the BSA-TBZ probe from solutions with different concentrations and subsequent blocking. It was found that the amount of antibodies bound to the surface increases with concentration of the used probe solution. The reason of this dependence is a difference in the BSA-TBZ probe composition in protein monolayers resulting from the blocking step. Therefore, contact pin-printing of 100 μg/mL BSA-TBZ solution has been recognized as an optimal procedure for surface biofunctionalization.

# *4. Conclusions*

This Thesis presents the characterization of the structure and properties of two types of macromolecular surfaces designed for applications in biotechnology. The first class of surfaces involves solid substrates functionalized with grafted polymers, including polymer patterns, developed for formation of interfaces with controlled interactions with biomolecules (**Papers I** and **II**). In turn, silicon-based substrates covered with multi-molecular biorecognition nanolayers and probe protein patterns, both aiming at biosensing applications, constitute the second class of characterized surfaces (**Papers III**, **IV** and **V**).

In line with the aim of the Thesis, several surface science techniques were applied and combined to examine both surface classes and to extend established so far methods of macromolecular surfaces' and patterns' characterization. As a result of this objective regarding substrates functionalized with grafted stimuli-responsive polymer, an analysis of temperature-sensitive properties at various pH conditions has been developed (**Paper I**) applying water contact angle measurements and surface morphology evaluation with AFM. Moreover, in course of the characterization of substrates patterned with lithographically grafted charged polymer, TOF-SIMS analysis of macromolecular surfaces has been extended to chemical imaging of micrometer polymer-on-polymer structures and evaluation of the quaternization reaction as an example of the post-polymerization modification (**Paper II**). Likewise, an analysis of biofunctionalization and assay protocols applied to biosensor transducers provided several achievements in development of methods of the macromolecular surfaces' characterization. Firstly, barely reported to date in-situ inspection of the surface of the micro-structured transducers of the on-chip biosensors has been performed using the TOF-SIMS technique (**Papers III** and **V**). A step-by-step examination of the immunosensor surface has been extended to tracking of the relative surface content in different molecules after subsequent protocol steps as well as to imaging of the molecules' distribution (**Papers III** and **V**). In addition, for the first time PCA has been successfully employed for classification of changes in composition of the multi-molecular layer formed on transducer surface in course of the functionalization and immunoassay (**Paper III**). One of the most important results of this Thesis is a development of a new method to estimate the amount of different proteins in multi-molecular layers, which bases on a combination of ellipsometry and TOF-SIMS techniques as described in **Paper IV**. Finally, an established evaluation of the antibody orientation by PCA of TOF-SIMS data has been extended to determination of the orientation of (both primary and secondary) antibodies located in multi-molecular layers resulting from an (indirect) immunoassay protocol.

The developed complex characterization of macromolecular surfaces has contributed to investigation of phenomena occurring on such surfaces and to optimization of their preparation

procedures aiming to improve the performance of their biotechnological applications. For stimuli-responsive substrates described in **Paper I** a comprehensive surface analysis revealed the unexpected dual thermal and pH sensitivity and provided the optimal polymerization time resulting in the most pronounced coatings' response. In turn, for substrates patterned with a lithographically grafted polymer (**Paper II**) such analysis demonstrated and explained the strong dependence of their morphology on applied electron beam energy as well as allowed to choose exposure conditions resulting in desired surface properties. Finally, an examination with complementary surface science techniques provided a complex picture of step-by-step modifications of the biosensor surface in course of the immunoassay. In particular, an enhanced immobilization efficiency by solution deposition by contact pin-printing (**Paper V**) as well as desorption phenomena during the blocking (**Paper V**) or immunoreaction step (**Papers III** and **IV**) were revealed. Consequently, performed analysis supported optimization of the biofunctionalization protocols (**Papers III** and **V**) which results in the improvement of sensors' repeatability and sensitivity.

# *References*


[1] S. Minko, Grafting on Solid Surfaces: "Grafting to" and "Grafting from" Methods, in: S. Manfred (Ed.), Polym. Surfaces Interfaces, Springer, 2008: pp. 2015–234.

[2] S. Edmondson, V.L.V. Osborne, W.T.S.W. Huck, Polymer brushes via surface-initiated polymerizations, Chem. Soc. Rev. 33 (2004) 14–22.

[3] A. Bhattacharya, P. Ray, Basic Features and Techniques, in: A. Bhattacharya, J.W. Rawils, P. Ray (Eds.), Polym. Grafting Crosslink., John Wiley & Sons, Inc., Hoboken, New Jersey, 2009: pp. 7–64.

[4] C. Padeste, S. Neuhaus, Polymer-on-Polymer Structures Based on Radiation Grafting, in: Polym. Micro- Nanografting, Elsevier, 2015: pp. 57–78.

[5] A. Kumar, A. Srivastava, I.Y. Galaev, B. Mattiasson, Smart polymers: Physical forms and bioengineering applications, Prog. Polym. Sci. 32 (2007) 1205–1237.

[6] J. Guo, L. Peng, J. Yuan, When dual and multi-responsiveness meet molecular brushes, Eur. Polym. J. 69 (2015) 449–459.

[7] Y. Stetsyshyn, J. Zemla, O. Zolobko, K. Fornal, A. Budkowski, A. Kostruba, V. Donchak, K. Harhay, K. Awsiuk, J. Rysz, A. Bernasik, S. Voronov, Temperature and pH dual-responsive coatings of oligoperoxide-graft-poly(N-isopropylacrylamide): Wettability, morphology, and protein adsorption, J. Colloid Interface Sci. 387 (2012) 95–105.

[8] T. Chen, I. Amin, R. Jordan, Patterned polymer brushes., Chem. Soc. Rev. 41 (2012) 3280–96.

[9] Q. Yu, L.K. Ista, R. Gu, S. Zauscher, G.P. López, Nanopatterned polymer brushes: conformation, fabrication and applications, Nanoscale. 8 (2016) 680–700.

[10] H.P. Brack, C. Padeste, M. Slaski, S. Alkan, H.H. Solak, Preparation of Micro- and Nanopatterns of Polymer Chains Grafted onto Flexible Polymer Substrates, J. Am. Chem. Soc. 126 (2004) 1004–1005.

[11] B. Gupta, N. Anjum, Plasma and Radiation-Induced Graft Modification of Polymer for Biomedical Applications, Adv. Polym. Sci. 165 (2003) 35–61.

[12] J.-H. Choi, R. Ganesan, D.-K. Kim, C.-H. Jung, I.-T. Hwang, Y.-C. Nho, J.-M. Yun, I.-B. Kim, Patterned Immobilization of Biomolecules by Using Ion Irradiation-Induced Graft Polymerization, J. Polym. Sci. Part A Polym. Chem. 47 (2009) 6124–6134.

[13] Y.G. Takei, T. Aoki, K. Sanui, N. Ogata, Y. Sakurai, T. Okano, Dynamic contact angle measurement of temperature-responsive surface properties for poly (N-isopropylacrylamide)

grafted surfaces, Macromolecules. 27 (1994) 6163–6166.

[14] F. Xia, L. Feng, S. Wang, T. Sun, W. Song, W. Jiang, L. Jiang, Dual-responsive surfaces that switch between superhydrophilicity and superhydrophobicity, Adv. Mater. 18 (2006) 432–436.

[15] P. Heinz, F. Bretagnol, I. Mannelli, L. Sirghi, A. Valsesia, G. Ceccone, D. Gilliland, K. Landfester, H. Rauscher, F. Rossi, Poly(N-isopropylacrylamide) Grafted on Plasma-Activated Poly(ethylene oxide): Thermal Response and Interaction With Proteins, Langmuir. (2008) 6166–6175.

[16] S. Rauch, P. Uhlmann, K.J. Eichhorn, In situ spectroscopic ellipsometry of pH-responsive polymer brushes on gold substrates, Anal. Bioanal. Chem. 405 (2013) 9061–9069.

[17] A. Kostruba, M. Ohar, B. Kulyk, O. Zolobko, Y. Stetsyshyn, Surface modification by grafted sensitive polymer brushes: An ellipsometric study of their properties, Appl. Surf. Sci. 276 (2013) 340–346.

[18] E.M. Benetti, S. Zapotoczny, G.J. Vancso, Tunable thermoresponsive polymeric platforms on gold by "photoiniferter"-based surface grafting, Adv. Mater. 19 (2007) 268–271.

[19] J. Zemła, M. Lekka, J. Wiltowska-Zuber, A. Budkowski, J. Rysz, J. Raczkowska, Integral geometry analysis of fluorescence micrographs for quantitative relative comparison of protein adsorption onto polymer surfaces, Langmuir. 24 (2008).

[20] S. Burkert, E. Bittrich, M. Kuntzsch, M. Müller, K.J. Eichhorn, C. Bellmann, P. Uhlmann, M. Stamm, Protein resistance of PNIPAAm brushes: Application to switchable protein adsorption, Langmuir. 26 (2010) 1786–1795.

[21] A. Kroning, A. Furchner, D. Aulich, E. Bittrich, S. Rauch, P. Uhlmann, K.J. Eichhorn, M. Seeber, I. Luzinov, S.M. Kilbey, B.S. Lokitz, S. Minko, K. Hinrichs, In Situ Infrared Ellipsometry for Protein Adsorption Studies on Ultrathin Smart Polymer Brushes in Aqueous Environment, ACS Appl. Mater. Interfaces. 7 (2015) 12430–12439.

[22] Q. Yu, Y. Zhang, H. Chen, Z. Wu, H. Huang, C. Cheng, Protein adsorption on poly(N-isopropylacrylamide)-modified silicon surfaces: Effects of grafted layer thickness and protein size, Colloids Surfaces B Biointerfaces. 76 (2010) 468–474.

[23] M. Cole, M. Jasieniak, H. Thissen, N.H. Voelcker, H.J. Griesser, Time-of-Flight-Secondary Ion Mass Spectrometry Study of the Temperature Dependence of Protein Adsorption onto Poly(N-isopropylacrylamide) Graft Coatings., Anal. Chem. 11 (2009) 14–23.

[24] R. Ducker, A. Garcia, J. Zhang, T. Chen, S. Zauscher, Polymeric and biomacromolecular brush nanostructures: Progress in synthesis, patterning and characterization, Soft Matter. 4 (2008).

[25] M. Senoner, W.E.S. Unger, SIMS imaging of the nanoworld: applications in science and technology, J. Anal. At. Spectrom. 27 (2012) 1050.

[26] A.M. Belu, D.J. Graham, D.G. Castner, Time-of-flight secondary ion mass spectrometry: Techniques and applications for the characterization of biomaterial surfaces, Biomaterials. 24 (2003) 3635–3653.

[27] M. Kaupp, A.S. Quick, C. Rodriguez-Emmenegger, A. Welle, V. Trouillet, O. Pop-Georgievski, M. Wegener, C. Barner-Kowollik, Photo-induced functionalization of spherical and planar surfaces via caged thioaldehyde end-functional polymers, Adv. Funct. Mater. (2014) 5649–5661.

[28] M.D.K. Ingall, C.H. Honeyman, J. V Mercure, P. a Bianconi, R.R. Kunz, Surface Functionalization and Imaging Using Monolayers and Surface-Grafted Polymer Layers, J. Am. Chem. Soc. 121 (1999) 3607–3613.

[29] E. Blasco, B. Yameen, A.S. Quick, P. Krolla-Sidenstein, A. Welle, M. Wegener, C. Barner-Kowollik, Designing ??-Conjugated Polymeric Nano- and Microstructures via Light Induced Chemistry, Macromolecules. 48 (2015) 8718–8728.

[30] P. Kozma, F. Kehl, E. Ehrentreich-Förster, C. Stamm, F.F. Bier, Integrated planar optical waveguide interferometer biosensors: A comparative review, Biosens. Bioelectron. 58 (2014) 287–307.

[31] F. Rusmini, Z. Zhong, J. Feijen, Protein immobilization strategies for protein biochips, Biomacromolecules. 8 (2007).

[32] D. Samanta, A. Sarkar, Immobilization of bio-macromolecules on self-assembled monolayers: methods and sensor applications., Chem. Soc. Rev. 40 (2011) 2567–2592.

[33] M. Angelopoulou, A. Botsialas, A. Salapatas, P.S. Petrou, W. Haasnoot, E. Makarona, G. Jobst, D. Goustouridis, A. Siafaka-Kapadai, I. Raptis, K. Misiakos, S.E. Kakabakos, Assessment of goat milk adulteration with a label-free monolithically integrated optoelectronic biosensor, Anal. Bioanal. Chem. 407 (2016).

[34] M. Kitsara, P. Petrou, D. Kontziampasis, K. Misiakos, E. Makarona, I. Raptis, K. Beltsios, Biomolecular layer thickness evaluation using White Light Reflectance Spectroscopy, Microelectron. Eng. 87 (2010).

[35] H.S. Mansur, R.L. Oréfice, W.L. Vasconcelos, Z.P. Lobato, L.J.C. Machado, Biomaterial with chemically engineered surface for protein immobilization, J. Mater. Sci. Mater. Med. 16 (2005).

[36] K. Awsiuk, A. Bernasik, M. Kitsara, A. Budkowski, P. Petrou, S. Kakabakos, S. Prauzner-Bechcicki, J. Rysz, I. Raptis, Spectroscopic and microscopic characterization of biosensor surfaces with protein/amino-organosilane/silicon structure, Colloids Surfaces B Biointerfaces. 90 (2012) 159–168.

[37] T. Porstmann, S.T. Kiessig, Enzyme immunoassay techniques an overview, J. Immunol. Methods. 150 (1992).

[38] S.C.B. Gopinath, T.H. Tang, M. Citartan, Y. Chen, T. Lakshmipriya, Current aspects in immunosensors, Biosens. Bioelectron. 57 (2014) 292–302.

[39] A.K. Trilling, J. Beekwilder, H. Zuilhof, Antibody orientation on biosensor surfaces: a minireview., Analyst. 138 (2013) 1619–27.

[40] A.B. González-Guerrero, M. Alvarez, A.G. Castaño, C. Domínguez, L.M. Lechuga, A comparative study of in-flow and micro-patterning biofunctionalization protocols for nanophotonic silicon-based biosensors, J. Colloid Interface Sci. 393 (2013).

[41] M. Veiseh, M.H. Zareie, M. Zhang, Highly selective protein patterning on gold-silicon substrates for biosensor applications, Langmuir. 18 (2002).

[42] A.D. Dias, D.M. Kingsley, D.T. Corr, Recent advances in bioprinting and applications for biosensing, Biosensors. 4 (2014) 111–136.

[43] K. Awsiuk, A. Budkowski, P. Petrou, A. Bernasik, M.M. Marzec, S. Kakabakos, J. Rysz, I. Raptis, Model immunoassay on silicon surfaces: Vertical and lateral nanostructure vs. protein coverage, Colloids Surfaces B Biointerfaces. 103 (2013) 253–260.

[44] K. Awsiuk, J. Rysz, P. Petrou, A. Budkowski, A. Bernasik, S. Kakabakos, Immobilization of oligonucleotide probes on silicon surfaces using biotin – streptavidin system examined with microscopic and spectroscopic techniques, 290 (2014) 199–206.

[45] K. Gajos, P. Petrou, A. Budkowski, K. Awsiuk, A. Bernasik, K. Misiakos, J. Rysz, I. Raptis, S. Kakabakos, Imaging and spectroscopic comparison of multi-step methods to form DNA arrays based on the biotin-streptavidin system, Analyst. 140 (2015) 1127–1139.

[46] E. Casero, L. Vázquez, A.M. Parra-Alfambra, E. Lorenzo, AFM, SECM and QCM as useful analytical tools in the characterization of enzyme-based bioanalytical platforms., Analyst. 135 (2010) 1878–1903.

[47] S. Ray, A.G. Shard, Quantitative analysis of adsorbed proteins by X-ray photoelectron spectroscopy, Anal. Chem. 83 (2011).

[48] M.F. Mora, J.L. Wehmeyer, R. Synowicki, C.D. Garcia, Investigating Protein Adsorption via

Spectroscopic Ellipsometry, in: D.A. Puleo, R. Bizios (Eds.), Biol. Interact. Mater. Surfaces, Springer, 2009: pp. 19–41.

[49] S.K. Vashist, C.K. Dixit, B.D. MacCraith, R. O'Kennedy, Effect of antibody immobilization strategies on the analytical performance of a surface plasmon resonance-based immunoassay, Analyst. 136 (2011).

[50] M.S. Wagner, D.G. Castner, Characterization of adsorbed protein films by time-of-flight secondary ion mass spectrometry with principal component analysis, Langmuir. 17 (2001).

[51] J.-B. Lhoest, M.S. Wagner, C.D. Tidwell, D.G. Castner, Characterization of adsorbed protein films by time of flight secondary ion mass spectrometry, J. Biomed. Mater. Res. 57 (2001).

[52] M. Henry, P. Bertrand, Surface composition of insulin and albumin adsorbed on polymer substrates as revealed by multivariate analysis of ToF-SIMS data, Surf. Interface Anal. 41 (2009).

[53] N. Giamblanco, G. Zhavnerko, N. Tuccitto, A. Licciardello, G. Marletta, Coadsorption-dependent orientation of fibronectin epitopes at hydrophilic gold surfaces, Soft Matter. 8 (2012).

[54] M.E. Wiseman, C.W. Frank, Antibody adsorption and orientation on hydrophobic surfaces, Langmuir. 28 (2012) 1765–1774.

[55] S. Chen, L. Liu, J. Zhou, S. Jiang, Controlling antibody orientation on charged self-assembled monolayers, Langmuir. 19 (2003).

[56] X. Zhao, F. Pan, B. Cowsill, J.R. Lu, L. Garcia-Gancedo, A.J. Flewitt, G.M. Ashley, J. Luo, Interfacial immobilization of monoclonal antibody and detection of human prostate-specific antigen., Langmuir. 27 (2011) 7654–7662.

[57] C. Dupont-Gillain, Orientation of adsorbed antibodies: In situ monitoring by QCM and Random sequential adsorption modeling, ACS Symp. Ser. 1120 (2012) 453–469.

[58] P. De Thier, J. Bacharouche, J.F.L. Duval, S. Skali-Lami, G. Francius, Atomic force microscopy analysis of IgG films at hydrophobic surfaces: A promising method to probe IgG orientations and optimize ELISA tests performance, Biochim. Biophys. Acta - Proteins Proteomics. 1854 (2015) 138–145.

[59] H. Wang, D.G. Castner, B.D. Ratner, S. Jiang, Probing the orientation of surface-immobilized immunoglobulin G by time-of-flight secondary ion mass spectrometry, Langmuir. 20 (2004).

[60] F. Liu, M. Dubey, H. Takahashi, D.G. Castner, D.W. Grainger, Immobilized antibody orientation analysis using secondary ion mass spectrometry and fluorescence imaging of

affinity-generated patterns, Anal. Chem. 82 (2010).

[61] V. Lebec, S. Boujday, C. Poleunis, C.-M. Pradier, A. Delcorte, Time-of-flight secondary ion mass spectrometry investigation of the orientation of adsorbed antibodies on sams correlated to biorecognition tests, J. Phys. Chem. C. 118 (2014).

[62] K. Awsiuk, A. Bernasik, M. Kitsara, A. Budkowski, J. Rysz, J. Haberko, P. Petrou, K. Beltsios, J. Raczkowska, Protein coverage on silicon surfaces modified with amino-organic films: A study by AFM and angle-resolved XPS, Colloids Surfaces B Biointerfaces. 80 (2010) 63–71.

[63] L. Fekete, K. Kůsová, V. Petrák, I. Kratochvílová, AFM topographies of densely packed nanoparticles: A quick way to determine the lateral size distribution by autocorrelation function analysis, J. Nanoparticle Res. 14 (2012).

[64] O. Ouerghi, A. Touhami, A. Othmane, H. Ben Ouada, C. Martelet, C. Fretigny, N. Jaffrezic-Renault, Investigating specific antigen/antibody binding with the atomic force microscope, Biomol. Eng. 19 (2002).

[65] Z. Lv, J. Wang, G. Chen, L. Deng, Imaging recognition events between human IgG and rat anti-human IgG by atomic force microscopy, Int. J. Biol. Macromol. 47 (2010).

[66] H. Fujiwara, Spectroscopic Ellipsometry: Principles and Applications, John Wiley & Sons, 2007.

[67] SENTECH Instruments GmbH, http://www.sentech.com/en/SE-800-PV__305/ (accessed March 30, 2017).

[68] D. Briggs, Surface analysis of polymers by XPS and static SIMS, Cambridge University Press, 1998.

[69] J.C. Vickerman, D. Briggs, eds., TOF-SIMS: Materials Analysis by Mass Spectrometry, 2nd edn., IM Publications LLP, 2013.

[70] D.J. Graham, D.G. Castner, Multivariate analysis of ToF-SIMS data from multicomponent systems: The why, when, and how, Biointerphases. 7 (2012) 1–12.

## *List of Abbreviations*

| | |
|---|---|
| 2whm | doubled value of width-at-half-maximum |
| AFM | atomic force microscopy |
| Ala | alanine |
| anti-mIgG | goat polyclonal antibody against mouse |
| anti-OTA Mab | mouse monoclonal antibody against ochratoxin A |
| anti-TBZ Mab | mouse monoclonal antibody against thiabendazole |
| APTES | (3-aminopropyl)triethoxysilane |
| Arg | arginine |
| ARXPS | angle resolved X-ray photoelectron spectroscopy |
| Asn | asparagine |
| Asp | aspartic acid |
| BB-MZI | broad-band Mach-Zehnder interferometer |
| BSA | bovine serum albumin |
| BSA-TBZ | bovine serum albumin and thiabendazole conjugate |
| Cys | cysteine |
| DAG | diacylglycerols |
| DNA | deoxyribonucleic acid |
| EBL | electron beam lithography |
| e-beam | electron beam |
| ETFE | poly(ethene-alt-tetrafluoroethene) |
| EUV- interference lithography | extreme ultraviolet interference lithography |
| FA | fatty acids |
| Gln | glutamine |
| Glu | glutamic acid |
| Gly | glycine |
| His | histidine |
| IgG | immunoglobulin G |
| Ile | isoleucine |
| LcH | lentil lectin |
| LCST | lower critical solution temperature |
| Leu | leucine |
| Lys | lysine |
| Mab | mouse monoclonal antibody |
| Met | methionine |
| OEG | oligoethylene glycol |

| | |
|---|---|
| OTA | ochratoxin A |
| OTA-OVA | ochratoxin A and ovalbumin conjugate |
| OVA | ovalbumin |
| QPDMAEMA | quaternized poly(oligo(ethylene glycol)ethyl ether methacrylate) |
| PCA | principal component analysis |
| PCs | principal components |
| PDMAEMA | poly(dimethylaminoethyl methacrylate) |
| PEG | polyethylene glycol |
| Phe | phenylalanine |
| PNIPAM | poly(N-isopropylacrylamide) |
| POEGMA | poly(oligo(ethylene glycol) methacrylate) |
| POEGMA246 | poly(oligo(ethylene glycol)ethyl ether methacrylate) |
| Pro | proline |
| RMS | root-mean-square |
| RT | room temperature |
| SAv | streptavidin |
| Ser | serine |
| TBZ | thiabendazole |
| Thr | threonine |
| TOF-SIMS | Time-of-flight secondary ion mass spectrometry |
| Trp | tryptophan |
| Tyr | tyrosine |
| UV | ultraviolet |
| XPS | X-ray photoelectron spectroscopy |

# *Acknowledgements*

First and foremost I would like to thank my supervisor prof. Andrzej Budkowski for scientific guidance, enlightening discussions and his leniency for my balancing of scientific work and maternity.

I would also like to thank my auxiliary supervisor dr hab. Jakub Rysz for his help and advice, especially during TOF-SIMS measurements. A special thank you goes to dr Celestino Padeste for the opportunity of an internship in Paul Scherrer Institute and for his hospitality during my visits in Switzerland. I would like to express my gratitude to dr Panagiota Petrou and all coworkers from N.C.S.R. 'Demokritos' for the preparation of samples as well as help and cooperation in the framework of the FOODSNIFFER project. I am very thankful to dr Yurij Stetsyshyn for samples preparation, valuable discussions and cooperation within the project on stimuli-responsive polymer coatings. I would like to thank dr Kamil Awsiuk for sharing his experience with me and for his assistance during measurements with surface science techniques. I would like to thank prof. Andrzej Bernasik for XPS measurements and help with data analysis. I am very grateful to all my colleagues from the Macromolecular Nanofilms Group, dr. Joanna Raczkowska, dr. Joanna Zemła, dr. Mateusz Marzec, mgr. Monika Biernat and mgr. Paweł Dąbczyński, for help, cooperation and friendly atmosphere.

Finally, I thank my husband, Alek, for his love and support.

This work was supported by the EU funded project "FOODSNIFFER" (FP7-ICT8-318319). I would like to acknowledge financial support from the M. Smoluchowski Kraków Research Consortium in the framework of the FOCUS grant and the KNOW scholarship.

# Paper I

## *Temperature and pH dual-responsive POEGMA-based coatings for protein adsorption*

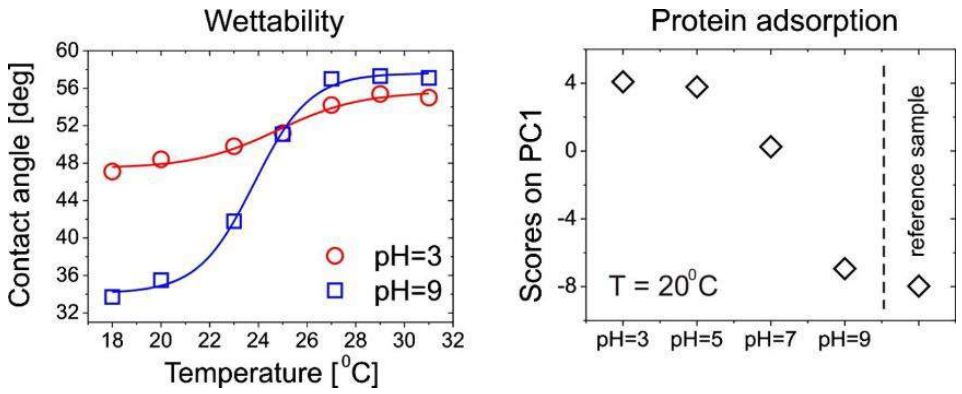


Highlights

- Poly(oligo(ethylene glycol) methacrylate) was polymerized from glass surface.
- Thermal but also pH-response is observed.
- Thermal sensitivity, observed in wettability, diminishes with decreasing pH.
- Such transition induces changes in protein adsorption.

Journal of Colloid and Interface Science 411 (2013) 247–256

Contents lists available at ScienceDirect

Journal of Colloid and Interface Science

www.elsevier.com/locate/jcis

# Temperature and pH dual-responsive POEGMA-based coatings for protein adsorption

Yurij Stetsyshyn [a,*], Katarzyna Fornal [b], Joanna Raczkowska [b,*], Joanna Zemla [b], Andrij Kostruba [c], Halyna Ohar [a], Mariya Ohar [a], Volodymyr Donchak [a], Khrystyna Harhay [a], Kamil Awsiuk [b], Jakub Rysz [b], Andrzej Bernasik [d], Andrzej Budkowski [b]

[a] "Lvivska Polytechnika" National University, S. Bandery 12, 79013 Lviv, Ukraine
[b] Smoluchowski Institute of Physics, Jagiellonian University, Reymonta 4, 30-059 Kraków, Poland
[c] Lviv Academy of Commerce, Samtshuk 9, and Lviv Institute for Physical Optics, Dragomanov 19, 79011 Lviv, Ukraine
[d] AGH University of Science and Technology, Faculty of Physics and Applied Computer Science, al. A. Mickiewicza 30, 30-059 Kraków, Poland

ARTICLE INFO

*Article history:*
Received 27 June 2013
Accepted 5 August 2013
Available online 23 August 2013

*Keywords:*
Stimuli-responsive polymer coatings
Graft polymerization
Wettability
Protein adsorption
Time of Flight-Secondary Ion Mass Spectrometry

ABSTRACT

Poly(oligo(ethylene glycol)ethyl ether methacrylate (POEGMA246) coatings were successfully fabricated using novel approach via polymerization from oligoperoxide grafted to premodified glass substrate. Wettability, content and composition of coatings fabricated with different polymerization times were determined using contact angle measurements, ellipsometry and Time of Flight-Secondary Ion Mass Spectrometry (TOF-SIMS). Thermo- and pH-responsive properties of POEGMA246 coatings were found to depend significantly on concentration of the grafted POEGMA246. Coatings fabricated with polymerization time 30 h exhibit not only temperature- but also pH-dependence of wettability. Thermal response of wettability, measured between 20 and 32 °C, was prominent at pH 9 and 7 and diminished or was absent at pH 5 and 3, indicating a transition between hydrated loose coils and hydrophobic collapsed chains, blocked at low pH. Protein adsorption, observed by fluorescence microscopy and analyzed semi-quantitatively using integral geometry approach, decreased dramatically for model protein (lentil lectin labeled with fluorescein isothiocyanate) at transition from pH 5 to pH 9, showing only very weak thermal-dependence. Strong protein adsorption response to pH and very weak one to temperature was confirmed by TOF-SIMS and Principal Component Analysis.

© 2013 Elsevier Inc. All rights reserved.

## 1. Introduction

In recent years, considerable efforts have been focused in developing polymeric materials able to change their physicochemical properties upon external triggers such as temperature, pH, light, and magnetic field. Considerable part of this research has been devoted to the stimuli-responsive polymeric surfaces. Stimuli-responsive polymeric surfaces are required for production of selective membranes, sensors and separation systems, for targeted drug delivery and nanoparticle translocation, for fabrication of mechanical actuators and transducers [1–4]. In particular, there is an increased interest in the polymeric surfaces which can change their affinity towards proteins and cells under external stimuli [1,2] and therefore can be potentially useful for several biomedical applications such as smart bioactive surfaces, selective bioseparation or hyperthermia-induced drug delivery [5,6]. Special attention has been given to polymer-cell hybrid multi-responsive systems [7,8].

Among diversities of the thermoresponsive polymers, poly(oligo(ethylene glycol) methacrylates) – POEGMAs deserve special attention [9,10]. These nonlinear poly(ethylene glycols) (PEG) analogues are biocompatible, uncharged, water-soluble, nontoxic, nonimmunogenic polymers and therefore the most applied synthetic polymer in the biomedical field [9–12]. Their thermoresponsive properties and the effect of side chain length on the *lower critical solution temperature* (LCST) point [13,14], as well as antifouling/stealth behavior [9,10,15–17] and antibacterial properties at room temperature [18] have been discussed in details. The studies performed by Chilkoti et al. for surfaces coated with POEGMA using surface-initiated atom transfer radical polymerization from a self-assembled monolayer on gold surfaces [15], showed that the resulting brushes reduced the adsorption of proteins from 100% of serum or fibronectin solution to the detection limit of the technique. Trend thermo-switchable materials prepared using the POEGMA-platform were developed by Lutz et al., who investigated intensively POEGMAs with various structures [10,17] and

* Corresponding authors.
*E-mail addresses:* yrstecushun@ukr.net (Y. Stetsyshyn), joanna.raczkowska@u-j.edu.pl (J. Raczkowska).

0021-9797/$ - see front matter © 2013 Elsevier Inc. All rights reserved.
http://dx.doi.org/10.1016/j.jcis.2013.08.007

suggested on switching between cell attachment and detachment at different temperatures.

Most of currently studied thermoresponsive POEGMA-contained systems can react almost exclusively to a single external trigger. To broaden the range of possible applications, numerous studies are aimed to fabricate multi-responsive polymer systems. In the huge family of homoPOEGMAs two homopolymers –poly(2-(2-methoxyethoxy)) ethyl methacrylate and poly(oligo(ethyleneglycol)ethyl ether methacrylate – (POEGMA246), which exhibit lower critical solution temperatures close to the physiological one (26 and 24 °C, respectively), are good candidates to produce multi-responsive complexes for biological applications. The polymers and copolymers of 2-(2-methoxyethoxy)ethyl methacrylate were described in details [19,20]. In contrast, POEGMA246 systems have been described only in limited literature [21,22].

Multi-responsive polymeric materials were fabricated for various copolymers [23–25], tri-block copolymers [26] and hydrogels [27]. In an another approach, temperature and pH dual-responsive POEGMA based polymer brushes on solid surfaces were synthesized using the radical polymerization of poly(di(ethylene glycol) methyl ether methacrylate-co-methacrylic acid) copolymers "from the surface" of initiators grafted to silicon [28]. Dual stimuli-response brushes were formed in a two-step procedure, including atom transfer radical polymerization "from the surface" and then hydrolysis of tert-butyl acrylate fragments to acrylate [29].

Motivated by the strong progress on multi-responsive polymeric materials [23–29], the novel dual-stimuli-response polymeric coatings of oligoperoxide-graft-POEGMA246 attached to glass are presented here. In our former paper [30] the fabrication method of temperature and pH dual-responsive coatings using graft polymerization of PNIPAM brushes "from the surface" of oligoperoxide, grafted to a native glass surface functionalized with (3-aminopropyl)triethoxysilane (APTES), was reported. This strategy is extended in this paper, where brushes "from the surface" of oligoperoxide, grafted to a native glass surface functionalized with APTES were fabricated by grafted polymerization of POEGMA246. The composition, thickness, morphology and wettability of resulting coatings were analyzed using Time of Flight-Secondary Ion Mass Spectrometry (TOF-SIMS), ellipsometry, Atomic Force Microscopy (AFM) and contact angle measurements, respectively. Both, thermal and pH-response of the POEGMA246-based coatings is demonstrated here, as reported earlier for block [29] and copolymer [28] brushes. Moreover, the huge influence of the thicknesses of the POEGMA246 nanolayers on thermo- and pH-sensitivity of modified surfaces was shown. Transition changes of surface roughness and protein adsorption, were observed with AFM and fluorescence microscopy, respectively. Finally, protein adsorption response to temperature and pH was confirmed with TOF-SIMS. Surprisingly, for low pH values, the commonly known antifouling POEGMA properties were not preserved and strong protein adsorption to the novel coatings was observed.

## 2. Experimental section

### 2.1. Materials

Pyridine and other organic solvents were purified as reported by Weissenerger et al. [31]. Polyethylene glycol (PEG-9) was supplied by Merck Chem. Co. Oligo(ethylene glycol)ethyl ether methacrylate – OEGMA246 (Mr-246) and 3-aminopropyltriethoxysilane (APTES) were supplied by Sigma–Aldrich. Lentil lectin, LcH, labeled with fluorescein isothiocyanate, was purchased from Biokom (Poland).

Tert-butyl hydroperoxide was obtained as described in [32] and purified by vacuum rectification. The fraction boiling in the temperature range of 45–47 °C (at 1.6 kPa) was collected. It had the refractive index $n_d^{20} = 1.4002 \pm 0.00002$, in accord with previous reports ($n_d^{20} = 1.4010$ [32]).

Pyromellitic acid chloride. In a 500 ml round-bottomed flask equipped with a thermometer and a reflux condenser, connected with water scrubber, 43.6 g (0.2 mol) of pyromellitic dianhydride and 91.6 g (0.44 mol) of $PCl_5$ were mixed and boiled in the oil bath until the mixture became homogeneous. Afterwards, it was additionally mixed for 15–16 h at 130–135 °C. The reflux condenser was then replaced by a Liebig condenser and approximately 60–63 g of $POCl_3$ was distilled off during 8 h. Then the temperature of the mixture was increased to 180–185 °C. The crude product was recrystalized then from gasoline yielding 51.2 g (78.1%) of a colorless crystalline product with the melting point 67 °C (in accord with the literature value 68 °C [33]) and acid number AN = 1373 mg KOH/g (calculated value is 1368 mg KOH/g).

Oligoperoxide with residual acid chloride groups. 4.6 g (0.014 mol) of pyromellitic acid chloride was dissolved in 15 ml of anhydrous dichlorethane, placed in three-necked flask equipped with stirrer, and 1.26 g (0.014 mol) of tert-butylhydroperoxide was added. The mixture was cooled down to 5 °C, and then 1.1 g (0.014 mol) of pyridine, dissolved in 10 ml of anhydrous dichlorethane, was added dropwise at 5 °C. Then the suspension was mixed for 1 h. Subsequently 5.6 g (0.014 mol) of PEG-9 was added and again the solution of 2.2 g (0.028 mol) pyridine in 10 ml of anhydrous dichlorethane was admixed dropwise. The mixture was then stirred for another 3 h and the temperature was rised gradually up to the room temperature. The precipitate of pyridinium chloride was filtered out. The solvent was distilled out and the pellet was dried in vacuum (100–200 Pa) at 40 °C for 3 h, yielding 8.2 g (81%) of oligoperoxide. The pellet had a yellowish resin-like appearance. Its characteristics are summarized as follows: content of active oxygen – 1.9% (calc. 2.2%); content of active chlorine – 5.4% (calc. 4.9%); AN = 163.1 mg KOH/g (calculated value is 155.3 mg KOH/g); infrared spectra showed characteristic bands of ν(C=O) in Ar—C(O)Cl, ν(C=O) in ester group at 1760 and 1752 $sm^{-1}$; doublet at 1390, 1365 $sm^{-1}$, referred to $d(C(CH_3)_3)$ and a band of tert-butoxy group at 848 $sm^{-1}$.

### 2.2. Preparation of coatings. Modification of glass surfaces with oligoperoxide

Glass plates (20 × 20 mm) (1) were dipped into 0.2% (w/w) methanolic solution of APTES for 24 h. After the incubation, loosely-attached silane molecules were removed with methanol in Soxhlet's apparatus. Then the plates functionalized with APTES (2) were dipped into 1% solution of oligoperoxide in arid dioxan for a certain period (grafting time of 24 h). Similarly, loosely-attached oligoperoxide was removed with dioxan in Soxhlet's apparatus during 4 h. As a result oligoperoxides grafted to aminated surfaces were obtained (3) in Scheme 1 [30].

### 2.3. Polymerization of POEGMA246 brushes

Glass plates with grafted oligoperoxide (3) were placed in a container with 0.1 M aqueous solution of the monomer OEGMA246, and heated under argon atmosphere at 90 °C for a certain period (polymerization time from 2 to 48 h), resulting in the oligoperoxide-*graft*-POEGMA246 coatings (4). Then the plates coated with polymerized POEGMA246 were washed with water in Soxhlet's apparatus for 4 h and dried. The modification procedure of peroxided glass surface by POEGMA246 and hypothetical schema of the surface modified by POEGMA246 brushes with low (4a) and high (4b) grafting densities are sketched in Scheme 1.

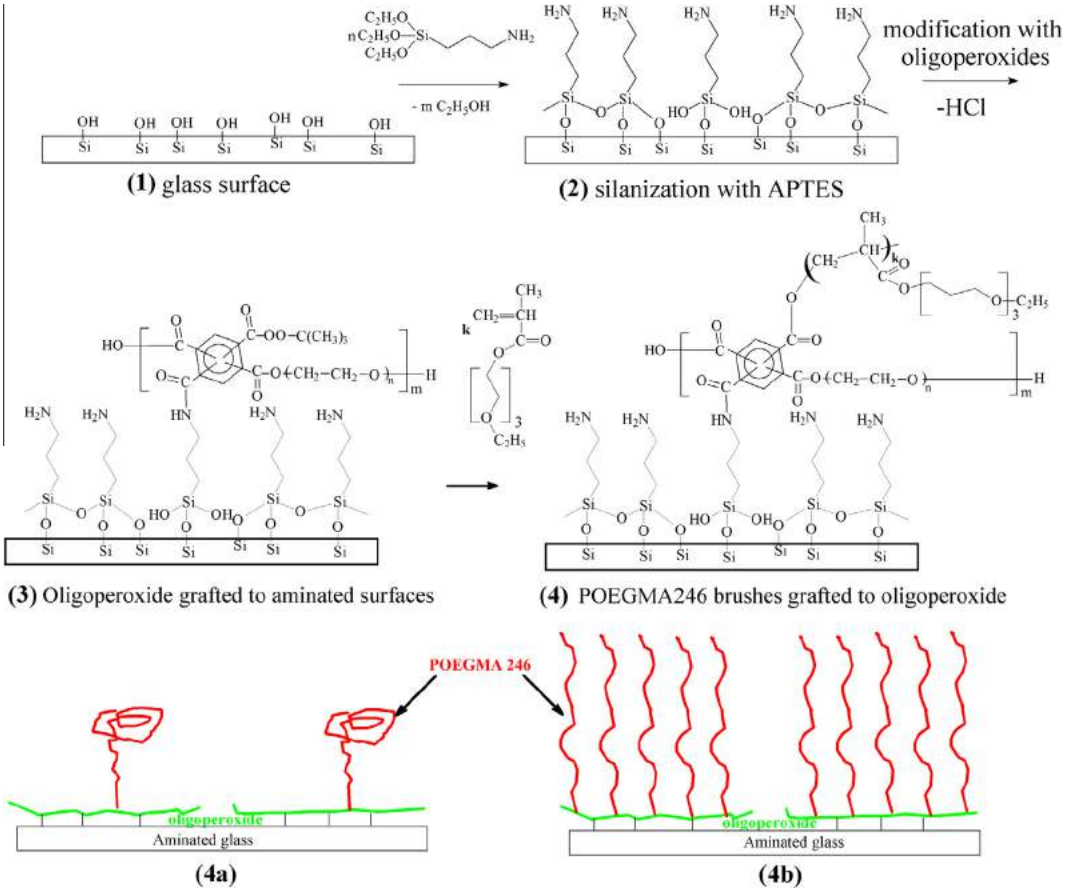


**Scheme 1.** Functionalization of glass surface (1) with amino-terminated APTES film (2), subsequent grafting of oligoperoxide (3) and polymerization of OEGMA246, initiated by peroxide groups of oligoperoxide, and resulting in POEGMA246 brushes (4). Surface modified by POEGMA246 brushes with low (4a) and high (4b) grafting densities.

### *2.4. Characterization of coatings. Water contact angle measurements (CA)*

Static contact angle experiments were performed by the sessile drop technique using a Kruss EasyDrop (DSA15) instrument with the Peltier temperature-controlled chamber. The measurements were carried out at temperatures ranging from 18 to 33 °C to determine thermal response of the oligoperoxide-*graft*-POEGMA246 coatings. Temperature was measured by thermocouple in contact with sample surface. To determine wettability corresponding to a given pH, the sample was immersed for 15 min in a buffer solution with the required pH, then dried carefully and finally placed in the temperature-controlled chamber of the EasyDrop instrument. Prior to the buffer exposure leading to the measurement at different pH, the sample was immersed in deionized water for 30 min and dried under stream of nitrogen. Contact angles were expressed as the average of ten measurements at different spots.

A buffer with pH close to 9 was made from 0.1 M aqueous solution of borax ($Na_2B_4O_7$). Buffer solutions with pH values of 7, 5 and 3 were prepared from 82.5%, 51.0% and 20.5%, respectively, (v/v) mixtures of 0.2 M disodium phosphate ($Na_2HPO_4$) and 0.1 M citric acid solution.

### *2.5. Ellipsometry*

Measurements were carried out with a serial null-ellipsometer LEF-3M, equipped with the "polarizer–compensator-specimen-analyzer" arrangement, enabling angular positions of polarization elements to be determined within a 0.01° precision. A He—Ne single-mode laser (light wavelength $\lambda = 632.8$ nm) was used as a light source. Polarization parameters of light reflected from a sample (angles $\Psi$ and $\Delta$) were determined using the two-zone technique (in the third and fourth measuring zone) for angle of incidence $\varphi$ varied between 58° and 63° (with a 1° step). This $\varphi$-range, corresponding to the region of the pseudo-Brewster angle (where $\Delta \approx \pi/2$ or $3\pi/2$), ensures maximal sensitivity. The iterative procedure using mono- and two-layer models was used to fit the ($\Psi$, $\Delta$) data recorded at optimal experimental conditions [34] and yielded average thickness $d$ (and refractive index $n$) for APTES and oligoperoxide-*graft*-POEGMA coatings, respectively.

The molecular masses of the grafted polymer brushes were calculated concerning ellipsometry data and kinetic parameters of the polymerization using equation:

$$M = \frac{C_p}{C_0(1 - e^{-k\tau}) \cdot n}$$

where $M$ is the molecular mass (g/mol), $C_p$ is the concentration of the POEGMA on the surface (from Fig. 2) (g/m$^2$), $C_0$ is initial concentration of peroxided groups of oligoperoxide on the surface (mol/m$^2$) ($C_0 = 2.38 \times 10^{-6}$ mol/m$^2$), $k$ is first order constant of the initiation at 90 °C ($k = 8.1 \times 10^{-6}$ s$^{-1}$), $\tau$ is polymerization time (s), $n$ is the polymerization effectiveness on the surface ($n = 0.4$) [35].

### *2.6. Protein adsorption*

Lentil lectin (LcH) labeled with fluorescein isothiocyante (adsorbing blue, $\lambda_{abs} = 490$ nm, and emitting green fluorescence light, $\lambda_{emit} = 525$ nm) was taken as a model protein to examine

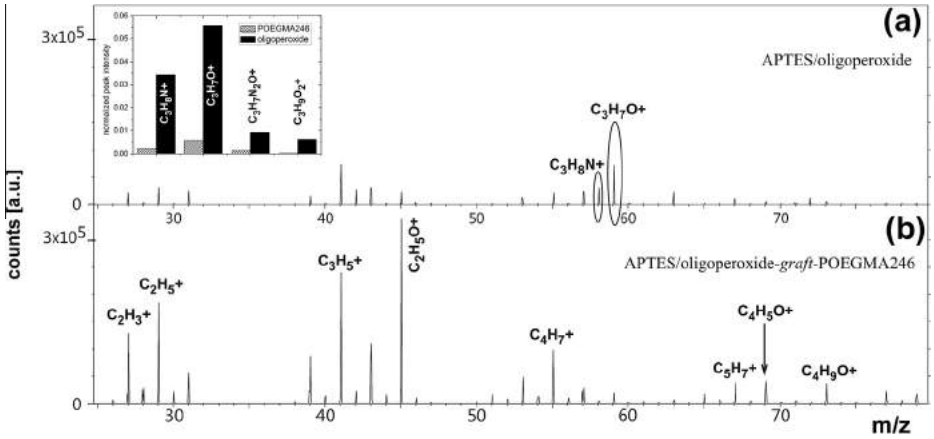


**Fig. 1.** Representative positive ion TOF-SIMS spectra of APTES-modified glass surface after subsequent steps of oligoperoxide grafting for 24 h (a) and POEGMA246 polymerization for 48 h (b). The signals characteristic and unique for the coating following each fabrication step are marked with secondary ion names and ellipses, respectively. The inset in (a) shows normalized intensities of peaks unique for oligoperoxide layer, recorded after each fabrication step.

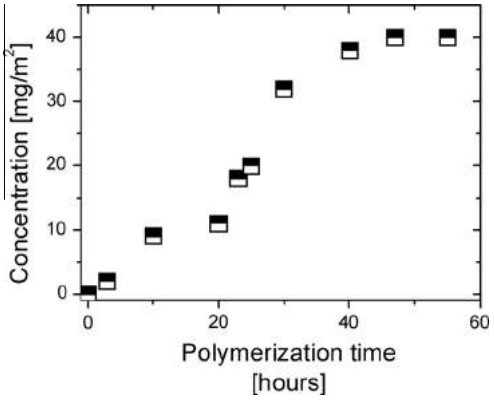


**Fig. 2.** Concentration of grafted POEGMA246 versus polymerization time.

adsorption to the oligoperoxide-*graft*-POEGMA246 coatings at different pH and temperatures.

Four LcH solutions, with different pH values and constant concentration equal to 125 μg/mL, were prepared using four different buffers. Phosphate buffer saline (PBS) was used as the neutral buffer (pH = 7.4). The pH = 3 and 5 buffers were prepared by adding dropwise HCl to the PBS. The buffer with pH = 9 was obtained by adding NaOH to the PBS buffer.

To examine pH-controlled protein adsorption, a 80 μl drop of each protein solution was placed on the oligoperoxide-*graft*-POEGMA246 substrates (obtained after 30 h of POEGMA246 polymerization) for incubation time of 15 min. Then each sample was rinsed carefully with the buffer of pH equal to the one of the protein solution used. Finally, each sample was dried in nitrogen stream. Additionally, prior to the examination with TOF-SIMS, the samples were rinsed with deionized water and dried with nitrogen.

To study temperature-dependent adsorption, a drop of the protein solution with pH = 9 or 5 was placed (for incubation time of 15 min) on each of the oligoperoxide-*graft*-POEGMA246 substrates (obtained after 30 h of POEGMA246 polymerization) kept at 20 and 32 °C. Then, all samples were rinsed with the buffer to remove non-adsorbed proteins and dried under nitrogen stream.

### 2.7. Optical fluorescence microscopy

Protein adsorption to the oligoperoxide-*graft*-POEGMA246 coatings was examined using optical microscope Olympus BX51, equipped with a 100 W halogen lamphouse, filter U-MNG2 ($\lambda_{exit}$ = 470–490 nm, $\lambda_{emit}$ > 510 nm) and camera type DP72. All images were recorded for dried samples using the Cell^F program.

Two series of experiments were performed to study the impact of pH and temperature on the protein adsorption. The recording conditions were adjusted separately for both experimental series.

### 2.8. TOF-SIMS

To examine the surface chemistry after each fabrication step of the oligoperoxide-*graft*-POEGMA246 coatings and to examine protein adsorption to the coatings at various pH, Time of Flight-Secondary Ion Mass Spectrometry (TOF-SIMS) measurements were performed using the TOF.SIMS 5 (ION-TOF GmbH) instrument, equipped with 30 keV bismuth liquid metal ion gun. $Bi_3$ clusters were used as the primary ions with the ion dose density lower than $10^{12}$ ion/cm$^2$ to ensure static mode conditions. Pulsed low energy electron flood gun was used for charge compensation. For each sample, high mass resolution spectra were acquired from four different and nonoverlapping spots (200 μm × 200 μm area each). For all spectra, the minimal mass resolution ($m/\Delta m$) at $C_4H_5$ ($m/z$ = 53) peak was above 5500. Mass calibration was performed with H, $H_2$, CH, $C_2H_2$ and $C_4H_5$ peaks. The complex multiple TOF-SIMS spectra acquired to examine pH-controlled protein adsorption were examined with Principal Component Analysis (PCA) to enhance detection of subtle differences in surface chemistry of the samples.

## 3. Results and discussion

The oligoperoxide-*graft*-POEGMA246 coatings attached to glass were prepared in a three-step process, all steps outlined in Scheme 1 (for the details see Experimental Section): first, the native glass surface was modified with APTES. Then oligoperoxide was grafted, taking advantage of the interaction between amino groups of APTES layer and pyromellitic chloroanhydride fragments in oligoperoxide molecules. Finally, the POEGMA246 brushes were fabricated using polymerization "from the surface" of oligoperoxide. The composition and temperature-sensitive wettability of the oligoperoxide-*graft*-POEGMA246 coatings, fabricated with different polymerization times are described in Section 3.1. The impact of pH on the thermal response of wettability is discussed in Section 3.2. In turn, controlled protein adsorption to the coatings fabricated with polymerization time 30 h is presented in Section 3.3.

### 3.1. Composition and wettability of oligoperoxide-graft-POEGMA246 coatings

#### 3.1.1. Chemical composition and surface coverage with POEGMA246 (TOF-SIMS and ellipsometry)

In our previous work [30] the three-step fabrication process of the novel dual-stimuli-responsive polymeric coatings of oligoperoxide-*graft*-PNIPAM attached to glass surface was reported. In the present work similar method was developed to fabricate stimuli-responsive polymeric coatings of oligoperoxide-*graft*-POEGMA246. The POEGMA246 brushes were polymerized from the oligoperoxide, the latter attached to the glass premodified with APTES. To verify the overall composition of the coatings, Time of Flight-Secondary Ion Mass Spectrometry (TOF-SIMS) was applied. TOF-SIMS was working in the so called static mode, known for superior chemical specificity (mass resolution $m/\Delta m > 7800$) and surface sensitivity characterized by sampling depth less than 2 nm. Representative positive ion TOF-SIMS spectra, recorded for glass surface preliminary modified with APTES, after each of the successive fabrication step are presented in Fig. 1.

Positive ion TOF-SIMS spectrum of glass surface premodified with APTES after subsequent grafting of oligoperoxide for 24 h (Fig. 1a) depicts $C_3H_8N^+$, $C_3H_7O^+$, $C_3H_7N_2O^+$ and $C_3H_9O_2^+$ peaks, unique for oligoperoxide molecules [30]. Two of them, $C_3H_7N_2O^+$ and $C_3H_9O_2^+$ are not presented in Fig. 1, as they are hardly visible in the given scale. TOF-SIMS spectrum recorded for POEGMA246 brushes after 48 h of polymerization from the surface of oligoperoxide (Fig 1b), reveals series of peaks characteristic for POEGMA246: $C_2H_5O^+$, $C_4H_5O^+$ and $C_4H_9O^+$, and also $C_2H_3^+$, $C_2H_5^+$, $C_3H_5^+$, $C_4H_7^+$ and $C_5H_7^+$ ions. The normalized intensities of four peaks unique for oligoperoxide layer, presented as inset in Fig. 1, are reduced by 94%, 90%, 85% and 96% for $C_3H_8N^+$, $C_3H_7O^+$, $C_3H_7N_2O^+$ and $C_3H_9O_2^+$, respectively, indicating complete coverage of the surface with POEGMA246 brushes.

Thicknesses of grafted layers was examined using ellipsometry. Typical thickness of APTES, measured by ellipsometry for the conditions used for glass functionalization, was equal to 0.5 nm (in accord with literature [36]). Maximal thickness of oligoperoxide film, used as a substrate for OEGMA246 polymerization did not exceed 1.5 nm [37]. The average thickness of POEGMA246 brush increased with polymerization time up to 37–40 nm for 40 h, whereas the refractive index did not change (see Fig. S1 in the Supporting Information).

To calculate oligoperoxide and POEGMA concentrations in grafted nanolayers ellipsometric data was used. Assuming oligoperoxide and POEGMA bulk density as 1.35 g/cm$^3$ and 1.0 g/cm$^3$, respectively, the calculated concentration of oligoperoxide is constant and equals to 2 mg/m$^2$, whereas the concentration of POEGMA (Fig. 2) increases from 0 to 40 mg/m$^2$ for coatings prepared with increasing polymerization times.

The calculation of the grafting density of POEGMA chains on peroxided glass surface was performed using the equation:

$$\sigma = \frac{h\rho N_A}{M} \quad (1)$$

where the $\sigma$ is the grafting density (chains/nm$^2$), h is the dry layer thickness measured by ellipsometry (nm), $\rho$ is the POEGMA bulk density, $N_A$ is Avogadro's constant, and $M$ (g/mol) is the molecular mass of the POEGMA brushes grafted onto the surface. Molecular masses and grafting densities obtained for different polymerization times are presented in Table 1.

The molecular masses of POEGMA brushes fabricated during polymerization increased with increasing polymerization time. Analogously, grafting densities of POEGMA brushes increased and for the POEGMA246 layers fabricated for 40 h equaled approximately 0.4 chains/nm$^2$, which is very similar to the values previously described (0.1–0.4 chains/nm$^2$) [38,39].

**Table 1**
Molecular masses and grafting densities of POEGMA246 brushes at different polymerization times.

| Polymerization time | $M$ (g/mol) | $\sigma$ (chains/nm$^2$) |
|---|---|---|
| 10 | 29,000 | 0.14 |
| 20 | 35,650 | 0.25 |
| 30 | 55,800 | 0.33 |
| 40 | 61,300 | 0.39 |
| 48 | 61,300 | 0.39 |

The presented data demonstrate the concentration of oligoperoxide in coating close to 2 mg/m$^2$, significantly smaller than the concentration of the grafted POEGMA246. The influence of concentration of the POEGMA246 on the properties of coatings will be discussed in subsequent sections.

#### 3.1.2. Influence of POEGMA246 polymerization time on temperature-sensitive properties of as prepared POEGMA246 coatings (Contact Angle and ellipsometry)

To examine the temperature-sensitive properties of POEGMA246 attached to glass surfaces, contact angles of sessile water droplets on the oligoperoxide-*graft*-POEGMA246 coatings were measured between 18 and 33 °C, for samples fabricated for different POEGMA246 polymerization times (varied from 0 to 48 h). The results, presented in Fig. 3, show almost no thermal response of the pure oligoperoxide layer (stars in Fig. 3).

Oligoperoxide-*graft*-POEGMA246 coatings fabricated with the polymerization times ranging from 23 to 48 h demonstrate significant wetting changes from hydrophilic to hydrophobic for temperatures raising from 18 to 32 °C. They correspond to POEGMA246 brush transition from hydrated state with loose coils (at lower temperatures) to hydrophobic state with collapsed chains (at higher temperatures) [9]. In earlier works [9,21,22] POEGMA246 bulk phase transition in aqueous solution was characterized by a sharp transition at $T_C$ = 26 °C. In contrast, oligoperoxide-*graft*-POEGMA246 coating fabricated with the polymerization time 10 h (Fig. 3) and 20 h – our data non-presented here (ellipsometrically determined POEGMA concentration – 9 and 11 mg/m$^2$, respectively) did not demonstrate typical temperature-sensitive behavior. Moreover, the values of contact angles are very similar to those recorded for surface modified only with oligoperoxide. This phenomenon can be explained by blocking of the typical temperature-sensitive properties of the POEGMA246 as a result of complexation between carboxyl groups of the oligoperoxide and ether groups of the POEGMA246 [40,41]. Similar interactions have

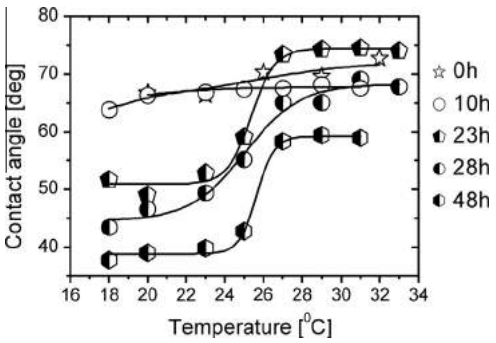


**Fig. 3.** Temperature dependence of water contact angle determined for the oligoperoxide-*graft*-POEGMA246 coatings fabricated wih different polymerization times (marked by different symbols as indicated in the legend). Solid lines were generated by sigmoidal function.

been observed between poly(carboxylic acids) and poly(ethylene oxide) even in the neutral pH regime [40]. The ratio of concentrations of —COOH (carboxyl) groups, able to take part in complex, and —$COO^-$ (carboxylate) groups of the oligoperoxide at neutral pH (after immersion in distilled water) is constant. Concentration of ether groups in POEGMA varies for coatings fabricated for the different polymerization times.

Fig. 4a shows water contact angles of POEGMA246 coatings at 20 °C as a function of polymerization time. For POEGMA246 polymerization times up to 23 h and corresponding concentration of the POEGMA246 coverage under 18 mg/$m^2$, the observed contact angles depict surface more hydrophobic than expected, which can be explained as a result of complex creation of POEGMA246 ether groups and the oligoperoxide carboxyl groups, which is possible even in the solid state [40,42]. The complexation is schematically sketched in Fig. 4c. For low concentration of the grafted brushes, POEGMA246 ether groups are completely blocked by oligoperoxide carboxyl groups whereas for higher concentration of the POEGMA246 brushes some ether groups remain unblocked (Fig. 4d). Therefore, for polymerization time above 23 h, hydrophility of the surfaces and typical temperature-sensitive behavior is observed. The difference between upper and lower contact angle, plotted versus polymerization time (Fig. 4b) also shows significant change in surface properties for samples fabricated with times longer than 20 h.

Using the ellipsometry, the influence of concentrations of the grafted POEGMA246 brushes on their temperature-sensitive behavior was confirmed. The water content in the structure of the oligoperoxide-graft-POEGMA246 coatings immersed in water was calculated assuming refractive index of POEGMA246 and water equal to 1.5 and 1.33, respectively. The water content in the POEGMA246 coating after 10 h polymerization is at 20 °C – 82.3% and at 31 °C – 81.1%, suggesting no temperature-sensitive properties for this concentration of grafted POEGMA246. In contrast, for samples fabricated with polymerization time of 30 h were demonstrated temperature transition of POEGMA246 coating. Calculated water content was 91.6% and 87.1% at 20 °C and 31 °C, respectively, accompanied additionally by a change in the refractive index value (see Figs. S2 and S3 in the Supporting Information).

The above confirms the hypothesis that temperature-sensitive behavior of the polymerized "from the surface" POEGMA246 brushes depends on the concentration ratio of oligoperoxide and POEGMA246. For POEGMA246 nanolayers with concentration lower than 20 mg/$m^2$ temperature-sensitive properties were blocked for all examined temperatures, even at neutral pH (as prepared). For concentration of the POEGMA246 coatings higher than 20 mg/$m^2$, the chains form brushes at lower temperatures, but above $T_c$ they are presumably in the mushroom regime, leading to significant change in the properties of the coating.

### 3.2. Temperature and pH-induced dual response of oligoperoxide-*graft*-POEGMA246 coatings (CA)

Thermal response of water contact angle for the oligoperoxide-*graft*-POEGMA246 coatings fabricated for different polymerization time was examined at conditions corresponding to different pH (Fig. 5). The temperature dependence of water contact angle was measured at four pH values ranging from 3 to 9 and additionally at pH – 11, for POEGMA246 polymerized for 20 h. Almost no thermal and pH-responses of water contact angle for the pure oligoperoxide layer grafted to glass surface was observed (Fig 5a).

Similar behavior was found for oligoperoxide-*graft*-POEGMA246 nanolayer with polymerization time 20 h and concentration of POEGMA246 equal to 11 mg/$m^2$. Here, the typical temperature-sensitive behavior was observed only for pH = 11. In contrast, for oligoperoxide-*graft*-POEGMA246 coating fabricated for 30 h of POEGMA246 polymerization and concentration of POEGMA246 close to 30 mg/$m^2$, temperature dependence of water contact angle, measured at four pH values ranging from 3 to 9, shows a huge pH-sensitivity of the layer (Fig. 5c). Characteristic morphologies of oligoperoxide-*graft*-POEGMA246 coatings after 30 h of polymerization, modified both with pH and temperature, were also recorded with AFM (see Fig. S4 in the Supporting Infor-

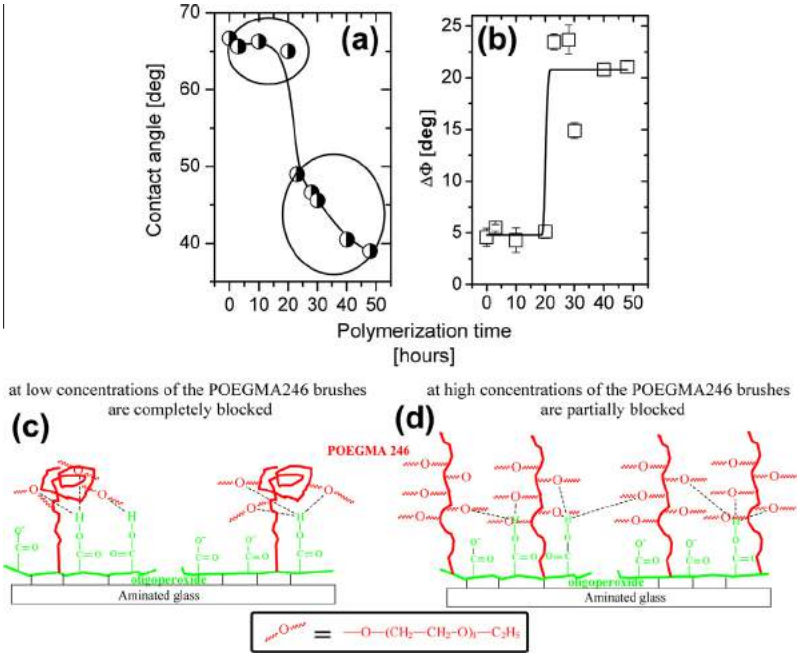


**Fig. 4.** Water contact angle at 20 °C (a) and $\Delta\Phi$ – difference between upper (at 31 °C) and lower (20 °C) contact angle (b) plotted for oligoperoxide-*graft*-POEGMA246 as a function of POEGMA polymerization time. Solid lines are a guide to eye. Completely (c) and partially (d) blocked POEGMA brushes (20 °C) at low and high POEGMA246 concentrations, respectively.

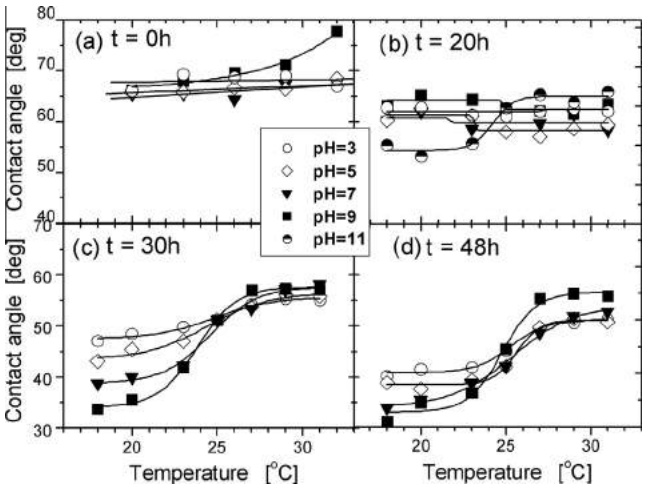


**Fig. 5.** Temperature dependence of water contact angle, determined at pH values of 3, 5, 7, and 9 on oligoperoxide-*graft*-POEGMA246 coatings after 0 (a), 20 (b), 30 (c) and 48 h (d) of POEGMA246 polymerization. Solid lines were generated by a sigmoidal function.

mation). For the coating after 48 h of POEGMA246 polymerization (Fig. 5d), a huge temperature dependence accompanied by only a weak pH-dependent variation of water contact angle was observed. This behavior may be attributed to the concentration of POEGMA246 ether groups in the brushes fabricated for polymerization time 48 h, higher than can be blocked by oligoperoxide carboxyl groups for all examined pH values. While the pure POEGMA246 brushes are not pH-sensitive [28], the oligoperoxide-graft-POEGMA246 coatings for some ratio between the oligoperoxide and POEGMA246 show strong response to pH.

In our previous work [30] thermal and pH dual-sensitivity was observed for PNIPAM polymerized from oligoperoxide attached to the substrate. Thermal response of wettability, manifested around $T_C$ = 27–30 °C, was prominent at pH 9 and 7 with PNIPAM transition from hydrated loose coils to hydrophobic collapsed chains and diminished or absent at pH 5 and 3 when only the hydrophobic surface was observed at all polymerization times. In contrast, represented here POEGMA-based systems have different properties at different polymerization times. It can be assumed that behavior of the grafted POEGMA246 nanolayer is determined by POEGMA246 polymerization time and, accordingly, concentration of the POEGMA246 and the concentration ratio of the oligoperoxide and POEGMA246. A similar system was fabricated by Laloyaux and co-workers, where varying the composition of the copolymer in methacrylic acid units from 4 to 14 mol% one switches the brushes from a pH modulated thermo-responsive behavior to a temperature-modulated pH-responsive behavior in water.

Interpolymer complexes, formed by systems of specific interactions between carboxylic groups of ionogenic polymers and proton-accepting nonionic polymers, for example, poly(ethylene oxide), have been intensively developed for more than 4 decades [40,41]. It has been demonstrated that the interaction between these polymers is governed by hydrogen bonding. In a solution the polycomplex exists at alkaline conditions, whereas at acid conditions the interaction results in phase separation. In the neutral pH region some interactions between the two polymers were also observed [28,40,41].

As asserted before, POEGMA246 concentration has significant influence on the thermal response of oligoperoxide-*graft*-POEGMA246 coatings for constant oligoperoxide concentration. To explain that, it is essential to consider the dynamical equilibrium between the —COOH (carboxyl) and —$COO^-$ (carboxylate) groups. To change the dynamical equilibrium of the —COOH ↔ —$COO^-$ groups it is enough to immerse the polymer in a buffer solution. For acid conditions —COOH groups dominate, while —$COO^-$ groups are dominant for alkaline conditions, leading to an increase in the degree of ionization at a given pH. It was demonstrated using Fourier Transform infrared spectroscopy, that at low pH the acid groups are protonated and form dimers involving intra- or intermolecular H-bonds [28]. At high pH, the acid groups are deprotonated. Only protonated acid groups are able to create complexes with ether oxygens of the POEGMA.

A hypothetical scenario of van der Waals interactions and hydrogen bonding between ether oxygens of the POEGMA246 brushes, carboxyl groups of oligoperoxide and water molecules at various pH and temperatures for POEGMA246 coatings fabricated for different polymerization times was proposed. For high pH values typical thermal response of wettability with well expressed LCST (Fig. 5, $t$ = 20 h at pH = 11, $t$ = 30 h at pH = 7 and 9, $t$ = 48 h all cases) can be observed, similarly to that described for the poly(oligoethylene glycol) copolymers [29]. In this case, the properties of coating can be mainly attributed to the hydrogen bonds between ether oxygens of poly(ethylene glycol) and water hydrogens at $T < T_c$. This balance is disrupted at $T > T_c$, where polymer–polymer interactions are thermodynamically favored in comparison to polymer–water interactions [43]. This induces POEGMA246 transition from hydrated loose coils to hydrophobic collapsed chains. In this case, deprotonated (—$COO^-$) groups dominate and creation of complexes with POEGMA is no longer possible. While pure POEGMA246 chains are not pH-sensitive [28], the oligoperoxide-*graft*-POEGMA246 coatings show strong response to pH at some concentration of POEGMA246.

At low pH, where thermo-sensitive properties are blocked, protonated (—COOH) groups dominate enabling the creation of complexes with ether oxygens of POEGMA246.

### 3.3. Controlled protein adsorption to oligoperoxide-graft-POEGMA246 coatings

Novel antifouling materials, potentially used as medical implants, drug delivery carriers, biosensors and membrane materials are much-desired nowadays [44]. Special attention is given to PEG-based materials [9,10,15–18], which demonstrate low-fouling ability to prevent nonspecific protein adsorption and cell adhesion, due to the hydration layer near their own surface [45–47], that forms a physical and energetic barrier for protein adsorption on the surface. The strength of surface hydration is primarily determined by physicochemical properties of materials (i.e. molecular weight and surface chemistry) and their surface packing (i.e. film thickness, packing density and chain conformation) [44]. Moreover, high PEG chain mobility plays an important role in protein resistance, especially for long-chain polymers. When a protein approaches the surface, the compression of the polymer chains causes steric repulsion to prevent protein adsorption due to unfavorable decrease in entropy [48].

Only few studies have been devoted to the temperature dependence of protein adsorption on PEG and OEG films. Temperature dependence of proteins adsorption (lipase and fibrinogen) on poly- and oligo(ethylene glycol)-terminated alkanethiolate monolayers prepared on Au and Ag surfaces has been studied by Grunze et al. It was found that films, which are protein resistant at room temperature, remain inert at elevated temperatures. For films which are not inert at room temperature, the amount of adsorbed protein increases with temperature [49]. In an another work, Grunze and coworkers have also shown that adsorption of proteins pyruvate kinase and lysozyme to the surface modificated with oligo(ethylene glycol)-containing thiol is very low at room temperature (under LCST) and can drastically increase at temperatures above LCST [16]. The ellipsometric measurements on PEG films

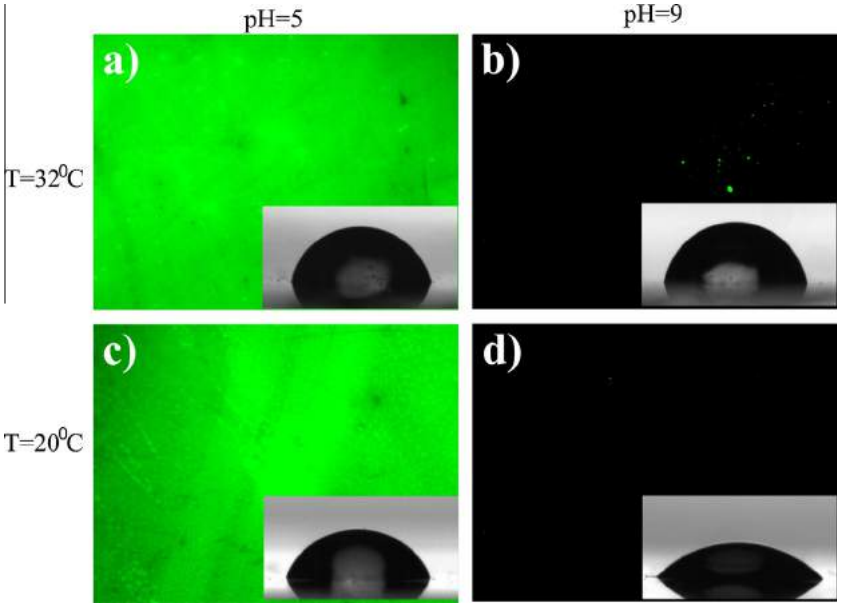


**Fig. 6.** Fluorescence micrographs of lentil lectin LcH proteins (labeled with fluorescein isothiocyanate) adsorbed to oligoperoxide-*graft*-POEGMA246 coating (after 30 h of POEGMA246 polymerization) and recored for values of pH 5 (a, c) and 9 (b, d) at temperatures of 20 (c, d) and 32 °C (a, b). The size of the images is 270 μm × 150 μm. Corresponding photographs of water droplets are presented in the insets.

between 17 and 71 °C showed an increasing amount of adsorbed serum proteins at higher temperatures [50]. This effect was attributed to temperature-induced changes in the film structure, which affect the dipole strength of the PEG films and thus the interaction between the coated surface and the proteins. A similar behavior was observed by Leckband et al. who found that grafted PEG brushes exhibit protein resistance at room temperature but lose their protein repulsive properties above 35 °C [51].

The effect of pH on bovine serum albumin adsorption (BSA) on the PEGylated membrane has been studied by Stamm and coworkers [52], where protein adsorption has been investigated at three different pH values (3, 4.7 and 8) indicating maximum adsorption of BSA at pH 4.7.

In the present work, the lentil lectin from Lens culinaris (LcH) labeled with fluorescein isothiacyante was used as a model protein to evaluate protein adsorption [53] to the coatings. Lectins are proteins that are able to bind specifically with α-D-mannose present on cell surfaces [54]. Therefore, tunable lectin adsorption to dual-responsive surfaces would potentially allow to initiate and control several biological processes on such surfaces.

Although protein adsorption may be affected not only by the surface but also by protein properties, that can be modified by external factors, such as pH or temperature [53], the used lentil lectin LcH do not show significant changes in molecular structure for the range of interest [55–57].

*3.3.1. pH-response of protein adsorption observed by fluorescence*

It was demonstrated in Section 3.2.1 that optimal dual thermo- and pH-sensitive properties are observed for coatings after 30 h of POEGMA246 polymerization. Hence, this type of film has been chosen to investigate lentil lectin adsorption at pH 9, 7, 5 and 3 and at temperatures of 20 and 32 °C. To confirm protein adsorption dependence on the unique properties of oligoperoxide-*graft*-POEGMA246 coating, the control experiment of protein adsorption to glass surface for different pH was performed.

The representative fluorescence micrographs showing the adsorption of lentil lectin to oligoperoxide-*graft*-POEGMA246 coatings are shown in Fig. 6 for pH = 5 (a, c) and 9 (b, d) and $T$ = 20 (c, d) and 32 °C (a, b). Samples prepared at pH = 9 reveal no (Fig. 6d) or hardly visible (Fig. 6b) fluorescence, implicating very weak or even zero-protein adsorption to the investigated surfaces. As the anti-fouling properties of POEGMA are commonly known, this result fulfills the expectations.

Surprisingly, for pH = 5 (Fig. 6a and c), strong fluorescence is clearly visible for both discussed temperatures, suggesting significant reduction of anti-fouling properties of oligoperoxide-*graft*-POEGMA coating leading to strong, temperature-independent protein adsorption. Thus, we obtained pH-sensitive surfaces (after 30 h of POEGMA246 polymerization) with switched properties for controlled protein adsorption. In contrast, PNIPAM-based surfaces that were described in our previous work [30] demonstrated the temperature- and pH-controlled lentil lectin adsorption. Results of the control experiment, performed on the glass surface, show no visible difference in fluorescence micrographs recorded for different pH and temperature values. In all cases strong fluorescence can be observed.

To provide more detailed description of the fluorescence micrographs, they were analysed semiquantitatively, using integral geometry approach [30,58,59] which provides average values of fluorescence intensity, corresponding to each sample but

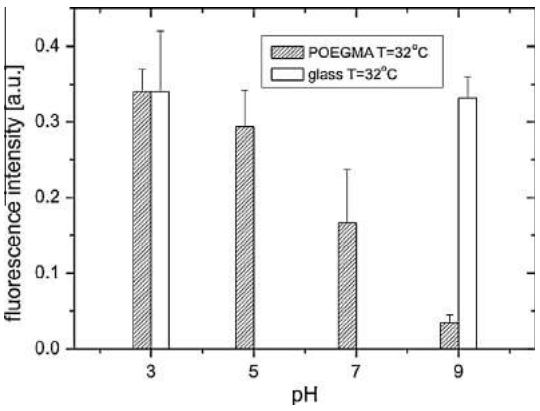


**Fig. 7.** Fluorescence intensity of lentil lectin LcH proteins adsorbed to oligoperoxide-*graft*-POEGMA246 coating and glass surface at $T$ = 32 °C.

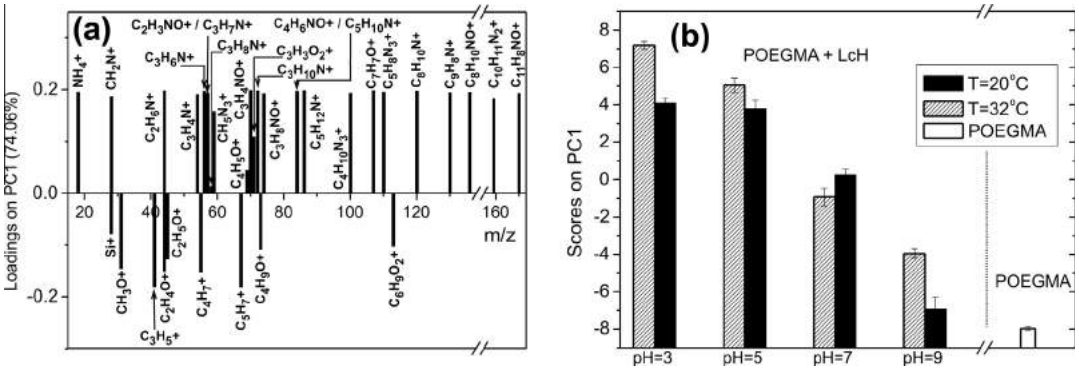


**Fig. 8.** PCA analysis of TOF-SIMS spectra: PC1 loadings (a) and PC1 scores (b).

normalized for all recorded micrographs. Calculated intensities of the analyzed micrographs are presented in Fig. 7.

Fluorescence intensity, proportional to the protein adsorption to oligoperoxide-*graft*-POEGMA246 coating is neglibly small for pH = 9 and increases monotonically with decreasing pH, reaching eventually for pH = 3 the same level as obtained for the reference measurement of protein adsorption to the glass. For the control samples fluorescence intensity remains constant for all pH values, indicating strong dependence of protein adsorption on the pH-tunable properties of oligoperoxide-*graft*-POEGMA246 coatings rather than on the other experimental conditions.

As mentioned above, PEG-based materials are non/low-fouling due to high degree of hydration that forms physical and energetic barriers for protein adsorption and high PEG chain mobility, which causes steric repulsion that prevents protein adsorption. Disappearance of the proteins low-fouling properties in the POEGMA modified surfaces at pH 3, 5 and 7 may be connected with breaking of hydrogen bonds between the ether oxygens of fragments of POEGMA246 and water molecules and due to breaking of the hydration layer close to POEGMA246 surface. It could be explained due to competitive interactions between ether oxygens of the POEGMA brushes and carboxyl groups of oligoperoxide or water molecules. It seems that ratio of the carboxyl no ionized groups to ether oxygens for coating with polymerization times 30 h is sufficient to destroy the hydration layer even at neutral pH. Moreover, formation of those bonds leads to considerable weakening in POEGMA chain mobility and can be the additional factor leading to the disappearance of non/low-fouling properties.

*3.3.2. Response of protein adsorption observed by TOF-SIMS*

To confirm results obtained by the analysis of fluorescence micrographs, the TOF-SIMS technique was applied to trace protein adsorption to oligoperoxide-*graft*-POEGMA246 coatings at different temperatures (20 °C, 32 °C) and pH (3, 5, 7 and 9). Four positive ion TOF-SIMS spectra were recorded for each analyzed sample. Additionally bare oligoperoxide-*graft*-POEGMA246 layer was measured as the reference sample. To enhance the reliability of this experimental method, simultaneous PCA analysis was performed, as described in details in our previous work [30]. Eight peaks characteristic for the POEGMA coatings, namely ($CH_3O^+$, $C_3H_5^+$, $C_2H_4O^+$, $C_2H_5O^+$, $C_4H_7^+$, $C_5H_7^+$, $C_4H_9O^+$, $C_6H_9O_2^+$) and twenty-four ones typical for proteins were chosen for detailed PCA analysis, as presented in Fig. 8a.

Eighteen of considered protein peaks reflect the fragments of amino acids building LcH [60]: $C_2H_6N^+$ (Ala); $C_3H_7N^+$ and $C_5H_{10}N^+$ (Lys); $CH_5N_3^+$, $C_4H_{10}N_3^+$ and $C_5H_8N_3^+$ (Arg); $C_3H_8NO^+$ (Thr); $C_3H_4NO^+$ (Asp); $C_3H_3O_2^+$ (Ser); $C_4H_{10}N^+$ (Val); $C_4H_6NO^+$ (Gln); $C_5H_{12}N^+$ (Leu); $C_7H_7O^+$ and $C_8H_{10}NO^+$ (Tyr); $C_5H_8N_3^+$ (His); $C_8H_{10}N^+$ (Phe); $C_9H_8N^+$, $C_{10}H_{11}N_2^+$ and $C_{11}H_8NO^+$ (Trp).

The $C_4H_5O^+$ peak, although recognized as threonine (Thr), does not contribute to the PCA analysis, as it is characteristic for bare oligoperoxide-*graft*-POEGMA246 coating too (see Fig. 1b).

The calculated scores on PC1 are presented in Fig. 8b. For $T$ = 32 °C the PCA results reveal the same character as fluorescence intensities (Fig. 7). Protein adsorption increases monotonically with decreasing pH. Although the PC1 score for pH = 9 is significantly higher than the one calculated for the reference sample, it still remains more than 3 times smaller as compared to the value recorded for pH = 3, implicating non-zero but very weak protein adsorption to POEGMA246 brushes.

Slightly different behavior was observed for protein adsorption at $T$ = 20 °C. Here, the initial PC1 value for pH = 9 decreases by more than 6 times as compared to pH = 3 and equals approximately to the value recorded for the reference sample, depicting non-fouling character of oligoperoxide-*graft*-POEGMA246 nanolayer. Additionally, for pH lower than 5 no further increase in the amount of adsorbed proteins was observed.

Despite the minor differences in PC1 scores for temperatures below and above $T_c$, overall PCA analysis confirms the results obtained for fluorescence micrographs. The non-fouling properties of oligoperoxide-*graft*-POEGMA coatings are almost temperature independent but show strong dependence on pH.

## 4. Summary and conclusions

Novel approach to fabricate POEGMA246 coatings attached to glass, involving polymerization from oligoproxide grafted to the glass surface modified with APTES, was presented. The overall composition of the coatings was confirmed by static TOF-SIMS and ellipsometry after subsequent fabrication steps. Measurements of water contact angle revealed temperature-induced changes in hydrophobicity of the modified surfaces (as prepared) only for coatings fabricated for times longer than 23 h of polymerization (concentration of the grafted dry POEGMA246 layer is close to 20 mg/m$^2$). For POEGMA246 concentrations lower than 20 mg/m$^2$, blocking of the temperature-induced changes was observed. It was explained due to interactions between ether oxygens of the POEGMA246 brushes and carboxyl groups of oligoperoxide dominating over competitive interactions with water molecules.

Strongly pronounced thermal and pH dual-sensitivity, reported earlier for copolymer [28] POEGMA246 brushes, was observed only for POEGMA246 coatings fabricated for the polymerization time of 30 h. Thermal response of wettability, manifested about $T_C$ = 24–26 °C, was prominent at pH 9 and 7 and diminished at pH 5 and 3 when only the relatively hydrophobic surface was observed. The change in surface properties may be related to POEGMA246 transition from relatively hydrated loose coils to relatively hydrophobic collapsed chains.

Dual-responsive oligoperoxide-graft-POEGMA246 coatings were applied to examine the controlled protein adsorption using fluorescence microscopy. Lentil lectin from Lens culinaris, LcH (labeled with fluorescein isothiacyante), was used as a model protein. At pH = 9 very weak or even zero-protein adsorption to the investigated surfaces was observed for both studied temperatures. In contrast, for pH = 5, strong fluorescence was clearly visible for both discussed temperatures, suggesting significant reduction of antifouling properties of oligoperoxide-graft-POEGMA246 coating, leading to strong, temperature-independent protein adsorption. Thus, pH-sensitive surfaces with fouling/very low-fouling switched properties for controlled protein adsorption were obtained. Results of the control experiment, performed on a glass surface, showed no visible difference in fluorescence micrographs recorded for different pH and temperatures, depicting strong fluorescence in all cases. The pH and temperature depended protein adsorption was additionally confirmed by TOF-SIMS. Multivariate analysis of TOF-SIMS spectra, performed with Principal Component Analysis, provided the relative evaluation of protein adsorption, more precise than the one yielded by semi-quantitative comparative fluorescence microscopy. In particular, extremely low but non-zero protein adsorption to POEGMA246 brushes at pH = 9 and both temperatures was demonstrated. The low-fouling properties of oligoperoxide-*graft*-POEGMA246 coatings were found to depend weakly on temperature and strongly on pH.

## Acknowledgments

The research described in this work was partly carried out thanks to the financial support of the European Regional Development Fund in the framework of the Polish Innovation Economy Operational Program (contract No. POIG.02.01.00-12-023/08) and M. Smoluchowski KRAKOW SCIENTIFIC CONSORTIUM, in the framework of the KNOW grant (FOCUS).

## Appendix A. Supplementary material

Supplementary data associated with this article can be found, in the online version, at http://dx.doi.org/10.1016/j.jcis.2013.08.007.

## References

[1] M. Motornov, Y. Roiter, I. Tokarev, S. Minko, Prog. Polym. Sci. 35 (2010) 174.
[2] M.A. Cole, N.H. Voelcker, H. Thissen, H.J. Griesser, Biomaterials 30 (2009) 1827.
[3] A. Synytska, E. Svetushkina, N. Puretskiy, G. Stoychev, S. Berger, L. Ionov, C. Bellmann, K.-J. Eichhorn, M. Stamm, Soft Matter 6 (2010) 5907.
[4] I. Luzinov, S. Minko, V.V. Tsukruk, Soft Matter 4 (2008) 714.
[5] H.G. Börner, J.-F. Lutz, Adv. Polym. Sci. 240 (2011).
[6] I.Y. Galaev, B. Mattiasson, Trends Biotechnol. 17 (1999) 335.
[7] R.F. Fakhrullin, A.I. Zamaleeva, M.V. Morozov, D.I. Tazetdinova, F.K. Alimova, A.K. Hilmutdinov, R.I. Zhdanov, M. Kahraman, M. Culha, Langmuir 25 (2009) 4628.
[8] R.F. Fakhrullin, V.N. Paunov, Chem. Commun. 18 (2009) 2511.
[9] Hu. Zhibing, Cai. Tong, Chi. Chenglin, Soft Matter 6 (2010) 2115.
[10] J.-F. Lutz, J. Polym. Sci. A 46 (2008) 3459.
[11] S. Ouasti, R. Donno, M.J. Sherratt, G. Terenghi, N. Tirelli, Biomaterials 32 (2011) 6456.
[12] Y.D. Park, N. Tirelli, J.A. Hubbell, Biomaterials 24 (2003) 893.
[13] S. Han, M. Hagiwara, T. Ishizone, Macromolecules 36 (2003) 8312.
[14] T. Ishizone, A. Seki, M. Hagiwara, S. Han, H. Yokoyama, A. Oyane, A. Deffieux, S. Carlotti, Macromolecules 41 (2008) 2963.
[15] A. Hucknall, S. Rangarajan, A. Chilkoti, Adv. Mater. 21 (2009) 2441.
[16] S. Balamurugan, L.K. Ista, J. Yan, G.P. Lopez, J. Fick, M. Himmelhaus, M. Grunze, J. Am. Chem. Soc. 127 (2005) 14548.
[17] E. Wischerhoff, K. Uhlig, A. Lankenau, H.G. Börner, A. Laschewsky, C. Duschl, J.-F. Lutz, Angew. Chem. Int. Ed. 47 (2008) 5666.
[18] X. Laloyaux, E. Fautré, T. Blin, V. Purohit, J. Leprince, T. Jouenne, A.M. Jonas, K. Glinel, Adv. Mater. 22 (2010) 5024.
[19] J.-F. Lutz, Adv. Mater. 23 (2011) 2237.
[20] X. Gao, N. Kucerka, M.-P. Nieh, J. Katsaras, S. Zhu, J.L. Brash, H. Sheardown, Langmuir 25 (2009) 10271.
[21] J.P. Magnusson, A. Khan, G. Pasparakis, A.O. Saeed, W. Wang, J. Am. Chem. Soc. 130 (2008) 10852.
[22] C. Chi, T. Cai, Z. Hu, Langmuir 25 (2009) 3814.
[23] J.A. Jones, N. Novo, K. Flagler, C.D. Pagnucco, S. Carew, C. Cheong, X.Z. Kong, N.A.D. Burke, H.D.H. Stover, J. Pol. Sci. A 43 (2005) 6095.
[24] S. Holappa, M. Karesoja, J. Shan, H. Tenhu, Macromolecules 35 (2002) 4733.
[25] S. Holappa, L. Kantonen, F.M. Winnik, H. Tenhu, Macromolecules 37 (2004) 7008.
[26] N. Jin, H. Zhang, S. Jin, M.D. Dadmun, B. Zhao, J. Phys. Chem. B 116 (2012) 3125.
[27] R. Paris, J. Garcia, I. Quijada-Garrido, Polym. Int. 60 (2011) 178.
[28] X. Laloyaux, B. Mathy, B. Nysten, A.M. Jonas, Macromolecules 43 (2010) 7744.
[29] S. Medel, J.M. Garcia, L. Garrido, I. Quijada-Garrido, R. Paris, J. Pol. Sci. A 49 (2011) 690.
[30] Y. Stetsyshyn, J. Zemla, O. Zolobko, K. Fornal, A. Budkowski, A. Kostruba, V. Donchak, K. Harhay, K. Awsiuk, J. Rysz, A. Bernasik, S. Voronov, J. Colloid Interface Sci. 38 (2012) 95.
[31] J. Riddick, W. Bunger, T. Sakano, A. Weissenerger, Organic Solvents: Physical Properties and Methods of Purification, Wiley, New York, 1986.
[32] N.A. Milas, D.M. Surgenor, J. Am. Chem. Soc. 68 (1946) 205.
[33] O. Bayer, J. Houben, E. Muller, In: Methoden der Organischen Chemie (Houben-Weyl), vol. 8, G. Thieme, Stuttgart, 1952. p. 464.
[34] G. Bootsma, F. Meyer, Surf. Sci. 14 (1969) 52.
[35] S. Voronov, S. Varvarenko, Peroxide-Containing Macromolecules onto Interface, Lvivska Polytechnika, Lviv, 2013.
[36] V.V. Tsukruk, V.N. Bliznyuk, Langmuir 14 (1998) 446.
[37] A. Kostruba, M. Ohar, B. Kulyk, O. Zolobko, Y. Stetsyshyn, Appl. Surf. Sci. 276 (2013) 340.
[38] A. Dworak, A. Utrata-Wesolek, D. Szweda, A. Kowalczuk, B. Trzebicka, J. Anioł, ACS Appl. Mater. Interfaces 5 (2013) 2197.
[39] W. Feng, R. Chen, J.L. Brash, S. Zhu, Macromol. Rapid Commun. 26 (2005) 1383.
[40] V.V. Khutoryanskiy, A.V. Dubolazov, Z.S. Nurkeeva, G.A. Mun, Langmuir 20 (2004) 3785.
[41] Z.S. Nurkeeva, V.V. Khutoryanskiy, G.A. Mun, A.B. Bitekenova, S. Kadlubowski, Y.A. Shilina, P. Ulanski, J.M. Rosiak, Colloids Surf. A 236 (2004) 141.
[42] L.A. Kanis, F.C. Viel, J.S. Crespo, J.R. Bertolino, A.T.N. Pires, V. Soldi, Polymer 41 (2000) 3303.
[43] K. Tasaki, J. Am. Chem. Soc. 118 (1996) 8459.
[44] S. Chen, L. Li, C. Zhao, J. Zheng, Polymer 51 (2010) 5283.
[45] J. Zheng, L. Li, H.K. Tsao, Y.J. Sheng, S. Chen, S. Jiang, Biophys. J. 89 (2005) 158.
[46] S. Herrwerth, W. Eck, S. Reinhardt, M. Grunze, J. Am. Chem. Soc. 125 (2003) 9359.
[47] S. Chen, L. Li, C.L. Boozer, S. Jiang, Langmuir 16 (2000) 9287.
[48] S.I. Jeon, J.H. Lee, J.D. Andrade, P.G. De Gennes, J. Colloid Interface Sci. 142 (1991) 149.
[49] D. Schwendel, R. Dahint, S. Herrwerth, M. Schloerholz, W. Eck, M. Grunze, Langmuir 17 (2001) 5717.
[50] J.M. Harris, Poly(ethylene glycol) Chemistry: Biotechnical and Biomedical Applications, Plenum Press, New York, 1992.
[51] D. Leckband, S. Sheth, A. Halperin, J. Biomater. Sci. Polym. Ed. 10 (1999) 1125.
[52] B.P. Tripathi, N.C. Dubey, S. Choudhury, M. Stamm, J. Mater. Chem. 22 (2012) 19981.
[53] M. Rabe, D. Verdes, S. Seeger, Adv. Colloid Interface. Sci. 162 (2011) 87.
[54] R. Loris, F. Casset, J. Bouckaert, J. Pletinckx, M.H. Dao-Thi, F. Poortmans, A. Imberty, S. Perez, L. Wyns, Glycoconj. J. 11 (1994) 507.
[55] R. Loris, T. Hamelryck, J. Bouckaert, L. Wyns, Biochim. Biophys. Acta 1383 (1998) 9.
[56] M.J. Marcos, R. Chehin, J.L. Arrondo, G.G. Zhadan, E. Villar, V.L. Shnyrov, FEBS Lett. 443 (1999) 192.
[57] R. Chehin, I. Iloro, M.J. Marcos, E. Villar, V.L. Shnyrov, J.L. Arrondo, Biochemistry 38 (1999) 1525.
[58] J. Zemła, M. Lekka, J. Witowska-Zuber, A. Budkowski, J. Rysz, J. Raczkowska, Langmuir 24 (2008) 10253.
[59] J. Zemła, M. Lekka, J. Raczkowska, A. Bernasik, J. Rysz, A. Budkowski, Biomacromolecules 10 (2009) 2101.
[60] A. Foriers, E. Lebrun, R. Van Rapenbusch, R. De Neve, A.D. Strosberg, J. Biol. Chem. 256 (1981) 5550.

**Supplementary Data**

# Temperature and pH dual-responsive POEGMA-based coatings for protein adsorption

*Yurij Stetsyshyn[1*], Katarzyna Fornal[2], Joanna Raczkowska[2*], Joanna Zemla[2], Andrij Kostruba[3], Halyna Ohar[1], Mariya Ohar[1], Volodymyr Donchak[1], Khrystyna Harhay[1], Kamil Awsiuk[2], Jakub Rysz[2], Andrzej Bernasik[4], Andrzej Budkowski[2]*

## 1. Refractive index of polymerized POEGMA246 brush as a function of polymerization time.

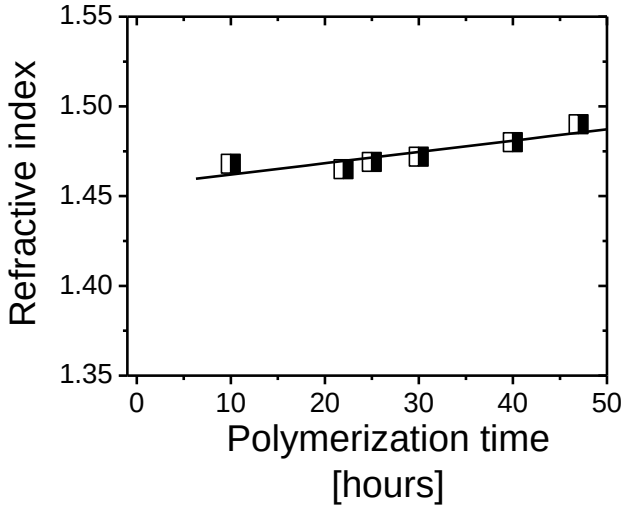


**Figure S1.** Refractive index of polymerized POEGMA246 brush in dry state**,** measured by ellipsometry (as prepared at room temperature) as a function of polymerization time. Solid lines are a guide to eye.

## 2. Refractive index of POEGMA246 brush as a function of temperature.

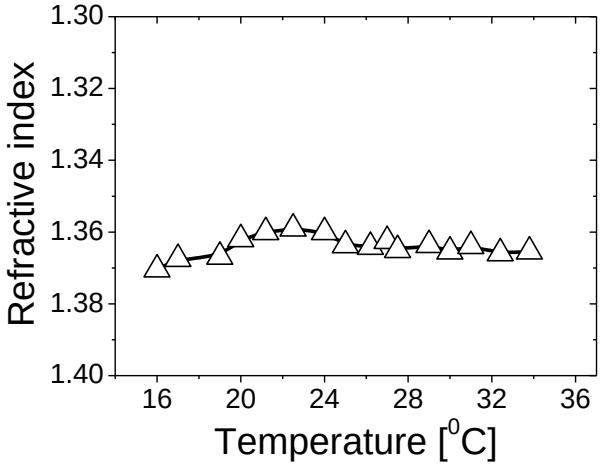


**Figure S2.** Temperature dependence of POEGMA246 thicknesses determined for the oligoperoxide-*graft*-POEGMA246 coatings with polymerization time 10 h.

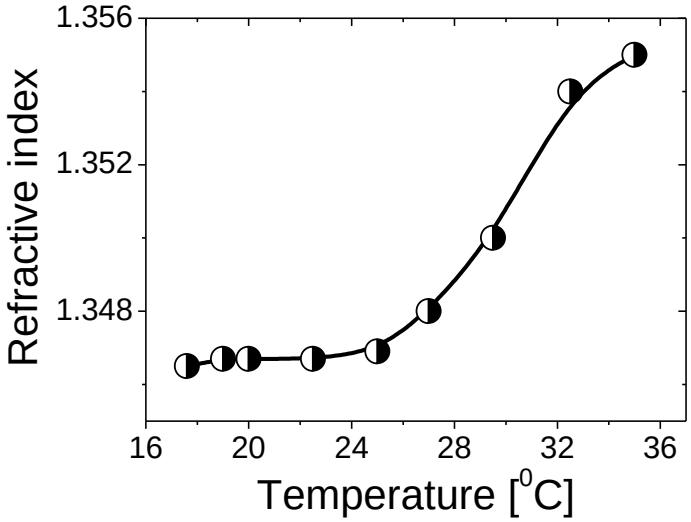


**Figure S3.** Temperature dependence of POEGMA246 thicknesses determined for the oligoperoxide-*graft*-POEGMA246 coatings with polymerization time 30 h.

## 3. Coatings morphology modified with temperature and pH (AFM).

Characteristic morphologies of oligoperoxide-*graft*-POEGMA246 coatings after 30h of polymerization, modified both, with pH and temperature, were recorded with AFM. Two series of AFM measurements were performed, for temperature T = 20˚C and 32˚C, i.e. below and above $T_c$, respectively. For each temperature the morphologies of oligoperoxide-*graft*-POEGMA246 coatings at four different pH, ranging from 3 to 9, were recorded and analyzed by means of self-correlation and average height of observed morphological structures.

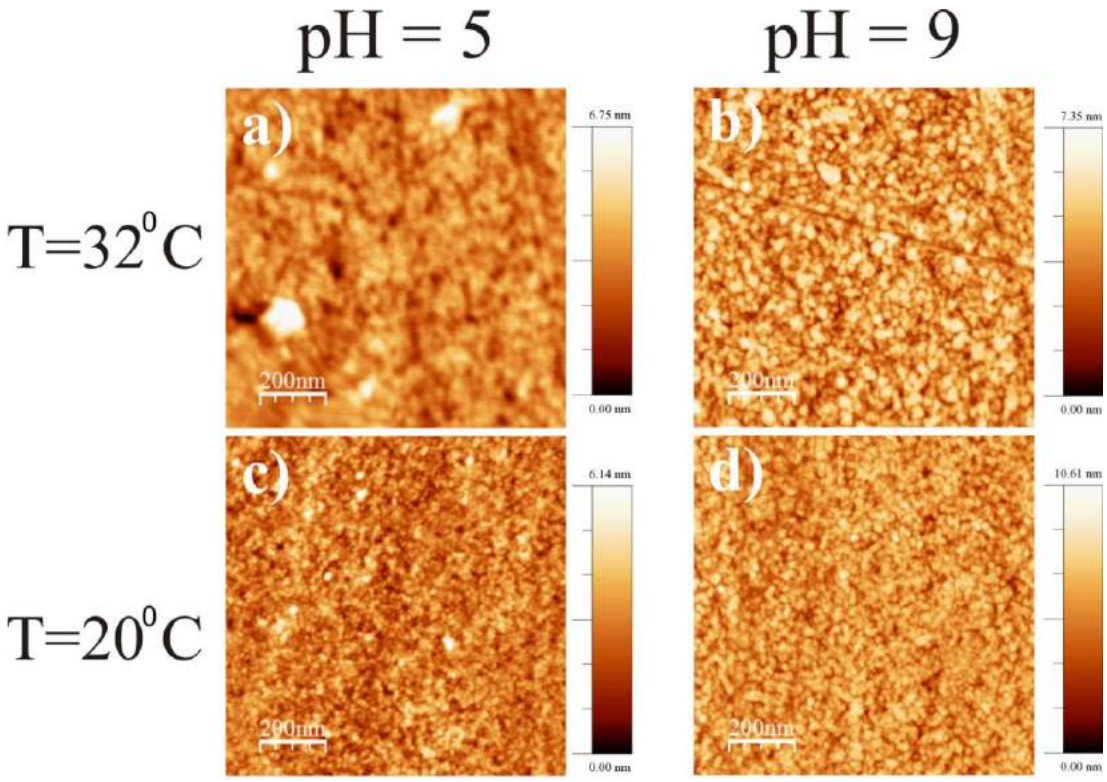


**Figure S4.** AFM surface images of oligoperoxide-*graft*-POEGMA246 coatings after 30 h of POEGMA246 polymerization, recored for values of pH 5 and 9 at temperatures of 20 and 32 ºC.

The exemplary AFM images, recorded for pH = 5 and 9, at both discussed temperatures, are presented in Figure S5. For T = 20˚C (Fig. S4a,b) increasing pH from 5 to 9 leads to the creation of better developed surface features. They become narrower and higher, which is reflected in reduction of self-correlation parameter (from 17 nm to 9 nm for pH = 5 and 9, respectively) accompanied by the

increasement of average height (from 3 nm to 5 nm for pH = 5 and 9, respectively).

The same kind of behaviors is observed for T = 32˚C (Fig. S4c,d). However, here the initial morphologies are significantly wider as compared to $T<T_c$. Self-correlation parameter decreases from 24 nm to 11 nm for pH = 5 and 9, respectively, whereas the average height changes from 2,8 nm to 4.1 for analogous pH values.

Comparison of AFM images recorded for different temperatures and pH values suggests stronger sensitivity of oligoperoxide-*graft*-POEGMA246 coatings to change of pH than to temperature.

# Paper II

## *Electron-beam lithographic grafting of functional polymer structures from fluoropolymer substrates*

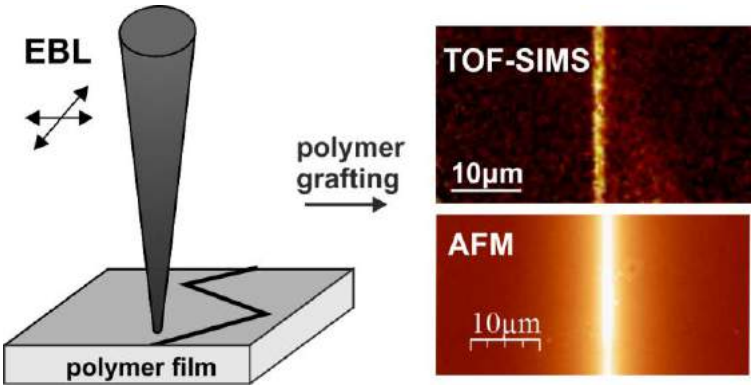


Highlights

- 2.5 and 100 keV electron beams form radical patterns on fluoropolymer films.
- Patterns initiate graft polymerization of poly(dimethylaminoethyl methacrylate).
- Grafted polymer-on-polymer structures are analyzed with AFM and TOF-SIMS.
- Surface and subsurface grafting dominates for low and high e-beam energy, respectively.
- Post-polymerization modification is enabled by quaternization and electrostatic binding.

LANGMUIR

Article

pubs.acs.org/Langmuir

# Electron-Beam Lithographic Grafting of Functional Polymer Structures from Fluoropolymer Substrates

Katarzyna Gajos,[†,‡] Vitaliy A. Guzenko,[‡] Matthias Dübner,[‡] Jakub Haberko,[§] Andrzej Budkowski,[†] and Celestino Padeste*[,‡]

[†]M. Smoluchowski Institute of Physics, Jagiellonian University, Łojasiewicza 11, 30-348 Kraków, Poland

[‡]Laboratory of Micro- and Nanotechnology, Paul Scherrer Institute, CH-5232 Villigen, Switzerland

[§]Faculty of Physics and Applied Computer Science, AGH University of Science and Technology, Mickiewicza 30, 30-059 Kraków, Poland

Supporting Information

**ABSTRACT:** Well-defined submicrometer structures of poly(dimethylaminoethyl methacrylate) (PDMAEMA) were grafted from 100 $\mu$m thick films of poly(ethene-*alt*-tetrafluoroethene) after electron-beam lithographic exposure. To explore the possibilities and limits of the method under different exposure conditions, two different acceleration voltages (2.5 and 100 keV) were employed. First, the influence of electron energy and dose on the extent of grafting and on the structure's morphology was determined via atomic force microscopy. The surface grafting with PDMAEMA was confirmed by advanced surface analytical techniques such as time-of-flight secondary ion mass spectrometry and X-ray photoelectron spectroscopy. Additionally, the possibility of effective postpolymerization modification of grafted structures was demonstrated by quaternization of the grafted PDMAEMA to the polycationic QPDMAEMA form and by exploiting electrostatic interactions to bind charged organic dyes and functional proteins.

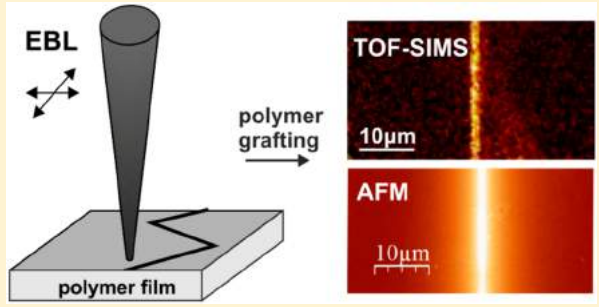


## INTRODUCTION

Radiation-induced grafting[1,2] has become an attractive and widely applied method for adapting properties of polymer substrates for specific applications by introduction of new functional groups to the surface. Polymer substrates are exposed to plasma, photons (extreme UV, X-rays, and $\gamma$-rays),[3−5] or particle beams (electrons and ions)[6,7] to create radical species that are stabilized as hydroperoxides or peroxides. These can act as initiators in a subsequent free radical polymerization of functional monomers, yielding the grafted polymer structures.[8,9] Advantages of the radiation-induced grafting approach for tailoring of polymer films include simple processing, no requirement for immobilizing initiators, and achievable high densities of grafted chains. Furthermore, the modification can be limited to the surface or extended into the bulk of the polymer support, depending on the irradiation conditions.[1,4,8,10]

Among polymer substrates, fluoropolymers make up a class of polymers with excellent bulk properties such as thermal stability, chemical resistance, low dielectric constants, and low water sorption.[11] The chemical inertness of fluoropolymers together with their susceptibility to radiation and effective formation of radicals during their radiolysis render radiation-induced grafting as a practical and effective method for their functionalization. Applications of grafted fluoropolymers include membranes for fuel cells[12−14] and microfiltration,[5,15−17] as well as applications in biomedicine.[10,18] Furthermore, grafting of functional polymers on chemically inert polymer substrates allows the desired properties of biointerfaces such as biocompatibility, controlled adsorption of proteins[7,19,20] and cells,[21] and antibacterial and antifouling properties to be achieved.[22,23]

The ability to control the physical and chemical surface properties in defined areas significantly increases the number of possible applications of grafted polymer substrates, for instance, for patterning of proteins and cells for bioassays, biosensing, and tissue engineering. In line with this demand, radiation-induced grafting can be easily combined with structuring technologies providing a versatile approach for fabrication of well-defined grafted polymer structures on polymer films.[8] Recently, several methods for patterned grafting of functional polymers were established by applying extreme UV,[3,24−27] X-rays,[10] and ions.[7,20,21] However, electron-induced patterned graft polymerizations have not been studied in detail,[3,8] mainly because of charging of nonconducting substrates. Thin capping layers of a conducting polymer were, for instance, used to overcome the charging problems in polymerizations conducted directly under a focused e-beam.[28]

Here, we report on the application of electron-beam lithography [e-beam lithography (EBL)] for direct generation of

**Received:** July 28, 2016
**Revised:** September 26, 2016
**Published:** September 27, 2016

ACS Publications © 2016 American Chemical Society



DOI: 10.1021/acs.langmuir.6b02808
*Langmuir* 2016, 32, 10641−10650

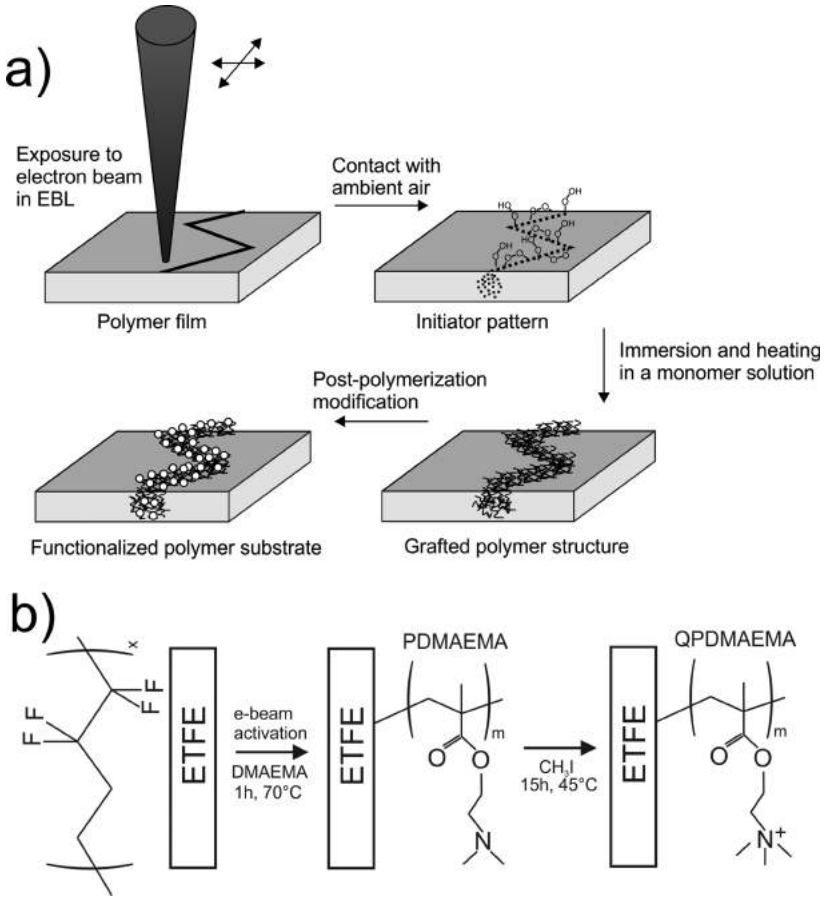


**Figure 1.** (a) Scheme of e-beam lithographic polymer grafting. The desired pattern is directly written on a polymer film by e-beam lithography to break bonds and create radical patterns. Radical species are stabilized as hydroperoxides or peroxides upon contact with ambient air and initiate the subsequent graft polymerization. Grafted polymer structures can be modified to obtain patterns with selected functionalities. (b) Scheme of ETFE modification: grafting of PDMAEMA and subsequent quaternization.

radical patterns at the surface of ETFE, which is a high-performance fluoropolymer with a generally low reactivity.[24] Upon contact with air, the radicals are converted into relatively stable peroxide and hydroperoxides species that serve as initiators for the subsequent grafting of polymer-on-polymer structures. The process is schematically depicted in Figure 1a. In contrast to other patterned grafting methods, this approach does not require any mask or an interferometric setup, and arbitrary patterns can be achieved in a simple way. Atomic force microscopy (AFM), time-of-flight secondary ion mass spectrometry (TOF-SIMS), and X-ray photoelectron spectroscopy (XPS) were applied for detailed morphological and chemical characterization of submicrometer line structures and micrometer square areas grafted after exposure of polymer substrates with electron beams with two different acceleration voltages. Grafting of poly(dimethylaminoethyl methacrylate) (PDMAEMA) was used to demonstrate the formation of biocompatible structures, their postpolymerization functionalization by a quaterization reaction, and the biofunctionalization by physisorption of proteins. The accessible submicrometer structure resolution and millimeter range of the modified area match perfectly with the requirements for bioapplications.

## EXPERIMENTAL SECTION

**Materials.** Extruded 100 $\mu$m thick films of ETFE (Nowoflon ET-6235, Nowofol GmBH, Siegsdorf, Germany) were placed between two 100 mm silicon wafers and hot pressed for 20 min at 220 °C with an applied pressure of 4 MPa to obtain flat surfaces. *N*,*N*-Dimethylaminoethyl methacrylate (DMAEMA, 98%, Aldrich), poly(ethylene glycol) (PEG, average $M_n$ of 380−420, Aldrich), iodomethane (99%, Aldrich), cyclohexanone (Aldrich), nitromethane (Aldrich), and 2-propanol (Aldrich) were used as received. Fluorescein sodium salt was purchased from Fluka, and bovine serum albumin (BSA) fluorescently labeled with Alexa Flour 555 and streptavidin (SAv) fluorescently labeled with Alexa Fluor 350 were purchased from Life Technologies.

**Activation of ETFE Films with Electrons.** Patterns of radicals were created in ETFE samples by irradiation with electrons using a direct writing EBL tool (Vistec EBPG 5000Plus) operated at an acceleration voltage of 100 kV. Activation was performed with a beam current of 10 nA and a dose range of 33−220 $\mu$C/cm$^2$. Three different test patterns were generated: single lines with various nominal widths (100 nm to 6 $\mu$m) for examination of the lateral resolution, sets of lines with interline distances of 1 and 10 $\mu$m for testing the overlap of line features, and squares with dimensions of 300 $\mu$m × 300 $\mu$m for spectroscopic measurements. Additionally, to investigate the impact of the electron energy on grafted structures, test experiments applying electron sources operated at an acceleration voltage of 2.5 keV were performed. For lateral-resolution examination, lines with a nominal width equal to 100 nm and different distances between lines were generated with a dose range of 0.2−3.2 nC/cm$^2$ using a LION LV1 EBL system (Leica Microsystems, Jena, Germany). Activation of larger ETFE surface areas, required for spectroscopic measurements, was performed using a scanning electron microscope (SEM, Zeiss Supra VP55). The 500 $\mu$m × 500 $\mu$m areas were irradiated for the time required to obtain a dose equal to 30 $\mu$C/cm$^2$. After activation, all ETFE samples were stored at −80 °C until they were grafted.


DOI: 10.1021/acs.langmuir.6b02808
*Langmuir* 2016, 32, 10641−10650

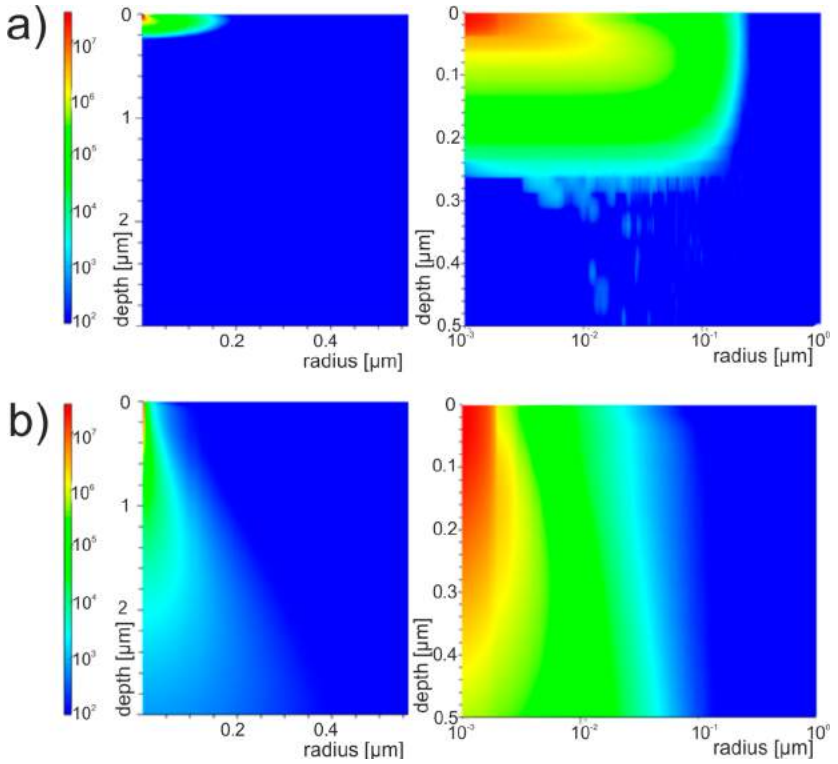


**Figure 2.** Monte Carlo simulation of the energy deposition (arbitrary units, logarithmic scale) of (a) 2.5 and (b) 100 keV electrons in the top 3 $\mu$m of an ETFE film. The close-ups at the right show the radial distribution on a logarithmic scale in the top 500 nm of the film.

**Grafting and Postpolymerization Modification of PDMAEMA.** *Grafting of PDMAEMA.* Activated ETFE samples were rinsed with acetone, dried in a stream of nitrogen, and placed into degassed solutions of *N*,*N*-dimethylaminoethyl methacrylate (20 vol %) and poly(ethylene glycol) (20 vol %) in cyclohexanone. Polymerization was performed at 70 °C for 1 h. The grafted sample was washed in sequence in cyclohexanone, 2-propanol, and water.

*Quaternization of PDMAEMA.* The grafted samples were immersed in degassed solutions of iodomethane (10 vol %) in nitromethane. The reaction was performed at 45 °C for 15 h. Then, the samples were washed in sequence in nitromethane, 2-propanol, and water.

**Characterization of Grafted Structures.** *Atomic Force Microscopy.* Topographic micrographs of grafted PDMAEMA structures were recorded using a Dimension IIIa Instrument (Veeco) working in tapping mode and AFM probes with a spring constant of 40 N/m, a tip radius of ~20 nm, and a resonant frequency of 325 kHz (NSC15/AlBS, Mikromash). Images were processed with second-order flattening procedures (Nanoscope software, Veeco).

*Time-of-Flight Secondary Ion Mass Spectrometry.* Surface chemical imaging and molecular composition analysis were performed using a TOF-SIMS 5 (ION-TOF GmbH) instrument equipped with a 30 keV bismuth liquid metal ion gun. $Bi_3^+$ clusters were used as primary ions with an ion dose density of $<10^{12}$ ions/cm$^2$ to ensure static-mode conditions. A low-energy electron flood gun was used for charge compensation. To examine the molecular surface composition of ETFE samples after PDMAEMA grafting and quaternization, the positive ion TOF-SIMS high-resolution mass spectra were recorded from several nonoverlapping 100 $\mu$m × 100 $\mu$m areas (resolution of 128 × 128 points). These areas were located inside 300 $\mu$m × 300 $\mu$m and 500 $\mu$m × 500 $\mu$m squares exposed with EBL and SEM, respectively. To examine the lateral resolution of the chemical modification, TOF-SIMS images of micrometer line structures were recorded in image mode (50 $\mu$m × 50 $\mu$m areas with a resolution of 128 × 128 points, corresponding to a pixel size of ~400 nm).

**X-ray Photoelectron Spectroscopy.** Modified ETFE surface chemical state analysis was performed with X-ray photoelectron spectroscopy using a PHI 5000 Versa Probe II (ULVAC-PHI) spectrometer equipped with an Al K$\alpha$ radiation source (1486.6 eV). Measurements were performed at a photoelectron takeoff angle $\Theta$ equal to 45° (with respect to the surface normal). High-resolution spectra were recorded with an analyzer pass energy of 23.5 eV from 100 $\mu$m × 100 $\mu$m areas located inside larger uniformly grafted squares. A dual-beam charge neutralizer was used to compensate for sample charging. The operating pressure in the analytical chamber during measurements was $<5 \times 10^{-7}$ Pa. All XPS peaks were referenced to the neutral (C−C) carbon C 1s peak at 284.6 eV. Spectrum backgrounds were subtracted using the Shirley method.

*Binding of Fluorescein to QPDMAEMA Structures.* The fluorescein anion was used to examine electrostatic binding to polycationic QPDMAEMA grafted from ETFE. Quaternized samples were immersed successively in water and phosphate buffer (50 mM, pH 7.4). Next, samples were incubated in a 0.1 mg/mL solution of fluorescein sodium salt in phosphate buffer for 30 min. After being incubated, samples were washed thoroughly with phosphate buffer and deionized water and dried carefully in a stream of nitrogen.

*Adsorption of Protein into PDMAEMA and QPDMAEMA Structures.* Fluorescently labeled bovine serum albumin (BSA) and streptavidin (SAv) were used as model proteins to examine the adsorption of protein into grafted PDMAEMA and QPDMAEMA structures. The substrates were washed successively in ethanol, water, and phosphate buffer (50 mM) and incubated in a 200 $\mu$g/mL protein solution in phosphate buffer for 1 h. The samples were then rinsed carefully with phosphate buffer and deionized water and dried carefully in a stream of nitrogen.

*Fluorescence Microscopy.* Immobilization of fluorescein and of labeled proteins to the substrates was examined using an Olympus BX51 optical microscope equipped with a 100 W halogen lamp and type DP72 camera. All images were recorded and processed using the software package CellF.

*Simulations.* The impact of electrons in the ETFE substrates, in particular the density of the deposited energy as a function of distance from the penetration point of the electron beam into the foil at different substrate depths, was simulated using the simulation code Penelope2011.[29,30]



DOI: 10.1021/acs.langmuir.6b02808
*Langmuir* 2016, 32, 10641−10650

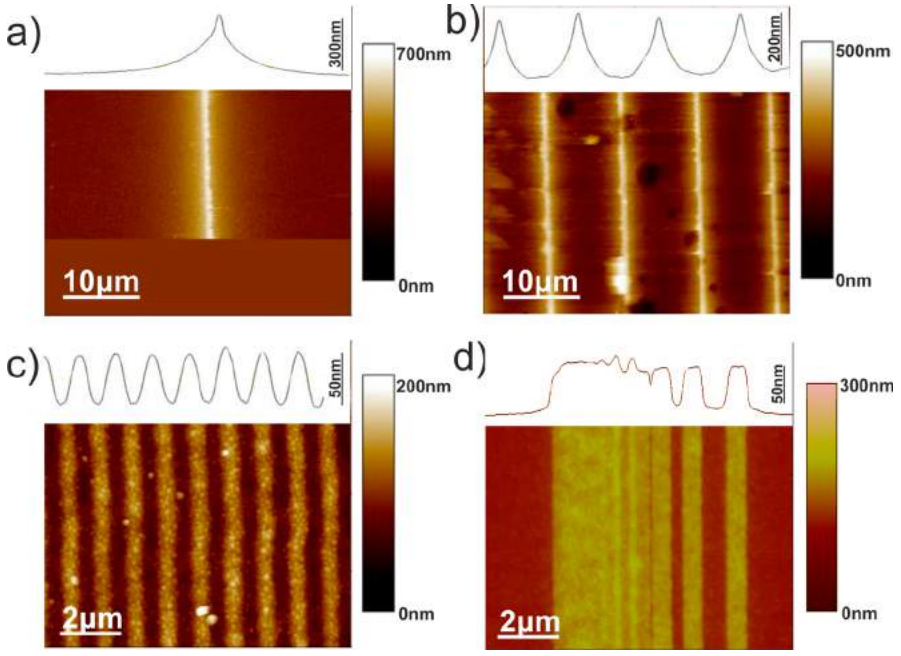


**Figure 3.** AFM images and corresponding line profiles of PDMAEMA line structures grafted on ETFE after defining radical patterns with an e-beam writer with different energies and distances between lines. (a and b) Lines written with 100 keV are well resolved but show pronounced tailing on both sides. (c) At narrow distances tailing overlap to a continuous background on which the structures are still well resolved. (d) Lines grafted after writing with 2.5 keV at various distances show an almost rectangular line profiles and no significant background.

## RESULTS AND DISCUSSION

**Simulation of Electron Energy Deposition in ETFE Substrates.** Radiation-induced cracking of chemical bonds in the substrate to create radicals is the first step of the grafting process. As long as the energy of the impinging electrons is sufficiently high to crack chemical bonds, it may be assumed that radical formation is closely related to the deposition of energy in the substrate. Note that the used e-beam energies are several orders of magnitude higher than typical binding energies of C−C, C−H, and C−F bonds. Model calculations based on Monte Carlo techniques, which are well established in EBL,[29,30] were used to estimate the penetration depth and spreading of electrons in the ETFE foils. The simulation accounts for the chemical composition and density of the polymer as well as the energy of impinging electrons. For the calculation, the bulk material is assumed to be amorphous and divided in cells according to the selected lateral and vertical grids; the energy loss density (point spread function) is represented as an average over all unit cells at a given distance from the impact point. Charging of the substrate, which will lead to broadening of exposed features, cannot be not taken into account for these calculations. Here, the deposition of energy was calculated for 2.5 and 100 keV electrons. Data shown in Figure 2 demonstrate very different profiles for low and high acceleration voltages. With an arbitrary limit set at 90% of the deposited energy above which it contributes significantly to the radical formation process, the conclusion is that at 2.5 keV electrons mainly affect the top 50 nm of the substrate while the horizontal spreading reaches ∼10 nm. With 100 keV electrons, the penetration depth increases by a factor of 5 while the extent of horizontal spreading is significantly reduced compared to that seen with the 2.5 keV beam. Accordingly, different grafting depths can be expected at the two different acceleration voltages: while surface grafting is the dominating process for activation with 2.5 keV electrons, a considerable contribution of bulk grafting must be expected for the 100 keV electrons.

**Grafting of Submicrometer Structures of PDMAEMA from ETFE Foils.** Representative AFM images of PDMAEMA line structures grafted from ETFE after defining radical patterns with EBL are presented in Figure 3. Well-defined line structures were grafted from the surfaces exposed to both high (Figure 3a−c) and low (Figure 3d) acceleration voltages. At high acceleration voltage, the height of grafted single lines written with 66 $\mu$C/cm$^2$ and a 100 nm nominal line width was ∼300 nm. The line profile is characterized by a peak of ∼100 nm in height and a very broad tailing. TOF-SIMS investigations (see TOF-SIMS Imaging of Grafted PDMAEMA Structures) indicate that surface grafting was significant only in the central area of the line profile. This indicates a significant contribution of grafting in the bulk of the polymer film, leading to material expansion and as a consequence bulging of the surface. When lines were written in the vicinity, the tailings were overlapping, leading to lower apparent structure heights. The effect of overlapping of the tailing was especially evident from patterns of lines written at a 1 $\mu$m distance (Figure 3c), where the single lines appear to be well resolved on top of a cushion ∼600 nm in height (Figure S3). In contrast, structures grafted from surfaces exposed to low-energy electrons showed basically no tailing and showed a rectangular line profile. This finding is interpreted as predominance of surface grafting.

For both energies, the height of grafted structures weakly depends on the applied electron dose, over the studied range (Figure S1). This indicates that the saturation of the surface with radicals occurs at very small doses. However, for high-energy electrons, the extent of tailing accompanying the single line and the height of the cushion formed at close line distances increase with the applied electron dose (Figures S2 and S3), revealing a still apparent impact of the dose on the degree of bulk grafting.



DOI: 10.1021/acs.langmuir.6b02808
*Langmuir* 2016, 32, 10641−10650

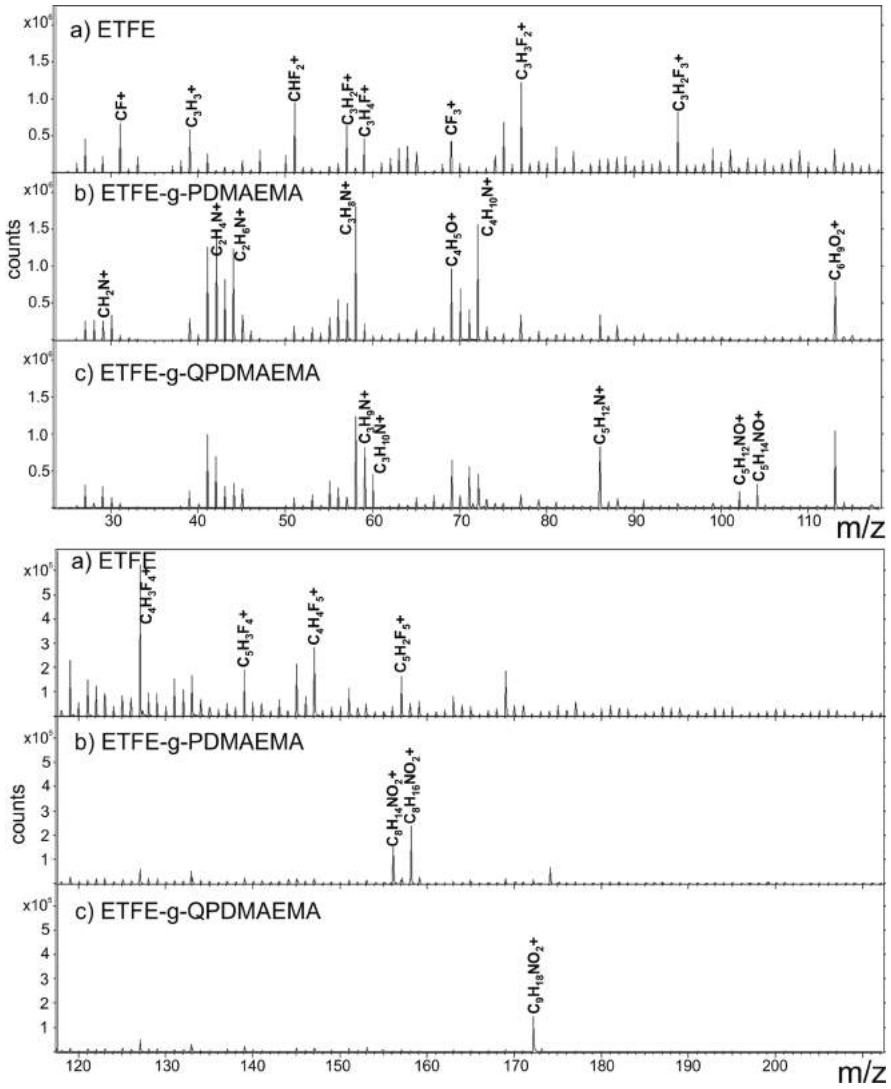


**Figure 4.** Representative positive TOF-SIMS spectra ($m/z$ 25−120 and 120−220 in two panels) of ETFE (a) before and (b) after PDMAEMA grafting and (c) after transformation to polycationic QPDMAEMA. The signals characteristic of each modification steps are marked with the secondary ion names.

The intrinsic resolution limit of grafted structures appeared to be ∼300 nm irrespective of the applied energy of electrons. This value is far above the focus that can be achieved with EBL and the nominal line width defined for both tools for the exposure. The experimental resolution limit appears to be caused by a widening of the beam focus by the accumulated charge at the surface and the secondary electrons produced by the interaction of the beam with the polymer substrate.

**Chemical Modification of ETFE Foils with PDMAEMA Examined with TOF-SIMS and XPS.** To verify the chemical surface modification of the ETFE films by grafting of PDMAEMA polymer chains, spectroscopic techniques such as time-of-flight secondary ion mass spectrometry (TOF-SIMS) and X-ray photoelectron spectroscopy (XPS) were applied. Both techniques are highly sensitive to the surface with mean attenuation depths of approximately 1−1.5 nm for TOF-SIMS working in static mode and 3 nm for XPS. Representative positive ion TOF-SIMS spectra recorded from ETFE films before and after the grafting procedure (following activation with 100 keV electrons with a dose of 33 $\mu C/cm^2$) are presented in panels a and b of Figure 4. The spectra of unmodified ETFE are dominated by peaks unique for this fluoropolymer such as $CF^+$ ($m/z$ 31), $CHF_2^+$ ($m/z$ 51), $C_3H_2F^+$ ($m/z$ 57), $C_3H_4F^+$ ($m/z$ 59), $CF_3^+$ ($m/z$ 69), $C_3H_3F_2^+$ ($m/z$ 77), $C_3H_2F_3^+$ ($m/z$ 95), $C_4H_3F_4^+$ ($m/z$ 127), $C_5H_3F_4^+$ ($m/z$ 139), $C_4H_4F_5^+$ ($m/z$ 147), and $C_5H_2F_5^+$ ($m/z$ 157).[31] In turn, the spectra recorded after PDMAEMA grafting exhibit a drastic decrease in the intensity of secondary ions originating from ETFE, and at the same time, pronounced peaks characteristic of PDMAEMA occur. Secondary ions such as $C_2H_4N^+$ ($m/z$ 42), $C_2H_6N^+$ ($m/z$ 44), $C_3H_8N^+$ ($m/z$ 58), $C_4H_5O^+$ ($m/z$ 69), $C_4H_{10}N^+$ ($m/z$ 72), $C_6H_9O_2^+$ ($m/z$ 113), $C_8H_{14}NO_2^+$ ($m/z$ 156), and $C_8H_{16}NO_2^+$ ($m/z$ 158) were identified as fragments of the grafted PDMAEMA chains.[32] These results confirm the effective modification of the surface of the ETFE film with PDMAEMA by e-beam-induced grafting.

To investigate the influence of activation conditions such as dose and electron energy on the degree of subsequent grafting, the normalized intensities of secondary ions characteristic of ETFE and PDMAEMA obtained for samples exposed to 100 keV (dose range of 30−100 $\mu C/cm^2$) and 2.5 keV (dose of 30 $\mu C/cm^2$) electrons were compared (Figure S4). However, the attenuation of signals characteristic of the ETFE substrate



DOI: 10.1021/acs.langmuir.6b02808
Langmuir 2016, 32, 10641−10650

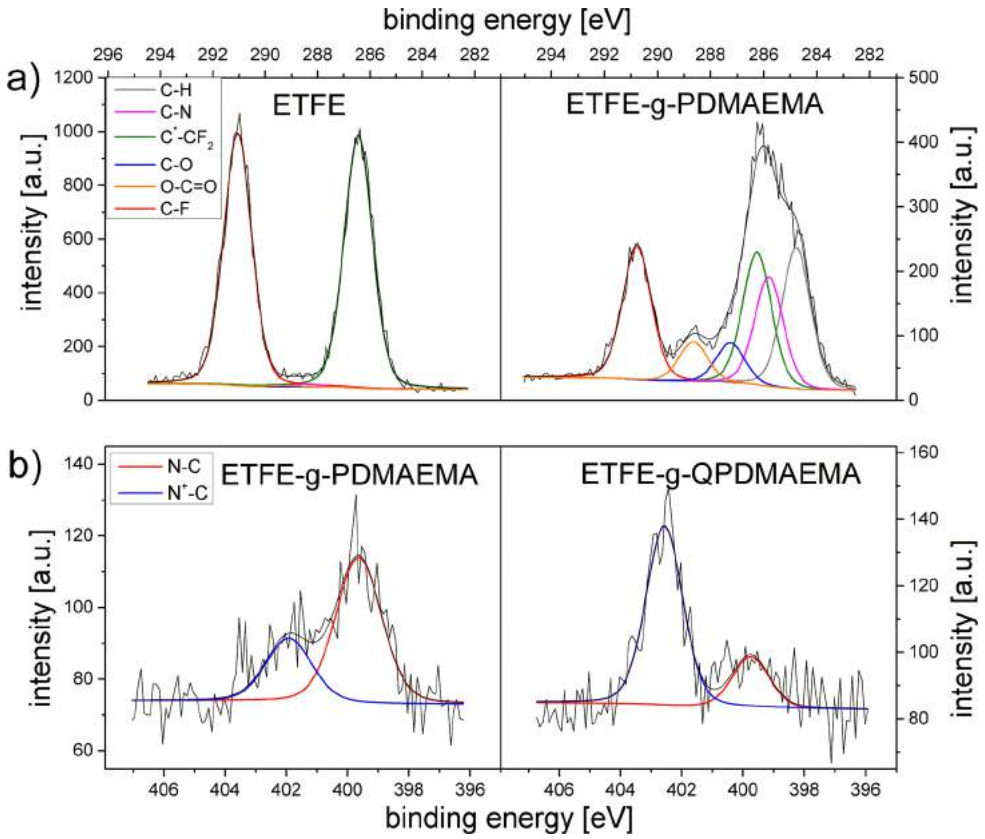


**Figure 5.** XPS examination of chemical surface modification of ETFE films. (a) High-resolution XPS C 1s spectra of untreated and PDMAEMA-grafted ETFE with individual peak assignments. (b) High-resolution N 1s spectra of the grafted ETFE before and after the quaternization reaction, indicating ~80% reaction yield.

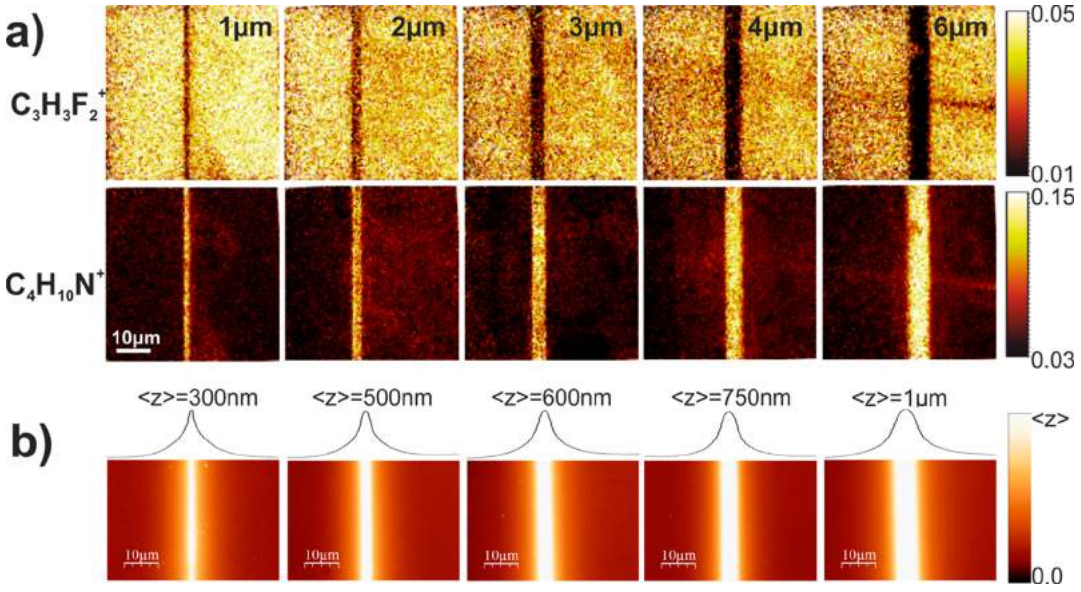


**Figure 6.** Analysis of PDMAEMA line structures grafted from ETFE films after radical line patterns had been defined with different line widths using EBL. (a) TOF-SIMS images recorded with ions characteristic of ETFE ($C_3H_3F_2^+$) and PDMAEMA ($C_4H_{10}N^+$). (b) AFM topographic images and corresponding line profiles. The nominal width of the lithographic exposure for each sample is indicated in panel a.

by a factor of 4−5 and the increase in the intensity of PDMAEMA ion fragments were comparable for all grafted samples. This suggests the similar surface grafting density of PDMAEMA chains and the low impact of the electron energy and dose, over the studied range, on the surface degree of grafting. However, the electron energy and dose dependence of the degree of bulk grafting are significant, as indicated by AFM analysis (see Grafting of Submicrometer Structures of PDMAEMA from ETFE Foils).

XPS measurements were performed for ETFE films before and after PDMAEMA grafting. The recorded high-resolution C 1s, O 1s, N 1s, and F 1s spectra are presented in Figure 5 and



DOI: 10.1021/acs.langmuir.6b02808
Langmuir 2016, 32, 10641−10650

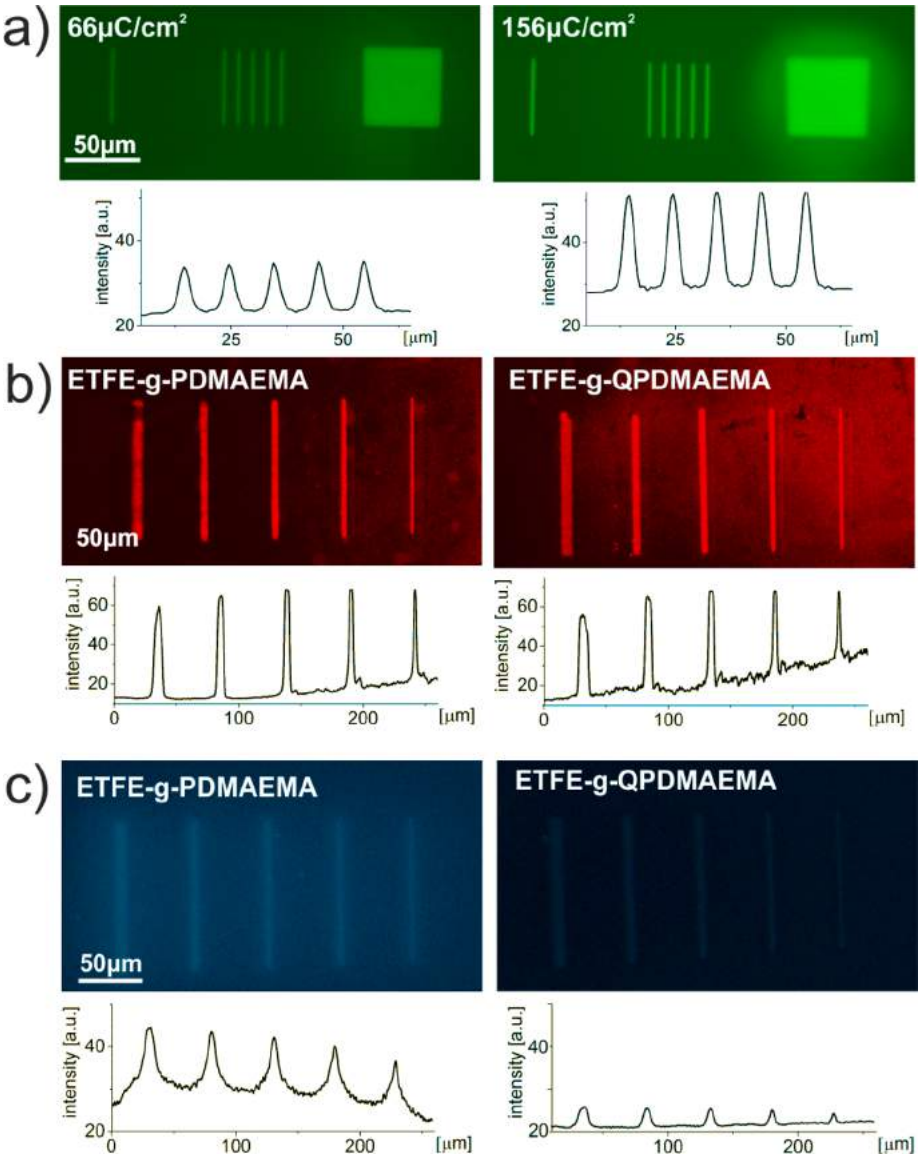


**Figure 7.** Fluorescence microscopic investigation. (a) Binding of fluorescein sodium salt to quaternized structures grafted after exposure with different e-beam doses. Binding of (b) BSA and (c) streptavidin to PDMAEMA structures before and after quaternization. Profiles below the images show the fluorescence intensities averaged over the length of the lines.

Figures S5 and S6. For untreated ETFE, the C 1s spectra show two peak components at 286.4 eV (due to C*−$CF_2$) and 291.0 eV (due to C−F)[33] of equal intensity. For the PDMAEMA-grafted samples, the C 1s envelope can be resolved into six contributions corresponding to different chemical groups specific for ETFE and PDMAEMA (C−H at 284.6 eV, C−N at 285.6 eV, C−O at 287.1 eV, and O−C═O at 288.8 eV).[34,35]

The degree of surface grafting of samples activated with the two different electron energies was compared on the basis of the relative intensity of the N 1s signal, which can uniquely be assigned to PDMAEMA in the system presented here. The obtained surface concentration of nitrogen equals 5.5 ± 0.5% and 5.2 ± 0.5% for an activation of the ETFE film with 100 and 2.5 keV electrons, respectively. This indicates a very similar surface composition irrespective of the activation conditions, confirming the findings from the TOF-SIMS measurements.

**TOF-SIMS Imaging of Grafted PDMAEMA Structures.** Imaging TOF-SIMS combines molecular chemical sensitivity with an excellent submicrometer spatial resolution. This provides a unique possibility of direct chemical imaging of complex microstructured surfaces, including mixed polymer systems such as polymer structures grafted onto a polymer film.

The TOF-SIMS images of secondary ions characteristic of ETFE ($C_3H_3F_2^+$, $m/z$ 77) and PDMAEMA ($C_4H_{10}N^+$, $m/z$ 72) polymers recorded for films with line structures grafted after activation with 100 keV electrons with a dose of 33 $\mu C/cm^2$ are presented in Figure 6. Because the application of imaging modes reduces mass resolution, thus hindering identification of individual peaks, the most specific signals for the support and graft polymers were selected from high-resolution mass spectra and used for imaging. Images of ions characteristic of ETFE show attenuation in the grafted line regions indicating coverage with the grafted chains. The lines coincide with the maximal intensity of the ions characteristic of PDMAEMA, confirming the spatially selective ETFE modification with PDMAEMA. In contrast to the AFM measurements, the TOF-SIMS images show very clear line definition without pronounced tailing.



DOI: 10.1021/acs.langmuir.6b02808
*Langmuir* 2016, 32, 10641−10650

**Formation of Polycationic QPDMAEMA Structures.** The possibility of postpolymerization modification (PPM) of grafted polymer structures is very powerful because it allows the introduction of specific functional groups and increases the number of possible applications of such mixed polymer substrates.[27,36] In the work presented here, the quaterinization of amine groups of PDMAEMA grafted into positively charged quaternary ammonium groups using iodomethane is demonstrated. To confirm the effective transformation to the polycationic QPDMAEMA form, spectroscopic techniques such as TOF-SIMS and XPS were applied.

Representative positive TOF-SIMS spectra recorded from ETFE modified with PDMAEMA after subsequent quaternization are presented in Figure 4c. The spectra show pronounced peaks that are characteristic of the polycationic QPDMAEMA form. Furthermore, the intensities of the signals characteristic of PDMAEMA are significantly reduced. Ion fragments $C_3H_9N^+$ ($m/z$ 59), $C_3H_{10}N^+$ ($m/z$ 60), $C_5H_{12}N^+$ ($m/z$ 86), $C_5H_{12}NO^+$ ($m/z$ 102), $C_5H_{14}NO^+$ ($m/z$ 104), and $C_9H_{18}NO_2^+$ ($m/z$ 172) were identified as being derived from QPDMAEMA chains. Additionally, high-resolution C 1s, N 1s, O 1s, F 1s, and I 3d5/2 XPS spectra (Figure 5b and Figure S7) of ETFE modified with QPDMAEMA were recorded. For elements such as carbon, oxygen, and fluoride, the quaternization reaction hardly affects the shape of the spectra or their atomic concentration. However, the carbon content increases by ∼2% as a result of the presence of additional methyl groups. In contrast, a drastic change in the N 1s spectra is observed after quaternization (Figure 5b). The N 1s signal can be resolved into two peak components corresponding to neutral C−N species at 399.7 eV and quaternary ammonium group $C-N^+$ species at 402.5 eV.[34,35,37,38] For substrates modified with PDMAEMA, the N 1s spectrum is dominated by the C−N peak component, associated with a side peak indicating a protonated ammonium group. As a result of the quaternization, the peak assigned to $C-N^+$ dominates the N 1s signal. The yield of quaternization at the surface was estimated from the ratio of the $C-N^+$ species to the total nitrogen species to reach ∼80%, confirming an effective formation of polycationic QPDMAEMA.[33,37,38] Moreover, the emergence of a peak at 618.3 eV is observed, corresponding to iodine anions ($I^-$), which are introduced as counterions with a surface concentration of ∼2%. The results of surface analysis with TOF-SIMS and XPS confirm a successful PPM of grafted PDMAEMA structures to the polycationic QPDMAEMA.

**Immobilization of Molecules to Grafted PDMAEMA and QPDMAEMA Structures.** To demonstrate the ability of selective immobilization of molecules into PDMAEMA and QPDMAEMA structures grafted after ETFE activation with the 100 keV e-beam, the adsorption of fluorescein sodium salt and of model proteins (BSA and SAv) was examined. Very well-defined patterns of negatively charged fluorescein were obtained on an ETFE film by electrostatic interaction with positively charged polycationic QPDMAEMA structures (Figure 7a). A higher fluorescence intensity corresponding to a higher density of bound molecules was observed when the larger dose was applied for creation of radicals. This suggests a penetration of small fluorescein molecules into the functionalized film due to the larger impact of the dose on the grafting in the subsurface region rather than at the surface of grafted films as discussed above (see Grafting of Submicrometer Structures of PDMAEMA from ETFE Foils and Chemical Modification of ETFE Foils with PDMAEMA Examined with TOF-SIMS and XPS). For the study of adsorption of protein to both PDMAEMA and polycationic QPDMAEMA structures, two model proteins were employed, namely, BSA with an isoelectric point of ∼4.7 and streptavidin with an isoelectric point close to 7 (Figure 7b,c). At pH 7.4, both proteins are selectively adsorbed to unmodified PDMAEMA structures. The width of formed protein line patterns corresponds to the different width of grafted line structures defined by the e-beam exposure. The quaternization of PDMAEMA results in positively charged QPDMAEMA, which is well-known to considerably swell in aqueous environments[39] and to reduce nonspecific protein adsorption due to high hydrophilicity.[37] Indeed, the repulsion of SAv, which is neutral at the applied pH, by quaternized QPDMAEMA is observed when compared to the situation in PDMAEMA structures. However, BSA protein is selectively adsorbed also into polycationic QPDMAEMA structures. These results indicate that the electrostatic interactions between negatively charged BSA and the quaternary ammonium group of QPDMAEMA dominate over the protein repulsion effect of the swollen hydrophilic polymer.[37,40]

## CONCLUSIONS

A successful application of e-beam lithography to high-resolution polymer grafting was demonstrated. In particular, the creation of initiator patterns with an e-beam writer and a subsequent free radical polymerization were applied to modify fluoropolymers with grafted PDMAEMA structures. Following this approach, the well-defined grafted polymer-on-polymer line structures were obtained with submicrometer resolution, as revealed via morphological analysis by AFM. The lateral resolution of the processes is in the range of 300 nm, given by charging effects that broaden the highly focused electron beams. The effective chemical surface modification with PDMAEMA was clearly evident from spectroscopic analysis via TOF-SIMS and XPS.

A comparison of the morphology of the polymer structures grafted after ETFE substrate exposure with different e-beam energies (2.5 and 100 keV) revealed a strong dependence on the electron acceleration voltage. A low acceleration voltage resulted in activation near the surface and preferential surface grafting, while higher energies led to considerable grafting in the subsurface region of the fluoropolymer film resulting in surface bulging. The effect of simultaneous formation of a surface topography and defined chemical modification might provide advantages for bioapplications, including the design of implant surfaces or use for cell growth studies.

Furthermore, the possibility of effective postpolymerization modification of grafted polymer structures was demonstrated. As a result of quaternization of grafted PDMAEMA, ETFE films functionalized with polycationic QPDMAEMA were obtained. The examination of modified substrates with surface-sensitive techniques such as TOF-SIMS and XPS confirmed the effective formation of positively charged quaternary ammonium species with the extent of surface quaternization estimated to be 80%. It was shown that the quaternization of PDMAEMA structures allows the spatially resolved immobilization of charged molecules and proteins by electrostatic interactions and reduces nonspecific adsorption. This suggests the application of such functionalized films as biofunctional surfaces based on charge-selective molecule immobilization.

The successful application of EBL to polymer grafting has several advantages such as the easy and fast pattern definition and fabrication process, the high resolution of grafted structures, and the possibility of various postpolymerization modifications.



DOI: 10.1021/acs.langmuir.6b02808
Langmuir 2016, 32, 10641−10650

Together with the demonstrated capability of such surfaces to selectively bind specific molecules, this makes the e-beam lithographic grafting an attractive technique for the generation of functional patterned substrates, in particular for biorelated applications.

## ■ ASSOCIATED CONTENT

### Supporting Information

The Supporting Information is available free of charge on the ACS Publications website at DOI: 10.1021/acs.langmuir.6b02808.

Additional AFM data revealing the impact of dose on grafted polymer structures, TOF-SIMS analysis of the influence of activation conditions on chemical surface modification with PDMAEMA, and additional XPS spectra recorded from the ETFE film before and after PDMAEMA grafting and quaternization reaction (PDF)

## ■ AUTHOR INFORMATION


### Corresponding Author

*E-mail: celestino.padeste@psi.ch.


### Notes

The authors declare no competing financial interest.

## ■ ACKNOWLEDGMENTS

This work is supported by the Polish Ministry of Science and Higher Education under Grant 7150/E/338/M/2015 and the M. Smoluchowski Krakow Scientific Consortium in the framework of the KNOW (grant FOCUS and KNOW scholarship). The acquisition TOF-SIMS equipment was supported by the European Regional Development Fund (POIG.02.01.00-12-023/08).

## ■ REFERENCES


(1) Dargaville, T. R.; George, G. A.; Hill, D. J.T.; Whittaker, A. K. High energy radiation grafting of fluoropolymers. *Prog. Polym. Sci.* **2003**, *28*, 1355−1376.

(2) Kabanov, V. Y.; Aliev, R. E.; Kudryavtsev, V. N. Present status and development trends of radiation induced graft polymerization. *Radiat. Phys. Chem.* **1991**, *37*, 175−192.

(3) Brack, H.-P.; Padeste, C.; Slaski, M.; Alkan, S.; Solak, H. H. Preparation of Micro- and Nanopatterns of Polymer Chains Grafted onto Flexible Polymer Substrates. *J. Am. Chem. Soc.* **2004**, *126*, 1004−1005.

(4) Farquet, P.; Padeste, C.; Borner, M.; Youcef, H. B.; Gursel, S. A.; Scherer, G. G.; Solak, H. H.; Saile, V.; Wokaun, A. Microstructured proton-conducting membranes by synchrotron-radiation-induced grafting. *J. Membr. Sci.* **2008**, *325*, 658−664.

(5) Deng, Q.; Chen, Y.; Sun, W. Preparation of polymer brushes from poly(vinylidene fluoride) surfaces by UV irradiation pretreatment. *Surf. Rev. Lett.* **2007**, *14*, 23−30.

(6) Massa, G.; Mazzei, R.; García Bermudez, G.; Filevich, A.; Smolko, E. Grafting of acrylic acid onto polypropylene films irradiated with argon ions. *Nucl. Instrum. Methods Phys. Res., Sect. B* **2005**, *236*, 272−276.

(7) Jung, Ch.-H.; Hwang, I.-T.; Kuk, I.-S.; Choi, J.-H.; Oh, B.-K.; Lee, Y.-M. Poly(acrylic acid)-Grafted Fluoropolymer Films for Highly Sensitive Fluorescent Bioassays. *ACS Appl. Mater. Interfaces* **2013**, *5*, 2155−2160.

(8) Padeste, C.; Neuhaus, S. Polymer-on-Polymer Structures Based on Radiation Grafting. In *Polymer Micro- and Nanografting*; Elsevier (William Andrew Publishing): Oxford, U.K., 2015; pp 11−41.

(9) Desai, S. M.; Singh, R. P. Surface Modification of Polyethylene. *Adv. Polym. Sci.* **2004**, *169*, 231−293.

(10) Gupta, B.; Anjum, N.; Plasma. and Radiation-Induced Graft Modification of Polymers for Biomedical Applications. *Adv. Polym. Sci.* **2003**, *162*, 25−60.

(11) Scheirs, J. *Moder fluoropolymers: high performance polymers for diverse application*, 1st ed.; Wiley: Chichester, U.K., 1997.

(12) Zhang, H.; Shen, P. K. Recent Development of Polymer Electrolyte Membranes for Fuel Cells. *Chem. Rev.* **2012**, *112*, 2780−2832.

(13) Chen, J.; Asano, M.; Maekawa, Y.; Yoshida, M. Suitability of some fluoropolymers used as base films for preparation of polymer electrolyte fuel cell membranes. *J. Membr. Sci.* **2006**, *277*, 249−357.

(14) Souzy, R.; Ameduri, B. Functional fluoropolymers for fuel cell membranes. *Prog. Polym. Sci.* **2005**, *30*, 644−687.

(15) Yamada, K.; Gondo, T.; Hirata, M. Application of DMAEMA-grafted expanded PTFE films to positively charged ultrafiltration membranes and their electrostatic sieve separation properties. *J. Appl. Polym. Sci.* **2001**, *81*, 1595−1604.

(16) Deng, B.; Yu, M.; Yang, X.; Zhang, B.; Li, L.; Xie, L.; Li, J.; Lu, X. Antifouling microfiltration membranes prepared from acrylic acid or methacrylic acid grafted poly(vinylidene fluoride) powder synthesized via pre-irradiation induced graft polymerization. *J. Membr. Sci.* **2010**, *350*, 252−258.

(17) Schulze, A.; Maitz, M. F.; Zimmermann, R.; Marquardt, B.; Fischer, M.; Werner, C.; Went, M.; Thomas, I. Permanent surface modification by electron-beam-induced grafting of hydrophilic polymers to PVDF membranes. *RSC Adv.* **2013**, *3*, 22518−22526.

(18) Desmet, T.; Morent, R.; De Geyter, N.; Leys, Ch.; Schacht, E.; Dubruel, P. Nonthermal Plasma Technology as a Versatile Strategy for Polymeric Biomaterials Surface Modification: A Review. *Biomacromolecules* **2009**, *10*, 2351−2378.

(19) Padeste, C.; Farquet, P.; Potzner, Ch.; Solak, H. H. Nanostructured bio-functional polymer brushes. *J. Biomater. Sci., Polym. Ed.* **2006**, *17*, 1285−1300.

(20) Choi, J.-H.; Ganesan, R.; Kim, D.-K.; Jung, Ch.-H.; Hwang, I.-T.; Nho, Y.; Yun, J.-M.; Kim, J.-B. Patterned Immobilization of Biomolecules by Using Ion Irradiation-Induced Graft Polymerization. *J. Polym. Sci., Part A: Polym. Chem.* **2009**, *47*, 6124−6134.

(21) Kim, W. J.; Jung, Ch.-H.; Hwang, I.-T.; Jung, Ch.-H.; Choi, J.-Ch; Hong, S.-K. Cell patterning on poly(sodium 4-styrenesulfonate)-patterned fluoropolymer substrate. *Nucl. Instrum. Methods Phys. Res., Sect. B* **2013**, *313*, 54−59.

(22) Chang, Y.; Chang, W.-J.; Shih, Y.-J.; Wei, T.-Ch; Hsiue, G.-H. Zwitterionic Sulfobetaine-Grafted Poly(vinylidene fluoride) Membrane with Highly Effective Blood Compatibility via Atmospheric Plasma-Induced Surface Copolymerization. *ACS Appl. Mater. Interfaces* **2011**, *3*, 1228−1237.

(23) Zou, X. P.; Kang, E. T.; Neoh, K. G. Plasma-induced graft polymerization of poly(ethylene glycol) methyl ether methacrylate on poly(tetrafluoroethylene) films for reduction in protein adsorption. *Surf. Coat. Technol.* **2002**, *149*, 119−128.

(24) Neuhaus, S.; Padeste, C.; Solak, H. H.; Spencer, N. D. Functionalization of fluoropolymer surfaces with nanopatterned polyelectrolyte brushes. *Polymer* **2010**, *51*, 4037−4043.

(25) Farquet, P.; Padeste, C.; Solak, H. H.; Gursel, S. A.; Scherer, G. G.; Wokaun, A. Extreme UV Radiation Grafting of Glycidyl Methacrylate Nanostructures onto Fluoropolymer Foils by RAFT-Mediated Polymerization. *Macromolecules* **2008**, *41*, 6309−6316.

(26) Dübner, M.; Gevrek, T. N.; Sanyal, A.; Spencer, N. D.; Padeste, C. Fabrication of Thiol-Ene "Clickable" Copolymer-Brush Nanostructures on Polymeric Substrates via Extreme Ultraviolet Interference Lithography. *ACS Appl. Mater. Interfaces* **2015**, *7*, 11337−11345.

(27) Dübner, M.; Spencer, N. D.; Padeste, C. Light-Responsive Polymer Surfaces via Postpolymerization Modification of Grafted Polymer-Brush Structures. *Langmuir* **2014**, *30*, 14971−14981.

(28) Idota, N.; Tsukahara, T.; Sato, K.; Okano, T.; Kitamori, T. The use of electron beam lithographic graft-polymerization on thermoresponsive polymers for regulating the directionality of cell attachment and detachment. *Biomaterials* **2009**, *30*, 2095−2101.

(29) Baró, J.; Sempau, J.; Fernández-Varea, J. M.; Salvat, F. PENELOPE: an algorithm for Monte Carlo simulation of the penetration and energy loss of electrons and positrons in matter. *Nucl. Instrum. Methods Phys. Res., Sect. B* **1995**, *100*, 31−46.




DOI: 10.1021/acs.langmuir.6b02808
*Langmuir* 2016, 32, 10641−10650

(30) Sempau, J.; Fernández-Varea, J. M.; Acosta, E.; Salvat, F. Experimental benchmarks of the Monte Carlo code PENELOPE. *Nucl. Instrum. Methods Phys. Res., Sect. B* **2003**, *207*, 107−123.
(31) Feng, J.; Chan, Ch.-M.; Weng, L.-T. Influence of chain sequence structure of polymers on ToF-SIMS spectra. *Polymer* **2000**, *41*, 2695−2699.
(32) Peng, Q.; Lai, D.; Kang, E. T.; Neoh, K. G. Preparation of Polymer-Silicon(100) Hybrids via Interface-Initiated Reversible Addition-Fragmentation Chain-Transfer (RAFT) Polymerization. *Macromolecules* **2006**, *39*, 5577−5582.
(33) Park, Y. W.; Inagaki, N. A New Approach for Selective Surface Modification of Fluoropolymers by Remote Plasmas. *J. Appl. Polym. Sci.* **2004**, *93*, 1012−1020.
(34) Karamdoust, S.; Yu, B.; Bonduelle, C. V.; Liu, Y.; Davidson, G.; Stojcevic, G.; Yang, J.; Lau, W. M.; Gillies, E. R. Preparation of antibacterial surfaces by hyperthermal hydrogen induced cross-linking of polymer thin films. *J. Mater. Chem.* **2012**, *22*, 4881−4889.
(35) Yang, Y.-F.; Hu, H.-Q.; Li, Y.; Wan, L.-S.; Xu, Z.-K. Membrane surface with antibacterial property by grafting polycation. *J. Membr. Sci.* **2011**, *376*, 132−141.
(36) Galvin, C. J.; Genzer, J. Applications of surface-grafted macromolecules derived from post-polymerization modification reactions. *Prog. Polym. Sci.* **2012**, *37*, 871−906.
(37) Tu, Q.; Wang, J.-Ch; Liu, R.; He, J.; Zhang, Y.; Shen, S.; Xu, J.; Liu, J.; Yuan, M.-S.; Wang, J. Antifouling properties of poly(dimethylsiloxane) surfaces modified with quaternized poly(dimethylaminoethyl methacrylate). *Colloids Surf., B* **2013**, *102*, 361−370.
(38) Laopa, P.; Vilaivan, T.; Hoven, V. Positively charged polymer brush-functionalized filter paper for DNA sequence determination following Dot blot hybridization employing a pyrrolidinyl peptide nucleic acid probe. *Analyst* **2013**, *138*, 269−277.
(39) Sanjuan, S.; Perrin, P.; Pantoustier, N.; Tran, Y. Synthesis and swelling behavior of pH-responsive polybase brushes. *Langmuir* **2007**, *23*, 5769−5778.
(40) Kusumo, A.; Bombalski, L.; Lin, Q.; Matyjaszewski, K.; Schneider, J. W.; Tilton, R. D. High Capacity, Charge-Selective Protein Uptake by Polyelectrolyte Brushes. *Langmuir* **2007**, *23*, 4448−4454.



DOI: 10.1021/acs.langmuir.6b02808
*Langmuir* 2016, 32, 10641−10650

# SUPPORTING INFORMATION

# Electron-beam lithographic grafting of functional polymer structures from fluoropolymer substrates

*Katarzyna Gajos[1,2], Vitaliy A. Guzenko[2], Matthias Dübner[2], Jakub Haberko[3], Andrzej Budkowski[1], Celestino Padeste[2]*

[1]M. Smoluchowski Institute of Physics, Jagiellonian University, Łojasiewicza 11, 30-348 Kraków, Poland

[2]Laboratory of Micro- and Nanotechnology, Paul Scherrer Institute, CH-5232 Villigen, Switzerland

[3]Faculty of Physics and Applied Computer Science, AGH University of Science and Technology, Mickiewicza 30, 30-059 Kraków, Poland

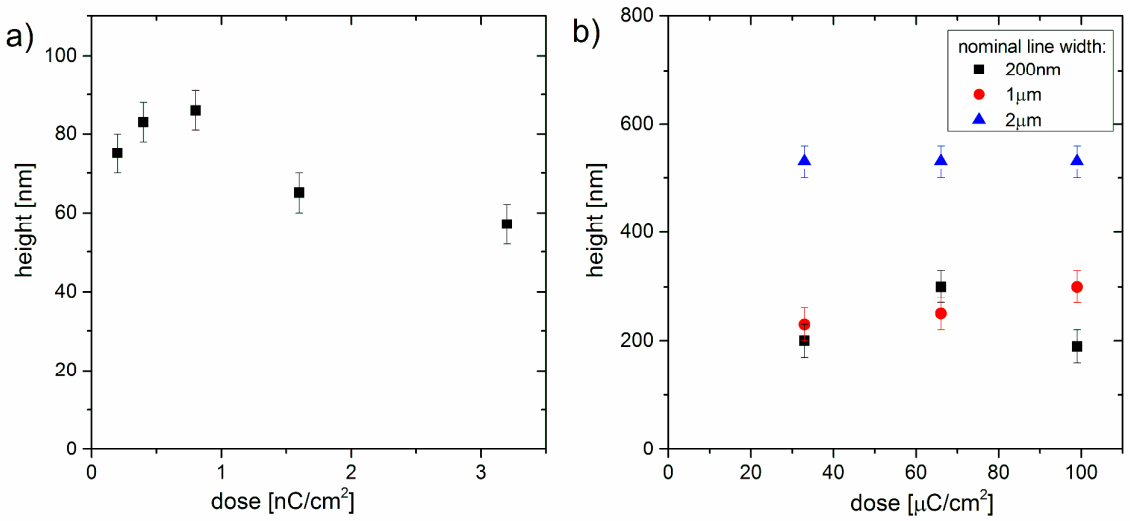


**Figure S1.** Dose dependence of the height of structures grafted from ETFE after defining radical patterns with EBL at (a) 2.5 keV and (b) 100 keV.

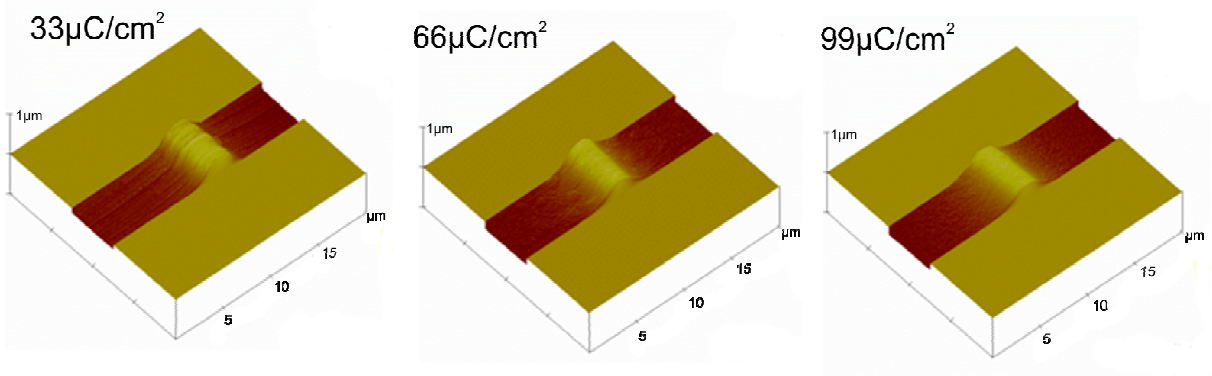


**Figure S2.** AFM images of PDMAEMA line structures grafted from ETFE after defining radical patterns with 100 keV EBL with 2 µm nominal line width and different doses.

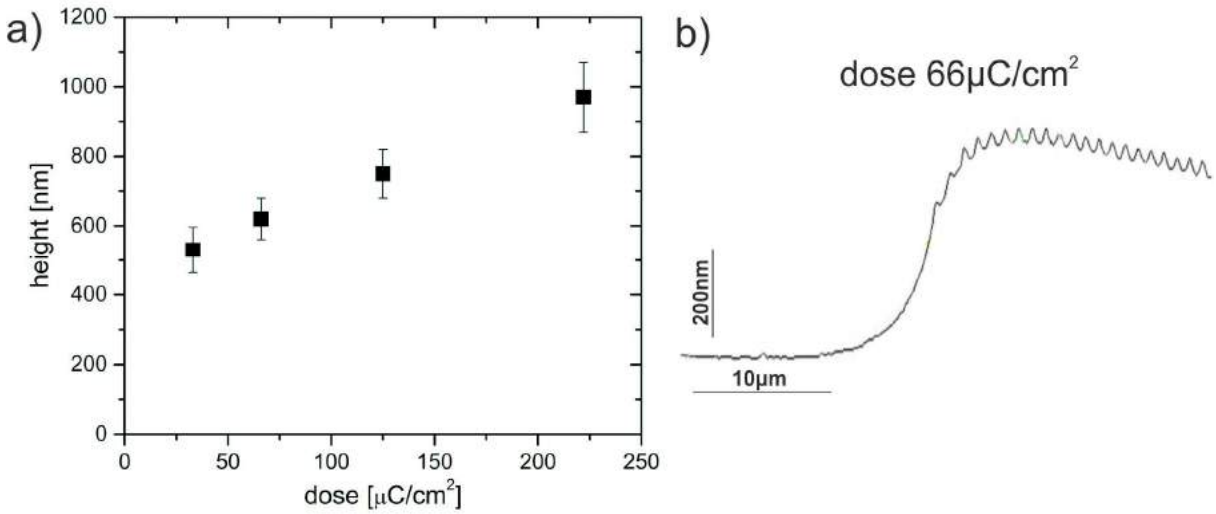


**Figure S3.** (a) Dose dependence of the AFM-determined height of a cushion formed on ETFE substrate after grafting of PDMAEMA line structures exposed with 1μm distance using 100 keV EBL. (b) cross-section perpendicular to the line structures showing the individual lines on top of the cushion resulting from sub-surface grafting.

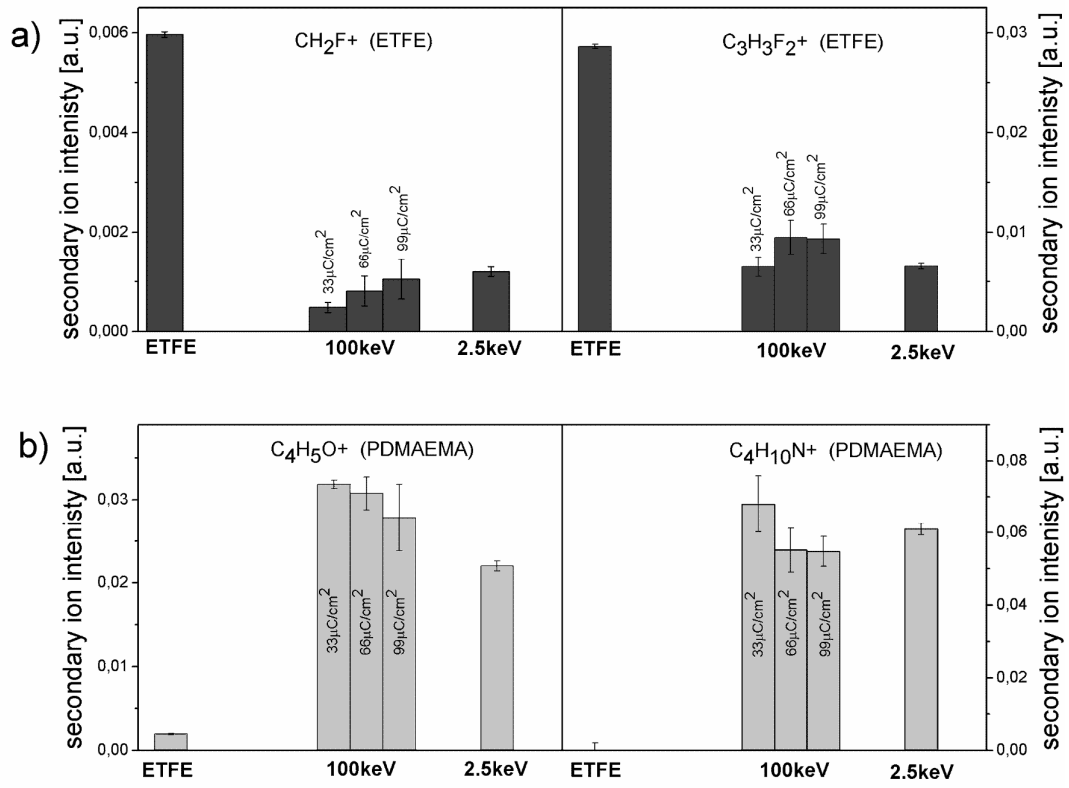


**Figure S4**. Normalized TOF-SIMS intensities of secondary ions characteristic for (a) ETFE ($CH_2F^+$ and $C_3H_3F_2^+$) and (b) PDMAEMA polymer ($C_4H_5O^+$ and $C_4H_{10}N^+$) determined for pristine ETFE, and ETFE after PDMAEMA-grafting following activation with 100 keV and 2.5 keV electrons.

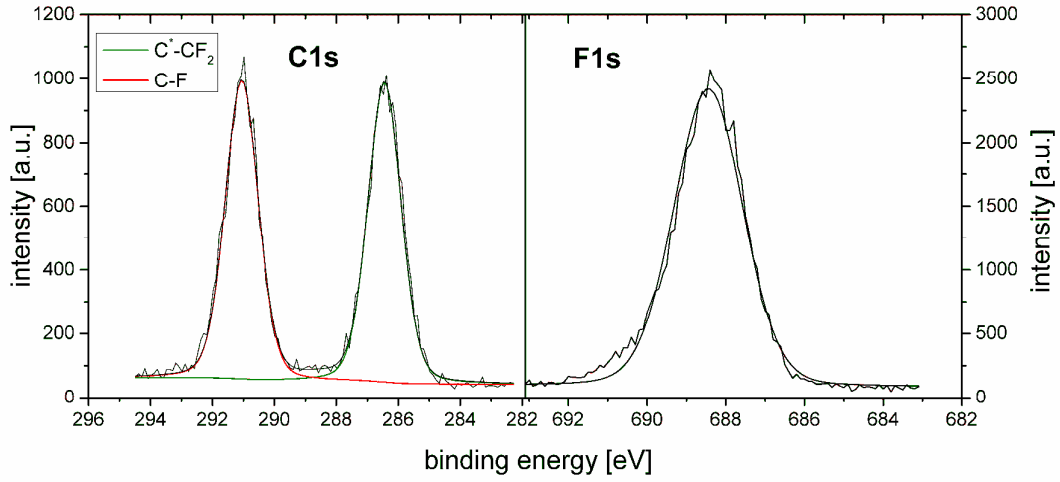


**Figure S5.** High resolution XPS spectra of C1s and F1s determined for untreated ETFE film.

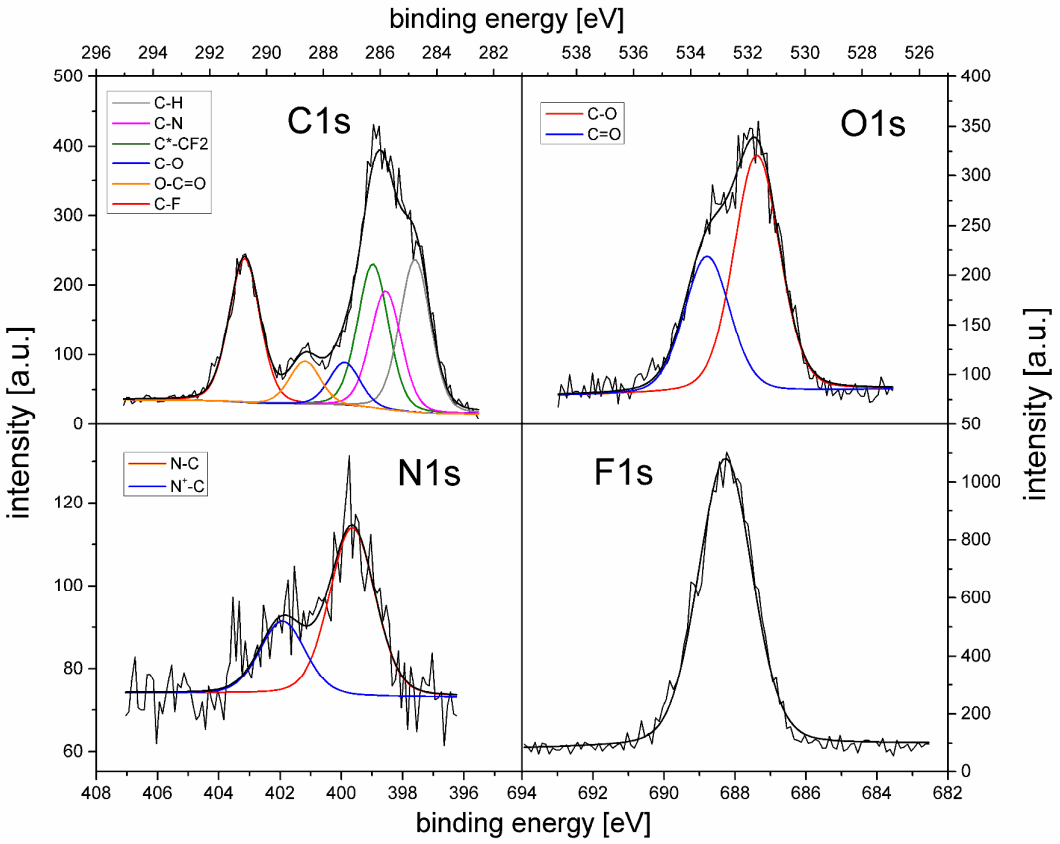


**Figure S6.** High resolution XPS spectra of C1s, O1s, N1s and F1s core shell determined for ETFE films after PDMAEMA grafting following activation with 100 keV electrons.

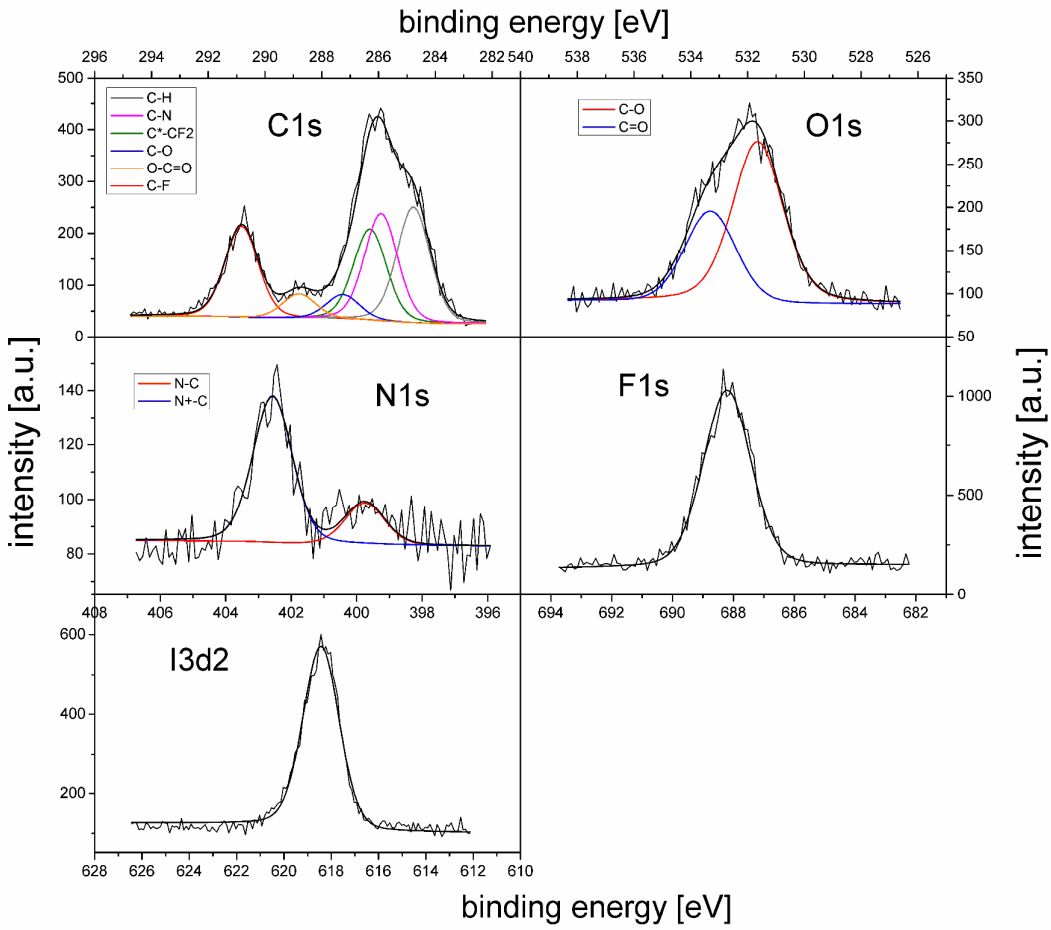


**Figure S7.** High resolution XPS spectra of C1s, O1s, N1s, F1s and I3d2 core shell determined for ETFE films after PDMAEMA grafting following activation with 100 keV electrons and subsequent quaternization reaction.

# Paper III

## *Imaging and chemical surface analysis of biomolecular functionalization of monolithically integrated on silicon Mach-Zehnder interferometric immunosensors*

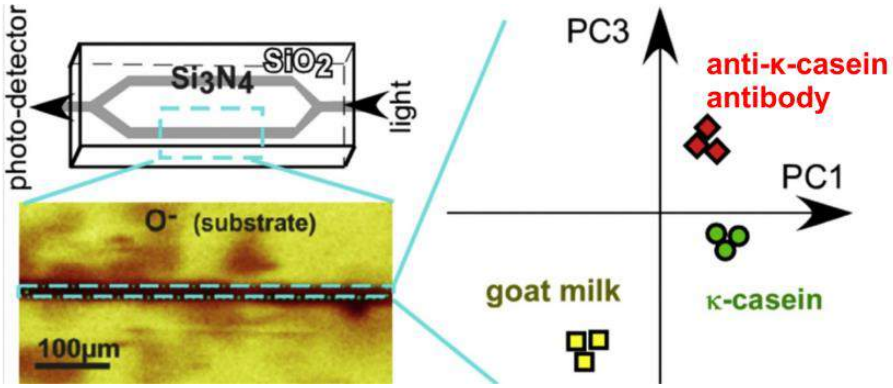


Highlights

- Optimization of probe immobilization with robotic spotter printing overlapping spots.
- In-situ inspection of microstructured surfaces of biosensors integrated on silicon.
- Imaging and chemical analysis of immobilization, surface blocking and immunoreaction.
- Insight with molecular discrimination into step-by-step sensor surface modifications.
- Optimized biofunctionalization improves sensor sensitivity and response repeatability.

Applied Surface Science 385 (2016) 529–542

Contents lists available at ScienceDirect

Applied Surface Science

journal homepage: www.elsevier.com/locate/apsusc

# Imaging and chemical surface analysis of biomolecular functionalization of monolithically integrated on silicon Mach-Zehnder interferometric immunosensors

Katarzyna Gajos[a,*], Michailia Angelopoulou[b], Panagiota Petrou[b], Kamil Awsiuk[a], Sotirios Kakabakos[b], Willem Haasnoot[c], Andrzej Bernasik[d,e], Jakub Rysz[a], Mateusz M. Marzec[e], Konstantinos Misiakos[f], Ioannis Raptis[f], Andrzej Budkowski[a]

[a] M. Smoluchowski Institute of Physics, Jagiellonian University, Łojasiewicza 11, 30-348 Kraków, Poland
[b] Institute of Nuclear & Radiological Sciences & Technology, Energy & Safety, NCSR Demokritos, P. Grigoriou & Neapoleos St, Aghia Paraksevi 15310, Athens, Greece
[c] RIKILT Wageningen UR, Akkermaalsbos 2, 6708 WB Wageningen, Netherlands
[d] Faculty of Physics and Applied Computer Science, AGH University of Science and Technology, Mickiewicza 30, 30-059 Kraków, Poland
[e] Academic Centre for Materials and Nanotechnology, AGH University of Science and Technology, Mickiewicza 30, 30-059 Kraków, Poland
[f] Department of Microelectronics, Institute of Nanoscience and Nanotechnology, NCSR Demokritos, P. Grigoriou & Neapoleos St, Aghia Paraksevi 15310, Athens, Greece

ARTICLE INFO

*Article history:*
Received 5 February 2016
Received in revised form 13 May 2016
Accepted 24 May 2016
Available online 26 May 2016

*Keywords:*
Biosensor functionalization
On-chip immunoassay
Multi-molecular coverage
Time-of-flight secondary ion mass spectrometry
X-ray photoelectron spectroscopy
Atomic force microscopy

ABSTRACT

Time-of-flight secondary ion mass spectrometry (imaging, micro-analysis) has been employed to evaluate biofunctionalization of the sensing arm areas of Mach-Zehnder interferometers monolithically integrated on silicon chips for the immunochemical (competitive) detection of bovine κ-casein in goat milk. Biosensor surfaces are examined after: modification with (3-aminopropyl)triethoxysilane, application of multiple overlapping spots of κ-casein solutions, blocking with 100-times diluted goat milk, and reaction with monoclonal mouse anti-κ-casein antibodies in blocking solution. The areas spotted with κ-casein solutions of different concentrations are examined and optimum concentration providing homogeneous coverage is determined. Coverage of biosensor surfaces with biomolecules after each of the sequential steps employed in immunodetection is also evaluated with TOF-SIMS, supplemented by Atomic force microscopy and X-ray photoelectron spectroscopy. Uniform molecular distributions are observed on the sensing arm areas after spotting with optimum κ-casein concentration, blocking and immunoreaction. The corresponding biomolecular compositions are determined with a Principal Component Analysis that distinguished between protein amino acids and milk glycerides, as well as between amino acids characteristic for Mabs and κ-casein, respectively. Use of the optimum conditions (κ-casein concentration) for functionalization of chips with arrays of ten Mach-Zehnder interferometers provided on-chips assays with dramatically improved both intra-chip response repeatability and assay detection sensitivity.
© 2016 Elsevier B.V. All rights reserved.

## 1. Introduction

The development of biosensors and their applications has expanded in the last decades to cover different areas, such as biomedical diagnostics [1–3], food safety and environmental monitoring [4], drug screening and security [5]. Still, further biosensor improvements are demanded, including fast and sensitive response [3,6], cost-efficient and miniaturized fabrication [3,6], as well as multi-analyte potential for point-of-need platforms [7,8]. Label-free detection is an extra asset for these devices, since the implementation of labels increases considerably the analysis cost and complicates the assay procedure [9]. The majority of transducers suited for label-free detection are optical based, mainly, on surface plasmon resonance (SPR) [10], optical waveguides [11,12], grating couplers [13], Mach-Zehnder [14,15] and Young interferometers [16], microring resonators [17,18], and reflectometric interference spectroscopy sensors [19,20], all providing high detection sensitivity. Independently of the specific transduction principle, in all sensors mentioned above, detection is based on reactions taking place in the vicinity of the transducer surface

* Corresponding author.
*E-mail address:* kasia.fornal@uj.edu.pl (K. Gajos).

http://dx.doi.org/10.1016/j.apsusc.2016.05.131
0169-4332/© 2016 Elsevier B.V. All rights reserved.

changing the effective refractive index. Thus, in order to take advantage of the inherent high detection sensitivity of these transducers, uniform and high quality chemical and biological surface functionalization is required.

Optical label free sensors, have essentially the ability to monitor all the stages of the biosensor functionalization procedure due to the build-up of the different chemical and biomolecular layers on the transducer surface. Nevertheless, the optical signals recorded provide information on a sum of phenomena that take place on the surface without being able to discriminate between them. For example, during immunoreaction two counterbalanced phenomena might occur; the specific analyte-antibody reaction which increases the biomolecular layer thickness and the simultaneous removal of proteins or other molecules from the surface that decreases the overall layer thickness. In addition, this approach although useful for research laboratories, is inconvenient when functionalization of transducers at wafer-scale for manufacturing purposes is targeted. In this case, biofunctionalization of the sensors employing robotic spotters that could apply multiple recognition biomolecules in parallel is preferable. To this end, powerful surface analysis techniques could provide useful insight information and help to standardize the biofunctionalization process [21–23].

Here, we employ Time-of-flight secondary ion mass spectrometry (TOF-SIMS) for imaging and molecular characterization of the biomolecular layers built-up on the sensing arms of Broad-Band Mach-Zehnder interferometers (BB-MZI) integrated on silicon chips to define optimum conditions for uniform biomolecules immobilization. Subtle differences in chip surface chemical composition between the sequential steps employed in biomolecule immobilization, surface blocking and immunoreaction are revealed by Principal Component Analysis (PCA) analysis of TOF-SIMS results. This analysis is complemented with results received by Atomic force microscopy (AFM) and X-ray photoelectron spectroscopy (XPS) on planar surfaces. These techniques are employed in the present study to optimize the biofunctionalization procedure of a newly developed Mach-Zehnder interferometer array monolithically integrated onto a silicon substrate along with their respective broad-band light sources [24,25]. The integrated light sources are silicon avalanche diodes that emit light when reversed biased beyond their breakdown point over a broad area of visible and near-infrared spectral region [26]. The Mach-Zehnder is made of a rib $Si_3N_4$ waveguide formed on a $SiO_2$ layer and covered with a 2.5-μm thick $SiO_2$ cladding layer on which the sensing regions are formed by etching 600-μm long and 20-μm wide windows over the one of the arms (sensing arm), whereas the reference arm is buried below the cladding layer (Fig. 1a). Ten such interferometers along with their respective light sources are realized on 36 $mm^2$ silicon chips, as shown in Fig. 1b, enabling multi-analyte determinations through deposition of specific recognition biomolecules onto the different sensors of a single chip. The sensor chemical and biological functionalization procedure includes the following steps: oxygen plasma cleaning/hydrophilization, modification with amine-silane to allow biomolecule immobilization through physical adsorption, deposition of recognition biomolecule, and blocking of the surface free binding sites. Due to the geometry and the relative position of the ten sensing arm windows, the deposition of recognition biomolecules could be achieved by spotting multiple overlapping spots. Thus, special care should be taken to achieve complete and uniform coverage of the sensing regions.

The combination of different surface analysis techniques to characterize the chemical modification and biofunctionalization of planar [21–23,27–35] and microstructured surfaces [36–38] has been applied by other investigators [21,27–32,36–38] as well as by our group [22,23,33–35]. Here, the changes in surface composition of microstructured sensor surfaces are recorded after each step of the procedure employed to detect adulteration of goat milk with bovine through immunochemical determination of bovine κ-casein content in goat milk. This is accomplished following a competitive immunochemical assay format, involving immobilization of bovine κ-casein onto the chip surface, blocking with whole fat goat milk and binding of mouse monoclonal anti-κ-casein antibodies. The complexity of the surface and the different properties of molecules interacting with the surface (proteins, lipids, micelles, etc.,) make the surface analysis particularly intriguing and valuable with respect to sensor performance optimization.

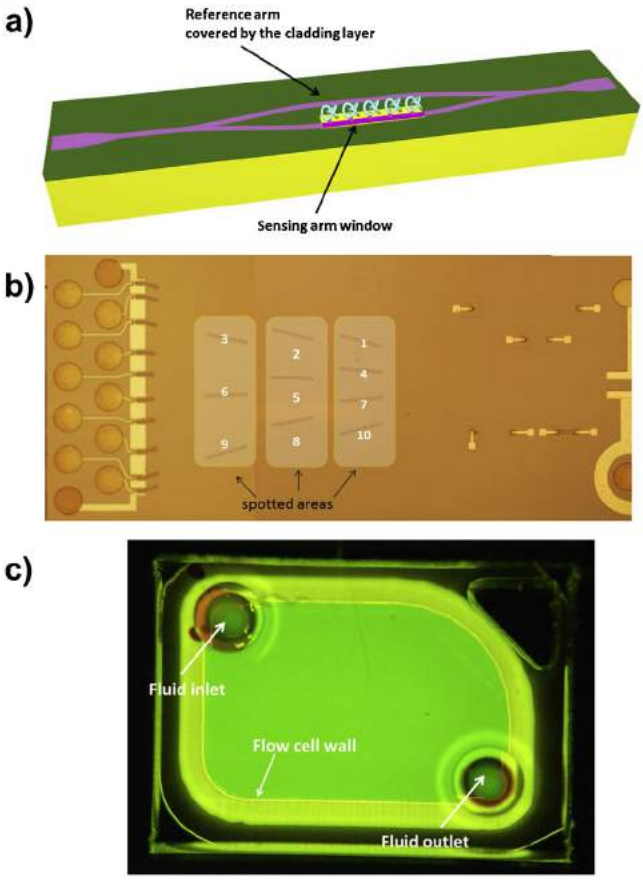


**Fig. 1.** (a) Schematic of the BB-MZI showing the window over the sensing arm where the specific recognition molecules were deposited. (b) Photograph of the chip accommodating ten integrated BB-MZIs. The areas of spotting around the sensing arm windows of the 10 BB-MZIs are also shown along with the sensor numbering. (c) Picture of the fluidic cell filled with a green fluorescent dye solution. (For interpretation of the references to colour in this figure legend, the reader is referred to the web version of this article.)

## 2. Experimental section

### 2.1. Fabrication of chips with integrated Mach-Zehnder interferometers and corresponding planar samples

Silicon wafers were purchased from Si-Mat (Kaufering, Germany). Optoelectronic silicon chips comprising ten $Si_3N_4$ waveguide Mach-Zehnder interferometers monolithically integrated onto the same silicon substrate along with their respective silicon avalanche diodes light sources were fabricated at the clean room facility of the Institute of Nanosciences and Nanotechnology of NCSR "Demokritos". The process flow applied for the fabrication of chips included low pressure chemical vapor deposition of $SiO_2$ and $Si_3N_4$, in addition to thermal oxidation and lithographic steps [25]. The sensing regions are formed by etching 600-μm long and 20-μm wide windows on the $SiO_2$ cladding layer (2.5 μm thick)

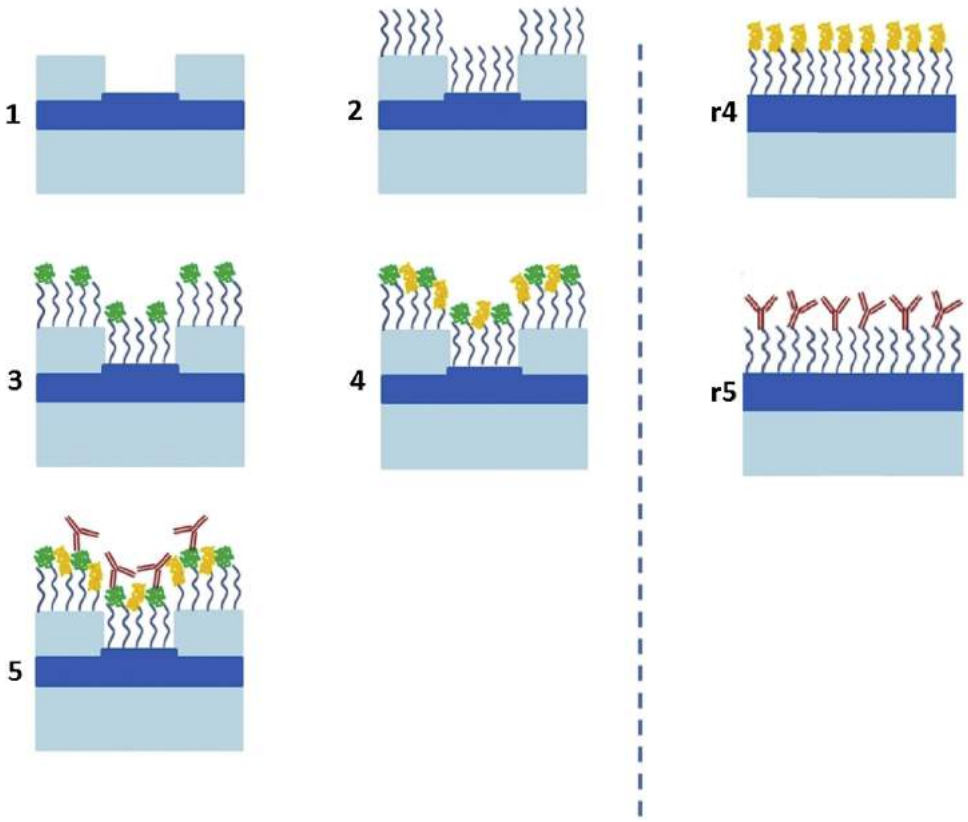


**Fig. 2.** Schematic of the procedure followed for chemical activation, biofunctionalization and immunoassay for detection of bovine κ-casein in goat milk on the chip sensing areas. Chips **(1)** were modified with APTES **(2)**, spotted with κ-casein **(3)**, blocked with diluted goat milk **(4)**, and exposed to a solution of two monoclonal antibodies against bovine κ-casein in diluted goat milk **(5)**. Reference samples modified with APTES were spotted with goat milk **(r4)** or monoclonal antibodies solution in goat milk **(r5)**.

deposited over the planar $Si_3N_4$ waveguides. These windows are open over one of the arms (sensing arm) of each Mach-Zehnder interferometer, thus, exposing the waveguides to solutions supplied through a fluidic cell [25]. The custom-made disposable fluidic module (Jobst Technologies GmbH; Freiburg, Germany) is comprised by a top layer made of poly(methyl methacrylate) with drilled inlet and outlet holes onto which a thick film adhesive photoresist was laminated and photolithographically patterned to create the flow channel wall (Fig. 1c). The fluidic is assembled with the chip at wafer scale by lamination. The fluidic design ensures smooth filing with aqueous solutions (see video in Supplementary material showing filling of the fluidic with solution of a fluorescent compound) and minimum reagents consumption (0.3 μL volume).

Apart from the chips, analysis was also performed on planar surfaces consisting of silicon wafer chips on which a 1-μm thick $SiO_2$ layer was created by low pressure chemical vapor deposition, and then an additional 150-nm thick $Si_3N_4$ layer was deposited on top to match the waveguides composition and surface properties.

### 2.2. Biosensor surface functionalization and immunoassay

3-Aminopropyl(triethoxysilane) (APTES), bovine serum albumin (BSA) and bovine κ-casein used for chemical activation and biofunctionalization of surfaces were purchased from Sigma Chemical Co. (St. Louis, MO, USA).

The chemical activation, biofunctionalization and immunoreaction steps performed either on the Mach-Zehnder sensing areas (denoted by **n** – integer) or the respective planar samples (denoted by primed integer, **n'**, whenever distinction of sample geometry is needed), are shown schematically in Fig. 2. Firstly, the surfaces (Fig. 2, sample 1) were cleaned and hydrophilized with oxygen plasma [26,35]. Secondly, they were silanized (Fig. 2, sample 2) through immersion in a 0.5% (v/v) aqueous APTES solution for 2 min, followed by gentle washing with distilled water, drying under $N_2$ flow, and baking for 20 min at 120 °C [35].

To cover the sensing areas of the chip (an area of about 1 mm × 2.4 mm), as it is schematically shown in Fig. 1b, with the κ-casein solutions (Fig. 2, sample 3) through spotting multiple overlapping spots were applied employing a standard microarray spotter (BioOdyssey Calligrapher Miniarrayer, Bio-Rad Inc.). Similarly, on the planar surfaces, an area of 7 mm × 7 mm was covered by deposition of multiple overlapping spots. All surfaces were then incubated at room temperature (RT) in a humidity chamber for 2 or 24 h, prior to washing with 10 mM phosphate buffer, pH 7.4, and distilled water. Solutions of κ-casein with concentration $C_s$ ranging from 5 to 200 μg/mL in 10 mM phosphate buffer, pH 7.4, were used for spotting. For the sample series described in Sections 3.2 and 3.3 casein solutions with $C_s$ = 200 μg/mL were applied. Next, blocking was performed by immersing the silicon dies in goat milk diluted in 1/100 volume ratio with the same phosphate buffer (Fig. 2, sample 4), followed by washing and drying as previously. Spotted and blocked surfaces were exposed to a solution containing a mixture of two mouse monoclonal antibodies (Mabs 6A-10 and 4G-10, developed by RIKILT against two different epitopes of bovine κ-casein), at a concentration of 1 μg/mL each, in goat milk 100-times diluted with 10 mM phosphate buffer, containing also 0.5 mg/mL BSA, so as to suppress non-specific binding of antibodies (Fig. 2, sample 5).

To enable easier interpretation of surface analysis results, reference planar samples modified with APTES and spotted with 100-times diluted goat milk (Fig. 2, sample r4) or the solution of Mabs against κ-casein (Fig. 2, sample r5) were also prepared.

All the samples were gently washed with phosphate buffer and distilled water and dried under $N_2$ flow prior to measurements with surface science techniques.

### 2.3. TOF-SIMS characterization of chip sensing areas and planar surfaces

Imaging and molecular characterization was performed on the sensing areas of the chips as well as on planar surfaces using the TOF.SIMS 5 (ION-TOF GmbH) instrument, equipped with 30 keV bismuth liquid metal ion gun. The $Bi_3^+$ clusters were used as primary ions with the ion dose density lower than $10^{12}$ ion/cm$^2$ to ensure static mode conditions. Low energy electron flood gun was used for charge compensation.

For all planar samples, positive and negative ion TOF-SIMS images and high mass resolution spectra were acquired from several non-overlapping 500 μm × 500 μm areas (with a resolution of 512 × 512 points). In the case of surfaces with millimeter-sized κ-casein domains, created via deposition of overlapping spots from solutions of different concentration, TOF-SIMS analyzed areas were always located inside each of the domains except for the reference. In addition, the 6 mm × 6 mm map of several casein domains (formed after 2 h of incubation) was acquired in stage scan mode with a resolution of 256 × 256 points. Molecular analysis was also performed on the sensing arm areas of separate chips (20 μm wide, 600 μm long), with the analyzed area of 15 μm × 480 μm located always inside each individual sensing region. The analyzed areas were defined by TOF-SIMS images determined with the sum of all ions.

High resolution mass spectra, with minimal mass resolution ($m/\Delta m$) > 5300 at $C_4H_5^+$ and $C_4H^-$ peaks, were acquired. Mass calibration was performed with $H^+$, $H_2^+$, $CH^+$, $C_2H_2^+$ and $C_4H_5^+$ peaks for positive secondary ions, and with $CH^-$, $C_2H^-$, $C_3^-$ and $C_4H^-$ peaks for negative secondary ions. All TOF-SIMS data were normalized with respect to the total ion intensity.

### 2.4. Compositional multivariate TOF-SIMS analysis with PCA

Principal Component Analysis (PCA) was performed for the TOF-SIMS positive ion spectra acquired from the chip sensing areas (15 μm × 480 μm regions, 3 spots per sample 3–5) as well as the corresponding (**3′**) and the reference (**r4, r5**) planar surfaces (100 μm × 100 μm regions, 4 spots per sample). Only selected peaks, characteristic for biomolecules (amino acids and milk glycerides, specified in the corresponding figures), were applied to PCA analysis. Prior to PCA, the intensities of selected peaks from each spectrum were normalized to the sum of selected peaks and then mean-centered. PCA was performed using PLS Toolbox (Eigenvector Research, Manson, WA) for MATLAB (MathWorks, Inc., Natick, MA).

### 2.5. XPS analysis of planar surfaces

Analysis by X-ray photoelectron spectroscopy (XPS) was applied to planar surfaces spotted with κ-casein, blocked and reacted with Mabs (**2′-5′**) as well as to reference samples (**r4, r5**), using a PHI 5000 Versa Probe II (ULVAC-PHI) spectrometer equipped with an Al Kα radiation source (1486.6 eV). Angle-resolved XPS (ARXPS) measurements for the evaluation of organic layer thickness (and surface density) were performed for four different values of photoelectron take-off angle θ (10°, 30°, 45° and 55° with respect to the surface normal). The corresponding sampling vertical depth varies between 9.5 and 5.5 nm (for photoelectrons Si 2p). A dual-beam charge neutralizer was used to compensate the charge-up effect. High resolution spectra were collected with analyzer pass energy of 23.5 eV. The operating pressure in the analytical chamber was less than $5 \times 10^{-7}$ Pa. All XPS peaks were referenced to the neutral (C—C) carbon C1s peak at 284.6 eV. Spectrum backgrounds were subtracted using Shirley method.

### 2.6. AFM characterization of planar surface

AFM imaging of the planar surfaces spotted with κ-casein, blocked and reacted with Mabs (**2′-5′**) as well as to reference samples (**r4, r5**), was performed in ambient conditions (in air at room temperature) with Agilent 5500 microscope working in non-contact mode. AFM probes with spring constant about 2 N/m, tip radius below 10 nm and resonant frequencies about 70 kHz were used. The set point and all gains were adjusted to obtain minimal noise and clear images of the analyzed surfaces. For each sample topographic images were acquired at several different areas.

The lateral surface nanostructures were described with the doubled width-at-half-maximum (2whm) received by applying the radial averaged autocorrelation function to topographic AFM micrographs. In addition, the vertical nanostructures were specified using the averaged parameters of height distribution in each AFM image, such as the average height (<h>) and the root-mean-square roughness (RMS). AFM micrographs were analyzed with the WSxM software provided by Nanotec Electronica S.L. [39] (downloadable at http://www.nanotec.es).

### 2.7. On-chip bovine κ-casein assay

Chips on which 7 out of 10 BB-MZIs have been spotted with κ-casein solution and the rest 3 with BSA and blocked through incubation with full fat goat milk diluted 100-times with 10 mM phosphate buffer, pH 7.4, were covered with fluidic modules and used for the assay. For this purpose, the encapsulated chips were placed on the docking station of a prototype apparatus which provides for both the electrical and fluidic connections [24]. A peristaltic pump (FH10, Thermo Fisher Scientific, USA) was used for the delivery of the reagent solution at a constant rate of 40 μL/min. Bovine κ-casein calibrators (0–1 μg/mL) were prepared in 50 times diluted goat milk with assay buffer (10 mM phosphate buffer, pH 7.4, containing 0.5% (w/v) BSA). These calibrators were mixed with antibodies solution containing the two anti-κ-casein monoclonal antibodies (33-4G10 and 33-6A10) at 1 μg/mL each in assay buffer at 1:1 vol ratio. After the equilibration of the chip with 100-times diluted goat milk in assay buffer, the mixtures of the calibrators with the antibodies were passed over the chip for 15 min. The transmission spectra (Fig. S1 in Supplementary material) of all ten BB-MZIs are recorded in a period of 10 s with 1 s integration time per BB-MZI by a miniaturized spectrometer (QE65000, Ocean Optics). The spectra are submitted to Discrete Fourier Transform to obtain the phase shifts in TE polarization [24]. The signal is calculated as the phase shift per min over a 5-min time window starting 3 min after the introduction of the calibrator/antibody mixture. For the preparation of the calibration curve, the phase shifts per min corresponding to different calibrators are plotted versus the bovine κ-casein concentration in the calibrator solutions.

## 3. Results and discussion

The objective of this study was to demonstrate the potential of microscopic and surface analysis methods as powerful tool for the optimization of biomolecules immobilization onto silicon transducers for label-free detection of analytes. This was exemplified using Mach-Zehnder interferometers integrated onto silicon chips (Fig. 1a) [24,25]. Each chip (9.3 × 4.0 mm$^2$) accommodates 10 Mach-Zehnder interferometers (BB-MZIs) non-linearly arranged onto the chip surface along with their broad-band light emitting

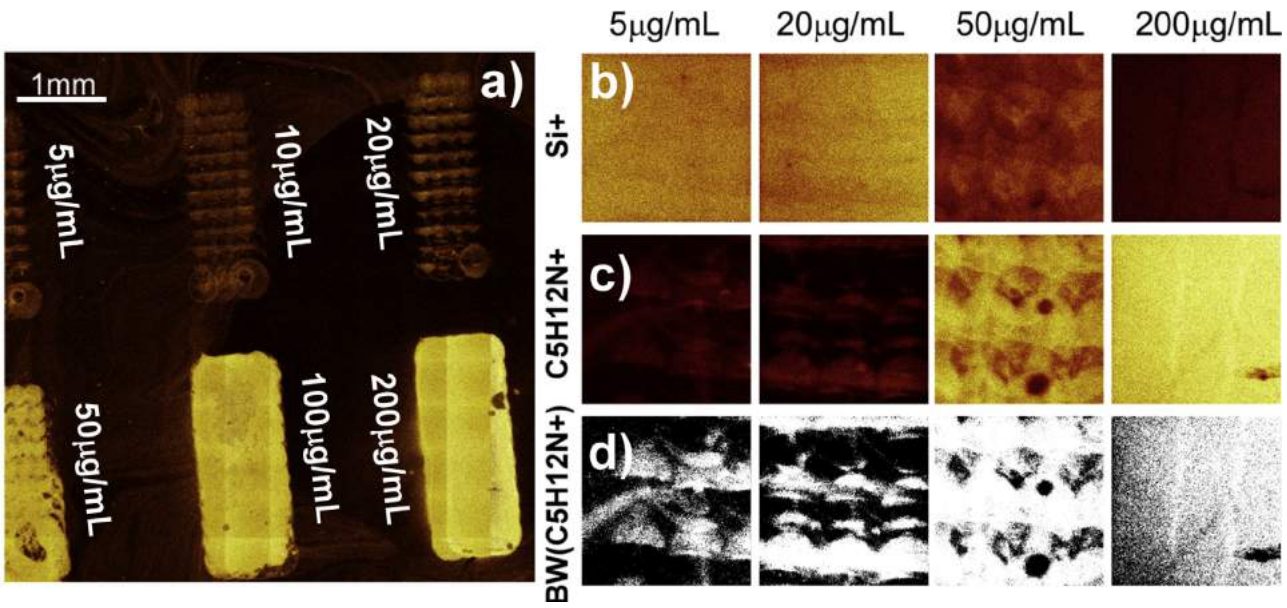


**Fig. 3.** (a) Millimeter-sized casein domains, created on planar surfaces by spotting of κ-casein solutions with concentrations ranging from 5 to 200 μg/mL, and imaged with low-resolution TOF-SIMS image using ions characteristic for the protein molecules ($C_5H_{12}N^+$ from Iso, Leu). (b and c) High-resolution TOF-SIMS images recorded with ions characteristic for the $Si_3N_4$ substrate ($Si^+$) and the protein molecules ($C_5H_{12}N^+$ from Iso, Leu) on areas spotted with κ-casein solution with concentration of 5, 20, 50 and 200 μg/mL. (d) Representative black and white images of $C_5H_{12}N^+$ maps (c) computed to show overlapping individual spots (with visible contact rings). Uniform surface coverage with proteins is obtained starting from κ-casein concentration of 100 μg/mL.

diodes. The Mach-Zehnder interferometers are formed by appropriate patterning of planar silicon nitride waveguides (Fig. 1a). Waveguides are covered with a $SiO_2$ cladding layer, except for a $20 \times 600\ \mu m^2$ section above the sensing arm from which the cladding layer has been removed to expose the waveguide to the samples run over the chip. Molecular interactions on the exposed waveguide surface, e.g. affinity binding of analytes to immobilized probes, change the effective refractive index over the sensing arm, that is translated into a wavelength independent phase difference with respect to the reference arm [10]. The two optical paths combine again creating the transmitted interference spectrum (see Fig. S1) which is collected by an external spectrometer, synchronized with the operation of the light sources through an electrical and computer controlled multiplexer. This way all ten sensors on the chip could be measured with the same spectrometer. Monitored shifts in the recorded spectra are converted to phase shifts through Discrete Fourier Transform.

To transform the Mach-Zehnder interferometers to biosensors the sensing arm areas should be modified by appropriate recognition biomolecules. This is achieved by chemical activation of the silicon chip surface via silanization and then deposition of recognition biomolecules through spotting. In the present work, the compositional and topographical changes in the surfaces of the BB-MZI sensing arm are recorded after each of the steps employed for functionalization the chip and assay for the determination of bovine κ-casein in goat milk (Fig. 2).

Since the reproducibility of the on-chip affinity assays, expressed as signal variation between different sensors, depends crucially on the homogeneity of recognition probe immobilization onto the sensing arm areas, TOF-SIMS was employed to determine the homogeneity of recognition biomolecule deposition, in the particular case bovine κ-casein, via spotting (analyzed in Section 3.1).

Then, the sensing arm areas of BB-MZIs (Fig. 2) corresponding to cleaned/hydrophilized chips **(1)**, chips modified with aminosilane (APTES) **(2)**, chips after κ-casein deposition/immobilization **(3)**, blocking **(4)**, and reaction with monoclonal antibodies against κ-casein (Mabs) **(5)** were analyzed with TOF-SIMS to gain information about the sensing areas coverage by the different molecules involved in the assay, their distribution on them (Section 3.2), as well as the composition of the biomolecular layers formed (Section 3.3). In addition, nanostructure, chemistry and thickness of consecutive molecular layers are examined by AFM and XPS on planar surfaces (denoted by primed integer) prepared following the same procedure as the chips with the difference that a larger surface area ($7 \times 7\ mm^2$) was spotted with κ-casein. Planar surfaces spotted with blocking and Mabs solution **(r4, r5)** are also used as references.

Finally, optimum conditions for biomolecular functionalization, determined with imaging and surface analysis, were evaluated through detection of κ-casein in real time with integrated on silicon BB-MZI immunosensors (Section 3.4).

### 3.1. Optimization of probe immobilization with microarray spotter

To achieve immobilization of recognition molecule, i.e., bovine κ-casein, onto the sensing arm areas of the 10 BB-MZIs of a single chip, deposition of κ-casein solutions using a microarray spotter equipped with a solid pin of 375-μm diameter through contact printing of multiple overlapping spots was applied. To optimize the on-chip probe immobilization using the aforementioned microarray spotter, we first analyzed with TOF-SIMS areas spotted on planar APTES-modified $Si_3N_4$ surfaces with κ-casein solutions of concentration ranging from 5 to 200 μg/mL.

#### 3.1.1. Chemical maps of immobilized probe

The distribution of immobilized κ-casein is visualized, as shown in Fig. 3a, by TOF-SIMS chemical map over an area of $6 \times 6\ mm^2$ recorded with secondary ions $C_5H_{12}N^+$ ($m/z = 86.10$) that are characteristic for protein fragments (in particular the amino acids: leucine and isoleucine) [30]. Separate rectangular protein domains, formed by contact printing arrays of $4 \times 11$ overlapping spots with a spot-to-spot distance of 200 μm (smaller than the nominal diameter of 375 μm of a round solid pin) are visible. Protein distribution develops as the concentration of κ-casein solution used for spotting increases. As shown individual spots merge

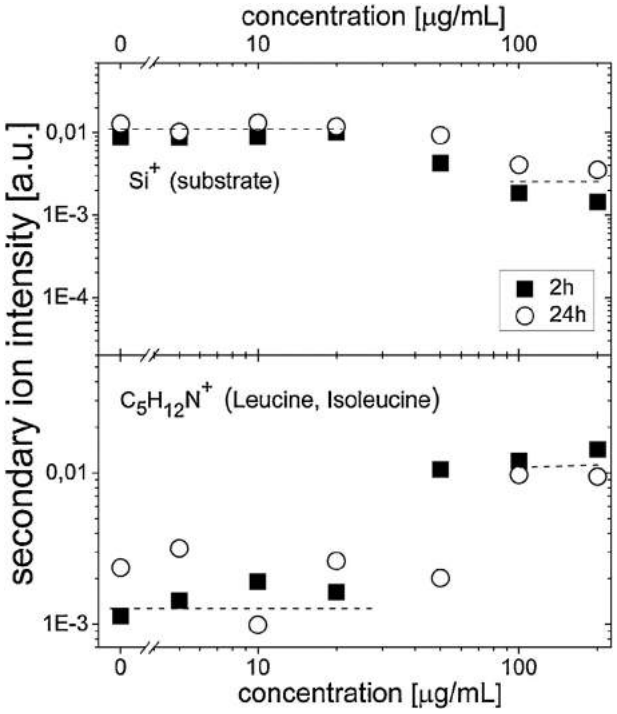


**Fig. 4.** Normalized TOF-SIMS intensities of secondary ions, $Si^+$, representative for $Si_3N_4$ substrate, and $C_5H_{12}N^+$, characteristic for protein, determined for surfaces contact-printed with casein solutions of different concentration (5–200 μg/mL) and then incubated for 2 or 24 h. Effective surface coverage with proteins is concluded starting from κ-casein concentration of 100 μg/mL.

to form uniformly covered areas starting from spotting solution concentration $C_s$ = 100 μg/mL. This is accompanied by higher surface concentration of κ-casein and a moderate increase of spotted areas dimensions, from ~0.8 × 2.2 $mm^2$ for $C_s$ = 10 μg/mL, to ~1.0 × 2.5 $mm^2$ for $C_s$ = 200 μg/mL, reflecting an increase in spot size.

In Fig. 3b and c, the inner structure of rectangular κ-casein coated domains corresponding to four different concentrations, $C_s$, of κ-casein spotting solution is depicted in the TOF-SIMS chemical maps (from an area of 500 × 500 $\mu m^2$) recorded with secondary ions characteristic for the substrate ($Si^+$; $m/z$ = 27.98) and the protein molecules ($C_5H_{12}N^+$), respectively. In addition, black and white images representative of κ-casein distribution and computed based on a published integral geometry analysis procedure [40,41] are provided in Fig. 3d. Individual spots with similar center-to-center distances and repeatable features are visible when solutions of κ-casein concentrations of 5, 20 and 50 μg/mL have been used for spotting. In particular, overlapping spots with clearly visible coffee-ring effect on the periphery and protein accumulation on the spot center in area corresponding to ~50% of the actual spot diameter can be observed. This inhomogeneous surface coverage with proteins, observed on micrometer scale, is reduced as the spotting solution concentration $C_s$ increases, and homogeneous coverage is achieved starting from κ-casein concentration of 100 μg/mL in the spotting solution.

### 3.1.2. Molecular characterization of biofunctionalized surfaces

The effect of κ-casein concentration in the spotting solution to the intensities of secondary ions $C_5H_{12}N^+$ and $Si^+$, normalized to the sum of all signals, are presented to Fig. 4. These signals reflect the relative content of the spotted surface in protein and Si substrate, i.e., in other words the surface coverage with protein molecules. The dependence of protein and substrate signals on κ-casein concentration $C_s$ in the spotting solutions is anti-correlated, with the protein signal to increase as the spotting concentration is increased and the substrate signal to decrease. Saturation of relative protein content is achieved for $C_s$ = 100 μg/mL, reflecting uniform coverage. In addition, the relation of $C_s$ with both casein and silicon TOF-SIMS signals is similar for the two incubation times used for probe immobilization, $t_i$ = 2 h and 24 h. Thus, the optimum parameters for spotting through multiple contact printing of chip like surfaces determined are $C_s$ = 100 μg/mL and $t_i$ = 2 h.

Contact printing using solid pins is a well-established spot formation technique [42] based on retention of solution quantities of a few nanoliters on the solid pin head which are then transferred by contact onto the substrate [43]. Contact radius of deposited droplet increases as the liquid surface tension decreases [44]. Also, it increases with increasing the liquid viscosity [44,45] or the substrate wettability [45,46]. Since viscosity of κ-casein solution increases with concentration $C_s$ [47], this explains the spot size increase with $C_s$, as deduced from Fig. 3. This effect originates also from the decrease in surface tension of κ-casein solutions [48,49] as the concentration increases up to the critical micelle concentration (~0.5 mg/mL for κ-casein [49]) and in accordance to the amphiphilic character of this protein [50].

Spot morphology reflects deposition and adsorption of biomolecules, that is greatly influenced by the evaporation of nanoliter droplet, which could follow either a pure evaporation mode or a sequence of two modes [51,52]. The first mode, with constant contact area and decreasing angle at pinned contact line, is typical for hydrophilic substrates resulting in 'coffee' ring stains [51–53]. The second mode, with constant angle of de-pinned contact line and decreasing contact area prevails on hydrophobic surfaces yielding peak-shaped spots [51,52]. The rings visible in spots depicted in Fig. 3c and d, printed on the APTES-modified surfaces with intermediate energy [54] using the solutions $C_s$ = 5, 20 and 50 μg/mL, reflect the 'coffee' stains of proteins accumulated by the outward flow of solution compensating its evaporation at the pinned contact line. As the evaporation process evolved, the depleted protein concentration could rise again for decreased contract area, resulting in pronounced spot centers. Such scenarios concerning individual spots are completed by additional features, such as coalescence, resulting from multiple droplet deposition. Still, the behavior of individual spots is decisive. κ-Casein solutions with increasing concentration $C_s$ yield droplets of higher wettability and lead to higher protein adsorption. Both factors result in more uniform overlapping spots, yielding homogeneous coverage starting from $C_s$ = 100 μg/mL, as confirmed by micro-analysis results averaged over millimeter surface areas (Fig. 4).

### 3.2. Imaging and molecular characterization of BB-MZI sensing arm areas

Changes in the structure and molecular content of integrated BB-MZIs sensing arm areas after each consecutive functionalization and affinity assay step are also studied with TOF-SIMS and supplemented by AFM and XPS examination of the respective planar surfaces. Resolution into molecular surface constituents is enabled by TOF-SIMS, yielding characteristic ion fragments of substrate, protein (amino acids) and milk (DiAcylGlycerols, Fatty Acids). These secondary ions are listed in Tables S1 and S2 of Supplementary material. In addition, ion fragments of amino acids with uniquely high abundance for each particular protein employed in the coating, blocking and assay procedures are used for its detection (see Table 1 for proteins amino acid composition).

### 3.2.1. Imaging of chip sensing areas with TOF-SIMS

Direct inspection of sensing arm areas of on-chip integrated BB-MZIs after functionalization/reaction steps (cf. Fig. 2 for notation) is provided in Fig. 5. The sensing arm windows are easily resolved

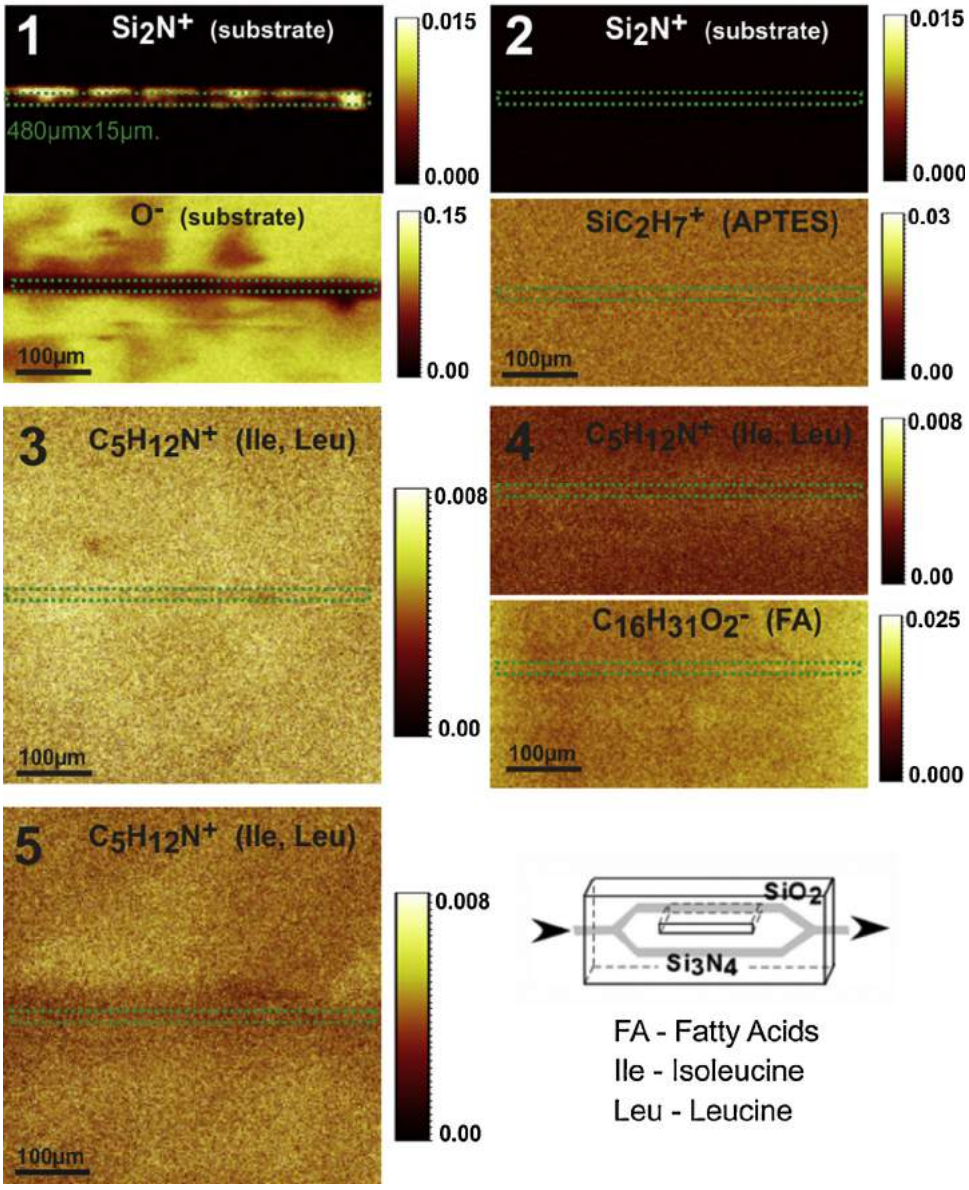


**Fig. 5.** Representative TOF-SIMS chemical images of the sensing arm areas of on-chip integrated Mach-Zehnder interferometers prior to any modification **(1)**, after modification with APTES **(2)**, immobilization of κ-casein by spotting **(3)**, blocking with diluted goat milk **(4)**, affinity binding of anti-κ-casein Mabs **(5)**. The images were recorded with the ions characteristic for exposed $Si_3N_4$ waveguide ($Si_2N^+$), cladding layer $SiO_2$ ($O^-$), APTES ($SiC_2H_7^+$), protein ($C_5H_{12}N^+$ ions from Ile, Leu) and goat milk ($C_{16}H_{31}O_2^-$ from FA). Regions inside the windows subjected to micro-analysis are marked with dashed lines.

on the maps determined with the sum of all secondary ions (not shown). The strong chemical contrast (signals $Si_2N^+$, $m/z = 69.97$ vs. $O^-$, $m/z = 16.00$) between the exposed $Si_3N_4$ waveguide area ($20 \times 600\ \mu m^2$ regions) and the surrounding $SiO_2$ cladding layer is visible for the chip surface prior to any modification **(1).** It is lost after uniform surface modification **(2)** with amino-silane nanolayer ($SiC_2H_7^+$; $m/z = 59.03$), as the nanolayer thickness is similar to the mean attenuation depth $\lambda_{SIMS}$ of secondary ion emission in organic films (1–1.5 nm for Si+, reduced for larger secondary ions) [27,28]. A homogeneous layer of immobilized probe **(3)** is then formed by multiple overlapping spots of κ-casein (here applied from the solution with $C_s$ concentration of 200 µg/mL), visualized with $C_5H_{12}N^+$ ions (from Leu and Ile) characteristic for all proteins (see Table 1). This spatially uniform protein signal is reduced after blocking **(4)** with goat milk ($C_{16}H_{31}O_2^-$, $m/z = 255.24$ from FA), apparently covering or partially removing immobilized κ-casein, whereas the laterally homogeneous protein presence in the outermost top regions of organic overlayer is recovered after binding **(5)** of Mabs to immobilized κ-casein. This specificity of the Mabs binding to the immobilized κ-casein is confirmed by the responses of BB-MZI sensors spotted with κ-casein as well as with BSA (non-specific binding), as shown in Section 3.4 and Fig. 10. Furthermore, the specificity is indicated from the fact that the sensor response increases as the concentration, $C_s$, of κ-casein in the spotting solution is increased.

### *3.2.2. Nanostructure determined through AFM and XPS inspection of planar surfaces*

Organic layers, that are uniform on TOF-SIMS micrographs, reveal their inner nanostructure when examined with AFM (Fig. 6a). The lateral nanostructure is characterized by the mean size of surface feature, 2whm (Fig. 6b), determined from a radial averaged autocorrelation function computed for an AFM micrograph. In turn, vertical nanostructure is specified using the parameters of height distribution in an AFM image, such as average height, <h> (Fig. 6c) or surface roughness, RMS (see Fig. S2 of Supplementary material). In

**Table 1**
Protein amino acid compositions for κ-casein[1] and Mabs[2].

| Amino acid | Composition | | |
|---|---|---|---|
| | κ-casein (%) | Mabs (%) | ratio of Mabs/κ-casein |
| Gly | 1.18 | 6.5 | 5.5 |
| *Ala* | *8.28* | *3.4* | *0.4* |
| Val | 6.51 | 8.97 | 1.4 |
| Leu | 4.73 | 5.88 | 1.2 |
| *Ile* | *7.10* | *3.4* | *0.5* |
| *Pro* | *11.83* | *6.81* | *0.6* |
| Ser | 7.69 | 12.4 | 1.6 |
| Thr | 8.88 | 8.66 | 1 |
| Cys | 1.18 | 2.63 | 2.2 |
| Met | 1.18 | 2.01 | 1.7 |
| Phe | 2.37 | 3.09 | 1.3 |
| Tyr | 5.33 | 4.95 | 0.9 |
| Trp | 0.59 | 2.01 | 3.4 |
| Asp | 2.37 | 4.25 | 1.8 |
| Asn | 4.73 | 5.26 | 1.1 |
| Glu | 7.10 | 4.8 | 0.7 |
| *Gln* | *8.88* | *3.71* | *0.4* |
| Lys | 5.33 | 6.03 | 1.1 |
| Arg | 2.96 | 3.25 | 1.1 |
| His | 1.78 | 2.01 | 1.1 |

[1][61], [2]Murine antibody data [32] were taken as representative for unknown composition of the used Mabs.

addition, the XPS thickness D of organic nanofilms (Fig. 6d) is evaluated from effective attenuation of substrate Si 2p photoelectrons using the angle-resolved XPS data. Such data are collected for mean vertical depth of electron escape, $\lambda_{XPS}\cos\theta$, with $\lambda_{XPS}$ = 3.2 nm for Si 2p [55], modified by photoelectron take-off angle θ [29,55]. The procedures to extract nanostructure parameters from AFM [22,33] and ARXPS [33–35] are described in previous publications [22,33–35]. Outline and parameters of the model applied to analyze the ARXPS data are presented in Section S5 of Supplementary material.

Surface nanostructures and their parameters (Fig. 6) can be summarized as follows: Modification of $Si_3N_4$ surfaces with APTES **(2′)** yields flat monomolecular amino-silane layers, characterized by <h> [35], D [22,23] and RMS [35] values similar to those reported in the literature [22,23,35]. Distinct nanostructures result from multiple spotting of goat milk diluted in buffer **(r4)**, solution of Mabs against κ-casein prepared in diluted goat milk **(r5)**, or κ-casein solution **(3′)**. The reference sample **(r4)** reveals relatively thick (D > 9.7 nm [55]) milk layer with large surface features (2whm = 28.6 nm), reflecting the multiple milk components. In turn, the reference sample **(r5)** consists of a much thinner organic overlayer with reduced surface features, similar in size to those reported (2whm = 16 nm [22]) for adsorbed gamma globulins with molecular weight $M_W$ of 150 kDa and dimensions 14.5 × 8.5 × 4 $nm^3$ [56]. Although the κ-casein monomer with

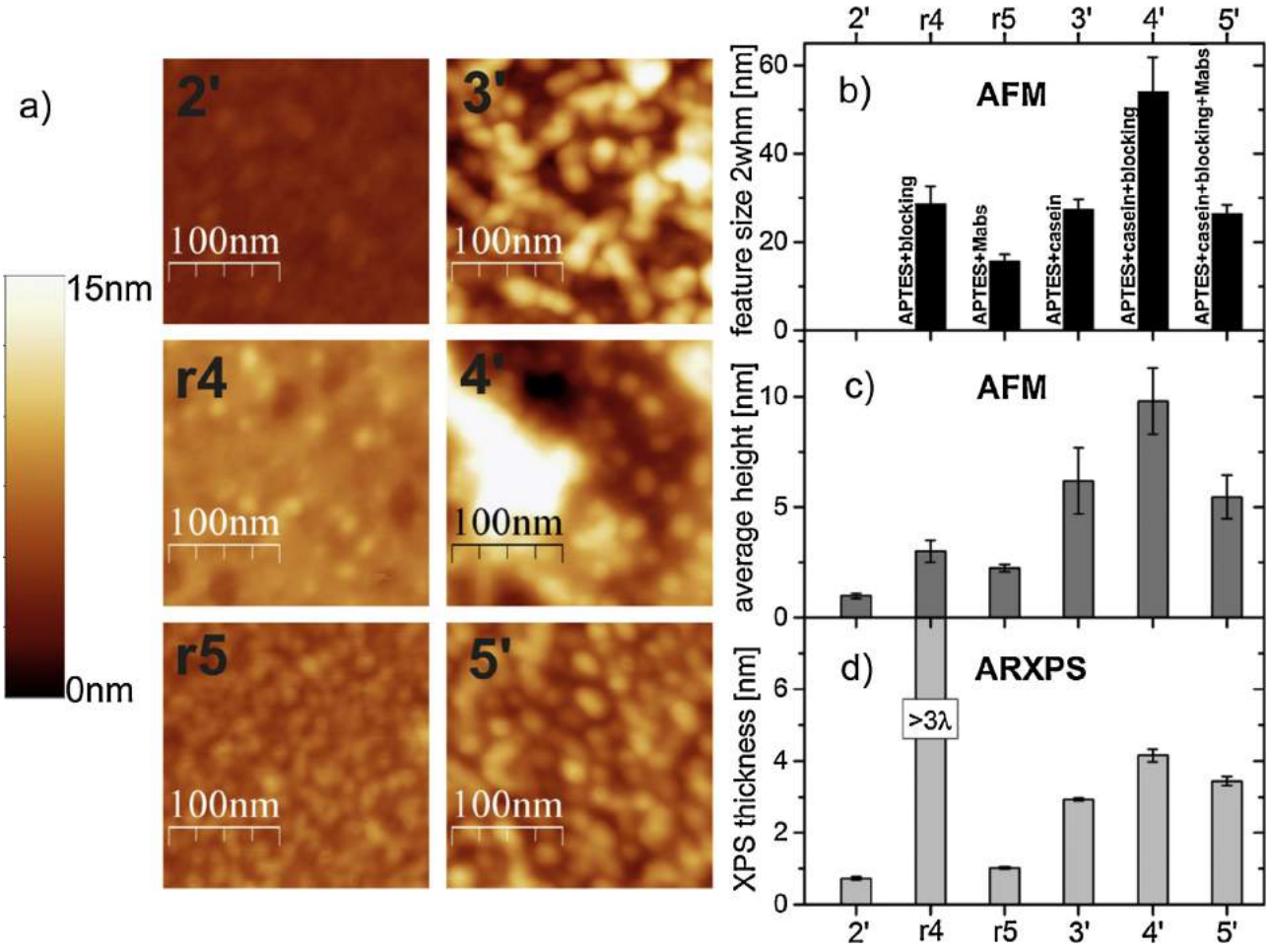


**Fig. 6.** AFM and XPS surface characterization of planar $Si_3N_4$ surfaces corresponding to consecutive functionalization, coating, blocking, and immunoreaction steps **(2'-5')** as well as to reference samples **(r4, r5)**. Representative topographic AFM micrographs (a) and nanostructure parameters (b–d). (b) Size of surface features 2whm computed from AFM topographic images. (c) Average height <h> determined from AFM histograms. (d) XPS thickness D of organic overlayer, describing effective attenuation of Si 2p core-level photoelectrons. For the sample r4, D > 3λ, XPS sampling depth ~9.7 nm. Error bars correspond to Standard Deviation values determined form 5 measurements on the same surface.

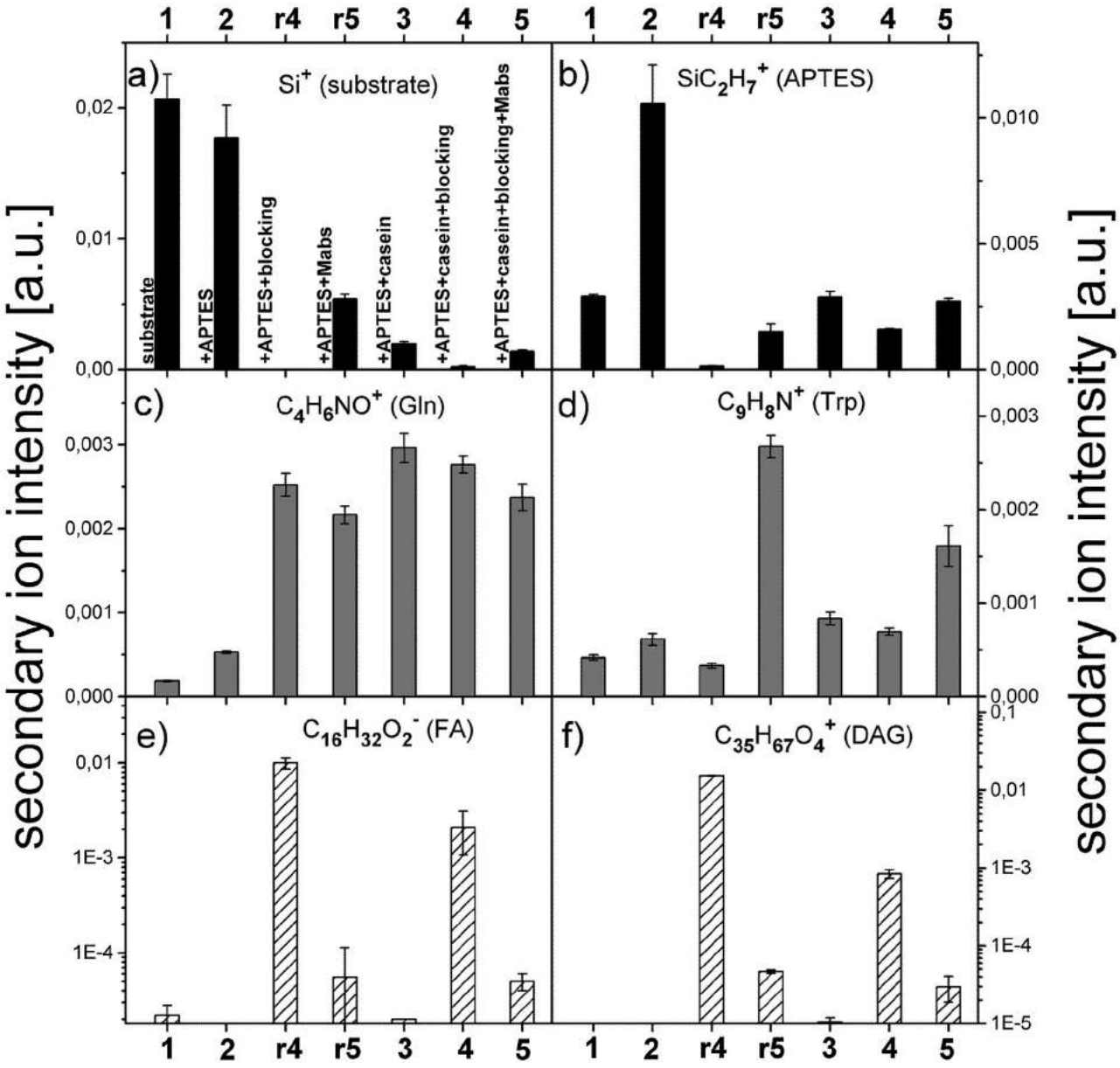


**Fig. 7.** TOF-SIMS analysis of multi-molecular layers formed on the sensing arm areas of the chip **(1–5)** as well as of reference planar surfaces **(r4, r5)** spotted with blocking solution (diluted goat milk) or Mabs solution. Normalized intensities of characteristic TOF-SIMS signals reflect (a) total organic coverage (anti-correlated with the intensity of substrate $Si^+$ ions), (b) formation of amino-silane film ($SiC_2H_7^+$ from APTES) and its coverage with (c) κ-casein ($C_4H_6NO^+$ from Gln), (d) Mabs ($C_9H_8N^+$ from Trp), or with (e) fatty acids ($C_{16}H_{32}O_2^-$) and (f) diacylglycerols ($C_{35}H_{67}O_4^+$) present in milk.

$M_W$ = 19 kDa and size of 7.4 nm [57] is smaller than gamma globulins, the surface **(3′)** exhibits lateral (2whm = 27.4 nm) and vertical (D and <h>) nanostructural parameters that are significantly larger than those formed by Mabs **(r5)**. Therefore, the overlayer observed for the sample **(3′)** must be formed by self-associated κ-casein molecules. Indeed, native κ-casein contains a series of polymers (mainly dimers to octamers) [58]. Also, κ-casein purified from bovine milk exists as a high molecular weight ($M_W \sim 1.18$ MDa) spherical complex with 19.2 nm size, prone to even higher degree of aggregation [58]. The difference in XPS thickness D (see Fig. 6d) between the samples **(3′)** and **(2′)** allows for the estimation of κ-casein surface density, using the protein mass density (1.37 g/cm$^3$) as a scaling factor [22,23,33,35]. The value calculated, 3.01 mg/m$^2$, is relatively high when compared with 6.8 mg/m$^2$, expected for the high $M_W$ complex of κ-casein [58]. This suggests surface coverage $\theta \sim 44\%$ not far from the predicted surface saturation value, $\theta_{sat}$ = 54% [59]. This result is a further indication of effective κ-casein immobilization.

Blocking with diluted milk **(4′)** of free surface sites, after κ-casein immobilization, results (see Fig. 6a) in patchy coverage of immobilized κ-casein layer with milk components (see also Fig. S3). The extremely large surface features and height variation are reflected by larger structural parameters (Fig. 6b–d). Subsequent affinity binding **(5′)** due to exposure to Mabs solution changes completely the overlayer topography, with the parameters 2whm, <h> and RMS reduced at least by one half as compared to the preceding step **(4′)**. This reduction resembles that discussed for the surface **(r4)** exchanged with **(r5)**, and indicates substantial milk removal. Apparently, adsorption or binding of proteins increases both the surface energy (to the values higher [60] than 32 mJ/m$^2$, specific for APTES [54]) and its hydrophilicity, repelling hydrophobic milk components. Finally, the parameters 2whm and <h> for sample **(5′)** are equal to the values for sample **(3′)**, indicating topography

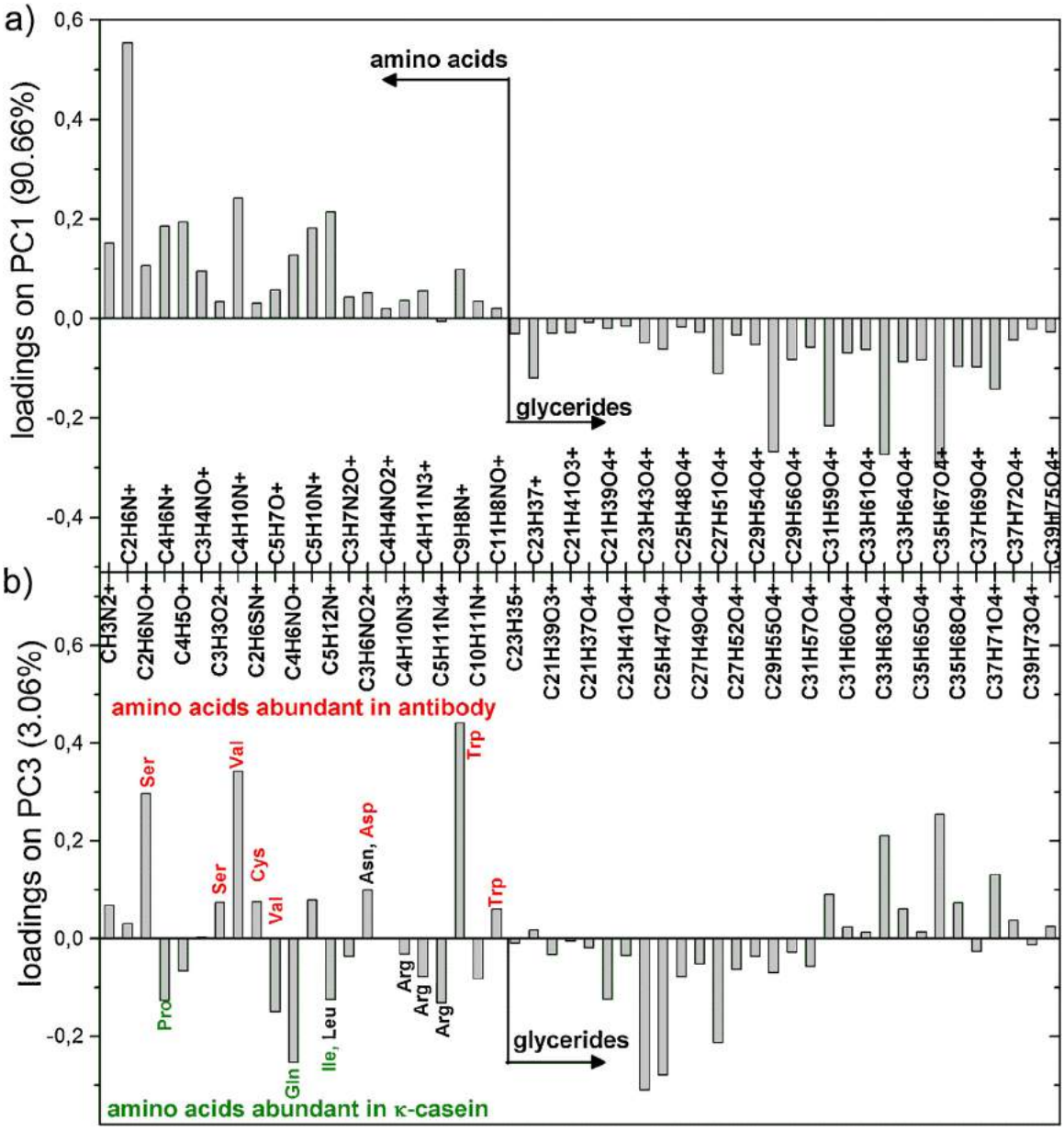


**Fig. 8.** PCA loading plots for the first (PC1) (a) and the third principal component (PC3) (b), showing the positive biomolecular fragments derived from TOF-SIMS analysis of on-chip sensing arm areas **(3–5)** and planar reference surfaces **(3′, r4, r5)**. Please note, that amino acid fractions (with $m/z < 171$) and glyceride fragments (with $m/z > 310$) load the PC1 in the positive and negative direction, respectively. Also, the fragments of amino acids that are abundant (cf. Table 1) in antibodies (Trp, Ser, Val, Asp, Cys) and in κ-casein (Gln, Pro, Ile) load the PC3 in the positive and negative direction, respectively.

dominated again by self-associated κ-caseins. In addition, smaller surface features visible in AFM micrograph **(5′)** (see Fig. 6a) might reflect Mabs molecules. The determined by XPS thickness D of the organic overlayer yields (after APTES value deduction) a protein surface density close to 3.71 mg/m$^2$. This value is 23% higher as compared to that for immobilized κ-casein.

### 3.2.3. Molecular TOF-SIMS characterization of chip sensing arm areas

The relative surface content in substrate and the different molecules employed in the chemical activation, biofunctionalization and immunoreaction procedure **(1–5)** is evaluated in Fig. 7. The normalized intensity of characteristic TOF-SIMS signals (listed in Tables S1 and S2 of Supplementary material) reflects formation of amino-silane film and its coverage with the proteins (κ-casein and Mabs) and milk components (represented by glycerides). In addition, Fig. 7 shows the results for reference planar samples **(r4–r5)** that confirm the specificity of some TOF-SIMS signals for goat milk, κ-casein and Mabs, when combined with the results from sample **(3)**. Negative ion fragments of Fatty Acids, e.g. $C_{16}H_{32}O_2^-$ ($m/z = 256.24$) (Fig. 7e), and positive ions from DiAcylGlyerols, e.g. $C_{35}H_{67}O_4^+$ ($m/z = 551.56$) (Fig. 7f), deduced as derived from glycerides, are indeed the most intense signals for the milk coated sample **(r4)**. In turn, ion fragments of glutamine ($C_4H_6NO^+$, $m/z = 84.05$, Gln) and tryptophan ($C_9H_8N^+$, $m/z = 130.17$, Trp), the amino acids with uniquely high abundance in κ-casein (8.88% Gln, 0.59% Trp) and antibodies (3.71% Gln, 2.01% Trp), are deduced (see Table 1) as characteristic for these two proteins. Indeed, these ion fragments of Gln (Fig. 7c) and Trp (Fig. 7d) are the most intense TOF-SIMS signals for the samples coated with κ-casein **(3)** and Mabs **(r5)**, respectively.

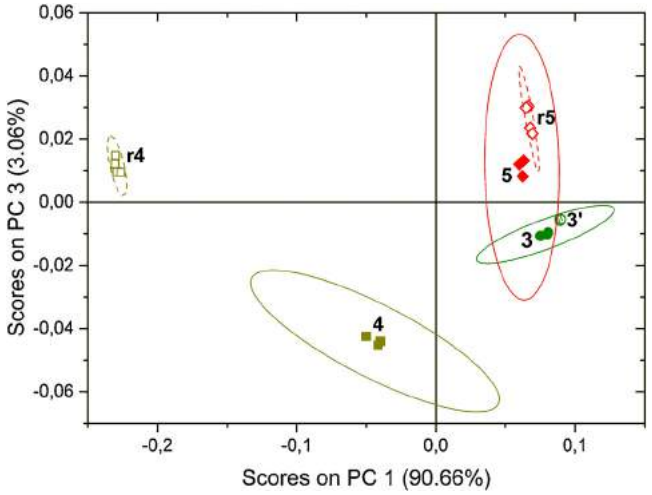


**Fig. 9.** PC1 vs. PC3 scores plot visualizes and classifies the step-by-step modifications of the chip sensing arm areas **(3, 4, 5)**, as compared to the differences between the respective planar reference surfaces **(3′, r4, r5)**. Grouped data points, marked with different symbols, correspond to the positive ion TOF-SIMS spectra. The ellipses drawn around each of the groups (solid lines for the biosensor surfaces and dashed lines of the references) represent the 95% confidence limit.

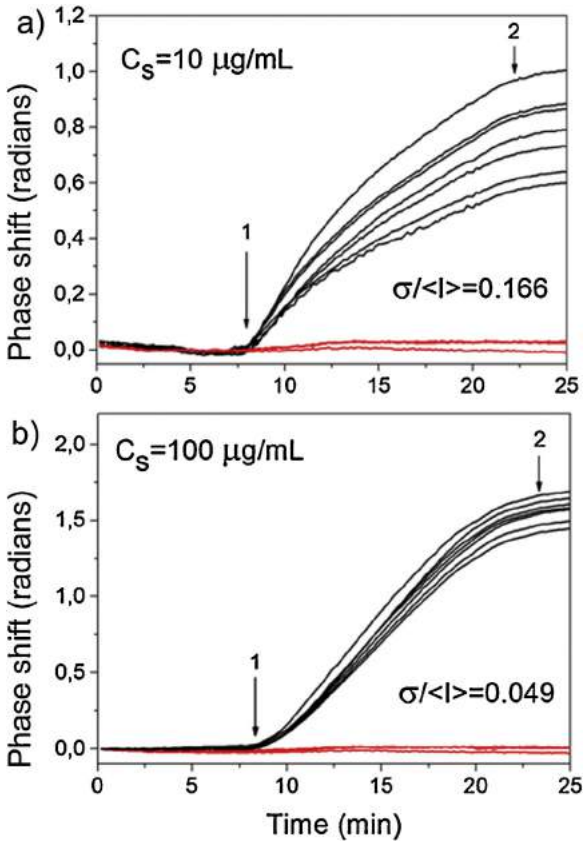


**Fig. 10.** Output phase shifts obtained from chips functionalized with 10 (a) or 100 µg/ml κ-casein (b). 7 out of 10 BB-MZIs of each chip were functionalized with κ-casein (black lines) and the rest 3 with the respective concentrations of BSA (red lines). Start to arrow 1: 100-times diluted goat milk in assay buffer; arrow 1 to 2: 100-times diluted goat milk containing the anti-κ-casein antibodies (1 µg/ml each); arrow 2 to end: 100-times diluted goat milk in assay buffer. (For interpretation of the references to colour in this figure legend, the reader is referred to the web version of this article.)

Since the TOF-SIMS intensities might be affected by several factors (contaminations from buffers, matrix substrate-induced effects, not fully resolved mechanism of ion formation), the conclusions drawn from an empirical comparison of single TOF-SIMS signals cannot be without reservations. Therefore we restrict ourselves to a qualitative rather than a quantitative sample-to-sample analysis of the results shown in Fig. 7. The signals characteristic for the substrate ($Si^+$) and APTES ($SiC_2H_7^+$) confirm (see Fig. 7a,b) effective silanization of chip sensing arm areas **(2)**. In addition, for all the samples **(2–5, r4, r5)** both TOF-SIMS signals anti-correlate with the determined by XPS thickness D of organic overlayer (cf. Fig. 6d). This is expected, since attenuation of both secondary ions and photoelectrons, emitted from the substrate, is described by an exponential function of organic layer thickness, although with different mean attenuation depths (the ratio $\lambda_{XPS}(Si\ 2p)/\lambda_{SIMS}$ is 1.9 for $Si^+$ but increases for larger secondary ions) [28]. Successive immobilization of κ-casein **(3)** is confirmed by reduced substrate signals and maximum intensity of the Gln ion fragments ($C_4H_6NO^+$) (Fig. 7c). Blocking with milk **(4)** is reflected by high signals ($C_{16}H_{32}O_2^-$, $C_{35}H_{67}O_4^+$) characteristic for glycerides (FA, DAG) (Fig. 7e,f). However, both are less intense than for **(r4)**, suggesting moderate coverage with milk of the surfaces already functionalized with κ-casein **(4)**. This might explain the somewhat diminished intensity of the Gln ion fragments ($C_4H_6NO^+$) as compared with **(3)** which however is higher than that received from **(r4)** (due to goat milk proteins). Subsequent exposure of sensing arm areas to solution of monoclonal antibodies prepared in diluted goat milk **(5)** results not only in effective affinity binding, confirmed by Trp ion fragments ($C_9H_8N^+$) from Mabs (Fig. 7d), but also in nearly complete removal of glycerides characteristic for milk coverage (Fig. 7e,f). This is not accompanied by any increase of the Gln signal characteristic for κ-casein **(5)**, reflecting its partial removal as compared to **(3).** Also, no build-up of signals from amino acids characteristic for BSA, the molecule added to Mabs solution to suppress non-specific binding (see Section 2.2), such as cysteine (signal $C_2H_6SN^+$, $m/z = 76.03$; with 6.0, 1.2 and 2.6% composition in BSA, κ-casein and Mabs, respectively) and glutamic acid ($C_4H_8NO_2^+$, $m/z = 102.06$; 10.1, 7.1 and 4.8%) is observed (not shown) for sample **(5)**.

### 3.3. Compositional multivariate TOF-SIMS analysis of functionalized chip sensing arm areas

To enhance detection of subtle differences in biomolecular composition of the sensing arm areas of the integrated on chips BB-MZIs between probe immobilization **(3)**, blocking **(4)** and immunoreaction step **(5)**, as compared to those between the respective planar references samples **(3′, r4, r5)**, Principal Component Analysis is applied on a set of 52 TOF-SIMS signals originating only from biomolecules. The corresponding positive ion fragments, unique for amino acids (22 signals) and milk glycerides (30 signals), are listed in Fig. 8. They are examined for 21 TOF-SIMS spectra from 6 analyzed samples. The performed multivariate analysis reveals the directions of uncorrelated major variations within this data set, so called Principal Components. The first PC captures the majority of the variance in the data (90.66%), and clearly distinguishes (see Fig. 8a) between glycerides (negative loadings) and protein amino acids (positive loadings). In addition, the third PC (3.06% of the variance) identifies the difference (see Fig. 8b) between amino acids abundant in Mabs (tryptophan, serine, valine and aspartic acid; cf. Table 1), yielding positive loadings, and those characteristic for κ-casein (glutamine, proline and isoleucine; cf. Table 1), providing negative loadings. Also, PC3 distinguishes between the glycerides fragments with $m/z < 494$ (negative loadings) and $m/z > 494$ (positive loadings).

Differences in the biomolecular surface compositions are expressed by the PC1 vs. PC3 scores plot (Fig. 9) on which the TOF-SIMS results acquired from different samples (points marked with different symbols) form six groups. The scores plot yields a direct method for visualization and classification of the step-by-step modifications of biosensor surfaces **(3, 4, 5)**, as compared to the differences between the respective planar references **(3′, r4, r5)**. The latter consist of the samples composed exclusively of goat milk **(r4)** and proteins: κ-casein **(3′)** and Mabs **(r5)**.

The results (Fig. 9) received from the analysis of the modified with κ-casein sensing arm areas of the integrated BB-MZIs **(3)** are similar to those for planar surfaces **(3′)**, with negative PC3 coordinate confirming proper probe functionalization. Sensing areas blocked with goat milk **(4)** have negative PC1 score values, distinct from that obtained for references **(r4)**, confirming moderate coverage with milk glycerides. In addition, they show negative PC3 coordinate with high magnitude that might indicate, in addition to κ-casein presence, also the mass distribution of milk glycerides different than in **(r4)**. Finally, the integrated BB-MZIs sensing arm areas after exposure to Mabs solution **(5)** have a PC1 coordinate similar to that of **(3)**, indicating effective removal of milk glycerides from the surfaces. Last but not least, their positive PC3 value is close to this for the reference **(r5)** but not much different from that for **(3′)** (see the ellipse of 95% confidence limit). This confirms effective affinity binding of Mabs to immobilized κ-casein more clearly than the comparison based on single TOF-SIMS signals (Fig. 7d).

### *3.4. Effect of spotting solution concentration on repeatability of biosensor signal*

The validity of the findings made by analyzing the sensing arm areas on integrated BB-MZI sensors (and corresponding planar surfaces) through TOF-SIMS towards optimization of the sensor biofunctionalization was evaluated through immunodetection of κ-casein in real-time with the integrated BB-MZIs sensors. For this purpose, 7 out of 10 BB-MZIs of chips were spotted with κ-casein solutions with $C_s$ concentrations of 10 or 100 μg/mL. The rest 3 BB-MZIs of each chip were spotted with the respective concentrations of BSA to serve as blanks. The chips were tested following the immunoassay protocol described in Section 2.7. In Fig. 10, real-time responses obtained by running a mixture of the antibodies with the zero calibrator (maximum signal) over a chip spotted with a 10 μg/mL κ-casein solution (Fig. 10a) or another one spotted with a 100 μg/mL κ-casein solution (Fig. 10b) are provided. As it can be concluded from the graphs, the sensor responded immediately after the introduction of the antibodies/zero calibrator mixture allowing real-time signal monitoring. It should be noted, that only the 7 out of 10 BB-MZIs that were spotted with κ-casein responded, whereas the 3 blank BB-MZIs did not provide any measurable response. Concerning the effect of κ-casein concentration used for coating of BB-MZIs on the variation of the signals recorded from the different sensors on the same chip, it was found that the variation was drastically reduced when a spotting concentration $C_s$ of 100 μg/mL was used instead of 10 μg/mL. The standard deviation-to-mean ratio of sensor signals calculated from chips spotted with 10 and 100 μg/mL of κ-casein were 0.166 and 0.049, respectively.

In Fig. S4 (see Supplementary material), bovine κ-casein calibration curves obtained with chips spotted either with 10 μg/mL (closed circles) or 100 μg/mL κ-casein solution (closed squares) are presented. The coefficients of the variation calculated over the range of the calibrators used ranged between 14.0 to 18.6% for the chips spotted with the 10 μg/mL κ-casein solution and between 3.2 to 4.9% for the chips spotted with the 100 μg/mL κ-casein solution. This reduction of signal variation had an enormous impact on the detection limit of the assay. Taking into account that the limit of detection is calculated as the analyte concentration corresponding to mean zero calibrator signal value −3SD, it was found that the limit of detection was reduced from 310 ng/mL calculated for chips spotted with 10 μg/mL to 63 ng/mL obtained with chips spotted with 100 μg/mL of κ-casein. Thus, a 5-fold improvement in assay detection sensitivity was achieved by optimizing the spotting concentration of bovine κ-casein. These results support the validity and usefulness of TOF-SIMS analysis in the process of optimization of sensor biofunctionalization.

## 4. Conclusions

TOF-SIMS imaging and micro-analysis was used to examine the protein surface patterns formed with a microarray spotter onto the sensing arm windows of integrated on silicon chips Mach-Zehnder interferometer arrays aiming to determination of bovine κ-casein in goat milk. Contrary to previous spectroscopic and microscopic studies, that examine step-by-step planar silicon surfaces, this work demonstrated a direct imaging and chemical TOF-SIMS inspection of sensing arm areas of Mach-Zehnder interferometers integrated on silicon chips after each step employed for probe immobilization and immunoassay performance including blocking with diluted full fat goat milk, a complex material. To maximize information of subtle differences in surface chemistry induced by the biofunctionalization and immunoassay procedure multivariate method of Principal Component Analysis was applied to TOF-SIMS data obtained from the analysis of sensing arm areas of integrated on silicon chip Mach-Zehnder interferometers. It was shown that principal components could clearly distinguish the biomolecules employed in the consecutive surface modification/immunoreaction steps, i.e., protein amino acids from milk glycerides, as well as, amino acids abundant in κ-casein from those characteristic for Mabs. All the individual molecular components used in the multi-step functionalization procedure of sensing arm areas were well discriminated by the different mass-resolved TOF-SIMS signals characteristic for amino-silane, κ-casein, milk glycerides, and Mabs. In addition, the nanostructure of molecular layers formed consecutively onto top of silicon chips was evaluated form the results received by AFM and ARXPS on planar surfaces, since both techniques cannot examine directly the trench-like geometry of chip sensing regions. The study concluded that a uniform but nanostructured overlayer of adsorbed protein probes characterized by self-associated rather than monomer κ-casein molecules with fractional coverage not far from reaching surface saturation with protein molecules is formed on an homogeneous amino-silane monolayer. Additional patchy coverage with goat milk components is obtained during blocking. Finally, exposure to Mabs solution leads to their binding onto the surface immobilized probe and promotes higher protein surface coverage, which repels hydrophobic milk components. Coexistence of Mabs and κ-casein on this final surface as well as partial desorption of the latter was concluded. Following the optimized conditions determined, the repeatability of the responses obtained for the sensors on the same chip was considerably improved with significant reduction of standard variation to mean signal value ratio and dramatic improvement of bovine κ-casein detection sensitivity with the sensor. Taking it overall, the complementary surface science methods are able to reveal the complex picture of step-by-step modifications of biosensor surfaces and to support optimization of surface biomolecule immobilization processes.

## Acknowledgments

This work was supported by the EU funded project “FOOD-SNIFFER” (FP7-ICT8-318319) and sponsored from the Polish state funds for science in the years 2014–15 granted for the realization

of co-financed international project. One of us (K.G.) is grateful for financial support from the M. Smoluchowski Kraków Research Consortium (in the framework of the KNOW scholarship).

## Appendix A. Supplementary data

Supplementary data associated with this article can be found, in the online version, at http://dx.doi.org/10.1016/j.apsusc.2016.05.131.

## References

[1] N.D. Oliver, C. Toumazou, A.E. Cass, D.G. Johnston, Glucose sensors: a review of current and emerging technology, Diabet. Med. 26 (2009) 197–210.
[2] C.I.L. Justino, T.A. Rocha-Santos, A.C. Duarte, Review of analytical figures of merit of sensors and biosensors in clinical applications, Trends Anal. Chem. 29 (2010) 1172–1183.
[3] I.B. Tahirbegi, M. Mir, S. Schostek, M. Schurr, J. Samitier, In vivo ischemia monitoring array for endoscopic surgery, Biosens. Bioelectron. 61 (2014) 124–130.
[4] R. Pilolli, L. Monaci, A. Visconti, Advances in biosensor development based on integrating nanotechnology and applied to food-allergen management, Trends Anal. Chem. 47 (2013) 12–26.
[5] G. Klenkar, B. Liedberg, A microarray chip for label-free detection of narcotics, Anal. Bioanal. Chem. 391 (2008) 1679–1688.
[6] P. Kozma, F. Kehl, E. Ehrentreich-Förster, C. Stamm, F.F. Bier, Integrated planar optical waveguide interferometer biosensors: a comparative review, Biosens. Bioelectron. 58 (2014) 287–307.
[7] G. Gauglitz, Point-of-care platforms, Annu. Rev. Anal. Chem. 7 (2014) 297–315.
[8] D. Duval, A.B. González-Guerrero, S. Dante, C. Domínguez, L.M. Lechuga, Interferometric waveguide biosensors based on Si-technology for point-of-care diagnostic, Proc. SPIE 8431 (2012) 84310P–84311.
[9] X. Fan, I.M. White, S.I. Shopova, H. Zhu, J.D. Suter, Y. Sun, Sensitive optical biosensors for unlabeled targets: a review, Anal. Chim. Acta 620 (2008) 8–26.
[10] M. Vala, K. Chadt, M. Piliarik, J. Homola, High-performance compact SPR sensor for multi-analyte sensing, Sens. Actuators B 148 (2010) 544–549.
[11] R. Horváth, J. Vörös, R. Graf, G. Fricsovszky, M. Textor, L.R. Lindvold, N.D. Spencer, E. Papp, Effect of patterns and inhomogeneities on the surface of waveguides used for optical waveguide lightmode spectroscopy applications, Appl. Phys. B 72 (2001) 441–447.
[12] K. Misiakos, P.S. Petrou, S.E. Kakabakos, D. Yannoukakos, H. Contopanagos, T. Knoll, T. Velten, M. DeFazio, L. Schiavo, M. Passamano, D. Stamou, G. Nounesis, Fully integrated monolithic optoelectronic transducer for real-time protein and DNA detection: the NEMOSLAB approach, Biosens. Bioelectron. 26 (2010) 1528–1535.
[13] J. Dübendorfer, R.E. Kunz, G. Jobst, I. Moser, G. Urban, Integrated optical pH sensor using replicated chirped grating coupler sensor chips, Sens. Actuators B 50–53 (1998) 210–219.
[14] K. Zinoviev, L.G. Carrascosa, J. Sánchez del Río, B. Sepúlveda, C. Domínguez, L. Lechuga, Silicon photonic biosensors for lab-on-a-chip applications, Adv. Opt. Technol. 2008 (2008) 383927.
[15] L. Zhuang, W. Beeker, A. Leinse, R. Heideman, P. van Dijk, C. Roeloffzen, Novel wideband microwave polarization network using a fully-reconfigurable photonic waveguide interleaver with a two-ring resonator-assisted asymmetric Mach-Zehnder structure, Opt. Express 21 (2013) 3114–3124.
[16] K. Schmitt, B. Schirmer, C. Hoffmann, A. Brandenburg, P. Meyrueis, Interferometric biosensor based on planar optical waveguide sensor chips for label-free detection of surface bound bioreactions, Biosens. Bioelectron. 22 (2007) 2591–2597.
[17] J.T. Kindt, R.C. Bailey, Biomolecular analysis with microring resonators: applications in multiplexed diagnostics and interaction screening, Curr. Opin. Chem. Biol. 17 (2013) 818–826.
[18] M.K. Park, J.S. Kee, J.Y. Quah, V. Netto, J. Song, Q. Fang, E. Mouchel La Fosse, G.Q. Lo, Label-free aptamer sensor based on silicon microring resonators, Sens. Actuators B 176 (2013) 552–559.
[19] R. Tünnemann, M. Mehlmann, R.D. Süssmuth, B. Bühler, S. Pelzer, W. Wohlleben, H.P. Fiedler, K.H. Wiesmüller, G. Gauglitz, G. Jung, Optical biosensors. Monitoring studies of glycopeptide antibiotic fermentation using white light interference, Anal. Chem. 73 (2001) 4313–4318.
[20] P.S. Petrou, D. Ricklin, M. Zavali, I. Raptis, S.E. Kakabakos, K. Misiakos, J.D. Lambris, Real-time label-free detection of complement activation products in human serum by white light reflectance spectroscopy, Biosens. Bioelectron. 24 (2009) 3359–3364.
[21] F. Liu, M. Dubey, H. Takahashi, D.G. Castner, D.W. Grainger, Immobilized antibody orientation analysis using secondary ion mass spectrometry and fluorescence imaging of affinity-generated patterns, Anal. Chem. 82 (2010) 2947–2958.
[22] K. Awsiuk, A. Budkowski, P. Petrou, A. Bernasik, M.M. Marzec, S. Kakabakos, J. Rysz, I. Raptis, Model immunoassay on silicon surfaces: vertical and lateral nanostructure vs. protein coverage, Colloids Surf. B 103 (2013) 253–260.
[23] K. Awsiuk, A. Bernasik, M. Kitsara, A. Budkowski, P. Petrou, S. Kakabakos, S. Prauzner-Bechcicki, J. Rysz, I. Raptis, Spectroscopic and microscopic characterization of biosensor surfaces with protein/amino-organosilane/silicon structure, Colloids Surf. B 90 (2012) 159–168.
[24] K. Misiakos, I. Raptis, A. Salapatas, E. Makarona, A. Botsialas, M. Hoekman, R. Stoffer, G. Jobst, Broad-band Mach-Zehnder interferometers as high performance refractive index sensors: theory and monolithic implementation, Opt. Express 22 (2014) 8856–8870.
[25] K. Misiakos, I. Raptis, E. Makarona, A. Botsialas, A. Salapatas, P. Oikonomou, A. Psarouli, P.S. Petrou, S.E. Kakabakos, K. Tukkiniemi, M. Sopanen, G. Jobst, All-silicon monolithic Mach-Zehnder interferometer as a refractive index and biochemical sensor, Opt. Express 22 (2014) 26803–26813.
[26] K. Misiakos, S.E. Kakabakos, P.S. Petrou, H.H.A. Ruf, Monolithic silicon optoelectronic transducer as a real-time affinity biosensor, Anal. Chem. 76 (2004) 1366–1373.
[27] C.D. Tidwell, D.G. Castner, S.L. Golledge, B.D. Ratner, K. Meyer, B. Hagenhoff, A. Benninghoven, Static time-of-flight secondary ion mass spectrometry and X-ray photoelectron spectroscopy characterization of adsorbed albumin and fibronectin films, Surf. Interface Anal. 31 (2001) 724–733.
[28] A. Delcorte, P. Bertrand, X. Arys, A. Jonas, E. Wischerhoff, B. Mayer, A. Laschewsky, ToF-SIMS study of alternate polyelectrolyte thin films: chemical surface characterization and molecular secondary ions sampling depth, Surf. Sci. 366 (1996) 149–165.
[29] J.A. Mielczarski, J. Dong, E. Mielczarski, Real time evaluation of composition and structure of concanavalin a adsorbed on a polystyrene surface, J. Phys. Chem. B 112 (2008) 5228–5237.
[30] M.S. Wagner, D.G. Castner, Characterization of adsorbed protein films by time-of-flight ion mass spectrometry with principal component analysis, Langmuir 17 (2001) 4649–4660.
[31] C. Brüning, S. Hellweg, S. Dambach, D. Lipinsky, H.F. Arlinghaus, Improving the interpretation of ToF-SIMS measurements on adsorbed proteins using PCA, Surf. Interface Anal. 38 (2006) 191–193.
[32] F. Liu, M. Dubey, H. Takahashi, D.G. Castner, D.W. Grainger, Immobilized antibody orientation analysis using secondary ion mass spectrometry and fluorescence imaging of affinity-generated patterns, Anal. Chem. 82 (2010) 2947–2958.
[33] K. Gajos, P. Petrou, A. Budkowski, K. Awsiuk, A. Bernasik, K. Misiakos, J. Rysz, I. Raptis, S. Kakabakos, Imaging and spectroscopic comparison of multi-step methods to from DNA arrays based on the biotin-streptavidin system, Analyst 140 (2015) 1127–1139.
[34] K. Awsiuk, A. Budkowski, M.M. Marzec, P. Petrou, J. Rysz, A. Bernasik, Effects on polythiophene surface structure on adsorption and conformation of bovine serum albumin: a multivariate and multitechnique study, Langmuir 30 (2014) 13925–13933.
[35] K. Awsiuk, A. Budkowski, A. Psarouli, P. Petrou, A. Bernasik, S. Kakabakos, J. Rysz, I. Raptis, Protein adsorption and covalent bonding to silicon nitride surfaces modified with organo-silanes: comparison using AFM, angle-resolved XPS and multivariate ToF-SIMS analysis, Colloids Surf. B 110 (2013) 217–224.
[36] M.J. Bañuls, R. Puchades, Á. Maquieira, Chemical surface modifications for the development of silicon-based label-free integrated optical (IO) biosensors: a review, Anal. Chim. Acta 777 (2013) 1–16.
[37] J. Escorihuela, M.J. Bañuls, J.G. Castelló, V. Toccafondo, J. García-Rupérez, R. Puchades, Á. Maquieira, Chemical silicon surface modification and bioreceptor attachment to develop competitive integrated photonic biosensors, Anal. Bioanal. Chem. 404 (2012) 2831–2840.
[38] P. Furbert, C. Lu, N. Winograd, L. DeLouise, Label-free optical detection of peptide synthesis on a porous silicon scaffold/sensor, Langmuir 24 (2008) 2908–2915.
[39] I. Horcas, R. Fernandez, J.M. Gomez-Rodriguez, J. Colchero, J. Gomez-Herrero, A.M. Baro, WSXM: a software for scanning probe microscopy and a tool for nanotechnology, Rev. Sci. Instrum. 78 (2007) 013705.
[40] J. Raczkowska, J. Rysz, A. Budkowski, J. Lekki, M. Lekka, A. Bernasik, K. Kowalski, P. Czuba, Surface patterns in solvent-cast polymer blend films analyzed with an integral-geometry approach, Macromolecules 36 (2003) 2419–2427.
[41] J. Zemła, M. Lekka, J. Wiltowska-Zuber, A. Budkowski, J. Rysz, J. Raczkowska, Integral geometry analysis of fluorescence micrographs for quantitative relative comparison of protein adsorption onto polymer surfaces, Langmuir 24 (2008) 10253–10258.
[42] I. Barbulovic-Nad, M. Lucente, Y. Sun, M. Zhang, A.R. Wheeler, M. Bussmann, Bio-microarray fabrication techniques—a review, Crit. Rev. Biotechnol. 26 (2006) 237–259.
[43] G. McHale, Surface free energy and microarray deposition technology, Analyst 132 (2007) 192–195.
[44] O. Gutmann, R. Niekrawietz, R. Kuehlewein, Ch P. Steinert, S. Reinbold, B. Heij, M. Daub, R. Zengerle, Non-contact production of oligonucleotide microarrays using the highly integrated TopSpot nanoliter dispenser, Analyst 129 (2004) 835–840.
[45] J.T. Smith, B.L. Viglianti, W.M. Reichert, Spreading diagrams for the optimization of quill pin printed microarray density, Langmuir 18 (2002) 6289–6293.
[46] Ch.-E. Ch. Ho, F.-G. Tseng, S. -Ch. Lin, Ch.-J. Ch. Su, Z.-Y. Liu, R.-J. Yu, Y.-Ch. Chen, H. Huang, Ch.-Ch. Chieng, Characterization of the surface tension and viscosity effects on the formation of nano-liter droplet arrays by an instantprotein micro stamper, J. Micromech. Microeng. 15 (2005) 2317–2325.

[47] H.F. Zoller, Casein viscosity studies, J. Gen. Physiol. 3 (1921) 635–651.
[48] A. Kessler, O. Menéndez-Aguirre, J. Hinrichs, C. Stubenrauch, J. Weiss, Properties of an alphas-casein-rich casein fraction: influence of dialysis on surface properties, miscibility, and micelle formation, J. Dairy Sci. 96 (2013) 5575–5590.
[49] H. Ecroyd, D. Thorn, Y. Liu, J.A. Carver, The dissociated form of κ-casein is the precursor to its amyloid fibril formation, Biochem. J. 429 (2010) 251–260.
[50] R.J. Hill, R.G. Wake, Amphiphile nature of κ-casein as the basis for its micelle stabilizing property, Nature 221 (1969) 635–639.
[51] V. Dugas, J. Broutin, E. Souteyrand, Droplet evaporation study applied to DNA chip manufacturing, Langmuir 21 (2005) 9130–9136.
[52] H.Y. Kim, S.E. Lee, M.J. Kim, J.I. Han, B.K. Kim, Y.S. Lee, J.H. Kim, Characterization and simulation of cDNA microarray spots using a novel mathematical model, BMC Bioinf. 8 (2007) 485.
[53] D. Mampallil, Some physics inside drying droplets, Resonance 19 (2014) 123–134.
[54] D. Janssen, D. De Palma, S. Verlaak, P. Heremans, W. Dehaen, Static solvent contact angle measurements, surface free energy and wettability determination of various self-assembled monolayers on silicon dioxide, Thin Solid Films 515 (2006) 1433–1438.
[55] D. Briggs, Surface Analysis of Polymers by XPS and Static SIMS, Cambridg University Press, Cambridge, 1998.
[56] K.-B. Lee, S.-J. Park, C.A. Mirkin, J.C. Smith, M. Mrksich, Protein nanoarrays generated by dip-pen nanolithography, Science 295 (2002) 1702–1705.
[57] S. Nakai, H.K. Wilson, E.O. Herreid, Calculation of the molecular size of κ-casein fractions obtained by gel-filtration after storage and rennin action, J. Dairy Sci. 49 (1966) 1557–1559.
[58] H.M. Farrell, P.H. Cooke, E.D. Wickham, E.G. Piotrowski, P.D. Hoagland, Environmental influences on bovine κ-casein: reduction and conversion to fibrillar (amyloid) structures, J. Protein Chem. 22 (2003) 259–273.
[59] M. Cieśla, J. Barbasz, Random sequential adsorption of trimers and hexamers, J. Mol. Model. 19 (2013) 5423–5427.
[60] K.S. Birdi, J. Jeppesen, Surface chemical properties of biopolymers determined by contact angle measurements, Colloid Polym. Sci. 256 (1978) 261–265.
[61] Universal Protein Resource. http://www.uniprot.org (accessed 02.02.15). ID: P02668.

# Supplementary Material

# Imaging and chemical surface analysis of biomolecular functionalization of monolithically integrated on silicon Mach-Zehnder interferometric immunosensors

Katarzyna Gajos[a*], Michailia Angelopoulou[b], Panagiota Petrou[b], Kamil Awsiuk[a], Sotirios Kakabakos[b], Willem Haasnoot[c], Andrzej Bernasik[d,e], Jakub Rysz[a], Mateusz M. Marzec[e], Konstantinos Misiakos[f], Ioannis Raptis[f], Andrzej Budkowski[a]

[a]M. Smoluchowski Institute of Physics, Jagiellonian University, Łojasiewicza 11, 30-348 Kraków, Poland

[b]Institute of Nuclear & Radiological Sciences & Technology, Energy & Safety, and

[f]Department of Microelectronics, Institute of Nanoscience and Nanotechnology, NCSR Demokritos, P. Grigoriou & Neapoleos St, Aghia Paraksevi 15310, Athens, Greece

[c]RIKILT Wageningen UR, Akkermaalsbos 2, 6708 WB Wageningen, Netherlands

[d]Faculty of Physics and Applied Computer Science and

[e]Academic Centre for Materials and Nanotechnology, AGH University of Science and Technology, Mickiewicza 30, 30-059 Kraków, Poland

* Corresponding author

*E-mail address*: kasia.fornal@uj.edu.pl

**S1. Video showing filling of the fluidic unit with solution of a fluorescent compound.**

See the file Mov04905.mpg (4,2 Mb)

**S2. Additional information on molecular ion fragments that are characteristic TOF-SIMS signals**

**Table S1.** Characteristic Positive Molecular Fragments and Their Exact Masses Used for TOF-SIMS Analysis.

| substrate, amino acid or | fragment | exact | reference |
|---|---|---|---|
| amino acid, APTES | $NH_4^+$ | 18.03 | [S3] |
| substrate | $H_3O^+$ | 19.02 | [S4] |
| substrate | $Si^+$ | 27.98 | |
| amino acid, APTES | $CH_4N^+$ | 30.04 | [S3] |
| amino acid, APTES | $C_2H_4N^+$ | 42.04 | [S3] |
| arginine (Arg) | $CH_3N_2^+$ | 43.03 | [S3] |
| APTES | $C_3H_7^+$ | 43.06 | [S4] |
| substrate | $SiO^+$ | 43.97 | |
| alanine (Ala) | $C_2H_6N^+$ | 44.05 | [S3] |
| substrate | $SiOH^+$ | 44.98 | |
| APTES | $SiC_2H_7^+$ | 59.03 | |
| serine (Ser) | $C_2H_6NO^+$ | 60.04 | [S3] |
| substrate | $SiH_2O_2^+$ | 61.98 | |
| substrate | $SiH_3O_2^+$ | 62.99 | |
| proline (Pro) | $C_4H_6N^+$ | 68.05 | [S3] |
| threonine (Thr) | $C_4H_5O^+$ | 69.04 | [S3] |
| substrate | $Si_2N^+$ | 69.97 | |
| asparagine (Asn) | $C_3H_4NO^+$ | 70.03 | [S3] |
| serine (Ser) | $C_3H_3O_2^+$ | 71.01 | [S3] |
| valine (Val) | $C_4H_{10}N^+$ | 72.09 | [S3] |
| cysteine (Cys) | $C_2H_6SN^+$ | 76.03 | [S3] |
| valine (Val) | $C_5H_7O^+$ | 83.05 | [S3] |
| glutamine (Gln) | $C_4H_6NO^+$ | 84.05 | [S3] |
| lysine/leucine/isoleucine | $C_5H_{10}N^+$ | 84.09 | [S3] |
| leucine/isoleucine (Leu/Ile) | $C_5H_{12}N^+$ | 86.10 | [S3] |
| asparagine (Asn) | $C_3H_7N_2O^+$ | 87.05 | [S3] |
| asparagine/ aspartic acid | $C_3H_6NO_2^+$ | 88.03 | [S3] |

| | | | |
|---|---|---|---|
| asparagine (Asn) | $C_4H_4NO_2^+$ | 98.01 | [S3] |
| arginine (Arg) | $C_4H_{10}N_3^+$ | 100.08 | [S3] |
| arginine (Arg) | $C_4H_{11}N_3^+$ | 101.08 | [S3] |
| substrate | $Si_3N_2^+$ | 111.95 | |
| arginine (Arg) | $C_5H_{11}N_4^+$ | 127.11 | [S3] |
| tryptophan (Trp) | $C_9H_8N^+$ | 130.17 | [S3] |
| tryptophan (Trp) | $C_{10}H_{11}N^+$ | 145.09 | [S3] |
| tryptophan (Trp) | $C_{11}H_8NO^+$ | 170.08 | [S3] |
| glyceride/cholesterol | $C_{23}H_{35}^+$ | 311.26 | |
| monoacylglycerols | $C_{23}H_{37}^+$ | 313.28 | |
| monoacylglycerols | $C_{21}H_{39}O_3^+$ | 339.30 | [S2] |
| monoacylglycerols | $C_{21}H_{41}O_3^+$ | 341.31 | [S2] |
| diacylglycerols | $C_{21}H_{37}O_4^+$ | 353.27 | |
| diacylglycerols | $C_{21}H_{39}O_4^+$ | 355.29 | |
| diacylglycerols | $C_{23}H_{41}O_4^+$ | 381.34 | |
| diacylglycerols | $C_{23}H_{43}O_4^+$ | 383.34 | |
| diacylglycerols | $C_{25}H_{47}O_4^+$ | 411.40 | |
| diacylglycerols | $C_{25}H_{48}O_4^+$ | 412.40 | |
| diacylglycerols | $C_{27}H_{49}O_4^+$ | 437.43 | |
| diacylglycerols | $C_{27}H_{51}O_4^+$ | 439.45 | |
| diacylglycerols | $C_{27}H_{52}O_4^+$ | 440.45 | |
| diacylglycerols | $C_{29}H_{54}O_4^+$ | 466.44 | |
| diacylglycerols | $C_{29}H_{55}O_4^+$ | 467.44 | |
| diacylglycerols | $C_{29}H_{56}O_4^+$ | 468.47 | |
| diacylglycerols | $C_{31}H_{57}O_4^+$ | 493.48 | |
| diacylglycerols | $C_{31}H_{59}O_4^+$ | 495.48 | |
| diacylglycerols | $C_{31}H_{60}O_4^+$ | 496.46 | |
| diacylglycerols | $C_{33}H_{61}O_4^+$ | 521.50 | [S2] |
| diacylglycerols | $C_{33}H_{63}O_4^+$ | 523.51 | [S2] |
| diacylglycerols | $C_{33}H_{64}O_4^+$ | 534.51 | |
| diacylglycerols | $C_{35}H_{65}O_4^+$ | 549.53 | [S2], [S1] |
| diacylglycerols | $C_{35}H_{67}O_4^+$ | 551.56 | [S2], [S1] |
| diacylglycerols | $C_{35}H_{68}O_4^+$ | 552.53 | |
| diacylglycerols | $C_{37}H_{69}O_4^+$ | 577.53 | [S2] |
| diacylglycerols | $C_{37}H_{71}O_4^+$ | 579.55 | [S2], [S1] |
| diacylglycerols | $C_{37}H_{72}O_4^+$ | 580.54 | |
| diacylglycerols | $C_{39}H_{73}O_4^+$ | 605.56 | |
| diacylglycerols | $C_{39}H_{75}O_4^+$ | 607.61 | [S2] |

**Table S2.** Characteristic Negative Molecular Fragments and their Exact Masses Used for TOF-SIMS Analysis.

| substrate, amino acid, sugar or fatty | fragment | exact mass | reference |
|---|---|---|---|
| amino acid | $C_2H_2N^-$ | 40.02 | |
| sugar/amino acid | $C_2HO^-$ | 41.01 | |
| substrate | $SiN^-$ | 41.98 | |
| amino acid | $CNO^-$ | 42.00 | [S3] |
| substrate | $SiO^-$ | 43.97 | |
| substrate | $SiOH^-$ | 44.98 | |
| sugar/amino acid | $CHO_2^-$ | 45.00 | |
| amino acid | $C_3H_2N^-$ | 43.97 | |
| sugar/amino acid | $C_2H_2O_2^-$ | 58.01 | |
| substrate | $SiO_2^-$ | 59.97 | |
| substrate | $SiO_2H^-$ | 60.98 | |
| amino acid | $C_3NO^-$ | 66.00 | |
| amino acid | $C_3H_2NO^-$ | 68.02 | |
| substrate | $Si_2N^-$ | 69.94 | |
| fatty acid | $C_8H_{15}O_2^-$ | 143.11 | |
| fatty acid | $C_{10}H_{19}O_2^-$ | 171.14 | |
| fatty acid | $C_{12}H_{23}O_2^-$ | 199.17 | |
| fatty acid | $C_{14}H_{27}O_2^-$ | 227.21 | [S2] |
| fatty acid | $C_{15}H_{29}O_2^-$ | 241.22 | |
| fatty acid | $C_{16}H_{29}O_2^-$ | 253.22 | [S2], [S1] |
| fatty acid | $C_{16}H_{31}O_2^-$ | 255.24 | [S2], [S1] |
| fatty acid | $C_{16}H_{32}O_2^-$ | 256.24 | |
| fatty acid | $C_{18}H_{33}O_2^-$ | 281.25 | [S2], [S1] |
| fatty acid | $C_{18}H_{35}O_2^-$ | 283.27 | [S2] |
| fatty acid | $C_{18}H_{36}O_2^-$ | 284.37 | |

**S3. Transmission spectrum of the integrated Mach-Zenhder interferometer**

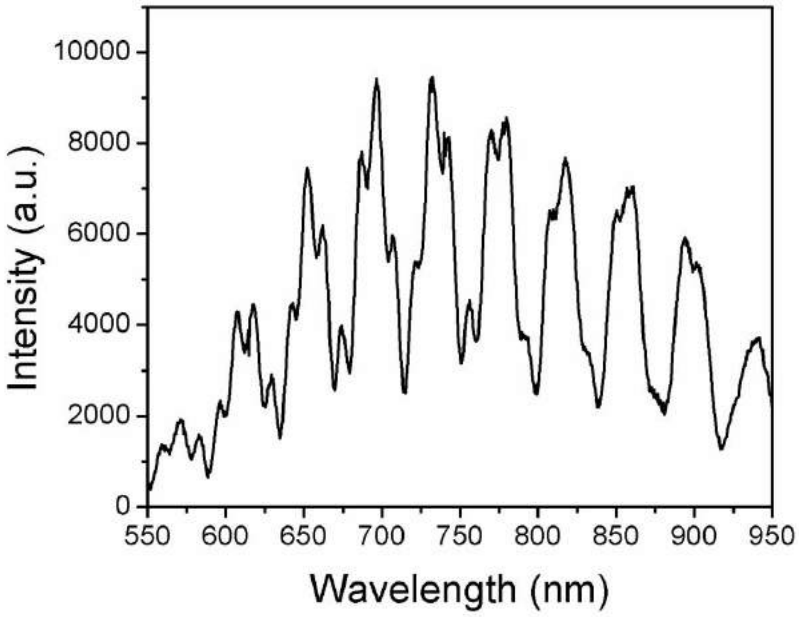


**Figure S1.** Output spectrum from an integrated BB-MZI as recorded by the external spectrometer. Two oscillation frequencies are apparent: a higher one for the TM polarization and a lower for the TE polarization.

**S4. Surface roughness of the examined planar samples**

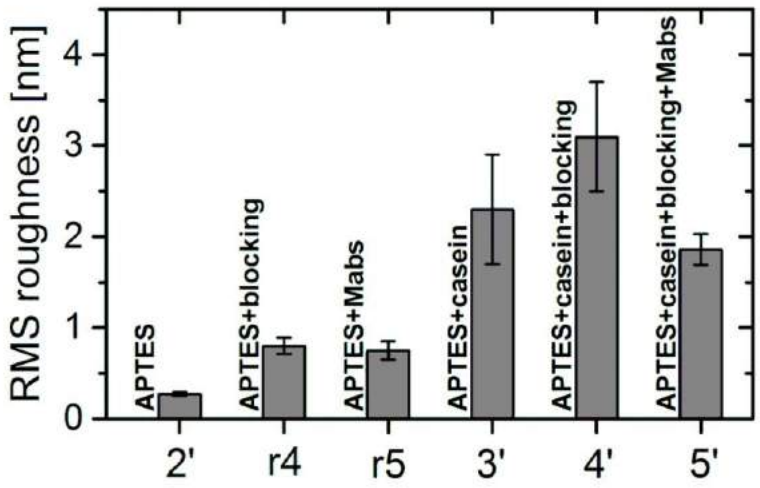


**Figure S2.** Mean square roughness RMS determined from the AFM histograms obtained from the planar $Si_3N_4$ surfaces spotted, blocked and immunoreacted as the chips (**2'-5'**) and the reference samples spotted with diluted milk and Mabs solution (**r4, r5**).

**S5. Outline and parameters of the model used to analyze ARXPS data**

The thickness of the whole organic layer D can be estimated based on the attenuation of the Si 2p photoelectrons characteristic for the substrate. The XPS intensity of Si 2p signal, recorded for different take-off angles Θ and recalculated using tabulated sensitivity factors [S5], is normalized with respect to the XPS signals of all elements present in the sample to yield the Θ-dependent atomic concentration $X_{Si}$. The thickness of organic layer D is obtained from simple linear regression using the equation (1):

$$\ln\left(X_{Si}/Z_{Si}\right) = -D/\lambda_{Si}\cos\theta \qquad (1)$$

The molar fraction of Si atoms $Z_{Si}$ is represented by the atomic concentration of 38.6(1.7)%, determined from the measurements of bare $Si_3N_4$ surface and averaged for all take-off angles Θ.

**S6. Additional AFM images, taken with higher scan range, revealing impact of blocking procedure**

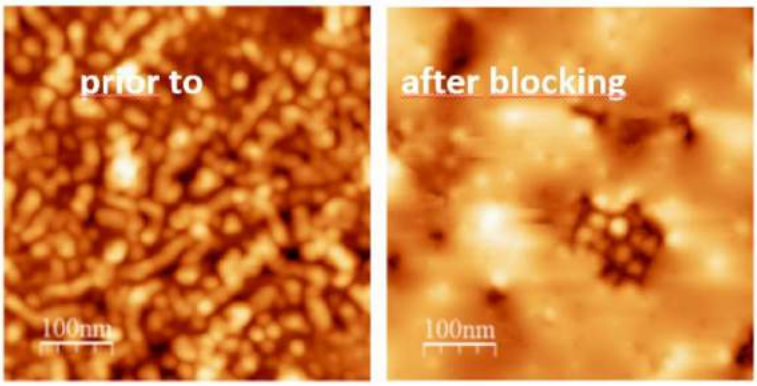


**Figure S3.** Additional topographic AFM micrographs of the planar samples prior to **(3')** and after blocking **(4')** with diluted goat milk. Blocking results in patchy coverage of immobilized κ-casein by milk components.

**S7. Bovine κ-casein calibration curves obtained with the BB-MZI chips**

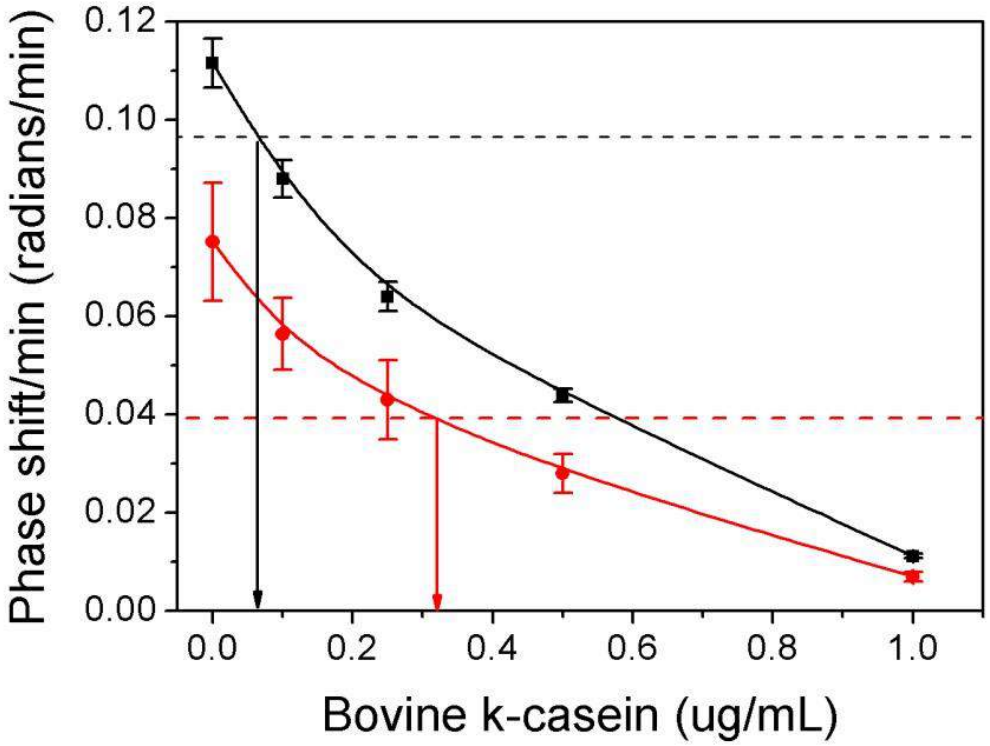


**Fig. S4.** Calibration curves obtained from chips spotted with κ-casein solutions with concentrations of 10 (closed circles) and 100 μg/mL (closed squares). Each point is the mean value of 3 chips ± SD. Dotted lines correspond to mean zero calibrator signal value -3SD for the respective calibration curves; arrows indicate the respective limits of detection.

**References:**

[S1] P. Malmberg, H. Nygren, K. Richter, Y. Chen, F. Dangardt, P. Friberg, Y. Magnusson, Imaging of lipids in human adipose tissue by cluster ion TOF-SIMS, Microsc. Res. Tech. 70 (2007) 828-835.

[S2] M. K. Passarelli, N. Winograd, Lipid imaging with time-of-flight secondary ion mass spectrometry (ToF-SIMS), Biochim. Biophys. Acta, Mol. Cell Biol. Lipids 1811 (2011) 976-990.

[S3] M. S. Wagner, D. G. Castner, Characterization of Adsorbed Protein Films by Time-of-Flight Ion Mass Spectrometry with Principal Component Analysis, Langmuir 17 (2001) 4649-4660.

[S4] K. Awsiuk, A. Budkowski, A. Psarouli, P. Petrou, A. Bernasik, S. Kakabakos, J. Rysz, I. Raptis, Protein adsorption and covalent bonding to silicon nitride surfaces modified with organo-silanes: Comparison using AFM, angle-resolved XPS and multivariate ToF-SIMS analysis, Colloids Surf., B 110 (2013) 217-224.

[S5] Multipak Software Manual version 9, ULVAC-PHI, Inc., 2011

# Paper IV

## *Indirect immunoassay on functionalized silicon surface: Molecular arrangement, composition and orientation examined step-by-step with multi-technique and multivariate analysis*

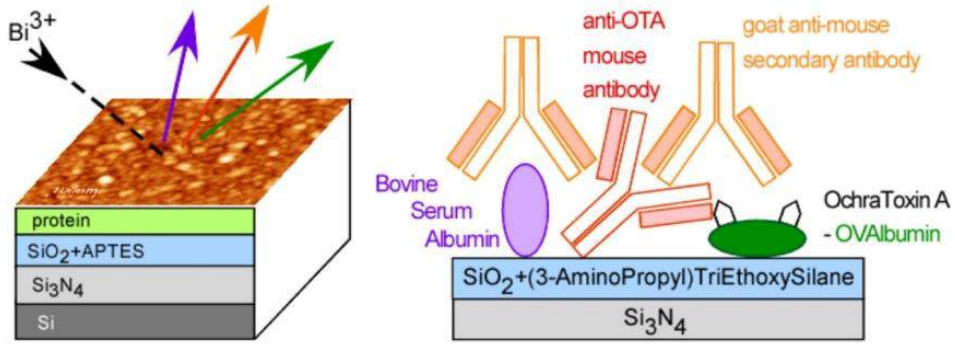


Highlights

- Biofunctionalization and indirect immunoassay protocol analyzed for $Si_3N_4$ surface.
- Analyte-protein conjugate and blocking protein desorb during primary immunoreaction.
- Grouped secondary antibodies cover protein monolayer that contains primary antibody.
- Indirect immunoassay orients differently primary and secondary antibody.
- Orientation of directly immobilized antibodies depends on their surface density.

Colloids and Surfaces B: Biointerfaces 150 (2017) 437–444

Contents lists available at ScienceDirect

Colloids and Surfaces B: Biointerfaces

journal homepage: www.elsevier.com/locate/colsurfb

# Indirect immunoassay on functionalized silicon surface: Molecular arrangement, composition and orientation examined step-by-step with multi-technique and multivariate analysis

Katarzyna Gajos[a,*], Andrzej Budkowski[a], Varvara Pagkali[b], Panagiota Petrou[b], Monika Biernat[a], Kamil Awsiuk[a], Jakub Rysz[a], Andrzej Bernasik[c], Konstantinos Misiakos[d], Ioannis Raptis[d], Sotirios Kakabakos[b]

[a] M. Smoluchowski Institute of Physics, Jagiellonian University, Łojasiewicza 11, 30-348 Kraków, Poland
[b] Institute of Nuclear & Radiological Sciences & Technology, Energy & Safety NCSR Demokritos, P. Grigoriou & Neapoleos St., Aghia Paraksevi 15310, Athens, Greece
[c] Faculty of Physics and Applied Computer Science, AGH University of Science and Technology, Mickiewicza 30, 30-059 Kraków, Poland
[d] Department of Microelectronics, Institute of Nanoscience and Nanotechnology, NCSR Demokritos, P. Grigoriou & Neapoleos St., Aghia Paraksevi 15310, Athens, Greece

ARTICLE INFO

*Article history:*
Received 12 July 2016
Received in revised form 11 October 2016
Accepted 3 November 2016
Available online 5 November 2016

*Keywords:*
Indirect immunoassay
Antibody orientation
Biosensor functionalization
TOF-SIMS
Principal Component Analysis
Surface analysis

ABSTRACT

The arrangement, composition and orientation of immunoreagents employed in an indirect immunoassay for determination of mycotoxin OchraToxin A (OTA) are specified for $Si_3N_4$ substrate, aiming to imitate biosensor transducers made of the same material. $Si_3N_4$ surfaces are examined after modification with (3-aminopropyl)triethoxysilane, spotting with OTA-ovalbumin conjugate (probe), blocking with bovine serum albumin, reaction with a mouse monoclonal antibody against OTA and, finally, reaction with a goat anti-mouse secondary antibody. Atomic force micrographs, their autocorrelation and height histogram parameters, show the stepwise development of a multi-component monolayer covered by groups of secondary antibody molecules. Time-Of-Flight Secondary Ion Mass Spectrometry reveals the composition of probe and blocking protein, as well as their partial desorption during the primary immunoreaction. Ellipsometry provides surface amount of all proteins, increasing step-by-step from 0.7 to 6.9 mg/m$^2$. In addition, ellipsometry combined with TOF-SIMS reveals the mass loadings of different molecules in the intermediate and the final overlayer. Based on this, some orientations of the immobilized molecules are proposed and a molar ratio of ~2.5 for secondary to primary antibody is calculated. The orientations of the primary and secondary antibody are further clarified by Principal Component Analysis of TOF-SIMS data, through which a side-on and a head-on orientation is deduced for the primary and the secondary antibody, respectively. These findings demonstrate how the combination of multiple surface analysis techniques can provide insight on the arrangement, composition and orientation of biomolecules in the course of multi-step procedures employed in biosensors.

© 2016 Elsevier B.V. All rights reserved.

## 1. Introduction

Since their discovery over 50 year ago, immunochemical methods have become one of the most powerful analytical tools [1], further exploited by the massive development of immunosensors which have found application in areas ranging from biomedical diagnostics to food safety and drug screening [2].

For silicon-based immunosensors, the surface should be appropriately functionalized prior to the immobilization of the specific immunoreagents, whereas a blocking step should be performed prior to immunoreaction to eliminate non-specific binding of reagents during the immunoreaction. The immunosensor analytical performance depends on the arrangement/orientation of immunoreagents on its surface as well as the amount of immobilized molecules. Commonly, *molecular arrangement* is concluded from spectroscopic [3–6], quartz crystal microbalance [7] or Atomic Force Microscopy data [4,6,8,9]. Nevertheless, all these approaches seem not sufficient to provide insight of what is happening onto the surface, when different molecules are involved which are

* Corresponding author.
*E-mail address:* katarzyna.gajos@doctoral.uj.edu.pl (K. Gajos).

http://dx.doi.org/10.1016/j.colsurfb.2016.11.009
0927-7765/© 2016 Elsevier B.V. All rights reserved.

not only introduced but also partly removed from the surface during the successive modification/immunoreaction steps [10]. Therefore, surface examination with a method that could provide *discrimination between immobilized onto surface molecules*, such as Time-of-Flight Secondary Ion Mass Spectrometry, is expected to provide valuable information and help to improve immunosensors performance. In addition, such a surface examination after each functionalization and assay steps is rarely provided by the usually applied surface characterization methods [11].

Here, such a *step-by-step surface characterization* is applied in order to define *molecular arrangement* and *composition* during the course of an *indirect immunoassay* for the detection of mycotoxin, OchraToxin A (OTA). The assay is accomplished by immobilization of an OTA conjugate with ovalbumin on the surface, followed by immunoreaction with a monoclonal anti-OTA antibody (primary antibody) and a secondary antibody as a mean to increase the specific signal. It should be noted that although several investigations have been performed to define the orientation of immobilized antibodies (e.g. [5–7,9,12–14]), this is the first time the research is extended to cover *molecular orientation of* both *the primary and secondary antibody*, observed directly on functionalized surface in the course of an indirect immunoassay, and compared with the situation on reference surfaces spotted with these antibodies. Thus, in the present study, direct determination of antibody orientation is provided by Principal Component Analysis of TOF-SIMS data [4,12], performed for multi-component protein overlayers.

## 2. Experimental section

### 2.1. Materials

Silicon wafers were purchased from Si-Mat (Kaufering, Germany). 3-aminopropyltriethoxysilane (APTES), bovine serum albumin (BSA), and ovalbumin (OVA) were purchased form Sigma-Aldrich (Darmstadt, Germany). The synthesis of OTA-OVA conjugate was performed as described in a previous publication [15]. The mouse monoclonal anti-OTA antibody (anti-OTA Mab; isotype IgG1, κ) was purchased from Soft Flow Hungary Ltd. (Hungary). Affinity purified polyclonal goat anti-mouse IgG antibody (secondary antibody) was from Merck Millipore (Darmstadt, Germany). The water used throughout the study was double distilled.

### 2.2. Surface functionalization and assay protocol

The biofunctionalization and immunoassay steps are shown schematically in Fig. 1. Firstly, $Si_3N_4$ surfaces **(1)**, cleaned and hydrophilized with oxygen plasma, were immersed in a 0.5% (v/v) aqueous APTES solution for 2 min, followed by gentle washing with distilled water, drying under $N_2$ stream and curing for 20 min at 120 °C. Then, a 200 μg/mL OTA-OVA solution in 50 mM carbonate buffer, pH 9.2 was spotted **(2)** (over 7 mm × 7 mm areas) on the surfaces using the BioOdyssey Calligrapher Mini Arrayer (Bio-Rad Laboratories, Inc.) [10]. The spotted samples were incubated in a humidity chamber for 18 h and washed with a 10 mM Tris-HCl buffer, pH 8.25, and distilled water. Blocking **(3)** was performed by immersing the samples in a 10 mg/mL BSA solution in 0.1 M $NaHCO_3$, pH 8.5, for 2 h followed by washing and drying as previously. Reaction with the primary antibody **(4)** was performed through incubation of the samples for 1 h with a 4 μg/mL solution of anti-OTA Mab in 50 nM Tris-HCl buffer, pH 7.8, containing 9 g/L NaCl and 5 g/L BSA (assay buffer). After that, the samples were washed and dried as previously, and then incubated with a 10 μg/mL secondary antibody solution in assay buffer **(5)** for 1 h. Additionally, reference samples were prepared by spotting directly solutions of 4 μg/mL of anti-OTA Mab **(r4)** or 10 μg/mL of secondary antibody in 50 mM carbonate buffer, pH 9.2 **(r5)**. The reference samples were washed with buffer and distilled water and dried under $N_2$ stream.

### 2.3. AFM surface examinations

Agilent 5500 microscope working in a non-contact mode (resonant frequency ~70 kHz, tip radius ~7 nm, spring constant ~2 N/m) under ambient conditions was used to acquire AFM images from different areas of each sample. The WSxM software was used (downloadable at http://www.nanotec.es) for processing of the images.

### 2.4. TOF-SIMS surface characterization

A TOF.SIMS 5 (ION-TOF GmbH) instrument equipped with $Bi_3^+$ ion clusters (30 keV liquid metal ion gun) was used. Ion dose density was lower than $10^{12}$ ion/cm$^2$ (static mode). A low energy electron flood gun was used for charge compensation. High mass resolution positive ion static TOF-SIMS spectra were acquired from six non-overlapping 100 μm × 100 μm areas of each sample. Mass calibration was performed with $H^+$, $H_2^+$, $CH^+$, $C_2H_2^+$ and $C_4H_5^+$ peaks. A minimal mass resolution ($m/\Delta m$) > 5300 at $C_4H_5^+$ was obtained. To investigate differences in molecular coverage rather than changes in relative composition, TOF-SIMS data that have been obtained with dose density and primary beam current identical for all measurements are used without normalization. Surface sensitivity of TOF-SIMS experiments using $Bi_3^+$ primary ions was described [16] by exponential decay of signal intensity as a function of organic overlayer thickness, and characterized by escape depth of secondary ions of ~4 nm [16]. This value corresponds to uniform protein layer [11] with surface density of ~5.5 mg/m$^2$.

### 2.5. Multivariate TOF-SIMS analysis with PCA

Principal Component Analysis was performed for the positive TOF-SIMS spectra using the PLS Toolbox (Eigenvector Research, Manson, WA) for MATLAB (MathWorks, Inc., Natick, MA). The intensities of selected peaks from each spectrum were normalized to the sum of selected peaks and mean-centred prior to running PCA.

### 2.6. Ellipsometry measurements

The Sentech SE800 (Sentech Instruments GmBH) Spectroscopic Ellipsometer (wavelength range of 320–700 nm, fixed angle of incidence ~70°) along with the SpectraRay 3 software was used. Average thickness was estimated by fitting model predictions to Ψ and Δ relations, assuming the Cauchy dispersion formula. The three-layer model consisted of silicon substrate/$Si_3N_4$/mixed $SiO_2$ and APTES layer/protein overlayer. Fixed refractive index values n = 3.87 for Si, 2.01 for $Si_3N_4$ [17], 1.46 for both $SiO_2$ and APTES [18], and 1.53 for proteins [19] were used. The thickness of $Si_3N_4$ layer (122.5 nm), as well that of mixed $SiO_2$ and APTES layer (6.3 nm), both obtained from measurements performed on a bare silanized surface, were taken into account to fit the thickness of protein layer.

## 3. Results and discussion

### 3.1. Multi-step procedure for silicon surface modification leading to indirect assay

The reagents and assay procedure employed in the present study have been previously applied for the determination of OTA in beer samples employing an array of integrated on silicon Mach-Zehnder Interferometric sensors based on $Si_3N_4$ waveguides [10,15]. Thus,

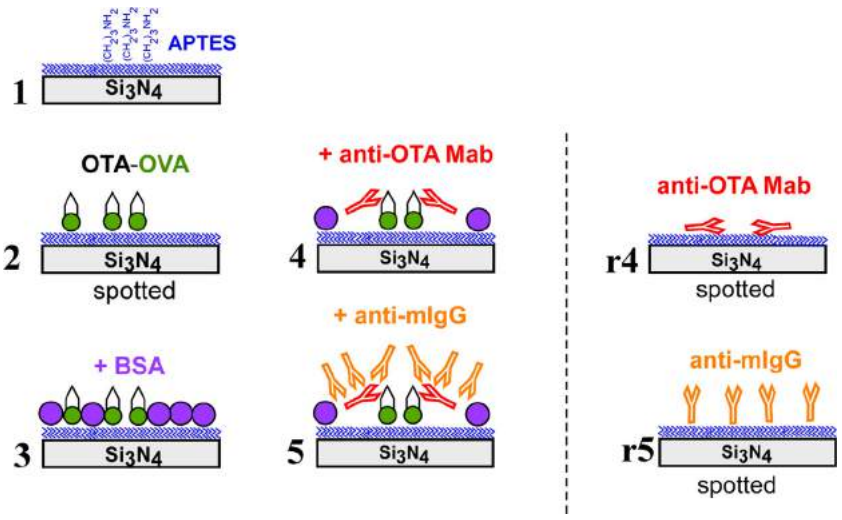


**Fig. 1.** Schematic of the procedure employed for biofunctionalization of $Si_3N_4$ surfaces (**1**–**3**) and indirect immunoassay for detection of mycotoxin OTA (**4**-**5**). $Si_3N_4$ surfaces were modified with APTES (**1**), spotted with OTA-OVA conjugate (**2**), blocked with BSA (**3**), and reacted first with the anti-OTA Mab (**4**), and then with a secondary antibody (anti-mIgG) (**5**). Reference samples were directly spotted with primary (**r4**) and secondary antibody (**r5**).

in the present work $Si_3N_4$ surfaces prepared in a similar way to integrated waveguides were employed in order to mimic the molecular arrangements in the particular sensor. In the aforementioned sensor, a competitive immunoassay format, schematically depicted in Fig. 1, is applied to determine traces of mycotoxin OTA in beer samples through incubation of calibrators or samples with the anti-OTA Mab prior to reaction with the immobilized onto the sensors surface OTA-OVA probe. Thus, all the surfaces examined in the present study correspond to zero calibrator.

The procedure of $Si_3N_4$ surface modification (Fig. 1) consists of: **(1)** chemical activation with amino-silane (APTES); **(2)** immobilization of the probe OTA-OVA (spotted from solution); **(3)** blocking of non-specific binding with bovine serum albumin (BSA); **(4)** specific binding of primary mouse monoclonal antibody against OTA (anti-OTA Mab); **(5)** binding of secondary goat anti-mouse IgG antibody (anti-mIgG). Amino-silanized $Si_3N_4$ surfaces spotted with primary **(r4)** and secondary antibody **(r5)** are used as references. The specificity of anti-OTA Mab binding to the silicon surfaces after functionalization with OTA-OVA conjugate [steps **(1)**–**(3)**] was confirmed by the negligible response of Mach-Zehnder Interferometric sensors spotted [in step **(2)**] with OVA instead of the OTA-OVA conjugate, as well as by the fact that the response of OTA-OVA spotted sensors increased as the concentration of OTA-OVA conjugate in the spotting solution was increased, as shown in our relevant publication [15]. Moreover, it should be noted that the sensor blocking procedure (and hence of plain $Si_3N_4$ surfaces) and composition of assay buffer has been optimized in order to eliminate non-specific binding of both the anti-OVA Mab and secondary antibody.

### 3.2. Molecular arrangement and composition after functionalization and assay steps

#### 3.2.1. Overlayer nanostructure visualized with AFM

AFM topographic images recorded after each one of the successive functionalization and immunoassay steps (Fig. 2a) reveal laterally uniform nanostructured molecular overlayers. Lateral nanostructure is described by the mean size of surface features *2whm* (Fig. 2b) provided by a radial averaged autocorrelation function computed for each AFM micrograph [11]. In turn, vertical nanostructure in an AFM image is characterized by the parameters of height distribution [11], such as average height $\langle h \rangle$ (Fig. 2c) and the root-mean-square surface roughness *RMS* (Fig. 2d).

Chemical activation of $Si_3N_4$ surface with APTES (**1**) yields self-assembled amino-silane monolayers (see Fig. 2) characterized by nanostructure parameters values of $\langle h \rangle = 0.85$ ($\pm 0.10$) nm and $RMS = 0.21$ ($\pm 0.01$) nm, identical to those reported in previous publications [11]. Subsequent spotting with the OTA-OVA probe (**2**) leads to partial surface coverage with proteins with distinct increments of $\Delta\langle h \rangle \sim 1.0$ nm and $\Delta RMS \sim 0.4$ nm. Well marked surface features with mean size *2whm* ~19 nm, correspond to OVA molecules which have a predicted apparent size of 19 and 23 nm for half-spherical and spherical shapes of immobilized molecules, respectively, as calculated taking into account the molecule nominal dimensions $9.4 \times 3.6 \times 3.6\ nm^3$ [20] and the broadening caused by the AFM tip (with 7 nm radius) [11]. The subsequent treatment of the surface with BSA **(3)** increases the surface coverage with proteins, resulting in increments of $\Delta\langle h \rangle \sim 2.2$ nm and $\Delta RMS \sim 0.3$ nm. Nevertheless, the mean size of surface features is hardly altered ($\Delta 2whm \sim 1$ nm), since the nominal dimensions ($9.0 \times 5.5 \times 5.5\ nm^3$ [21]) and apparent size of BSA (18–22 nm provided by the relevant models [11]) are similar to those of OVA.

The first immunoassay step **(4)**, that involves exposure of the functionalized surface to primary antibody, induces hardly any change in both average height $\Delta\langle h \rangle \sim 0.2$ nm and mean size of surface features $\Delta 2whm \sim 1$ nm, accompanied by minor increment in surface roughness $\Delta RMS \sim 0.2$ nm (Fig. 2). These parameters, as well as the original AFM images that are similar to those of step **(3)**, suggest that the primary antibody is incorporated into a *multi-component monolayer*. In addition, the primary immunoreaction is accompanied by partial desorption of blocking protein (BSA) and probe (OTA-OVA) (discussed in the Section 3.2.2). This accords with the minimal change in *2whm* observed, especially if one considers the fact that apparent size of IgG molecule, 25–28 nm (predicted according to [11] for a nominal size of $14.5 \times 8.5 \times 4.5\ nm^3$ [22]) is not much larger compared to that of the two albumins (e.g. up to 23 nm for OVA).

Finally, the second immunoreaction **(5)** results in a significant increase of vertical nanostructure parameters, $\Delta\langle h \rangle \sim 1.8$ nm and $\Delta RMS \sim 0.5$ nm, accompanied by a huge expansion of lateral nanostructure, reflected by nearly two-fold increase in the mean size of surface features *2whm* ~40 nm (see Fig. 2b). The *2whm* value is the same with the apparent size predicted for a group of two IgG molecules [11]. These striking changes in biomolecular overlayer reflect *efficient affinity binding* between primary and secondary antibodies, resulting in coverage of the multi-component protein

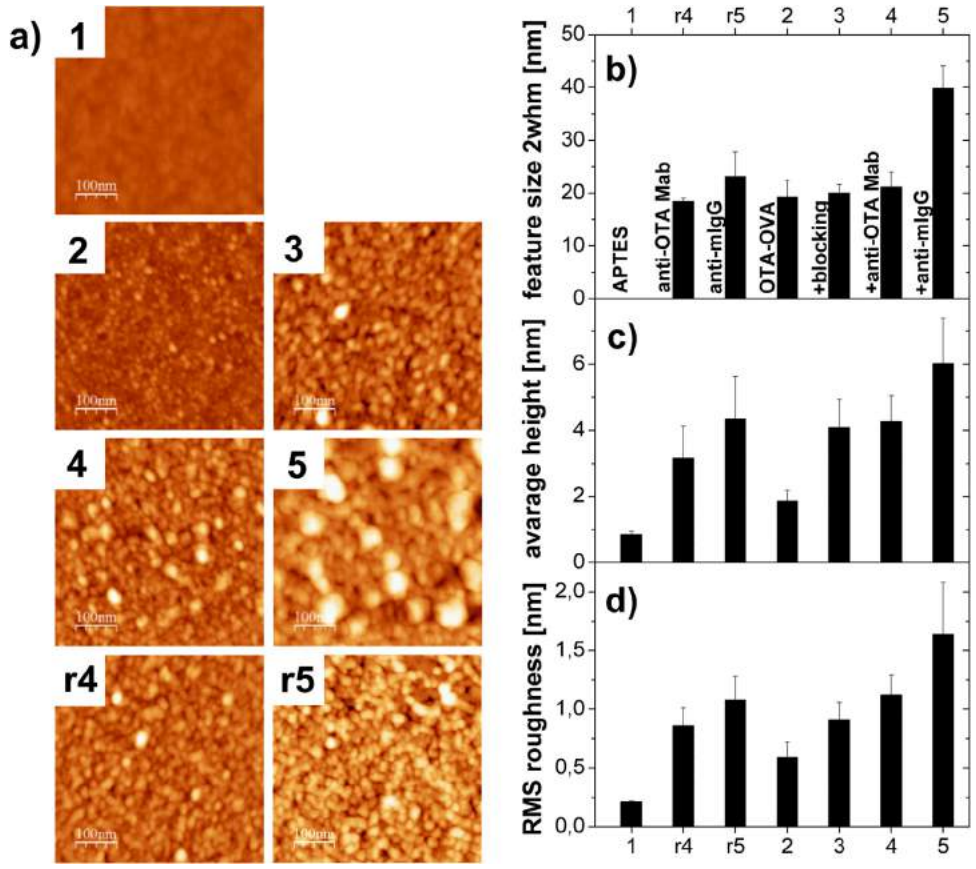


**Fig. 2.** (a) Representative topographic AFM micrographs (with identical height-range of 10 nm) and (b–d) nanostructure parameters obtained from the $Si_3N_4$ surfaces **(1-5)** after each one of the successive functionalization/immunoassay steps. The respective data for reference samples (**r4**, **r5**) are also provided. The nanostructure parameters calculated were: (b) the mean size of surface features, *2whm*, (c) the mean value of average height <*h*>, and (d) the root mean square roughness *RMS*. Error bars are standard deviations determined from 4 to 6 AFM images or height histograms of the same surface.

monolayer formed after the primary immunoreaction by grouped anti-mIgG molecules. The coverage of this additional protein layer must be relatively high, since it is not well penetrated by the AFM tip resulting in a somewhat limited height increment, $\Delta$<*h*>, when compared to IgG dimensions.

Furthermore, the nanostructures formed on the reference surfaces directly spotted with anti-OTA Mab (**r4**) or anti-mIgG (**r5**) are comparable (see Fig. 2) to those determined for protein monolayers formed on the surface prior to (**3**) and after the first immunoreaction (**4**). However, the average height of anti-OTA Mab overlayer (**r4**) is smaller by about one-quarter of that of anti-mIgG (**r5**), reflecting lower surface coverage, possibly due to the lower concentration of the first in the spotting solution. Moreover, the mean size of surface features *2whm* for sample (**r4**) is distinctively smaller (~18 nm), than that determined for sample (**r5**) (~23 nm). The former result accords with the size determined by AFM for Fc ($7.0 \times 6.3 \times 3.1$ nm$^3$ [23]) or Fab ($8.2 \times 5.0 \times 3.8$ nm$^3$ [23]) antibody fragments, while the latter with the apparent size of whole IgG molecule (25–28 nm). Recent AFM experiments show that the different IgG fragments can be resolved as separate surface features in layers of IgG molecules with specific orientations [8]. Thus, these different *2whm* values (Fig. 2b) could point to *different molecular orientation* of anti-OTA Mab (**r4**) and anti-mIgG molecules (**r5**), a suggestion confirmed by the results presented in Sections 3.2.3 and 3.3.

### 3.2.2. *Overlayer composition of probe and blocking protein examined with TOF-SIMS*

TOF-SIMS can distinguish between ion fragments of different amino acids. When the concentration and arrangement of amino acids in different protein molecules are not the same, characteristic TOF-SIMS signals can be ascribed to different proteins. The composition of OVA, BSA and model antibody provided in Table 1 [4,24] indicates amino acids with distinguishably high concentration in some of these proteins, such as methionine (4.4% in OVA, 0.7% in BSA, 2.0% in antibody) and glutamic acid (8.8% in OVA, 10.1% in BSA, 5.1% in antibody). Thus, the respective ion fragments are suggested as characteristic TOF-SIMS signals for OVA (Fig. 3a) and OVA and BSA (Fig. 3b), respectively. Comparison of the experimental results (Fig. 3) obtained for the surfaces functionalized with OTA-OVA (**2**) and BSA (**3**) and the reference surfaces (**1** or APTES, **r4**, **r5**) show that indeed the methionine TOF-SIMS signal is specific for OVA; while the glutamic acid signal is characteristic for both albumins (OVA and BSA), with small contributions from antibodies (anti-OTA Mab, anti-mIgG). Similar analysis has failed to provide a mass signal specific for the two antibodies.

The TOF-SIMS signals presented in Fig. 3 enable an insight into composition of OVA and cumulative albumin (OVA and BSA) in the protein overlayer after the different biofunctionalization and assay steps. Thus, the blocking procedure (**3**) introduces BSA molecules at the surface while preserving the existing coverage with OTA-OVA probe. Subsequently, both *probe* (OTA-OVA) *and blocking protein* (BSA) are partly *desorbed* during the primary immunoreaction step creating a multi-component monolayer (**4**). Then, the secondary antibody molecules cover the multi-component monolayer without affecting the pre-existing composition (**5**). Taking it overall, the picture provided by TOF-SIMS (Fig. 3) is consistent with that formed by the AFM analysis of the respective surfaces (Fig. 2). A more precise analysis of the surface composition and structure is attempted

**Table 1**
Comparison of amino acid composition (%) of OVA [24], BSA [24] and model antibody [4] (see Supplementary data for similar analysis made for the composition of model antibody reported in other publications [31,32]). The last column marks the amino acids with a composition ratio in Fc to $F(ab')_2$ fragments larger than 1.5 (based on Ref. [4]).

| amino acids | OVA (%) | BSA (%) | Antibody (%) | Fc>>Fab ($Fc/F(ab')_2 > 1.5$) |
|---|---|---|---|---|
| alanine/ala | 9.1 | 8.0 | 5.1 | |
| arginine/arg | 3.9 | 4.0 | 2.8 | |
| (Asparagine)/(Asn) | 3.9 | 2.4 | 4.6 | |
| aspartic acid/asp | 4.4 | 6.9 | 4.8 | |
| cysteine/cys | 0.3 | 6.0 | 2.0 | |
| (Glutamine)/(Gln) | 3.9 | 3.4 | 4.3 | |
| glutamic acid/glu | 8.8 | 10.1 | 5.1 | |
| (Glycine)/(Gly) | 4.9 | 2.7 | 5.4 | |
| histidine/his | 1.8 | 2.9 | 1.9 | + |
| isoleucine/ile | 6.5 | 2.4 | 3.4 | + |
| leucine/leu | 8.3 | 10.5 | 5.9 | |
| lysine/lys | 5.2 | 10.1 | 6.2 | + |
| methionine/met | 4.4 | 0.7 | 2.0 | |
| phenylalanine/phe | 5.2 | 4.6 | 3.9 | + |
| PROLINE/PRO | 3.6 | 4.8 | 6.3 | + |
| SERINE/SER | 9.8 | 4.8 | 12.5 | |
| THREONINE/THR | 3.9 | 5.7 | 8.8 | |
| TRYPTOPHAN/TRP | 0.8 | 0.3 | 2.0 | |
| TYROSINE/TYR | 2.6 | 3.4 | 4.6 | |
| (Valine)/(Val) | 8.0 | 6.2 | 8.3 | |

*Notation*: all-caps for both antibody/BSA and antibody/OVA > 1.25; lowercase for either BSA/antibody or OVA/antibody > 1.25; underlined for $Fc/(Fab')_2 > 1.5$; names and abbreviations in brackets for other amino acids.

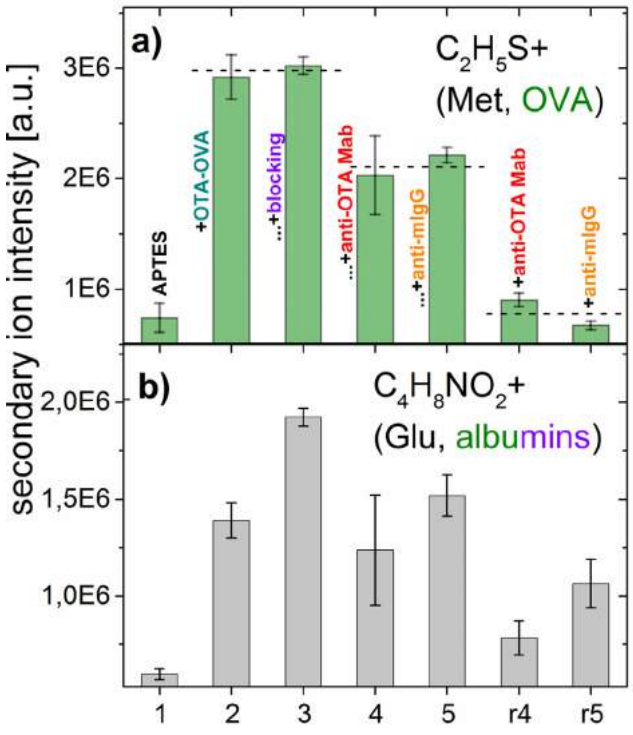


**Fig. 3.** TOF-SIMS analysis of multi-molecular layers formed on $Si_3N_4$ surfaces after each one of biofunctionalization/immunoassay steps (**1**–**5**) as well as for the reference samples (**r4**, **r5**). The signal intensities of secondary ions: (a) $C_2H_5S^+$ (from methionine) – specific for OVA, and (b) $C_4H_8NO_2^+$ (from glutamic acid) – characteristic for both albumins (OVA, BSA; with small contributions from antibodies) are provided. Error bars are standard deviations determined from 6 spectra acquired for each sample.

in the Section 3.2.3, where the TOF-SIMS data are combined with ellipsometry results.

### 3.2.3. Determination of proteins amount on the silanized surfaces by ellipsometry

The thickness D of protein overlayer was determined by ellipsometry using the multi-layer model described in Section 2.6. Then,

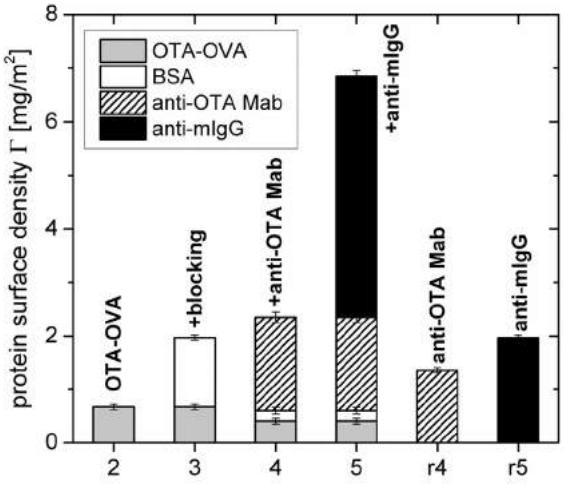


**Fig. 4.** Total protein surface density Γ (heights of stacked columns) and component mass loadings of different biomolecules (gray, white, hatched and black columns for OTA-OVA, BSA, primary and secondary antibody, respectively) determined with ellipsometry and evaluated with TOF-SIMS (Fig. 3) after each one of the individual biofunctionalization/immunoassay steps taking place on the $Si_3N_4$ surfaces. Error bars are standard deviations determined from 3 ellipsometric measurements of the same surface.

the protein surface density Γ was estimated after each one of the surface modification steps (Fig. 4) following the Cuypers one-component approach [25]:

$$\Gamma = D * \rho = d * (M/A) * (n_p^2 - 1)/(n_p^2 + 2) \quad (1)$$

A value of refractive index, $n_p = 1.53$ [19], and a ratio of molecular weight to molar refractivity M/A = 4.14 g/mL [25] are assumed for all the proteins [19,25].

*3.2.3.1. Mass loadings of different biomolecules.* Based on AFM and TOF-SIMS results, it has been concluded that the addition of new molecules upon blocking (**3**) and secondary immunoreaction (**5**) is not accompanied by any distinct change of the pre-existing surface protein coverage. On the other hand, the surface coverage by the two albumins, OTA-OVA and BSA, is reduced during the primary immunoreaction (**4**). To evaluate the mass loadings of different pro-

teins on the formed multi-component layer, the ellipsometric data are considered in combination with the TOF-SIMS signal intensities (Fig. 3), $I'(\mathbf{n}) = I(\mathbf{n}) - I(\mathbf{1})$, determined always with reference to bare silanized surface (**1**). Also, the assumption is made that the ratio of component contribution to TOF-SIMS signal and component mass loading, $I'^{component}(\mathbf{n})/\Gamma^{component}(\mathbf{n})$, for sample (**4**) is the same with those of samples with pure components, i.e., sample (**2**) for the signal $C_2H_5S^+$ from OTA-OVA, and samples (**3**) and (**r4**) for the signal $C_4H_8NO_2^+$ corresponding to the two albumins and primary antibody, respectively. This is equivalent to assuming that TOF-SIMS spectra show linear correlation with organic surface composition [26,27].

The ellipsometric data provide by subtraction for the steps (**2**) and (**3**) a surface density of 0.7 and 1.3 mg/m$^2$ for OTA-OVA and BSA, respectively (see gray and white columns in Fig. 4). Both these mass loadings, when calculated as described above, are reduced upon the first immunoreaction (**4**) to 0.4 for OTA-OVA and 0.2 mg/m$^2$ for BSA. This leads to a value of 1.8 mg/m$^2$ for the primary antibody (hatched column in Fig. 4) in order to match a total protein amount $\Gamma$ of 2.4 mg/m$^2$. Taking into account that these molecular mass loadings are preserved upon the second immunoreaction (**5**) and that the total amount of protein determined equals 6.9 mg/m$^2$, a surface density of 4.5 mg/m$^2$ is calculated for the secondary antibody. In turn, mass loading of 1.4 mg/m$^2$ and 2.0 mg/m$^2$, are determined for the primary and the secondary antibody, respectively, from the analysis of amino-silanized reference surfaces where the two molecules have been directly spotted.

*3.2.3.2. Evaluation of immunoactivity.* The determined surface amounts of secondary (anti-mIgG) and primary (anti-OTA Mab) antibody yield a binding molar ratio of ~2.5. This confirms the AFM observations, that grouped secondary antibodies (with apparent group size equal to that of two IgG molecules) cover the multi-component monolayer containing the primary antibodies. We also note, that the binding molar ratio determined in this study is similar to the value of ~2.4, calculated in a previous study for secondary anti-rabbit IgG antibody binding on rabbit gamma-globulins adsorbed to silicon surfaces [11a].

*3.2.3.3. Preselection of molecular orientation of immobilized proteins.* Asymmetric proteins could adapt specific orientations upon their immobilization onto solid surfaces. These orientations define which protein part is exposed to the surrounding medium, thus regulating the biological activity of the immobilized molecules [28]. The surface density $\Gamma$ data can shed some light on dominant molecular orientation, as the latter specifies cross-sectional area and mass loading $\Gamma_{ind}$ of individual biomolecules [6,7,9,11,21,23]. In particular, the molecular architecture of albumins indicates two orientations [20,21]: side-on ($\Gamma_{ind}$ = 2.3 and 2.2 mg/m$^2$ for OVA and BSA, respectively) and end-on (5.7 mg/m$^2$ for OVA and 3.65 mg/m$^2$ for BSA). In turn, four distinct orientations are predicted for the antibody molecule taking into account the three lobe-shaped fragments (the two Fab and the one Fc fragment) [23]: flat-on (all three lobes attached to surface; 2.0 mg/m$^2$), side-on (Fc and one Fab at substrate; ~2.9 mg/m$^2$), end-on (Fab-up, Fc at surface; 2.6–5.5 mg/m$^2$) and head-on (Fc-up, both Fabs attached to the substrate; 2.6–5.5 mg/m$^2$).

To maximize fractional surface coverage, immobilized proteins prefer to adopt the molecular orientation that leads to a $\Gamma_{ind}$ value near to surface density value $\Gamma$ [28,29]. However, molecular mass loading $\Gamma_{ind}$ must be reasonably larger than $\Gamma$, since close packing of adsorbed molecules cannot be achieved [28,29]. Accordingly, side-on alignment is advocated for the directly adsorbed OTA-OVA molecules (**2**) with surface density value, $\Gamma$ = 0.7 mg/m$^2$ (cf. $\Gamma_{ind}$ values), whereas for the subsequently added BSA, that leads to a cumulative mass loading of 2.0 mg/m$^2$ (**3**), an end-on rather than side-on dominant orientation is expected. Since the surface coverage by both albumins is reduced considerably during the immunoreaction with the primary antibody (**4**), all orientations of anti-OTA Mab ($\Gamma$ = 1.8 mg/m$^2$) seem plausible except for flat-on orientation. Also, end-on alignment is excluded for geometrical reasons, since primary antibodies are incorporated into the multi-molecular monolayer. Thus it seems that most of the anti-OTA Mab molecules have a side-on or head-on orientation indicating binding of one or both binding sites located on the Fab fragments to the immobilized onto the surface OTA moieties. Finally, the protein monolayer created during the first immunoreaction is enveloped during the second one (**5**) by a huge amount of attached secondary antibody, 4.5 mg/m$^2$, that can be accommodated in a new monolayer only if the end-on or head-on orientations are adopted [7]. In turn, for the reference surfaces, a flat-on orientation is defined for the spotted primary antibody with a surface density of 1.4 mg/m$^2$ (**r4**), but more vertical, side-on or end-on (or head-on), orientations are indicated [7,9] for the spotted secondary antibody (**r5**) with higher mass loading of 2.0 mg/m$^2$. This difference could be due to the fact that the concentration of secondary antibody in the spotting solution was 2.5-times higher than the concentration of the primary antibody.

### 3.3. Orientation of the primary and secondary antibody and molecular arrangement from multivariate TOF-SIMS analysis

To determine subtle differences in amino acids composition between the *outermost regions* of the functionalized $Si_3N_4$ surfaces after the immunoreaction with primary (**4**) and secondary antibody (**5**), as compared to the situation on the reference surfaces spotted directly with these antibodies (**r4** and **r5**), multiple TOF-SIMS signals are examined simultaneously with multivariate PCA analysis (Fig. 5). The examined TOF-SIMS data set, consisting of the relative intensities of 38 amino acids fragments (listed in Fig. 6) from 24 spectra, can be visualized as 24 points in a 38-dimensional space. PCA reduces dimensionality of the data set while retaining its essential information by transforming the original signals into two principal components (PCs) that account for *uncorrelated* major variations within the data set. Thus, the PCA scores plot provided in Fig. 5a describes the surface compositions (24 points with different symbols for various surfaces) in terms of the principal components PC1 and PC2.

The first PC (PC1), that captures 86.28% of the total variance, is defined by the loadings plot presented in Fig. 6a. PC1 is loaded positively by the fragments of amino acids (marked with all-caps) that have higher abundance in the antibody than the albumin molecules (BSA and OVA, see Table 1). On the other hand, the amino acids (distinguished by lowercase) with higher abundance in the albumin (BSA or OVA) than the antibody molecule (see Table 1) contribute to the mass signals that loads PC1 negatively. While PC1 resolves antibody from albumin, the second PC (PC2) captures the largest residual variance in the data set, uncorrelated to that described by the PC1. Indeed, the loadings plot (Fig. 6b) shows that PC2 can be related to antibody orientation, as it is loaded negatively only by the dominant ion fragments of the amino acids (marked by underlined fonts) that are more abundant in the Fc than the F(ab')$_2$ fragments (see Table 1), indicating an antibody orientation that exposes the Fc fragment. In turn, the amino acids with higher abundance on the F(ab')$_2$ fragment point to other antibody orientations. It should be noted, that similar conclusions are drawn from PC1 and PC2 when amino-acid compositions for the IgG molecule from different literature sources are used [4,31,32] (see Supplementary data).

The interpretation of PC1 and PC2, based on the loadings plots (Fig. 6), could reveal subtle differences in amino acids composition between the *outermost regions* of different surfaces (Fig. 5). The determined compositions are grouped in four clusters of data

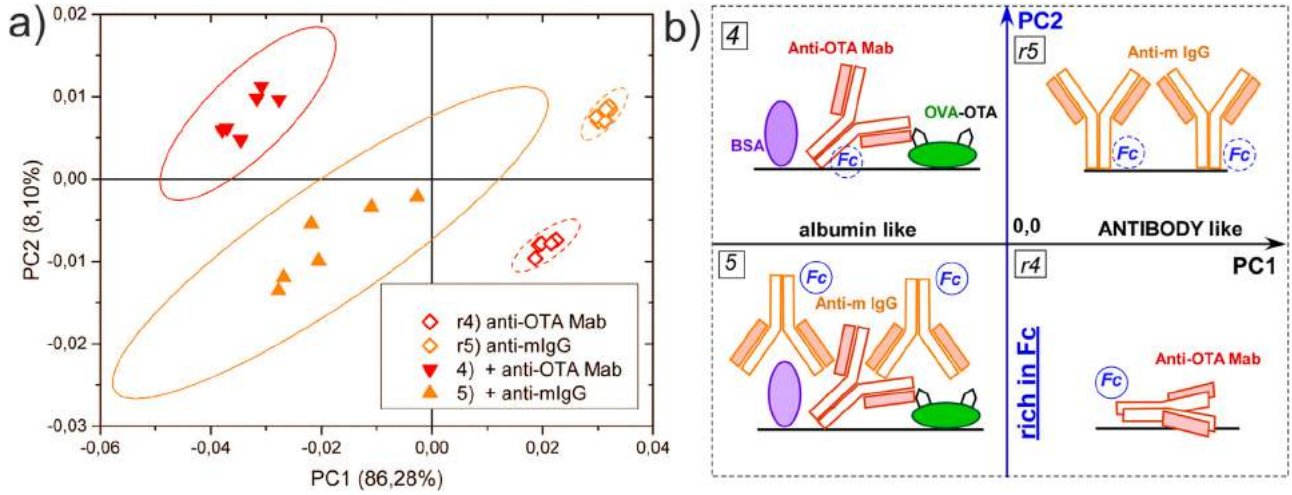


**Fig. 5.** (a) PCA scores plot (loadings for PC1 and PC2 are shown in Fig. 6) of the TOF-SIMS spectra recorded for functionalized $Si_3N_4$ surfaces after immunoreaction with primary (**4**) and secondary antibody (**5**) as well as for the reference surfaces (**r4**, **r5**) spotted directly with each one of the antibodies. The ellipses drawn around each of the grouped data points (solid lines for the surfaces (**4**), (**5**), and dashed lines for the references (**r4**), (**r5**)) represent the 95% confidence limit. (b) Molecular arrangement and orientation of primary and secondary antibody deduced for the surfaces examined with PCA in (a).

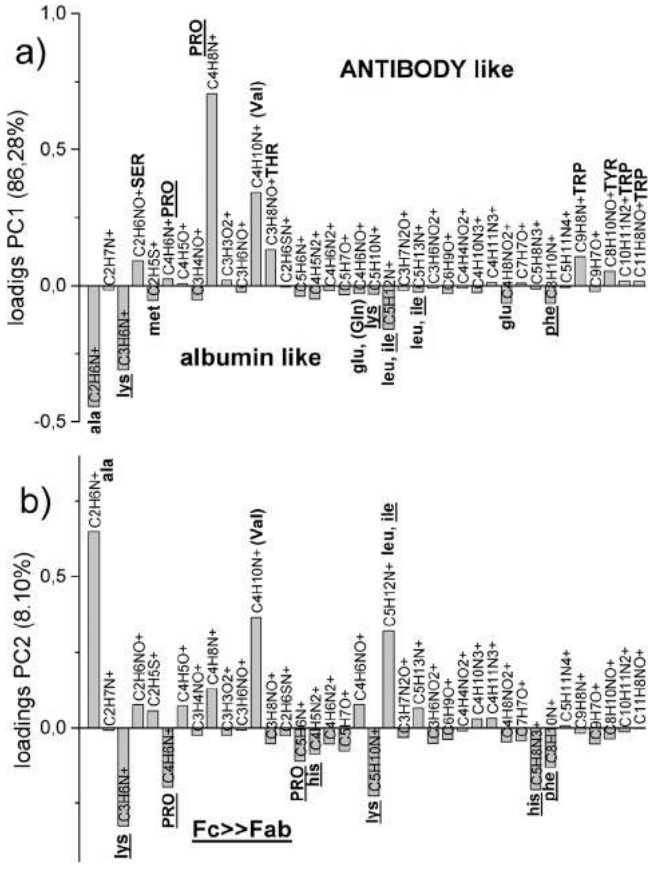


**Fig. 6.** Loadings plots for (a) the first and (b) the second Principal Component in Fig. 5a. Amino acids are attributed to the secondary ions based on Ref. [30] and supplemented by Ref. [4]. (a) PC1 is loaded positively by the signals from amino acids (marked with all-caps) with higher content in antibody than in albumin molecules (see Table 1). The amino acids yielding ion fragments loading negatively the PC1 (distinguished by lowercase) originate from albumin (OVA or BSA) rather than antibody molecules (Table 1). Other amino acids are marked by abbreviations given in brackets. (b) PC2 reflects the second major variation in TOF-SIMS data that is uncorrelated with that of PC1. PC2 is loaded negatively by ion fragments of the amino acids (underlined, see Table 1) characteristic for Fc fragment – indicating an antibody orientation that exposes the Fc fragment.

points, centered in different quadrants of the coordinate system PC1 vs. PC2. The first PC, resolving albumins from antibody molecules, have generally negative values for functionalized surfaces on which albumins have been immobilized (**4** and **5**), and positive values for reference surfaces spotted directly with antibodies (**r4** and **r5**). Additional coverage with secondary antibody (**5**) that reduces accessibility of albumins by TOF-SIMS, yields in negative PC1 values of lower magnitude for the cluster center.

The second PC resolves the different antibody orientations, with the exposure of Fc fragments indicated by the negative PC2 values. The sign of PC2 coordinate (see Fig. 5) changes for the data points corresponding to both the reference (**r4**, **r5**) and the indirect immunoassay surfaces (**4**, **5**). On the surfaces where the antibodies have been immobilized by direct spotting, the orientation of IgG molecules switches from *flat-on* alignment at low coverages (**r4**) to more *end-on* orientation for higher antibody surface density (**r5**). This is accompanied by reduced exposure of Fc fragments and increased exposure of Fab fragments, which leads to change of PC2 values from negative to positive. A less pronounced PC2 values change would be expected when the orientation switches to head-on or side-on alignment (alternatives suggested by ellipsometry) which correspond to more or less exposed Fc fragments, respectively.

In turn, the negative PC2 values for the cluster center corresponding to the functionalized surfaces after the second immunoreaction (see (**5**) in Fig. 5) reflect dominant *head-on*, hence Fc up, orientation of IgG molecules for the secondary antibodies that are bound to the multi-molecular monolayer containing the primary antibodies. In contrast, the positive PC2 values describe the primary antibodies that were embedded to the monolayer during the first immunoreaction (**4**), with a *side-on* orientation of the antibody molecules that leads to reduced exposure of Fc fragments. The embedment of primary antibody molecule between the BSA and OTA-OVA molecules, and the slight tilt of antibody due to specific binding of its Fab unit to exposed OTA moieties of the immobilized OTA-OVA conjugate, result to an additional shielding of the Fc fragments (see Fig. 5b). In contrast to these observations, an alternative head-on orientation, preselected also by ellipsometry for (**4**), with Fab units oriented towards the OTA-OVA conjugate, would result in negative PC2 values.

Taking it overall, our analysis shows that PCA of TOF-SIMS data specifies which molecular orientations, preselected by ellipsome-

try, are in fact acquired by the antibody molecules. In addition, the PCA shows that the dominant antibody orientation could be defined by the molar binding ratio for immunoadsorbed onto the surface antibodies (**4**, **5**) or the surface density in case of directly adsorbed onto the surface antibodies (**r4**, **r5**).

## 4. Conclusions

A procedure for silicon nitride surface functionalization and performance of an indirect immunoassay for detection of the mycotoxin OchraToxin A is examined *step-by-step* with multiple surface techniques including AFM, TOF-SIMS and ellipsometry. The analysis of the data received from the three techniques provides information not only about the molecular arrangement and composition of the protein layer and the changes after each step but also about the orientation of primary and secondary antibody.

Partial desorption of probe (OTA-OVA conjugate) and blocking protein (BSA) molecules is witnessed by TOF-SIMS during the immunoreaction with the primary (anti-OTA Mab) antibody. Moreover, AFM, TOF-SIMS and ellipsometry data reveal a *complex multi-component monolayer*, which accommodates primary antibodies along with the OTA-OVA and BSA molecules, and is covered by secondary antibodies after the completion of the immunoassay procedure. In addition, the AFM-based analysis resolves *specific surface features*, such as grouped secondary antibodies, that correspond to a binding molar ratio of ~2.5.

Analysis by ellipsometry and AFM, further supported by PCA analysis of TOF-SIMS data, provides also some hints about the *orientation of the immunoadsorbed primary and secondary antibody molecules* as compared to the orientations the same antibodies acquire when are directly immobilized onto the surfaces by spotting. In particular, this comparison revealed that the dominant antibody orientation is defined in the case of the immunoadsorbed antibodies by the molar binding ratio (changing from side-on to head-on as the molar binding ratio increases) or by the surface density (changing from flat-on to end-on as the surface density increases).

The concluded dominant IgG orientations result from a compromise between electrostatic and van der Waals forces [4,6,7,33,34] to which specific immunochemical reactions are ascribed. Thus, the flat-on orientation, expected for van der Waals interactions with the positively charged amino-terminated surface [4,7,33], changes into an end-on alignment as the surface coverage with the IgG increases due to accumulation of electric dipoles [4,6,33]. In turn, the combination of electrostatic interactions between the surface and the antibody Fc unit along with the specific Fab binding to the immobilized OTA-OVA molecule leads to the side-on orientation for the primary antibody and its embedment in the multi-molecular monolayer consisting also of OTA-OVA and BSA molecules. Finally, a head-on orientation is expected for the secondary antibodies that are immunoadsorbed onto the primary antibodies of the protein monolayer.

## Acknowledgments

This work was supported by the EU funded project "FOODSNIFFER" (FP7-ICT8-318319) and sponsored from the Polish state funds for science in the years 2014–15 granted for the realization of co-financed international project. The equipment used was purchased thanks to the financial support of the European Regional Development Fund (POIG.02.01.00-12-023/08). One of us (K.G.) is grateful for financial support from the M. Smoluchowski Kraków Research Consortium (in the framework of the KNOW scholarship).

## Appendix A. Supplementary data

Supplementary data associated with this article can be found, in the online version, at http://dx.doi.org/10.1016/j.colsurfb.2016.11.009.

## References

[1] R.S. Yalow, S.A. Berson, Nature 184 (1959) 1648–1649.
[2] T. Holford, F. Davis, S. Higson, Biosens. Bioelectron. 34 (2012) 12–24.
[3] K. Awsiuk, A. Budkowski, M.M. Marzec, P. Petrou, J. Rysz, A. Bernasik, Langmuir 30 (2014) 13925–13933.
[4] H. Wang, D.G. Castner, B.D. Ratner, S. Jiang, Langmuir 20 (2004) 1877–1887.
[5] X. Zhao, F. Pan, B. Cowsill, J.R. Lu, Langmuir 27 (2011) 7654–7662.
[6] S. Chen, L. Liu, J. Zhou, S. Jiang, Langmuir 19 (2003) 2859–2864.
[7] M.E. Wiseman, C. Frank, Langmuir 28 (2012) 1765–1774.
[8] A. Makky, T. Berthelot, C. Feraudet-Tarisse, H. Volland, P. Viel, J. Polesel-Maris, Sens. Actuators B 162 (2012) 269–277.
[9] P. de Thier, J. Bacharouche, J. Duval, S. Skali-Lami, G. Francius, Biochim. Biophys. Acta 1854 (2015) 138–145.
[10] K. Gajos, M. Angelopoulou, P. Petrou, K. Awsiuk, S. Kakabakos, W. Haasnoot, A. Bernasik, J. Rysz, M.M. Marzec, K. Misiakos, I. Raptis, A. Budkowski, Appl. Surf. Sci. 385 (2016) 529–542.
[11] (a) K. Awsiuk, A. Budkowski, P. Petrou, A. Bernasik, M.M. Marzec, S. Kakabakos, J. Rysz, I. Raptis, Colloids Surf. B 103 (2013) 253–260; (b) ibid. 90 (2012) 159–168.; (c) ibid. 11 (2013) 217–224.
[12] V. Lebec, S. Boujday, C. Poleunis, C.M. Pradier, A. Delcorte, J. Phys. Chem. C 118 (2014) 2085–2092.
[13] A.K. Trilling, J. Beekwilder, H. Zuilhof, Analyst 138 (2013) 1619–1627.
[14] N. Tajima, M. Takai, K. Ishihara, Anal. Chem. 83 (2011) 1969–1976.
[15] V. Pagkali, P.S. Petrou, A. Salapatas, E. Makarona, J. Peters, W. Haasnoot, G. Jobst, A. Economou, K. Misiakos, I. Raptis, S.E. Kakabakos, J. Hazard, Mater (2016) http://dx.doi.org/10.1016/j.jhazmat.2016.03.019.
[16] S. Muramoto, J. Brison, D.G. Castner, Anal. Chem. 84 (2012) 365–372.
[17] H.R. Philipp, J. Electrochim. Soc. 120 (1973) 295–300.
[18] J.A. Howarter, J.P. Youngblood, Langmuir 22 (2006) 11142–11147.
[19] J. Kim, J. Cho, P.M. Seidler, N.E. Kurland, V.K. Yadavalli, Langmuir 26 (2010) 2599–2608.
[20] J.H. Wang, J. Am. Chem. Soc. 76 (1954) 4755–4763.
[21] K. Rezwan, L.P. Meier, M. Rezwan, J. Vörös, M. Textor, L.J. Gauckler, Langmuir 29 (2004) 10055–10061.
[22] K.B. Lee, S.J. Park, C.A. Mirkin, J.C. Smith, M. Mrksich, Science 295 (2002) 1702–1705.
[23] J. Buijs, J.W. Lichtenbelt, W. Norde, J. Lyklema, Colloids Surf. B 5 (1995) 11–23.
[24] Universal Protein Resource. http://www.uniprot.org. (Accessed 22 April 2015) ID: P01012 and P02769.
[25] A.P. Cuypers, J.W. Corsel, M.P. Janssen, J.M. Kop, W.T. Hermens, H.C. Hemker, J. Biol. Chem. 258 (1983) 2426–2431.
[26] X.V. Eydne, P. Bertrand, Appl. Surf. Sci 141 (1999) 1.
[27] Y.-P. Kim, M.-Y. Hong, H.-K. Shon, D.-W. Moon, H.-S. Kim, T.-G. Lee, Appl. Surf. Sci. 252 (2006) 6801.
[28] M. Rabe, D. Verdes, S. Seeger, Adv. Colloid Interface Sci. 162 (2011) 87–106.
[29] Z. Adamczyk, Curr. Opin. Colloid Interface Sci. 17 (2012) 173–186.
[30] M.S. Wagner, D.G. Castner, Langmuir 17 (2001) 4649–4660.
[31] E. Kosobrodova, R.T. Jones, A. Kondyurin, W. Chrzanowski, P.J. Pigram, D.R. McKenzie, M.M.M. Bilek, Acta Biomater. 19 (2015) 128–137.
[32] F. Liu, M. Dubey, H. Takahashi, D.G. Castner, D.W. Grainger, Anal. Chem. 82 (2010) 2947–2958.
[33] J. Zhou, H.-K. Tsao, Y.-J. Sheng, S. Jiang, J. Chem. Phys. 121 (2004) 1050.
[34] K. Awsiuk, A. Budkowski, P. Petrou, M.M. Marzec, M. Biernat, T. Jaworska-Gołąb, J. Rysz, Colloids Surf. B 148 (2016) 278.

**Supplementary Data**

# Indirect immunoassay on functionalized silicon surface: molecular arrangement, composition and orientation examined step-by-step with multi-technique and multivariate analysis

*Katarzyna Gajos[1], Andrzej Budkowski[1], Varvara Pagkali[2], Panagiota Petrou[2], Monika Biernat[1], Kamil Awsiuk[1], Jakub Rysz[1], Andrzej Bernasik[3], Konstantinos Misiakos[4], Ioannis Raptis[4], Sotirios Kakabakos[2]*

*[1]M. Smoluchowski Institute of Physics, Jagiellonian University, Łojasiewicza 11, 30-348 Kraków, Poland*

*[2]Institute of Nuclear & Radiological Sciences & Technology, Energy & Safety NCSR Demokritos, P. Grigoriou & Neapoleos St, Aghia Paraksevi 15310, Athens, Greece*

*[3]Faculty of Physics and Applied Computer Science, AGH University of Science and Technology, Mickiewicza 30, 30-059 Kraków, Poland*

*[4]Department of Microelectronics, Institute of Nanoscience and Nanotechnology, NCSR Demokritos, P. Grigoriou & Neapoleos St, Aghia Paraksevi 15310, Athens, Greece*

## S1. Comparison of amino acid composition of model antibodies

Regarding the amino-acid composition of different IgG isotypes the relative literature data indicate that they are similar to a high degree, e.g., more than 90% for human IgG [RS1].

In addition, the primary (mouse anti-OTA Mab) is, as stated by the manufacturer, of IgG1, κ isotype and the secondary antibody (goat anti-mIgG), as a polyclonal antibody against a glycoprotein should consist of IgG1, IgG2 and IgG3 isotypes, although no specific information is provided by the antibody supplier. Thus, we consider that by adopting in the present study, for both the primary and the secondary antibody, the amino acid composition provided [4] for the mouse IgG1 isotype antibody against human chorionic gonadotropin, we are not too far from the actual situation.

Nevertheless, to further support that the amino acid composition from ref. [4] is representative for the analysis of the molecular composition and antibody orientation made in this study, we compare the results of the analysis based on amino acid composition provided by ref. [4] (main text) with those obtained when the amino acid composition from two other recent publications is taken into account; the one characterizing a rat anti-mouse CD34 (IgG2a type of constant region) antibody [31], and the second a murine IgG-class antibody [32].

### S.1.1 Analysis of molecular composition

#### S.1.1.1 TOF-SIMS signals characteristic for OVA and both albumins (OVA and BSA)

Conclusions made in **Section 3.2.2** on distinguishably high concentration of methionine (met) and glutamic acid (glu) in OVA and both albumins (OVA and BSA), respectively, that make the ion fragments of these amino acids the characteristic TOF-SIMS signals (**Fig. 3**) are valid whether the antibody composition is received from reference [4], [31] or [32] (see **Table S1**).

#### S.1.1.2 The interpretation of PC1 that resolves antibody from albumins

Also, the interpretation of the first principal component PC1 (**Fig. 6a**) that resolves antibody from albumin (OVA or BSA), is not modified if antibody composition is taken from [31], [32] or [4]. This is because the explanation of mass signals with dominant negative loadings on PC1 does not change, as they originate from the set of amino acids (distinguished by bold lowercase in **Table S1**) with higher abundance in the albumin than the antibody molecule. Similarly, the interpretation of all except

one ($C_8H_{10}NO^+$ from TYR for [4, 32] and (Tyr) [31]) signals with dominant positive loadings on PC1 is not modified, as they correspond to the set of amino acids (marked with bold all-caps in **Table S1**) that have bulk composition higher for antibody that albumin molecule.

**Table S1.** Comparison of amino acid composition (%) of OVA [24], BSA [24] and model antibody from Refs. [4], [31] and [32].

| OVA (%) | BSA (%) | antibody (%) [4] | amino acid [4] | antibody (%) [31] | a.a. [31] | antibody (%) [32] | a.a. [32] |
|---|---|---|---|---|---|---|---|
| **9.1** | **8.0** | **5.1** | **ala** | **4.0** | **ala** | **3.4** | **ala** |
| 3.9 | 4.0 | 2.8 | arg | 3.2 | arg | 3.3 | arg |
| 3.9 | 2.4 | 4.6 | (Asn) | 4.6 | (Asn) | 5.3 | ASN |
| 4.4 | 6.9 | 4.8 | asp | 3.7 | asp | 4.3 | asp |
| 0.3 | 6.0 | 2.0 | cys | 2.1 | cys | 2.6 | cys |
| **3.9** | **3.4** | **4.3** | **(Gln)** | **5.2** | **GLN** | **3.7** | **(Gln)** |
| **8.8** | **10.1** | **5.1** | **glu** | **3.9** | **glu** | **4.8** | **glu** |
| 4.9 | 2.7 | 5.4 | (Gly) | 7.1 | GLY | 6.5 | GLY |
| 1.8 | 2.9 | 1.9 | his | 2.5 | (His) | 2.0 | his |
| **6.5** | **2.4** | **3.4** | **ile** | **3.8** | **ile** | **3.4** | **ile** |
| **8.3** | **10.5** | **5.9** | **leu** | **7.7** | **leu** | **5.9** | **leu** |
| **5.2** | **10.1** | **6.2** | **lys** | **6.0** | **lys** | **6.0** | **lys** |
| **4.4** | **0.7** | **2.0** | **met** | **1.4** | **met** | **2.0** | **met** |
| **5.2** | **4.6** | **3.9** | **phe** | **4.0** | **phe** | **3.1** | **phe** |
| **3.6** | **4.8** | **6.3** | **PRO** | **6.6** | **PRO** | **6.8** | **PRO** |
| **9.8** | **4.8** | **12.5** | **SER** | **12.4** | **SER** | **12.4** | **SER** |
| **3.9** | **5.7** | **8.8** | **THR** | **9.1** | **THR** | **8.9** | **THR** |
| **0.8** | **0.3** | **2.0** | **TRP** | **1.8** | **TRP** | **2.0** | **TRP** |
| **2.6** | **3.4** | **4.6** | **TYR** | **3.2** | **(Tyr)** | **5.0** | **TYR** |
| **8.0** | **6.2** | **8.3** | **(Val)** | **7.8** | **(Val)** | **9.0** | **(Val)** |

Notation used: all-caps for both antibody/BSA and antibody/OVA > 1.25; lowercase for either BSA/antibody or OVA/antibody > 1.25; abbreviations in brackets for other amino acids. Bold for amino acids that contribute to the mass signals with dominant loadings on PC1 (see **Fig. 6a**).

### S.1.2 Analysis of antibody orientation

Finally, the interpretation of the second principal component PC2 (**Fig. 6b**), that resolves antibody orientation (in particular IgG orientation with exposed the Fc fragment deduced from the negative PC2 loadings), remains the same whether antibody composition is taken from [31], [32] or [4]. This is verified by the loadings on PC2 from mass signals that are the fragments of amino acids plotted in **Fig. S1** versus the ratio of amino acids in Fc and $F(ab')_2$ subunits [$Fc/F(ab')_2$], reported in [4] **(Fig.S1a)**,

[31] **(Fig.S1b)** and [32] **(Fig.S1c)**, respectively. Indeed, the relation between the sign of the PC2 loadings of the dominant mass signals and the amino acid ratio Fc/F(ab')$_2$ is preserved, regardless of the exact amino acid composition of model antibody [4, 31, 32].

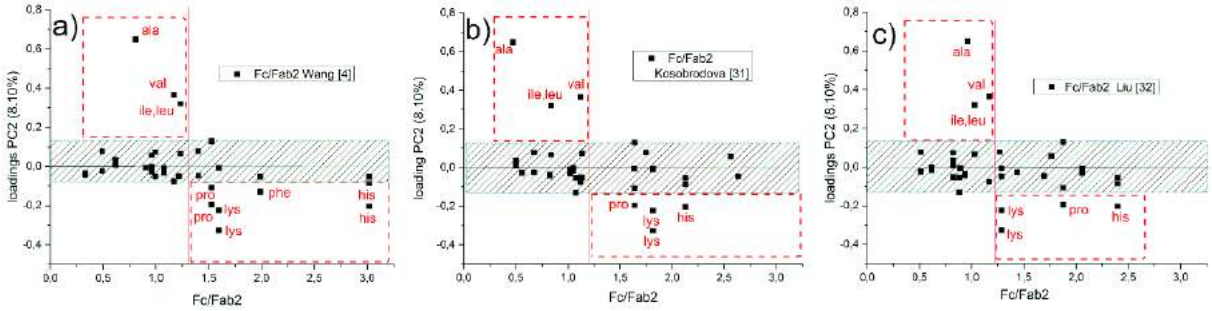


**Fig. S1.** Loadings on PC2 (shown in **Fig. 6b**) from mass signals that are the fragments of amino acids, plotted versus the amino acid ratio in Fc and F(ab')$_2$ subunits, Fc/F(ab')$_2$, reported in [4] **(a)**, [31] **(b)** and [32] **(c)**. Average Fc/F(ab')$_2$ values are used for the signals that correspond to amino acid pairs. Hatched areas mark data points that correspond to mass signals with lower values of PC2 loadings.

[RS1] G. Vidarsson, G. Dekkers, T. Rispens, Front. Immunol. 5 (2014) 520.

# Paper V

## *Contact pin-printing of albumin-fungicide conjugate for silicon nitride-based sensors biofunctionalization: Multi-technique surface analysis for optimum immunoassay performance*

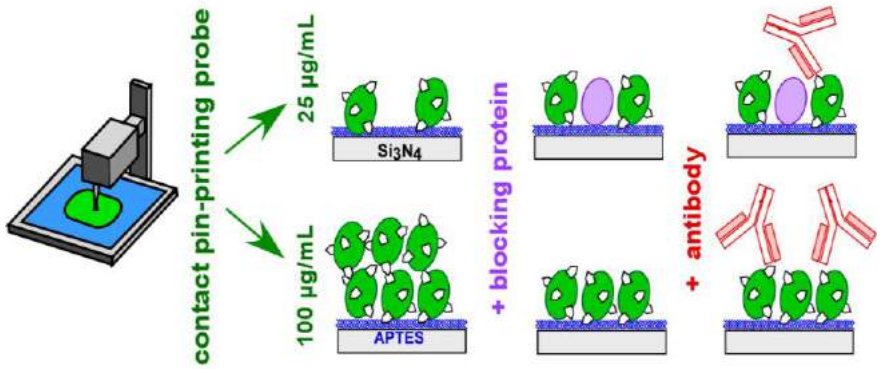


Highlights

- Contact pin-printing of overlapping probe spots and spotting by hand are compared.
- Contact pin-printing favors probe immobilization with two-fold higher surface density.
- Incomplete monolayer develops to bilayer as printing solution concentration increases.
- Blocking molecules complete probe monolayer but reduce probe bilayer.
- Surface immunoreaction increases with probe concentration in printing solution.

Applied Surface Science 410 (2017) 79–86

Contents lists available at ScienceDirect

Applied Surface Science

journal homepage: www.elsevier.com/locate/apsusc

Full Length Article

# Contact pin-printing of albumin-fungicide conjugate for silicon nitride-based sensors biofunctionalization: Multi-technique surface analysis for optimum immunoassay performance

Katarzyna Gajos[a,*], Andrzej Budkowski[a], Zoi Tsialla[b], Panagiota Petrou[b], Kamil Awsiuk[a], Paweł Dąbczyński[a], Andrzej Bernasik[c,d], Jakub Rysz[a], Konstantinos Misiakos[e], Ioannis Raptis[e], Sotirios Kakabakos[b]

[a] M. Smoluchowski Institute of Physics, Jagiellonian University, Łojasiewicza, 11, 30-348 Kraków, Poland
[b] Institute of Nuclear & Radiological Sciences & Technology, Energy & Safety, NCSR Demokritos, P. Grigoriou & Neapoleos St., Aghia Paraksevi 15310, Athens, Greece
[c] Faculty of Physics and Applied Computer Science, AGH University of Science and Technology, Mickiewicza 30, 30-059 Kraków, Poland
[d] Academic Centre for Materials and Nanotechnology, AGH University of Science and Technology, Mickiewicza 30, 30-059 Kraków, Poland
[e] Department of Microelectronics, Institute of Nanoscience and Nanotechnology, NCSR Demokritos, P. Grigoriou & Neapoleos St., Aghia Paraksevi 15310, Athens, Greece

ARTICLE INFO

*Article history:*
Received 7 February 2017
Received in revised form 8 March 2017
Accepted 9 March 2017
Available online 11 March 2017

*Keywords:*
Immunosensor biofunctionalization
Contact pin-printing
Silicon nitride
Atomic force microscopy
Time-of-flight secondary ion mass spectrometry
Spectroscopic ellipsometry

ABSTRACT

Mass fabrication of integrated biosensors on silicon chips is facilitated by contact pin-printing, applied for biofunctionalization of individual $Si_3N_4$-based transducers at wafer-scale. To optimize the biofunctionalization for immunochemical (competitive) detection of fungicide thiabendazole (TBZ), $Si_3N_4$ surfaces are modified with (3-aminopropyl)triethoxysilane and examined after: immobilization of BSA-TBZ conjugate (probe) from solutions with different concentration, blocking with bovine serum albumin (BSA), and immunoreaction with a mouse monoclonal antibody against TBZ. Nanostructure, surface density, probe composition and coverage uniformity of protein layers are evaluated with Atomic Force Microscopy, Spectroscopic Ellipsometry, Time-of-Flight Secondary Ion Mass Spectrometry and X-ray Photoelectron Spectroscopy. Contact pin-printing of overlapping probe spots is compared with hand spotted areas. Contact pin-printing resulted in two-fold increase of immobilized probe surface density as compared to hand spotting. Regarding BSA-TBZ immobilization, an incomplete monolayer develops into a bilayer as the concentration of BSA-TBZ molecules in the printing solution increases from 25 to 100 μg/mL. Upon blocking, however, a complete protein monolayer is formed for all the BSA-TBZ concentrations used. Free surface sites are filled with BSA for low surface coverage with BSA-TBZ, whereas loosely bound BSA-TBZ molecules are removed from the BSA-TBZ bilayer. As a consequence immunoreaction efficiency increases with the printing probe concentration.

© 2017 Elsevier B.V. All rights reserved.

## 1. Introduction

Surface functionalization with biomolecules is a crucial issue for the development of biosensors aiming to applications in medical diagnostics, monitoring of food safety or drug screening. The miniaturization and realization of arrays of multiple biosensors in a confined surface area often require the precise spatially resolved immobilization of probe molecules. For this purpose, besides the microfluidic-based approaches [1], surface patterning methods such as photolithography, soft lithography and printing are commonly used [2,3]. In particular, mass fabrication of integrated biosensors on silicon chips is facilitated by contact pin-printing technique, initially developed and established for the fabrication of DNA and protein microarrays [4,5]. Due to its simplicity and facile maintenance combined with high spots reproducibility contact pin-printing is nowadays the most prevalent microarrays fabrication technology [4], easily adapted for formation of arbitrary biomolecules patterns by spatially controlled solution deposition. This method has been already applied for biofunctionalization of individual transducers on silicon chips integrating arrays of interferometric biosensors [6–9].

* Corresponding author.
*E-mail address:* katarzyna.gajos@doctoral.uj.edu.pl (K. Gajos).

http://dx.doi.org/10.1016/j.apsusc.2017.03.100
0169-4332/© 2017 Elsevier B.V. All rights reserved.

The strategies for probe molecule immobilization on biosensor surfaces [10], including solution deposition by contact pin-printing, involve physical adsorption, covalent binding or affinity based interactions. All these probe immobilization strategies usually require the initial modification of substrate surface. Surface modification can be realized by means of self-assembled monolayers [6–8,11] or polymer brushes [12–15]. For biosensors with silicon-based transducer, protein immobilization by physical adsorption after surface modification with organosilanes is frequently applied, since it provides a simple but efficient approach [7,8,16–19]. However, due to the fact that the probes are not covalently attached onto the surface, there is a possibility of molecule desorption during the steps that follow their immobilization, i.e., upon blocking of free surface sites with a non-functional protein [20,21] and during specific binding reactions [6,22]. Therefore, surface examination and control of protein layer composition after each successive step of the protocol is highly desirable. The amount of biomolecules on surface could be quantified applying various spectroscopic techniques [16,23–27] often supported by Atomic Force Microscopy [23–25]. However, these methods do not discriminate between different proteins in the layer covering the sensor surface, an information that can be provided by Time-of-Flight Secondary Ion Mass Spectrometry [28]. In fact, only the step-by-step surface characterization with complementary surface science techniques allows to define the structure and composition of biomolecular layer resulting from immunoassays performed on silicon surfaces [6,22].

In this work we examine the impact of *probe surface density*, obtained during the surface biofunctionalization step by *contact pin-printing*, on protein layer composition created after each assay step and how this affects the assay performance. In particular, an immunoassay for detection of the fungicide thiabendazole (TBZ) based on surface functionalization by immobilization of a TBZ-conjugate with bovine serum albumin (BSA-TBZ) and subsequent blocking with BSA, followed by immunoreaction with a monoclonal anti-TBZ antibody is studied. The contact pin-printing is compared with solution deposition by hand using a precision pipette i.e., by macro-spotting. Complementary information about nanostructure, surface density and probe composition are provided by Atomic Force Microscopy, Spectroscopic Ellipsometry (as well as X-ray Photoelectron Spectroscopy) and Time-of-Flight Secondary Ion Mass Spectrometry, respectively. As a result the optimum conditions for the immunoassay are determined and related with surface phenomena taking place upon biofunctionalization.

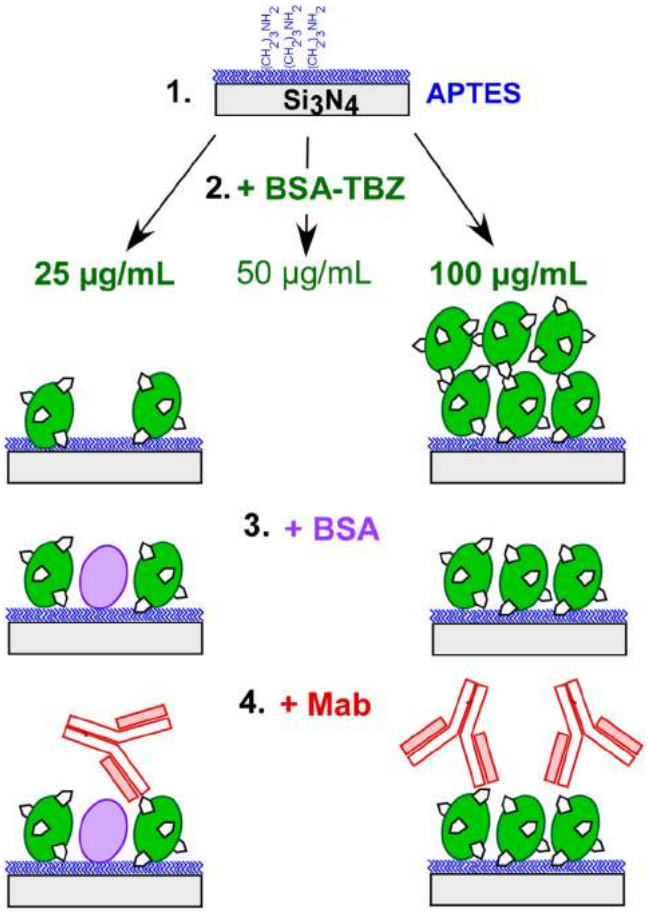


**Fig. 1.** Schematic of the procedure employed for biofunctionalization of $Si_3N_4$ surfaces and subsequent immunoassay for detection of fungicide TBZ. $Si_3N_4$ surfaces were modified with APTES (**1**), spotted with BSA-TBZ conjugate (probe) using solutions with different concentrations (25, 50 and 100 µg/mL) (**2**), blocked with BSA (**3**), and exposed to a solution of monoclonal antibody against TBZ (Mab) (**4**).

## 2. Experimental

### 2.1. Materials

Silicon wafers were purchased from Si-Mat (Kaufering, Germany). 3-Aminopropyltriethoxysilane (APTES) and bovine serum albumin (BSA) were purchased from Sigma-Aldrich (Darmstadt, Germany). The mouse monoclonal antibody against thiabendazole (Mab clone LIB-TN3C13), and the thiabendazole conjugate with bovine serum albumin (BSA-TN3C) were purchased from the Grupo de Inmunotecnologia of Universidad Politécnica de Valencia (Valencia, Spain) [29]. The water used throughout the study was double distilled.

### 2.2. Surface functionalization and assay protocol

The biofunctionalization and immunoassay steps are shown in Fig. 1. As a preliminary step a 1-µm thick $SiO_2$ layer and an additional 150 nm thick $Si_3N_4$ layer were created by low pressure chemical vapour deposition on silicon substrates to mimic the composition and surface properties of the waveguides of integrated on silicon Mach-Zehnder interferometers [6,30]. Cleaned and hydrophilized by oxygen plasma $Si_3N_4$ surfaces **(1)** were firstly silanized through immersion in a 0.5% (v/v) aqueous APTES solution for 2 min, followed by washing with distilled water, drying under stream of nitrogen and baking for 20 min at 120 °C. Then, two different approaches of surface functionalization with BSA-TBZ **(2)** were applied involving either contact pin-printing or hand spotting of BSA-TBZ solution. Contact pin-printing involved deposition of multiple overlapping spots over an area of 7 mm × 7 mm employing a standard microarray spotter (BioOdyssey Calligrapher Miniarrayer, Bio-Rad Inc.). For hand macro-spotting a 50 µL drop of solution was deposited on the silanized surface by pipette in order to cover approximately the same area (7 × 7 $mm^2$). The samples resulting from both spotting approaches were then incubated at room temperature in a humidity chamber for 18 h, prior to washing with 10 mM phosphate buffer, pH 7.4, containing 0.9% (w/v) NaCl and 0.05% (v/v) Tween 20. Solutions of BSA-TBZ with concentrations of 25, 50 and 100 µg/mL in 50 mM carbonate buffer, pH 9.2, were used. After that, blocking of free surface binding sites **(3)** was performed by immersing the samples in a 2% (w/v) BSA solution in 10 mM phosphate buffer, pH 7,4, containing 0.9% NaCl (w/v), followed by washing as previously. Spotted by contact pin-printing and blocked surfaces were incubated for 1 h with a 1 µg/mL solution of mouse monoclonal antibody against TBZ **(4)** in 10 mM phosphate buffer, pH 7.4, containing 0.9% (w/v) NaCl and 0.2% BSA (w/v) and after that washed as previously. Prior to measurements with sur-

face science techniques all the samples were gently washed with distilled water and dried under stream of nitrogen.

Apart from planar samples, the same functionalization and assay protocol was performed on silicon chips with integrated Mach-Zehnder interferometers. The chip sensing regions are defined as 600-μm long and 20-μm wide windows on the 2.5 μm thick $SiO_2$ cladding layer deposited over the planar $Si_3N_4$ waveguides. The detailed chip structure as well as fabrication and functionalization procedure were described in previous publication [6]. Due to the geometry of the sensing arm windows, the functionalized chips were characterized only with TOF-SIMS spectrometry.

### 2.3. Surface characterization with AFM

Topography AFM images of planar $Si_3N_4$ surfaces were recorded after each functionalization and assay steps under ambient conditions with an Agilent 5500 microscope working in non-contact mode. AFM probes with spring constant about 2 N/m, tip radius below 10 nm and resonant frequencies about 70 kHz were used. For each sample AFM micrographs were taken at several different areas. The WSxM software provided by Nanotec Electronica S.L. [31] (downloadable at http://www.nanotec.es) was applied for the analysis of AFM images.

### 2.4. Protein surface density evaluation with spectroscopic ellipsometry

The ellipsometry measurements were performed with a Sentech SE800 (Sentech Instruments GmBH) Spectroscopic Ellipsometer over a wavelength range of 320–700 nm and at a fixed angle of incidence equal to 70°. Results were analyzed with the SpectraRay 3 software. For the estimation of the average thickness of protein layer the Cauchy dispersion model was assumed and the three-layer model consisted of silicon substrate/$Si_3N_4$/mixed $SiO_2$ and APTES/protein layer was applied. Fixed refractive index values equal to n = 3.87 for Si, n = 2.01 for $Si_3N_4$ [32], n = 1.46 for both $SiO_2$ and APTES [33], and n = 1.53 [34] for proteins were used. A constant thickness of 96.9 nm for the $Si_3N_4$ layer and 13.1 nm for the mixed $SiO_2$ and APTES layer, obtained from fitting measurements performed on bare APTES modified surface, were taken into account to fit the thickness of protein layer. The protein surface density was estimated following the Cuypers one-component approach: $\Gamma = D^*\rho = d^*(M/A)^*(n_p^2-1)/(n_p^2+2)^2$ [35]. A value of refractive index, $n_p = 1.53$ [34], and a ratio of molecular weight to molar refractivity, M/A = 4.14 g/mL [35] are assumed for all the proteins [34,35].

### 2.5. Molecular surface characterization with TOF-SIMS

Surface characterization was performed using the TOF.SIMS 5 (ION-TOF GmbH) instrument, equipped with a 30 keV bismuth liquid metal ion gun. The $Bi_3^+$ clusters were used as primary ions with the ion dose density lower than $10^{12}$ ion/cm$^2$ to ensure static mode conditions. Low energy electron flood gun was used for charge compensation. For planar samples, positive ion high mass resolution TOF-SIMS spectra were acquired from several non-overlapping 100 μm × 100 μm areas of each sample (applied resolution was 128 × 128 points). In case of silicon chips with integrated Mach-Zechner interferometers, spectra were acquired from 500 μm × 500 μm areas (applied resolution was 512 × 512 points), thus covering the whole area of the single sensing arm. Molecular analysis was performed with the analyzed area of 15 μm × 480 μm located always inside each individual sensing region. Mass calibration was performed with $H^+$, $H_2^+$, $CH^+$, $C_2H_2^+$ and $C_4H_5^+$ peaks. Minimal mass resolution ($m/\Delta m$) > 5400 at $C_4H_5^+$ was obtained. TOF-SIMS data were normalized with respect to the total ion intensity.

### 2.6. XPS surface characterization

X-ray photoelectron spectroscopy measurements were performed applying a Versa Probe II (ULVAC-PHI) spectrometer equipped with an Al Kα radiation source (1486.6 eV). For all measurements a photoelectron take-off angle equal to 45° was applied and a dual-beam charge neutralizer was used to compensate for charge-up effects. High resolution spectra were collected with an analyzer pass energy of 23.5 eV. All XPS peaks were referenced to the hydrocarbon (C—C) C 1s peak at 284.8 eV and a Shirley background was subtracted.

## 3. Results and discussion

The reagents and assay protocol employed in this study were already implemented in a competitive indirect enzyme immunoassay for the determination of TBZ contaminations in wine samples [36]. In the present work such immunoassay was adapted to $Si_3N_4$ surface mimicking the surface of waveguides of integrated Mach-Zehnder interferometric biosensors on silicon chips [6,31]. A schematic of the $Si_3N_4$ surface biofunctionalization and subsequent immunoassay procedure is provided in Fig. 1. In brief, the whole procedure consists of the following steps: **(1)** chemical modification with amino-silane (APTES), **(2)** immobilization of BSA-TBZ conjugate probe by spotting from solutions with the 3 different concentrations 25, 50 and 100 μg/mL, **(3)** blocking of free surface sites with BSA, and finally **(4)** binding of the mouse monoclonal antibody against TBZ. While the amino-silanization of $Si_3N_4$ surface **(1)** is well described in literature [6,20,22,23], the other steps **(2–4)** are analyzed here with surface science techniques for the first time in order to optimize the procedure depicted in Fig. 1 and especially, the probe immobilization through contact pin-printing of overlapping spots **(2)**. All the surfaces examined in the present study correspond to zero calibrator of a competitive immunoassay format, i.e., a pure antibody solution not containing an analyte, resulting in the maximum signal obtained during the immunoassay.

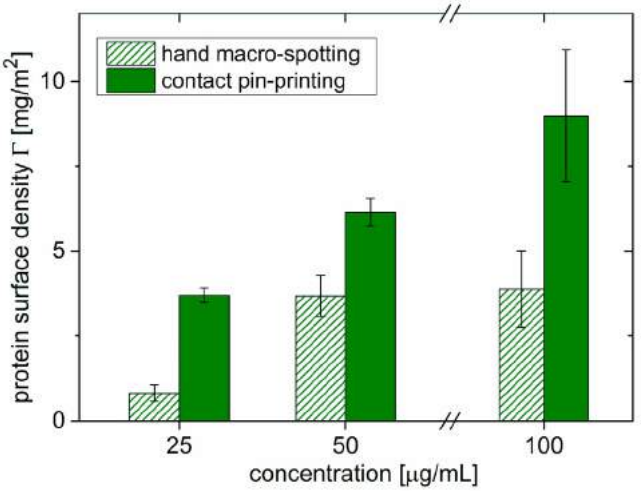


**Fig. 2.** Protein surface density Γ determined by ellipsometry for silanized $Si_3N_4$ surfaces functionalized with BSA-TBZ solutions with concentrations ranging from 25 to 100 μg/mL by hand macro-spotting (dashed columns) or contact pin-printing (filled columns). Error bars are standard deviations determined from 5 ellipsometric measurements of the same surface.

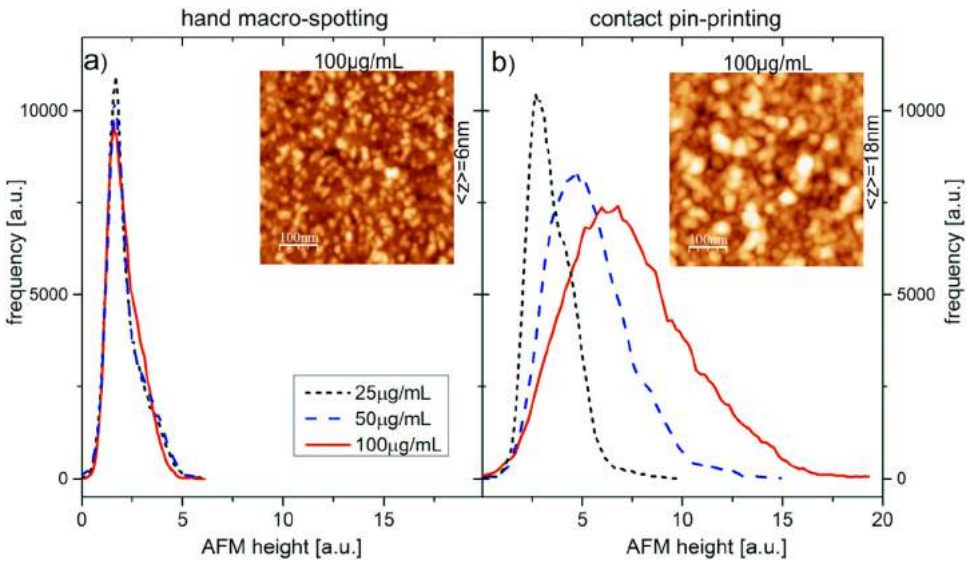


**Fig. 3.** AFM characterization of $Si_3N_4$ surface after functionalization with BSA-TBZ conjugate by hand macro-spotting (a) or contact pin-printing (b). The height histograms were determined from AFM images recorded from surfaces functionalized using solutions with different concentration of BSA-TBZ. Representative AFM micrographs of the surfaces prepared with both spotting techniques applying a 100 µg/mL BSA-TBZ solution are provided in inset images.

### *3.1. Probe immobilization: contact pin-printing vs. hand macro-spotting*

To optimize immobilization of BSA-TBZ onto silicon nitride surfaces two different strategies of solution deposition such as spotting multiple overlapping spots employing the contact pin-printing technique or placement of microlitre drops by pipette (hand macro-spotting) were compared for different solution concentrations. The probe surface density in the formed layers was evaluated from spectroscopic ellipsometry measurements as described in Section 2.4, while its nanostructure was revealed by AFM.

The protein surface density increases with solution concentration for both immobilization approaches as presented in Fig. 2. Contact pin-printing provides, however, much higher immobilization efficiency than hand macro-spotting, resulting in almost twice the protein surface density. A similar observation regarding the increased amount of immobilized molecules with respect to immobilization on large area by manual solution deposition was reported earlier for single spots of DNA [37] or DNA-protein conjugate [38] in microarrays. This effect was attributed to the rapid evaporation of nanoliter droplets deposited by contact pin-printing, thus leading to higher molecules concentration and hence increased adsorption kinetics on the surface [39]. Here, however, such an effect was observed for deposition of multiple overlapping spots covering a broad area with dimensions in the millimeter range.

The protein surface density values achieved following the hand macro-spotting strategy are ranging from $0.8 \pm 0.2$ to $3.9 \pm 1.1$ mg/m$^2$ for solution concentrations ranging from 25 to 100 µg/mL. These values indicate formation of a protein monolayer as can be deduced from literature data that report a saturation amount for BSA adsorption onto alumina of about 4.4 mg/m$^2$ [40]. In the case of contact pin-printing strategy, application of the solution with concentration of 25 µg/mL results in a protein amount of $3.7 \pm 0.2$ mg/m$^2$, that corresponds clearly to an unsaturated protein monolayer. Higher solution concentrations, however, yield surface densities of $6.1 \pm 0.4$ mg/m$^2$ and $9.0 \pm 1.9$ mg/m$^2$ for 50 and 100 µg/mL, respectively, and lead to the formation of protein multilayers. These findings are confirmed by the AFM data presented in Fig. 3 as height histograms from the respective recorded images. Each height distribution can be analyzed in terms of its mean value or average height <*h*>, standard deviation from <*h*> given by root-mean-square RMS roughness, and total spread that reflects the extent of overlayer [20,24]. Height histograms determined for the hand macro-spotting and contact pin-printing, applying the same range of solution concentrations, differ considerably. In particular, the spread of height distribution determined for the two spotting procedures can be correlated with the dimensions of a BSA molecule ($9.0 \times 5.5 \times 5.5$ nm$^3$) [41]. For the hand macro-spotting approach and the three different probe solution concentrations applied, the height extent is not larger than ca. 6–7 nm reflecting protein distribution within an unsaturated monolayer. On the other hand, for the contact pin-printing approach the distribution's spread increases significantly above this value as the BSA-TBZ solution concentration increases. Especially, the organic layer formed by applying the 100 µg/mL BSA-TBZ solution is characterized by a height extent of about 17 nm, indicating the formation of a BSA-TBZ protein bilayer.

Taking into account the enhanced immobilization efficiency revealed for contact pin-printing as compared to hand macro-spotting, this strategy of probe solution deposition proved to be advantageous for the functionalization of integrated on chip Mach-Zehnder interferometric immunosensors, and was applied in all the herein described experiments. To examine the effect of BSA-TBZ immobilization on sensing arms of Mach-Zehnder interferometers direct molecular imaging with TOF-SIMS was applied [6]. Maps of ion $C_5H_{10}N^+$ ($m/z = 84$) derived from BSA protein [42], which are presented in Fig. S1 in Supplementary Material, confirm the uniform coverage of sensing arm areas with BSA-TBZ molecules and the increase of immobilization efficiency by increasing the protein concentration of the printed solution.

### *3.2. Surface blocking: probe desorption induced by higher surface density*

The effect of the second functionalization step, that of blocking the free surface binding sites with BSA, was also examined for surfaces prepared by contact pin-printing of BSA-TBZ molecules from solutions with 3 different concentrations. AFM characterization provided the topography images of formed protein layers (Fig. 4) as well as insight into changes in their vertical and lateral nanostructures (Fig. 5). Vertical nanostructure is described by the parameters of height distribution of the AFM image, e.g., by the

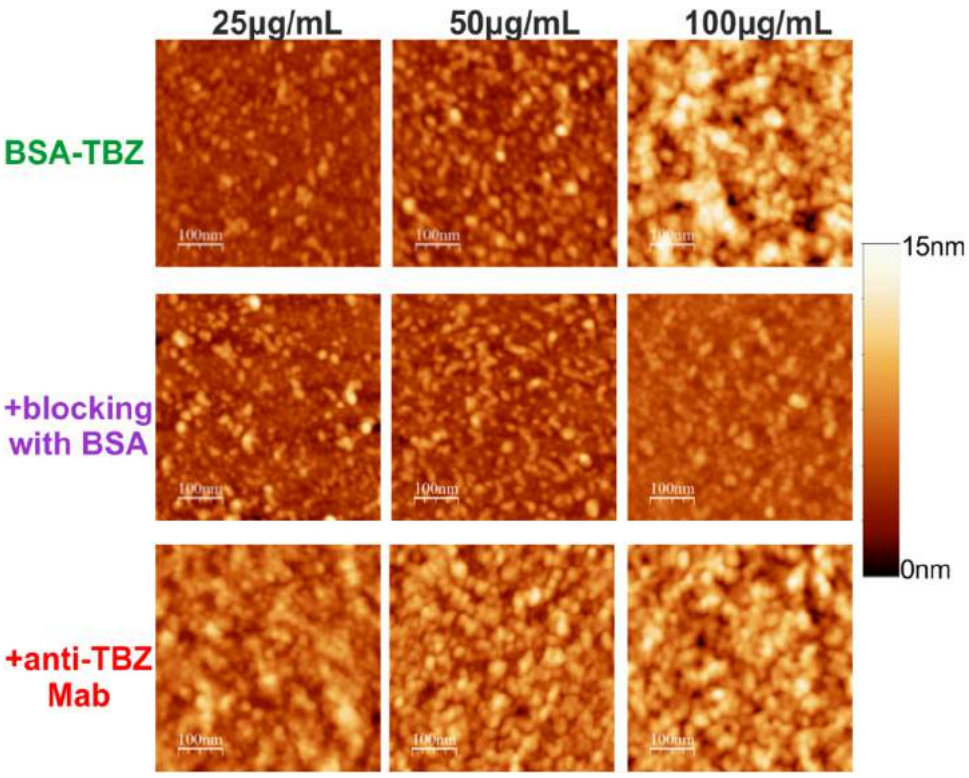


**Fig. 4.** Representative topographic AFM micrographs (with identical height-range of 15 nm) obtained from $Si_3N_4$ surfaces after contact pin-printing of BSA-TBZ solutions corresponding to different concentrations as well as the subsequent blocking and immunoreaction steps.

surface roughness, RMS [20,24]. In turn, lateral nanostructure is conveyed by the mean size of features, 2whm, determined from radial averaged autocorrelation function computed for AFM images [20,23]. The impact of blocking on the protein surface density was determined by ellipsometry (Fig. 6) and confirmed by XPS (Fig. S2 in Supplementary Material). Additionally, the relative amount of probe (BSA-TBZ) in the resulting protein layers is examined by TOF-SIMS (Fig. S3 in Supplementary Material).

The AFM data indicate that the blocking procedure leads to additional protein coverage of initially incomplete monolayer in case of the BSA-TBZ layer with the lowest surface density of ~3.7 mg/m$^2$, resulting from pin-printing from 25 µg/mL solution. A topographical change, visible in AFM image (Fig. 4), is conveyed by the significant increase of surface roughness (Fig. 5a), that depicts the vertical structures of the protein layer. On the other hand, the lateral nanostructure, characterized by surface features with mean size 2whm in the range of 20–24 nm, is hardly changed upon blocking as expected due to almost identical dimensions of BSA-TBZ and BSA molecules. In fact, the obtained mean size of features 2whm is in accordance with a predicted apparent size of BSA molecules of 18–22 nm, calculated taking into account the nominal dimensions of protein ($9.0 \times 5.5 \times 5.5$ nm$^3$ [41]) and broadening caused by the AFM tip (with 7 nm radius) [43,44]. Moreover, the increase of the surface protein amount up to ~4.9 mg/m$^2$, as determined by ellipsometry (Fig. 6), reveals the formation of a complete monolayer, consisting of both BSA-TBZ and BSA molecules. However, when the same blocking procedure was applied to the surface with the higher BSA-TBZ surface density ~9.0 mg/m$^2$, prepared by contact pin-printing of a 100 µg/mL solution, drastic reduction of both vertical extent of protein layer (Fig. 4 and Fig. 5a) and its surface density (Fig. 6) was observed. Also, the value of the features size 2whm (Fig. 5b), reflecting the high surface density of a protein bilayer (that prevents AFM image analysis from resolving individual BSA molecules), is reduced to the value characteristic for BSA. These data indicate protein desorption, while the resulting value of protein surface density of $4.8 \pm 0.5$ mg/m$^2$ points to reduction of the bilayer into a monolayer – consisting mainly of BSA-TBZ conjugate molecules. These changes of immobilized protein amount prior to and after blocking were confirmed by the XPS analysis presented in Fig. S2 in Supplementary Material. The changes of concentration of elements characteristic for protein (other contributions are negligible) and silicon substrate observed after blocking expressed as N1s/Si2p ratio, reflect changes in the protein surface coverage that match the results obtained by ellipsometry. Likewise, the concluded difference in the composition of the protein layers after blocking – with presence of mixed BSA-TBZ and BSA molecules when the 25 µg/mL printing solution was used, and essentially pure BSA-TBZ layer for the 100 µg/mL solution – is confirmed by the TOF-SIMS data (Fig. S3 in Supplementary Material). Thus, for the surfaces spotted using the 25 µg/mL BSA-TBZ solution, the intensity of TOF-SIMS signal characteristic for TBZ molecule ($C_{10}H_7N_3S^+$, $m/z = 202$ [45]) remains unchanged upon blocking, that adds the BSA molecules to the incomplete BSA-TBZ monolayer. On the other hand, for the surfaces spotted with the 100 µg/mL BSA-TBZ solution, blocking introduces a decrease in the characteristic TBZ signal to a value still higher than that for 25 µg/mL, reflecting a reduction of the pure BSA-TBZ bilayer.

In order to study in details the impact of the applied blocking procedure, the changes in both surface density and BSA-TBZ relative amount in the protein layer were analyzed more systematically with ellipsometry and TOF-SIMS for several additional samples (Fig. 7). The difference of the protein surface density (deduced from ellipsometry, Fig. 7a), and BSA-TBZ relative amount (from TOF-SIMS signal characteristic for TBZ, Fig. 7b), determined after and prior to blocking is plotted as a function of the initial amount of the immobilized probe molecules. An increase of protein surface density, accompanied with nearly unchanged intensity of the signal ascribed to TBZ conjugate, corresponds to adsorption of BSA dur-

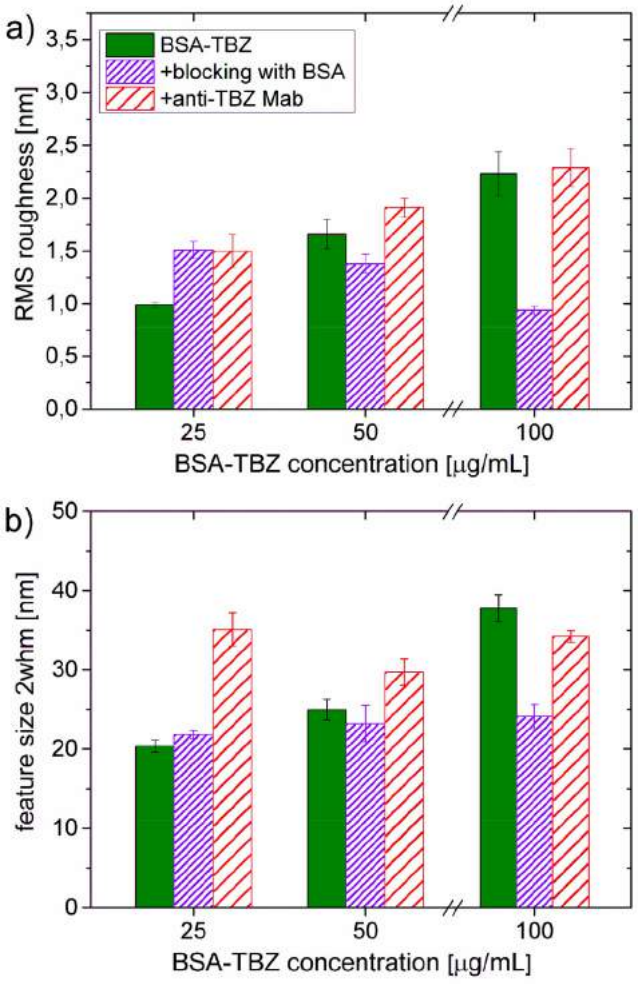


**Fig. 5.** Nanostructure parameters determined by AFM measurements of $Si_3N_4$ surfaces after each one of the functionalization and immunoassay steps corresponding to different concentrations of BSA-TBZ solution applied by contact pin-printing. (a) The root mean square roughness values were determined from AFM histograms and (b) the size of feature size 2whm was computed from the AFM topographic images. Error bars are standard deviations determined from 5 measurements of the same surface.

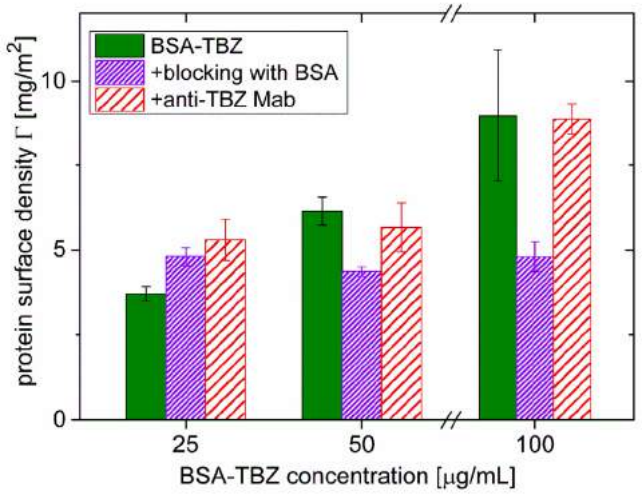


**Fig. 6.** Protein surface density Γ determined by ellipsometry for $Si_3N_4$ surfaces after functionalization by contact pin-printing of BSA-TBZ solutions of different concentration, blocking and immunoreaction steps. Error bars are standard deviations determined from 5 ellipsometric measurements of the same surface.

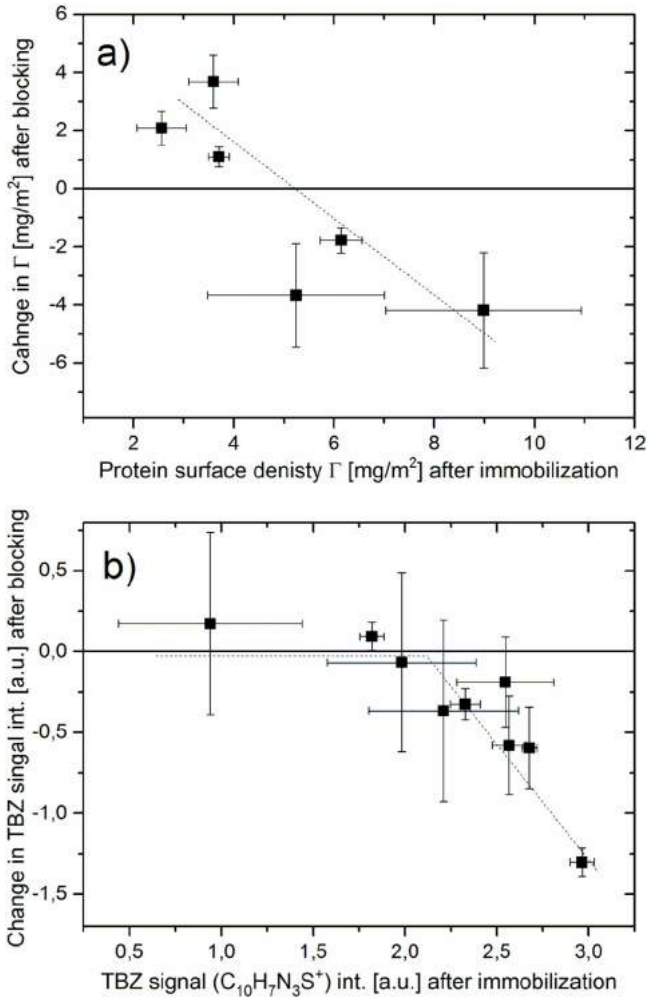


**Fig. 7.** The difference of protein surface coverage (a), and BSA-TBZ relative amount in the protein layer (b), determined after and prior to blocking procedure and plotted versus the initial amount of the immobilized probe. (a) Change of the total protein surface density deduced from ellipsometry as a function of surface density after BSA-TBZ immobilization. (b) Change of the intensity of TOF-SIMS signal ($C_{10}H_7N_3S^+$) characteristic for TBZ molecule as a function of the intensity of the same signal after BSA-TBZ immobilization. Error bars are standard deviations determined from several ellipsometric and TOF-SIMS measurements of the same surface.

ing blocking. In turn, a decrease of both the surface coverage and TBZ signal reflects desorption of BSA-TBZ conjugate molecules during blocking. The analysis performed reveals that, as the BSA-TBZ surface density increases, the effect of blocking procedure surprisingly changes from adsorption of BSA molecules to BSA-TBZ probe desorption. This reversal of the blocking step effect occurs for surface density of BSA-TBZ probe in the range of ~4.5 mg/m$^2$ that corresponds to surface coverage by a complete protein monolayer.

The change of the protein binding behavior from irreversible to reversible at a certain coverage level has been reported in several protein adsorption studies reviewed by M. Rabe [46]. In particular, for silicon surfaces modified with aminosilane similar phenomena of desorption of preadsorbed IgG during blocking with BSA at certain IgG surface density values was reported [20,21]. In case of BSA, such critical surface coverage seems to be related to the formation of a complete protein monolayer, followed by building of a second protein layer, according to a two-step adsorption process [25,41]. When the first protein layer is completed, the interaction between the BSA molecules present in solution and the surface is considerably attenuated. Consequently, the second layer is formed only through weaker protein–protein interactions [25,41]. Therefore,

proteins approaching the surface may hit the pre-adsorbed ones in the formed multilayer causing their desorption from the surface [46]. Considerable reduction of surface coverage with proteins upon blocking has been reported also previously [21].

### 3.3. Immunoreaction: efficiency dependent on probe solution concentration

The $Si_3N_4$ surfaces, that have been functionalized by contact pin-printing of the BSA-TBZ probe and blocked with BSA, were exposed to a solution of monoclonal anti-TBZ antibody to complete the basic steps of an immunoassay procedure. The formed protein layers were characterized in order to investigate the effect of BSA-TBZ concentration in the printing solution on the assay efficiency.

Analysis by AFM provided topography images of protein layers after the immunoreaction with the antibody (Fig. 4) as well as the parameters of their nanostructure (Fig. 5). The examination of lateral nanostructures reveals that the immunoreaction step induces a significant increase of the mean size of surface features, 2whm, from 20–25 nm to 30–35 nm for all printing solution concentrations used (Fig. 5**b**). This finding supports the affinity binding between BSA-TBZ and antibody molecules, since the specific protein binding can be observed in AFM images as enlargement of surface features [20,23,38]. In addition, although the protein layer nanostructures prior to immunoreaction were comparable for all probe concentrations in the printing solution, both the surface roughness RMS (Fig. 5a) and the AFM height extent (Fig. 4) increase after immunoreaction as the probe concentration in the printing solution increases. These observations accord with differences in protein amount added onto the surface after immunoreaction, as revealed by ellipsometry (Fig. 6) and XPS measurements (Fig. S2 in Supplementary Material). While for the surface functionalized with a 25 μg/mL BSA-TBZ solution, the increase of protein surface density is minimal, the employment of a 100 μg/mL probe solution results in nearly two-fold increase in the protein amount determined on the surface after immunoreaction. Based on the ellipsometry data, a molar binding ratio of ~2.7 for antibody to BSA-TBZ conjugate can be calculated in case a 100 μg/mL solution has been employed for the surface functionalization.

The results discussed above suggest that the efficiency of immunoreaction performed on the $Si_3N_4$ surfaces increases as the concentration of BSA-TBZ probe in the solution used for the functionalization of the surface increases. The main reason for such dependence is the difference in the relative amount of BSA-TBZ in the protein layer after the blocking procedure. The contribution of the probe molecules, which are the binding sites for the antibodies, in the protein layer formed on the surface after blocking increases with the concentration of BSA-TBZ used in the immobilization step as discussed in Section 3.2. Moreover, as revealed by the analysis of intensity of TOF-SIMS signal characteristic for TBZ molecule (Fig. S3 in Supplementary Material), the relative amount of BSA-TBZ molecules in the overall protein layer is preserved during immunoreaction excluding the hypothesis of probe desorption during this step.

## 4. Conclusions

Multiple surface science techniques including AFM, ellipsometry, XPS and TOF-SIMS were employed to examine silicon nitride surfaces after the subsequent steps of biofunctionalization and immunoreaction involved in an assay for the detection of fungicide TBZ. Such complex analysis of structure, protein density and probe composition of protein layers formed on silicon substrates provides crucial information about the optimal conditions of probe immobilization with respect to assay performance.

The comparison of two approaches for probe deposition, namely contact pin-printing and hand macro-spotting, revealed enhanced immobilization efficiency for the former, resulting in almost two-fold increase in protein surface density as compared to the later. This shows that contact pin-printing is advantageous for the biofunctionalization of integrated immunosensors on silicon chips. Probe (BSA-TBZ) monolayers and bilayers are formed at low and high concentrations of the printing solution, respectively. The effect of blocking procedure was also analyzed and its dependence on the initial surface density of immobilized probe was revealed. It was found, that BSA molecules used to block the free surface sites adsorb to the surfaces with low BSA-TBZ coverage to form a complete protein monolayer. On the other hand, in case of high surface coverage with BSA-TBZ molecules, blocking induces a reduction of the previously formed BSA-TBZ bilayers into monolayers. The differences in the BSA-TBZ amount in the different protein layers, formed after biofunctionalization and blocking, have direct impact on the immonoreaction efficiency, which increases as the printing solution concentration increases. The optimum conditions of surface biofunctionalization were found for a printing solution with a concentration of 100 μg/mL, leading to the highest efficiency of specific anti-TBZ antibody binding to the immobilized probe molecules.

## Acknowledgments

This work was supported by the EU funded project “FOOD-SNIFFER” (FP7-ICT8-318319) and sponsored from the Polish state funds for science in the years 2014-15 granted for the realization of co-financed international project. The equipment was purchased thanks to the financial support of the European Regional Development Fund (POIG.02.01.00-12-023/08). K.G. is grateful for financial support from the M. Smoluchowski Kraków Research Consortium (in the framework of the KNOW scholarship).

## Appendix A. Supplementary data

Supplementary data associated with this article can be found, in the online version, at http://dx.doi.org/10.1016/j.apsusc.2017.03.100.

## References

[1] S.H. Takayama, J.C. McDonald, E. Ostuni, M.N. Liang, P.J. Kenis, R.F. Ismagilov, G.M. Whitesides, Patterning cells and their environments using multiple laminar fluid flows in capillary networks, Proc. Natl. Acad. Sci. U. S. A. 96 (1999) 5545–5548.
[2] A.D. Dias, D.M. Kingsley, D.T. Corr, Recent advances in bioprinting and applications for biosensing, Biosensors 4 (2014) 111–136.
[3] T.F. Didar, A.M. Foudeh, M. Tabrizian, Patterning multiplex protein microarrays in a single microfluidic channel, Anal. Chem. 84 (2012) 1012–1018.
[4] I. Barbulovic-Nad, M. Lucent, Y. Sun, M. Zhang, A.R. Wheeler, M. Bussmann, Bio-microarray fabrication techniques – a review (review), Crit. Rev. Biotechnol. 26 (2006) 237–259.
[5] V. Romanov, S.N. Davidoff, A.R. Miles, D.W. Grainger, A critical comparison of protein microarray fabrication technologies, Analyst 139 (2014) 1303–1326.
[6] K. Gajos, M. Angelopoulou, P. Petrou, K. Awsiuk, S. Kakabakos, W. Haasnoot, A. Bernasik, J. Rysz, M.M. Marzec, K. Misiakos, I. Raptis, A. Budkowski, Imaging and chemical surface analysis of biomolecular functionalization of monolithically integrated on silicon Mach-Zehnder interferometric immunosensors, Appl. Surf. Sci. 385 (2016) 529–542.
[7] M. Angelopoulou, A. Botsialas, A. Salapatas, P. Petrou, W. Haasnoot, E. Makarona, G. Jobst, D. Goustouridis, A. Siafaka-Kapadai, I. Raptis, K. Misiakos, S. Kakabakos, Assessment of goat milk adulteration with a label-free monolithically integrated optoelectronic biosensor, Anal. Bioanal. Chem. 407 (2015) 3995–4004.
[8] V. Pagkalia, P. Petrou, A. Salapatas, E. Makarona, J. Peters, W. Haasnoot, G. Jobst, A. Economou, K. Misiakos, I. Raptis, S. Kakabakos, Detection of ochratoxin A in beer samples with a label-freemonolithically integrated optoelectronic biosensor, J. Hazard. Mater. 323 (Part A) (2017) 75–83.
[9] A.B. Gonzalez-Guerrero, M. Alvarez, A.G. Castano, C. Dominguez, L.M. Lechuga, A comparative study of in-flow and micro-patterning biofunctionalization

protocols for nanophotonic silicon-based biosensors, J. Colloid Interface Sci. 393 (2013) 402–410.
[10] M.J. Bañuls, R. Puchades, Á. Maquieira, Chemical surface modifications for the development of silicon-based label-free integrated optical (IO) biosensors: a review, Anal. Chim. Acta 777 (2013) 1–16.
[11] D. Samanta, A. Sarkar, Immobilization of bio-macromolecules on self-assembled monolayers: methods and sensor applications, Chem. Soc. Rev. 40 (2011) 2567–2592.
[12] Q. Peng, D.M.Y. Lai, E.T. Kang, K.G. Neoh, Preparation of polymer-silicon(100) hybrids via interface-initiated reversible addition-fragmentation chain-transfer (RAFT) polymerization, Macromolecules 39 (2006) 5577–5582.
[13] J. Ji, L. Li, K. Xia, L. Li, S. Shang, Poly(acrylic acid)-silicon hybrids prepared via a RAFT-mediated process and covalent immobilization of glucose oxidase, J. Macromol. Sci. Part A: Pure Appl. Chem. 49 (2012) 316–320.
[14] F. Liu, Y. Chen, Y. Wei, L. Li, S. Shang, Surface modification of polythiophene and poly(3-methyl thiophene) films by graft copolymerization, J. Appl. Polym. Sci. 123 (2012) 2582–2587.
[15] A. Budkowski, J. Klein, L. Fetters, Brush formation by symmetric and highly asymmetric diblock copolymers at homopolymer interfaces, Macromolecules 28 (1995) 8571–8578.
[16] M. Kitsara, P. Petrou, D. Kontziampasis, M. Misiakos, E. Makarona, I. Raptis, K. Beltsios, Biomolecular layer thickness evaluation using white light reflectance spectroscopy, Microelectron. Eng. 87 (2010) 802–805.
[17] H.S. Mansur, R.L. Orefice, W.L. Vasconcelos, Z.P. Lobato, L.J. Machado, Biomaterial with chemically engineered surface for protein immobilization, J. Mater. Sci. Mater. Med. 16 (2005) 333–340.
[18] E. Mavrogiannopoulou, P. Petrou, S. Kakabakos, K. Misiakos, Real-time detection of BRCA1 gene mutations using a monolithic silicon optocoupler array, Biosens. Bioelectron. 24 (2009) 1341–1347.
[19] M.-Ch Tu, Y.-T. Chang, Y.-T. Kang, H.-Y. Chang, P. Chang, T.-R. Yew, A quantum dot-based optical immunosensor for human serum albumin detection, Biosens. Bioelectron. 34 (2012) 286–290.
[20] K. Awsiuk, A. Budkowski, P. Petrou, A. Bernasik, M.M. Marzec, S. Kakabakos, J. Rysz, I. Raptis, Model immunoassay on silicon surfaces: vertical and lateral nanostructure vs. protein coverage, Colloids Surf. B 103 (2013) 253–260.
[21] K. Awsiuk, A. Psarouli, P. Petrou, A. Budkowski, S. Kakabakos, A. Bernasik, J. Rysz, I. Raptis, Spectroscopic and microscopic examination of protein adsorption and blocking of non-specific binding to silicon surfaces modified with APTES and GOPS, Procedia Eng. 25 (2011) 334–337.
[22] K. Gajos, A. Budkowski, V. Pagkali, P. Petrou, M. Biernat, K. Awsiuk, J. Rysz, A. Bernasik, K. Misiakos, I. Raptis, S. Kakabakos, Indirect immunoassay on functionalized silicon surface: molecular arrangement, composition and orinetation examined step-by-step with multi-technique and multivariate analysis, Colloids Surf. B 150 (2017) 437–444.
[23] K. Awsiuk, A. Bernasik, M. Kitsara, A. Budkowski, P. Petrou, S. Kakabakos, S. Prauzner-Bechcicki, J. Rysz, I. Raptis, Spectroscopic and microscopic characterization of biosensor surfaces with protein/amino-organosilane/silicon structure, Colloids Surf. B 90 (2012) 159–168.
[24] K. Awsiuk, A. Budkowski, A. Psarouli, P. Petrou, A. Bernasik, S. Kakabakos, J. Rysz, I. Raptis, Protein adsorption and covalent bonding to silicon nitride surfaces modified with organo-silanes: comparison using AFM, angle-resolved XPS and multivariate ToF-SIMS analysis, Colloids Surf. B 110 (2013) 217–224.
[25] M.P. Gispert, A.P. Serro, R. Cola, B. Saramago, Bovine serum albumin adsorption onto 316L stainless steel and alumina: a comparative study using depletion, protein radiolabeling, quartz crystalmicrobalance and atomic force microscopy, Surf. Interface Anal. 40 (2008) 1529–1537.
[26] R. Santanu, A.G. Shard, Qunatitative analysis of adsorbed prtoeins by X-ray photoelectron spectroscopy, Anal. Chem. 83 (2011) 8659–8666.
[27] L. Li, S. Chen, S. Jiang, Protein adsorption on alkanethiolate self-assembled monolayers: nanoscale surface structural and chemical effects, Langmuir 19 (2003) 1974–2982.
[28] M.S. Wagner, D.G. Castner, Characterization of adsorbed protein films by time-of-flight secondary ion mass spectrometry with principal component analysis, Langmuir 17 (2001) 4649–4660.
[29] A. Abad, J.J. Manclús, M.J. Moreno, A. Montoya, Determination of thiabendazole in fruit juices by a new monoclonal enzyme immunoassay, J. AOAC Int. 84 (2001) 156–161.
[30] K. Misiakos, I. Raptis, E. Makarona, A. Botsialas, A. Salapatas, P. Oikonomou, A. Psarouli, P. Petrou, S. Kakabakos, K. Tukkiniemi, M. Sopanen, G. Jobst, All-silicon monolithic Mach-Zehnder interferometer as a refractive index and biochemical sensor, Opt. Express 22 (2014) 26803–26813.
[31] I. Horcas, R. Fernandez, J.-M. Gomez-Rodriguez, J. Colchero, J. Gomez-Herrero, A.M. Baro, WSXM: A software for scanning probe microscopy and a tool for nanotechnology, Rev. Sci. Instrum. 78 (2007) 013705.
[32] H.R. Philipp, Optical properties of silicon nitride, J. Electrochim. Soc. 120 (1973) 295–300.
[33] J.A. Howarter, J.P. Youngblood, Optimization of silica silanization by 3-Aminopropyltriethoxysilane, Langmuir 22 (2006) 11142–11147.
[34] J. Kim, J. Cho, P.M. Seidler, N.E. Kurland, V.K. Yadavalli, Investigations of chemical modifications of amino-terminated organic films on silicon substrates and controlled protein immobilization, Langmuir 26 (2010) 2599–2608.
[35] A.P. Cuypers, J.W. Corsel, M.P. Janssen, J.M. Kop, W. Th Hermens, H.C. Hemker, The adsorption of prothrombin to phosphatidylserine multilayers quantitated by ellipsometry, J. Biol. Chem. 258 (1983) 2426–2431.
[36] Z. Tsialla, A. Ucles-Moreno, P. Petrou, A.R. Fernandez-Alba, S. Kakabakos, Development of an indirect enzyme immunoassay for the determination of thiabendazole in white and red wines, Intern. J. Environ. Anal. Chem. 95 (2015) 1299–1309.
[37] C.Y. Lee, G.M. Harbers, D.W. Grainger, L.J. Gamble, D.G. Castner, Fluorescence XPS, and TOF-SIMS surface chemical state image analysis of DNA microarrays, J. Am. Chem. Soc. 129 (2007) 9429–9438.
[38] K. Gajos, P. Petrou, A. Budkowski, K. Awsiuk, A. Bernasik, K. Misiakos, J. Rysz, I. Raptis, S. Kakabakos, Imaging and spectroscopic comparison of multi-step methods to from DNA arrays based on the biotin-streptavidin system, Analyst 140 (2015) 1127–1139.
[39] P. Gong, G.M. Harbers, D.W. Grainger, Multi-technique comparison of immobilized and hybridized oligonucleotide surface density on commercial amine-reactive microarray slides, Anal. Chem. 78 (2016) 2342–2351.
[40] H. Urano, S. Fukuzaki, Conformation of adsorbed bovine serum albumin governing its desorption behavior at alumina-water interfaces, J. Biosci. Bioeng. 90 (2000) 105–111.
[41] K. Rezwan, L.P. Meier, M. Rezwan, J. Voros, M. Textor, L.J. Gauckler, Bovine serum albumin adsorption onto colloidal Al2O3 particles: a new model based on zeta potential and UV–vis measurements, Langmuir 29 (2004) 10055–10061.
[42] M.S. Wagner, D.G. Castner;1, Characterization of adsorbed protein films by time-of-flight secondary ion mass spectrometry with principal component analysis, Langmuir 17 (2001) 4649–4660.
[43] Z.J. Lv, J.H. Wang, G.P. Chen, L.H. Deng, Imaging recognition events between human IgG and rat anti-human IgG by atomic force microscopy, Int. J. Biol. Macromol. 47 (2010) 661–667.
[44] O. Ouerghi, A. Touhami, A. Othmane, H. Ben Ouada, C. Martelet, C. Fretigny, N. Jaffrezic-Renault, Investigating specific antigen/antibody binding with the atomic force microscope, Biomol. Eng. 19 (2002) 183–188.
[45] I. Ferrer, J.F. Garcia-Reyes, A. Fernandez-Alba, Identification and quantitation of pesticides in vegetables by liquid chromatography time-of-flight mass spectrometry, TrAC, Trends Anal. Chem. 24 (2005) 671–682.
[46] M. Rabe, D. Verdes, S. Seeger, Understanding protein adsorption phenomena at solid surfaces, Adv. Colloid Interface Sci. 162 (2011) 87–106.

**Supplementary Material**

# Contact pin-printing of albumin-fungicide conjugate for silicon nitride-based sensors biofunctionalization: multi-technique surface analysis for optimum immunoassay performance

Katarzyna Gajos[a], Andrzej Budkowski[a], Zoi Tsialla[b], Panagiota Petrou[b], Kamil Awsiuk[a], Paweł Dąbczyński[a], Andrzej Bernasik[c,d], Jakub Rysz[a], Konstantinos Misiakos[e], Ioannis Raptis[e], Sotirios Kakabakos[b]

[a]M. Smoluchowski Institute of Physics, Jagiellonian University, Łojasiewicza 11, 30-348 Kraków, Poland

[b]Institute of Nuclear & Radiological Sciences & Technology, Energy & Safety NCSR Demokritos, P. Grigoriou & Neapoleos St, Aghia Paraksevi 15310, Athens, Greece

[c]Faculty of Physics and Applied Computer Science, AGH University of Science and Technology, Mickiewicza 30, 30-059 Kraków, Poland

[d]Academic Centre for Materials and Nanotechnology, AGH University of Science and Technology, Mickiewicza 30, 30-059 Kraków, Poland

[e]Department of Microelectronics, Institute of Nanoscience and Nanotechnology, NCSR Demokritos, P. Grigoriou & Neapoleos St, Aghia Paraksevi 15310, Athens, Greece

* Corresponding author

*E-mail address*: katarzyna.gajos@doctoral.uj.edu.pl

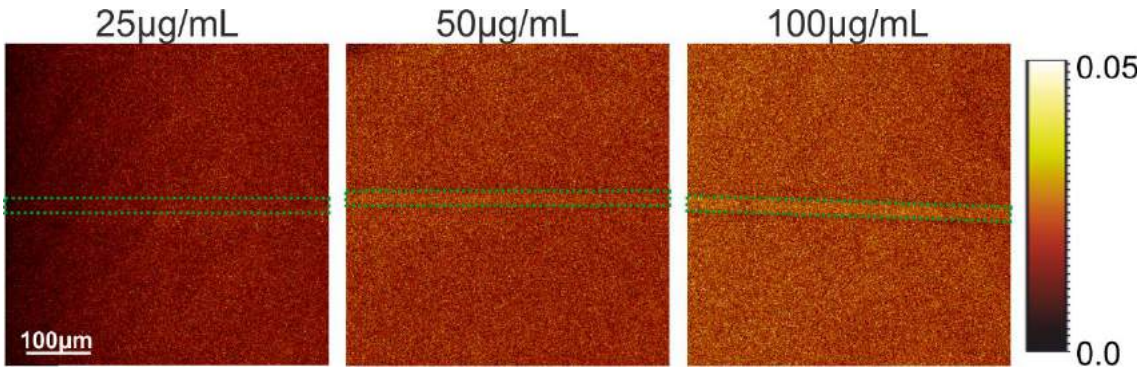


**Figure S1.** TOF-SIMS chemical images of ion $C_5H_{10}N^+$ characteristic for proteins recorded from the sensing arm areas of Mach-Zehnder interferometers integrated on silicon chips after functionalization by contact pin-printing of BSA-TBZ solution with different concentration. The sensing arm areas are marked with the green frame.

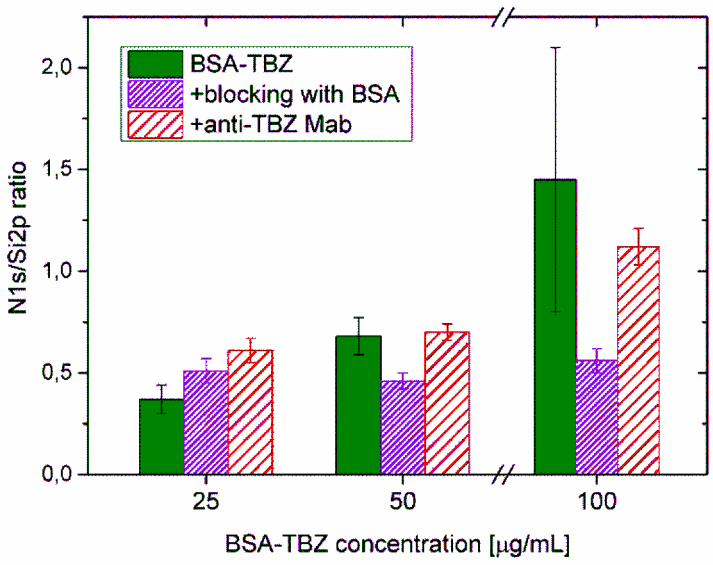


**Figure S2.** The N1s/Sip ratio of concentration of elements characteristic for proteins (N1s) and silicon substrate (Si2p) reflecting the amount of immobilized onto the surface protein as determined by XPS spectrometry. The ratio was evaluated for planar amino-silanized $Si_3N_4$ surfaces after functionalization by contact pin-printing of BSA-TBZ solutions with different concentrations as well as after the subsequent blocking and immunoreaction steps. The reference value of the ratio, $0.038 \pm 0.004$, was determined for the silanized $Si_3N_4$ substrate.

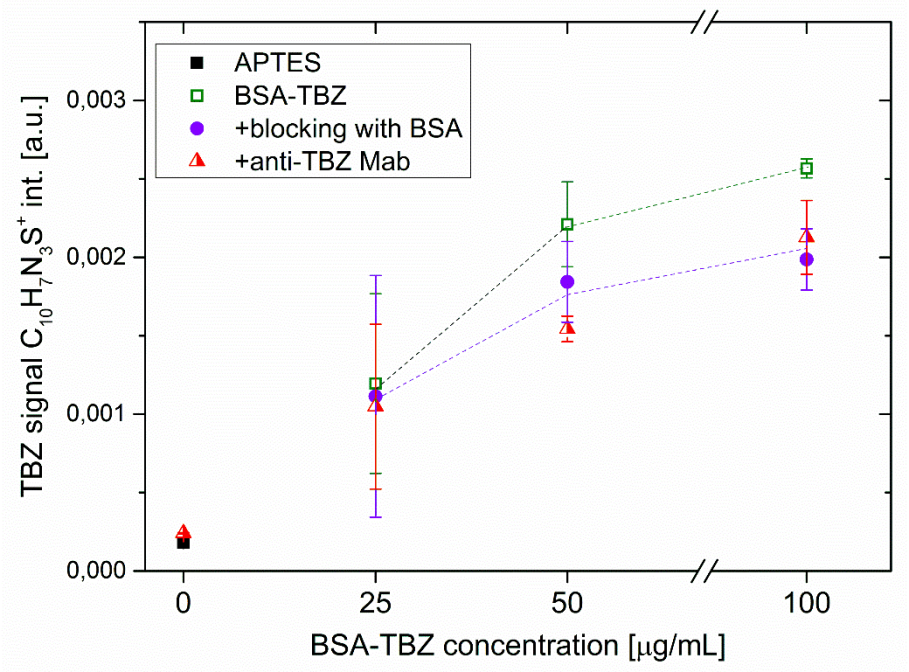


**Figure S3.** TOF-SIMS analysis of protein layers formed on sensing arm areas of Mach-Zehnder interferometers after functionalization by contact pin-printing of BSA-TBZ solutions with different concentrations as well as after the subsequent blocking and immunoreaction steps. The normalized intensity of TOF-SIMS signal $C_{10}H_7N_3S^+$ characteristic for TBZ molecule reflects the relative amount of BSA-TBZ conjugate in the protein layer.